UCLA
UCLA Electronic Theses and Dissertations

Title

Scalable Lithographic Approaches for Nanoscale Chemical Patterning and Hierarchical Nanostructure Fabrication

Permalink

https://escholarship.org/uc/item/49m3b18m

Author

Yang, Qing

Publication Date

2018

Peer reviewed|Thesis/dissertation

eScholarship.org Powered by the California Digital Library
University of California

UNIVERSITY OF CALIFORNIA

Los Angeles

Scalable Lithographic Approaches for Nanoscale Chemical Patterning and Hierarchical Nanostructure Fabrication

A dissertation submitted in partial satisfaction of the requirements for the degree of Doctor of Philosophy in Chemistry

by

Qing Yang

2018

© Copyright by

Qing Yang

2018

ABSTRACT OF THE DISSERTATION

Scalable Lithographic Approaches for Nanoscale Chemical

Patterning and Hierarchical Nanostructure Fabrication

by

Qing Yang

Doctor of Philosophy in Chemistry

University of California, Los Angeles, 2018

Professor Paul S. Weiss, Chair

The ability to fabricate materials, structures, devices, and systems with nanometer-scale precision is the key to obtain superior properties and performance. The scalability of lithographic approaches can promote them from research implementation to practical applications. My graduate research focuses on several unconventional lithographic techniques we have developed, which can create high-precision nanoscale patterns and three-dimensional (3D) hierarchical structures with high reproducibility, low cost, high throughput, and high precision.

A hybrid patterning strategy called polymer-pen chemical lift-off lithography (PPCLL) was developed. We used pyramidal and v-shaped polymer-pen arrays for the sub-micron chemical patterning. By introducing the stamp support system and height gradients, we obtained linear-arrays of chemical patterns with linewidths ranging from

sub-50 nm to sub-500 nm in sub-20 nm increments. We also showed our capability to tune feature size by controlling the compression distance. In doing so, we extended the patterning capability of PPCLL to generate more complex hollow patterns and gold nanorings. Self-collapse lithography (SCL) was another chemical lift-off lithography (CLL) based patterning technique. When elastomeric stamps with microscale relief features contacted with the self-assembled monolayer (SAM) functionalized substrates, the roof of the stamp collapses, resulting in the removal of SAM molecules in contact regions. With this technique, chemical patterns with feature size from ~2 μm to below 30 nm were obtained by decreasing stamp relief heights.

We developed a robust and general strategy called multiple-patterning nanosphere lithography (MP-NSL) to fabricate periodic 3D hierarchical nanostructures in a highly scalable and tunable manner. The application of MP-NSL enables the fabrication of silicon nanotubes at the wafer scale with nanometer-scale control of outer diameter, inner diameter, height, hole-depth, and pitch. By adopting a multiple-patterning nanosphere lithography strategy, we are able to fabricate mechanically stable volcano-shaped nanostructures, called "nanovolcanos" with controllable heights, hole diameters/depths, and pitches. The sub-20-nm sharp features of nanovolcanos enable penetration of cell membranes and minimize disruption of cell functions. Biomolecular payloads containing the gene-editing packages are assembled and encapsulated into supramolecular nanoparticles. The holes (calderas) of the nanovolcanos can carry high payloads of biomolecular cargos that are readily accessed once cell membranes are penetrated.

The dissertation of Qing Yang is approved.

Xiangfeng Duan

Yu Huang

Paul S. Weiss, Committee Chair

University of California, Los Angeles

2018

Dedicated to my son, Charles Yang

Table of Contents

List of Figures and Tables...ix

List of Abbreviations and Symbols...xxvi

Acknowledgments...xxx

Biographical Sketch...xxxv

Chapter 1. Lithography is the Path to the Nanoscale World

1.1 State-of-the-Art Lithography Techniques...2
1.1.1. Conventional Photolithography and Beyond...4
1.1.2. Benchtop Lithography Approach: Soft Lithography...6
1.1.3. Direct-Write Lithography Approaches: Electron-Beam Lithography and Scanning Probe Lithography...9
1.2 Chemical Lift-Off Lithography...10
1.3 Nanosphere Lithography...16
1.4 Conclusions and Dissertation Overview...19
1.5 References...21

Chapter 2. Polymer-Pen Chemical Lift-Off Lithography

2.1 Abstract...39
2.2 Introduction...40
2.3 Materials and Methods...43
2.4 Results and Discussions...47
2.5 Conclusions and Prospects...63
2.6 Supplementary Materials...64
2.7 References...69

Chapter 3. Deformation-Controlled Chemical Patterning *via* External Force Using Polymer-Pen Chemical Lift-Off Lithography

3.1 Abstract...81
3.2 Introduction...82

3.3 Materials and Methods....85
3.4 Results and Discussions....88
3.5 Conclusions and Prospects....95
3.6 Supplementary Materials....96
3.7 References....99

Chapter 4. Self-Collapse Lithography

4.1 Abstract....107
4.2 Introduction....108
4.3 Materials and Methods....111
4.4 Results and Discussions....114
4.5 Conclusions and Prospects....127
4.6 Supplementary Materials....128
4.7 References....131

Chapter 5. Multiple-Patterning Nanosphere Lithography for Fabricating Periodic Three-Dimensional Hierarchical Nanostructures

5.1 Abstract....141
5.2 Introduction....142
5.3 Materials and Methods....144
5.4 Results and Discussions....147
5.5 Conclusions and Prospects....160
5.6 Supplementary Materials....161
5.7 References....171

Chapter 6. Silicon Nanovolcanos for Direct Gene Delivery with High Efficiency and Cell Viability

6.1 Abstract....179
6.2 Introduction....180
6.3 Materials and Methods....182
6.4 Results and Discussions....184
6.5 Conclusions and Prospects....194
6.6 Supplementary Materials....195

6.7 References..200

List of Figures and Tables

Figure 1.1. Field emission scanning electron microscopy (FESEM) image of patterned 11-mercaptoundecanoic acid (MUDA) SAMs on a gold substrate. The figure is reprinted from reference 124 with permission..8

Figure 1.2. Schematic diagram of alkanethiol molecules self-assembled on a noble metal substrate. The figure is reprinted from reference 129 with permission............10

Figure 1.3. Schematic diagram illustrating the process of chemical lift-off lithography. The figure is reprinted from reference 86 with permission......................12

Figure 1.4. X-ray photoelectron spectroscopy measurements on PDMS stamps after CLL. The binding energies at 80 and 84 eV are characteristic of gold $4f_{5/2}$ and $4f_{7/2}$ transitions. Oxygen plasma is required for lift-off of SAM molecules. The figure is modified from reference 86 with permission..13

Figure 1.5. Chemical lift-off lithography can be used to pattern gold substrates as well as PDMS stamps. Scanning electron microscopy (SEM), atomic force microscopy (AFM), and variable-pressure SEM were used to characterize the materials. The figure is reprinted from reference 131 with permission...14

Figure 1.6. Applications of chemical lift-off lithography: (a) field-effect transistors (FET) based biosensor, (b) functional bio-substrates with improved DNA hybridization efficiencies, and (c) spin-filtering substrates. The figures are adapted from references 58, 133, 134 with permission...15

Figure 1.7. Experimental setup to prepare high-quality polystyrene monolayers *via* the *Langmuir-Blodgett* method...17

Figure 1.8. Nanosphere lithography can be used to fabricate a variety of nanostructures through single-step patterning (deposition or etching). In either case, oxygen plasma is first used to reduce the sphere size (A). For example, we can fabricate (B) silver bowties, (C) gold nanoholes, and (D) Si nanopillars........................18

Figure 2.1. Scanning electron microscopy (SEM) images of: (a) Si master with recessed pyramidal structures having base linewidths of 3 µm and a periodicity of 4 µm; (b) polydimethylsiloxane (PDMS) stamp with pyramidal polymer-pen arrays replicated from the master in (a); (c) polymer-pen chemical lift-off lithography (PPCLL) pattern produced using the stamp in (b) without external compression; (d) Si master with recessed v-shaped structures with base linewidths of 3.8 µm and a periodicity of 7 µm; (e) PDMS stamp with v-shaped polymer pen arrays replicated from the master in (d); (f) typical PPCLL pattern produced using the stamp in (b) without external compression. (Insets: high magnification SEM images) (The images (c) and (f) are processed to visualize the patterns better; the unprocessed images are shown in Figure S2.3)..48

Scheme 2.1. Schematic illustrations of polymer-pen chemical lift-off lithography (PPCLL) using pyramidal (top) and v-shaped (bottom) polymer pen arrays. In both cases, in the first step, hydroxyl-terminated alkanethiol molecules form self-assembled monolayers (SAMs) on Au/Cr/Si substrates. The polydimethylsiloxane (PDMS) stamps carrying the polymer-pen arrays are then activated with oxygen plasma treatment. In the second step, an activated PDMS stamp is brought into conformal contact with the SAM on a Au/Cr/Si substrate using a known vertical compression distance. Condensation reactions occur between the

hydroxyl-terminated SAM molecules and the activated PDMS stamp to form strong covalent bonds. In the third step, the PDMS stamp is lifted off of the substrate, removing a portion of SAM molecules (~70%) together with Au adatoms from the contact areas to produce a complementary pattern on the substrate and an organogold monolayer on the stamp in the regions of contact. The contact/feature linewidth (L) is controlled by the vertical compression distance (z) of the stamp during contact *via* the relationship $L = f(z)$......50

Figure 2.2. (a) Simulation: cross-sectional view of a v-shaped polymer pen (base linewidth: 4-μm) vertically compressed onto a rigid Au surface with a vertical compression distance of z and a resulting contact linewidth of $L = f(z)$. (b) Simulation results: increasing the vertical compression distance z leads to increased contact linewidth (L). The relationship between vertical compression distance z and L is fitted using the quadratic equation $L = f(z) = a + bz + cz^2$, where a, b, and c are constants......53

Figure 2.3. (a) Illustration of a polydimethylsiloxane (PDMS) stamp used in polymer-pen chemical lift-off lithography (PPCLL) having support elements (taller v-shaped polymer pens with flat tips) interleaved with v-shaped polymer pens (sharp tips with designed base linewidths w_i): before contact, after placement on a substrate but with no vertical compression, and after vertical compression. Here, D_0 ($D_0 > h_i$) is the initial vertical distance from the base of the polymer pens to the surface of each substrate before contact; h_i is the height of a polymer pen; D_i is distance from the polymer pen tip to the substrate, $D_i = D_0 - h_i$; z is the vertical compression distance and L is resulting contact linewidth. (b) Simulation of results

where v-shaped polymer pen base linewidths (*w*) and vertical compression distances (*z*) were varied to control contact-dependent linewidths (*L*), *i.e.*, *L = f(w, z)*......56

Figure 2.4. (a) A scanning electron microscope (SEM) image of a polymer-pen array having designed height gradients and a stamp support system; Inset: cross-sectional view to show height differences. (b) A SEM image of a polymer-pen chemical lift-off lithography (PPCLL) pattern produced by the stamp in (a). (c) A plot of experimental and simulation results of the relationship between the linewidths of the PPCLL patterns and the v-shaped polymer pen base linewidths. Below are four SEM images of typical PPCLL patterned lines corresponding to the four data points circled in different colors. Note, L_1, L_2, L_3, and L_4 are measured linewidths; w_1, w_2, w_3, and w_4 are the corresponding base linewidths in nm. (The images (b) and insets of (c) are processed to visualize the patterns better; the unprocessed images are shown in Figures S2.3 and S2.4.)......59

Table 2.1. Measured and simulated patterning results of polymer-pen chemical lift-off lithography using stamp support elements and v-shaped polymer pens over a series of designed base linewidths. All values are in nm......60

Figure 2.5. (a) After polymer-pen chemical lift-off lithography (PPCLL) patterning, thiolated DNA molecules are inserted into the patterned regions and fluorescently labeled complementary target DNA is hybridized on the substrate. (b) A typical fluorescence microscopy image after hybridization. (False color (green) is used to enhance pattern image.)......62

Scheme S2.1. The fabrication scheme of silicon masters and polydimethylsiloxane (PDMS) stamps..64

Figure S2.1. Atomic force microscope (AFM) height images of (a) inverted pyramid on a silicon master and (b) protruding pyramid on a polydimethylsiloxane (PDMS) stamp. The AFM data were collected using a Bruker Dimension Icon Scanning Probe Microscope. Surface roughness was measured inside the square dashed-line areas for each image using the instrument software, Nanoscope Analysis. The R_a is the arithmetic average of absolute values and R_q is the root mean square of the data points..65

Figure S2.2. A scanning electron microscope image of a polydimethylsiloxane (PDMS) stamp with gradient arrays. Insets: photographs of (i) a silicon master and (ii) a PDMS stamp..66

Figure S2.3. Unprocessed images of Figures 2.1c, 2.1f, and 2.4b......................................67

Figure S2.4. A full set of scanning electron microscope images of line patterns with a series of different linewidths ($L_{measured}$) patterned from a series of corresponding v-shaped polymer pens with linewidths ($w_{measured}$) as listed in Table 2.1......................68

Figure 3.1. (a,b) Scanning electron microscopy (SEM) images of silicon masters and PDMS stamps consist of flat-tip pyramid arrays (base linewidth = 15.2 ± 0.1 μm, tip = 3.6 ± 0.1 μm). (c) The change of tip dimensions over silicon etching time. Inset: illustration of the anisotropic etching of Si(100) to generate recessed silicon pyramids. Note: image (b) was taken at a 30° relative to the surface normal...............88

Figure 3.2. Schematic illustrations of deformation-controlled polymer-pen chemical lift-off lithography (PPCLL) with and without external force. Polymer-pen chemical

lift-off lithography without external force: the oxygen-plasma-activated PDMS stamp was brought into conformal contact with the SAM-coated Au/Cr/Si substrate and compressed only by its weight F_0. The stamp was then lifted-off to remove a layer of organogold monolayer from the contact areas, leaving complementary square arrays on the gold surface. The square size (L) can be expressed as $L = f(F_0)$. After multiple cycles of PPCLL without external force, the tip areas of the stamp are fully "deactivated". Polymer-pen chemical lift-off lithography with external force: tip-deactivated stamp was brought into contact with a fresh SAM-coated Au/Cr/Si substrate with external stress of F_1. After chemical lift-off, a hollow pattern with feature thickness of $\Delta L=1/2\ (f(F_0+F_1)-f(F_0))$ was created..90

Figure 3.3. (a) Scanning electron microscopy (SEM) images of square chemical pattern fabricated by polymer-pen chemical lift-off lithography (PPCLL) without external weight. (c) After selective Au etching, Au square holes were observed. The dimension of chemical patterns was identical to the tip size, but the Au square holes were slightly larger due to lateral etch. (b,d) SEM images of hollow chemical pattern fabricated by deformation-controlled polymer-pen chemical lift-off lithography (DC-PPCLL) and hollow Au rings after etching..92

Figure S3.1. Water contact angle measurement of the polydimethylsiloxane (PDMS) stamp before and after oxygen plasma treatment..96

Figure S3.2. Scanning electron microscopy (SEM) images of Au nanorings with different numbers of polymer-pen chemical lift-off lithography (PPCLL) without external weight. The number of defects in the central gold regions decreased with increased number of "deactivations" steps...97

Figure S3.3. Scanning electron microscopy (SEM) image of hollow Au nanorings over a large area after selective etching......98

Figure 4.1. Schematic illustration of self-collapse lithography (SCL). (a,d) Hydroxyl-terminated alkanethiols form a self-assembled monolayer (SAM) on the surface of a Au/Ti-coated Si substrate. A polydimethylsiloxane (PDMS) stamp is activated by oxygen plasma treatment. (b,e) The activated stamp is brought into conformal contact with the SAM-coated Au surface without externally applied forces. (c,f) The chemical lift-off process removes the SAM from regions of the functionalized surface in direct contact with the stamp, thereby producing a pattern from molecules remaining in non-contacted regions......115

Table 4.1. Gap linewidths (L) produced using stamps with different channel heights (h) and channel widths (w), with a fixed Young's modulus (E = 1.75 MPa)......117

Figure 4.2. (a, b) Scanning electron microscope (SEM) images of linear arrays with sub-200 nm linewidths created by self-collapse lithography using a stamp with microchannel features (6 µm channel width, 300 nm channel height). (c) Schematic illustration of a collapsed stamp (L: gap linewidth; w: channel width; and h: channel height). (d) Plot of gap linewidths L obtained using different channel heights h with a fixed Young's modulus of 1.75 MPa. The channel width for each data point is listed in Table 4.1. Insets correspond to a representative SEM image for each data point.....118

Table 4.2. Gap linewidths (L) produced using stamps with different Young's moduli (E), and a fixed channel height (h = 400 nm) and width (w = 10 µm)......119

Figure 4.3. (a) Schematic illustration of the self-collapse model used in finite element analysis (FEA) simulations, where σ_r represents the restoring stress and σ_a denotes

the adhesion stress between the PDMS stamp and the substrate. (b) A typical FEA simulation result illustrating the stress distribution on a self-collapse stamp (only the restoring stresses normal to the substrate are depicted). (c) Relationships between simulated stresses and gap sizes *L* at different channel heights *h*. (d) Experimentally measured gap widths and channel heights (squares) plotted with simulated values (circles, triangles) using Young's moduli (*E*) of 2.0 and 2.1 MPa. (e) Simulated gap linewidths plotted as a function of channel height with a parabolic fit. (f) Plots of simulated and experimental results showing variations in gap linewidths at different values of *E*..120

Figure 4.4. (a–c) Schematic illustrations of a ring chemical pattern fabricated *via* self-collapse lithography (SCL). (a) Hydroxyl-terminated alkanethiols form a self-assembled monolayer (SAM) on the surface of an Au/Ti-coated Si substrate. (b) A stamp with recessed circular features is activated by oxygen plasma and then placed into conformal contact with the functionalized Au surface, without an external force. The central portions of the recessed features on the stamp contact the underlying SAM in smaller circular regions due to self-collapse. (c) The chemical lift-off process removes the SAM in direct contact with the polydimethlysiloxane (PDMS) surfaces from the Au substrate, leaving raised (dark), ring-like SAM patterns behind. (d–f) Contrast enhanced SEM images of (d) ring patterns (*L* ~1.71 µm), patterned by SCL with a stamp with recessed circles (50 µm in diameter and 1 µm in height), (e) a ring pattern (*L* ~235 nm) patterned using recessed circles (40 µm in diameter and 400 nm in height), and (f) raised (dark) squares (*L* ~1.71 µm)

patterned with recessed square structures (100 μm on each edge and 1 μm in height)....123

Figure 4.5. Optical microscope images of Au micro/nanostructures fabricated by self-collapse lithography (SCL) followed by selective etching. (a) The Au rings with linewidths of 1.71 μm were fabricated using stamps patterned with 100-μm-diameter circles recessed by 1 μm. (b) Here, Au lines 870 nm wide were fabricated using stamps possessing recessed linear features that were 40 μm wide and 700 nm deep. (c) Sub-2 μm Au squares fabricated using stamps patterned with recessed square features that were 100 μm on an edge and 1 μm in height. (d) Sub-250 nm Au squares fabricated using stamps with recessed squares that were 40 μm in width and 400 nm in height....125

Figure S4.1. Plots of simulation results at different Young's moduli. The relationships between stress at the critical point and gap linewidths at a 400-nm channel height are shown....128

Figure S4.2. Scanning electron microscope (SEM) images of (a) ring patterns (L ~1.71 μm) patterned by a stamp with recessed circles (50 μm diameter and 1 μm height). (b) A ring pattern (L ~235 nm) by a stamp with recessed circles (40 μm diameter and 400 nm height), (c) hollow squares (L ~1.71 μm) by a stamp with recessed square structures (100 μm length and 1 μm height)....129

Figure S4.3. Scanning electron microscope (SEM) images of line patterns at the corners with a stamp height of 500 nm....130

Figure 5.1. Self-aligned multiple-patterning nanosphere lithography (MP-NSL) for Si nanotube arrays. (A) A schematic illustration of the process. Step 1: a monolayer of close-packed polystyrene (PS) nanospheres is formed at a water/air interface, then transferred onto a Si wafer. The size of the nanospheres defines the ultimate pitches (p) of the Si nanotubes. Step 2: oxygen plasma RIE reduces the sphere size and defines the outer diameters (d_o) of Si nanotubes. Step 3: deep reactive ion etching (DRIE) etches Si into nanopillars by using the nanospheres as masks. The outer heights (h_o) of Si nanotubes are controlled by the etch time. Step 4: a second oxygen plasma RIE further reduces the sizes of polymer nanoparticles and defines the inner diameters (d_i) of Si nanotubes. Step 5: Ni is deposited to form Ni nanorings on the Si nanopillars and it functions as a DRIE mask. Step 6: polystyrene nanoparticles are removed by 10 min oxygen plasma etching to expose the center part of the Si nanopillars. Step 7: DRIE is performed again to etch holes and to define the hole depth (h_i). Step 8: Ni is removed by HCl and pristine Si nanotube arrays are obtained. Scanning electron microscope (SEM) images of key intermediates: (B) monolayer of closed-packed polystyrene nanospheres (diameter: 1 μm) formed on a Si wafer; (C) polystyrene nanoparticles on Si wafer after first size reduction; (D) polystyrene nanoparticles on top of periodic Si nanopillar arrays; (E) second size reduction of polystyrene nanoparticles by oxygen plasma (step 4); and (F) Ni nanorings on top of Si nanopillars. The region displayed as dark is Si and the region displayed as bright is Ni. (G) Etching of the inner regions by DRIE to form Si nanotubes (step 7). Images (D, E, G) were taken at a tilt of 30°. Scale bars: 1 μm..148

Table 5.1. Controlling size reduction of polystyrene nanospheres by oxygen plasma reactive ion etching (RIE)..150

Table 5.2. Controlling sidewall thicknesses (*w*) of Si nanotubes by varying the etch time difference between two oxygen plasma reactive ion etching................................153

Figure 5.2. (A-H) Scanning electron micrographs (SEM) of representative periodic Si nanotube arrays with different parameters in nm: pitch (*p*), outer diameter (d_o), inner diameter (d_i), sidewall thickness ($w = (d_o - d_i)/2$), and outer height (h_o). Images were recorded at a tilt of 30°. (Units: nm)..153

Table 5.3. Tuning the outer/inner heights (h_o/h_i) of Si nanotubes by controlling the duration of deep reactive ion etching..154

Figure 5.3. (A) Schematic illustration of tuning the outer and inner diameters (d_o and d_i, respectively) of Si nanotubes. (B) Top-view scanning electron microscopy (SEM) images of Si nanotubes fabricated from 1 µm polystyrene nanospheres with d_o = 730 ± 7 nm, and sidewall width ($w=(d_o-d_i)/2$) from 105 ± 5 nm to 290 ± 7 nm (scale bar: 400 nm); (C) Top-view SEM images of Si nanotubes fabricated from 2 µm polystyrene (PS) nanospheres with d_o = 1340 ± 12 nm, and *w* from 120 ± 12 nm to 420 ± 8 nm (scale bar: 400 nm). (D) Oxygen plasma reactive ion etching (RIE) time dependent size reduction of polystyrene nanoparticles. (E) Oxygen plasma RIE time dependent *w* corresponding to (B,C) with d_o = 1340 ± 12 nm. (F) Schematic illustrations of independent control of h_o and h_i. From left to right, $h_o > h_i$, $h_o = h_i$, and $h_o < h_i$. Bottom: SEM images of corresponding Si nanotube cross-sections prepared by focused ion beam milling with Pt (white part) as protection layer (scale bar: 500 nm). (G) Plot of DRIE time dependence of h_o and h_i. Si etch rates were

0.66 μm/min for h_o and 0.50 μm/min (0-3 min)/ 0.18 μm/min (3-8 min) for h_i, respectively....156

Figure 5.4. (A) By using multiple-patterning nanosphere lithography, a variety of periodic hierarchical nanostructures have been designed and fabricated: Si nanotowers with two levels, three levels, and four levels with tunable heights (including negative heights for selected levels) and diameters for each level; configurable concentric plasmonic Au nanorings/nanodisk on Si substrates (solid/hollow two-level nanotowers), SiO_2 nanostructures (two-level nanotowers), and flexible polydimethylsiloxane (PDMS) substrates (negatively replicated hollow nanotowers). (B) Reflection visible-infrared spectra of Au/Si nanotowers with different dimensions. Solid lines are the experiment results and dotted lines are corresponding simulation results. (Sample sizes in nm, sample i: p=900, d_1=530, h_1=300, d_2=320, h_2=230, and t_{Au}=50; Sample ii: p=900, d_1=570, h_1=230, d_2=320, h_2=300, and t_{Au}=50). Note that, the spectra (500 to 6000 nm) were collected using two different spectrometers with different ranges (500 to 2500 nm and 2500 to 6000 nm respectively) and stitched together at 2500 nm for comparison to simulations (see detailed description in the supporting information)....158

Figure S5.1: (A) A typical scanning electron microscope (SEM) image of close-packed 1 μm polystyrene spheres in micro-scale. (B) A photograph of Si wafers fully covered by close-packed 1 μm polystyrene spheres. The reflected colors indicate the well-ordered configuration of the polystyrene microspheres. (C) The corresponding fast Fourier transform (FFT) of the SEM image....162

Figure S5.2. (A) A typical scanning electron microscope (SEM) image of a large area of the silicon nanotube arrays. (B) The corresponding fast Fourier transform (FFT) of the image. (C) A typical SEM image of large-area silicon nanotube arrays recorded at a tilt of 30°..........163

Figure S5.3. A typical scanning electron microscope (SEM) image of a large area of silicon nanostructures recorded at a tilt of 30°..........164

Figure S5.4. A typical scanning electron microscope image of polystyrene nanospheres with oblate ellipsoid shapes after oxygen plasma reactive ion etching..........165

Figure S5.5. Enhancing the adhesion between the polystyrene nanospheres and the underlying silicon substrate before dry etching helps to prevent tilting of the etched polymer nanoparticles, which could lead to asymmetries in the final pillar/nanotube arrays without heating..........166

Figure S5.6. (A) A high-resolution scanning electron microscope (SEM) image of silicon nanopillars made *via* the Bosch process. The top surfaces of the silicon nanopillars are smooth. The average distance between valleys and peaks on the sidewall of a silicon nanopillar is ~25 nm. (B) A high-resolution SEM image of four-level silicon nanotowers shows the smooth surfaces on the four levels..........167

Figure S5.7. A scanning electron microscope (SEM) image of periodic silicon nanopillars with smooth sidewalls fabricated by single-step deep reactive ion etching..........168

Figure S5.8. A high-resolution scanning electron microscope (SEM) image of 50 nm Au evaporated silicon nanostructures..........169

Figure S5.9. (A) The visible-infrared reflectance spectra of sample ii. Insets: simulation results of the electric-field distribution of sample ii under photoexcitation (cross section). (B,C) Simulation of charge distributions on the Au surfaces on different layers of the sample ii at the two major dips (1830 nm and 4500 nm), from which we can see the 1830 nm mode is a combination of different multipole modes from the three layers; while the 4500 nm mode corresponds to the quadrupole modes of all three layers..170

Figure 6.1. (a) Schematic of the nanovolcano fabrication process. An array of polystyrene (PS) spheres is first assembled on a silicon wafer, which is then exposed to oxygen plasma to reduce the sphere size. Single-step dry etching of the silicon defines the cone-shape structure. Next, a thin layer of nickel is deposited to serve as a protective layer prior to removal of the polystyrene spheres. Hole-depth can be controlled independently *via* a second drying etching step. The nickel layer is removed by immersing substrates into hydrochloric acid. Scanning electron micrographs of representative (b) silicon nanovolcanos with hole diameters of 610 ± 20 nm and height of 3.0 ± 0.1 µm. (c, d) Top and side views of a typical nanovolcano: edge width is generally less than 20 nm. Note: for (b) and (d), images were taken at 30° tilt. Therefore, the actual height should be double the measured height..185

Table 6.1. Summary of Fabrication Conditions and Measured Dimensions of Nanovolcanos..187

Figure 6.2. (a) The reversible assembly of supramolecular nanoparticles (SMNPs) relies on the molecular recognition between adamantane (Ad) and β-cyclodextrin

(β-CD) motifs. (b) Three molecular building blocks of supramolecular nanoparticles: cyclodextrin-grafted polyethyleneimine (CD-PEI) and adamantane-grafted polyamidoamine dendrimer (Ad-PAMAM) first assemble into hydrogel networks that encapsulate desired biomolecular cargos (*e.g.,* nucleic acids) within the cationic core. The addition of adamantane-grafted poly(ethylene glycol) (Ad-PEG) both constrains the growth of SMNPs and increases water solubility...188

Figure 6.3. (a) Schematic overview of the nanovolcano-mediated cell transfection process: (i) first, silicon nanovolcanos are functionalized with Ad-motifs *via* a two-step surface modification procedure. (ii) freshly prepared supramolecular nanoparticles (SMNPs) are loaded into the nanovolcanos. (iii) U87 glioblastoma cells cultured on top of substrates. Scanning electron microscopy (SEM) reveals several key stages during the transfection process. (b) Upon addition of the SMNP suspension, the nanovolcanos were fully loaded with nanoparticles (false-colored in red). (c) Overview of U87 cells cultured on top of nanovolcanos. (d) Cross-sectional SEM image of nanovolcanos interacting with a U87 cell. The nanovolcanos are false-colored in blue to visualize their relative positions compared to the cell membrane. The tops of nanovolcanos penetrated the cell membranes. (e) Cross-sectional SEM image demonstrating the active intracellular uptake of two nanoparticles (false-colored in red). Note: (d) and (e) were milled by focused ion beam (FIB) and imaged by tilting the stage 52°. The original SEM images can be found in Supporting Information, Figure S6.5..190

Figure 6.4. (a) Supramolecular nanoparticles (SMNPs) encapsulated with eGFP plasmid are used to transfect U87 cells. (b) Supramolecular nanoparticles (SMNPs)

loaded with anti-GFP short interfering RNA (siRNA) are delivered to GFP-expressing U87 cells..193

Figure S6.1. The size distribution of supramolecular nanoparticles (SMNPs) measured by dynamic light scattering (DLS). The average diameter of SMNPs is 130 ± 30 nm..195

Figure S6.2. Full fabrication process of silicon nanovolcanos. (1) polystyrene microspheres are assembled into close-packed monolayers at water/air interface and then transferred to silicon substrate. (2) Oxygen plasma is used to reduce sphere size. (3) Single-step deep reactive ion etching (DRIE) is used to etch silicon with desired cone angle. (4) A thin film of nickel (~15 nm) is deposited as the protection layer. (5) Polystyrene spheres are removed by adhesive tape and a second single-step DRIE is used for hole etching. (6) Nickel film is removed by immersing substrates into hydrochloric acid. (7) Assemble supramolecular nanoparticles into the holes..196

Figure S6.3. Dry etching of silicon nanocones with different C_4F_8/SF_6 ratio. The apex diameters as well as hole diameters become larger with increased C_4F_8. For example, in (a) C_4F_8/SF_6 = 23 sccm/27 sccm, and in (b) C_4F_8/SF_6 = 25 sccm/27 sccm................197

Figure S6.4. Representative scanning electron microscope (SEM) images of silicon nanovolcanos with different parameters. (a) Column #2 in Table 6.1: pitch = 2.0 μm; height = 2.5 ± 0.1 μm; hole diameter = 740 ± 30 nm. (b) Column #3 in Table 6.1: pitch = 2.0 μm; height = 1.6 ± 0.1 μm; hole diameter = 1000 ± 30 nm. (c) Column #4 in Table 6.1: pitch = 1.0 μm; height = 1.8 ± 0.1 μm; hole diameter = 550 ± 20 nm. (b)

Column #5 in Table 6.1: pitch = 5.0 μm; height = 4.7 ± 0.1 μm; hole diameter = 1650 ± 50 nm..........198

Figure S6.5. Original scanning electron microscope (SEM) images for Figure 6.3b, 6.3d, and 6.3e..........199

List of Abbreviations and Symbols

National Nanotechnology Initiative (NNI)

Integrated circuits (ICs)

Lithium-ion battery (LIB)

Nanometer (nm)

Micrometer (µm)

Centimeter (cm)

Electron-beam lithography (EBL)

Scanning probe lithography (SPL)

Chemical lift-off lithography (CLL)

Polydimethylsiloxane (PDMS)

Nanosphere lithography (NSL)

Silicon dioxide (SiO_2)

Ultraviolet (UV)

Extreme ultraviolet (EUV)

Microcontact printing (µCP)

Replica molding (REM)

Self-assembled monolayers (SAMs)

Field emission scanning electron microscopy (FESEM)

11-mercaptoundecanoic acid (MUDA)

Kilovolt (kV)

Atomic force microscopy (AFM)

X-ray photoelectron spectroscopy (XPS)

Scanning electron microscopy (SEM)

Field-effect transistors (FET)

Picomolar (pM)

Deoxyribonucleic acid (DNA)

Polystyrene (PS)

Localized surface plasmon resonance (LSPR)

Three-dimensional (3D)

Polymer-Pen Chemical Lift-Off Lithography (PPCLL)

Focused Ion-Beam (FIB)

Hydroxyl (OH)

Polymer-Pen Lithography (PPL)

Potassium Hydroxide (KOH)

Reactive Ion Etching (RIE)

Silicon (Si)

Chromium (Cr)

Gold (Au)

Micromole (μM)

Milimolar (mM)

Ethylenediaminetetraacetic acid (EDTA)

Two dimensional (2D)

Rounds per minute (RPM)

Hydrofluoric acid (HF)

Deformation-controlled polymer-pen chemical lift-off lithography (DC-PPCLL)

Tridecafluoro-1,1,2,2-tetrahydrooctyl-1-trichlorosilane (TFOCS)

Integrated Systems Nanofabrication Cleanroom (ISNC)

Deionized (DI)

Self-Collapse Lithography (SCL)

Two-Dimensional (2D)

Nitrogen gas (N_2)

Finite Element Analysis (FEA)

Megapascal (MPa)

Multiple-Patterning Nanosphere-Lithography (MP-NSL)

Sodium Dodecyl Sulfate (SDS)

Inductively Coupled Plasma Reactive Ion Etching (ICP-RIE)

Deep Reactive Ion Etching (DRIE)

Nickel (Ni)

Finite-Difference-Time-Domain (FDTD)

Infrared (IR)

Ultraviolet-Visible-Near Infrared (UV-VIS-NIR)

Integrating Sphere Attachment (ISR)

Polarization Modulation-Infrared Reflection-Adsorption Spectroscopy (PM-IRRAS)

Fast Fourier Transform (FFT)

Enhanced Green Fluorescent Protein (eGFP)

Ribonucleic Acid (RNA)

4’,6-Diamidino-2-Phenylindole (DAPI)

Nanovolcano (SNV)

Small Interfering RNA (siRNA)

Dulbecco's Modified Eagle's Medium (DMEM)

Cyclodextrin-Grafted Polyethyleneimine (CD-PEI)

Adamantane-Grafted Polyamidoamine Dendrimer (Ad-PAMAM)

Adamantane-Grafted Poly(ethylene glycol) (Ad-PEG)

American Type Culture Collection (ATCC)

Radio Frequency (RF)

Supramolecular Nanoparticles (SMNPs)

Dimethyl Sulfoxide (DMSO)

Charge-Coupled Device (CCD)

Dynamic Light Scattering (DLS)

Cyclodextrin (CD)

β-Cyclodextrin (β-CD)

Adamantane (Ad)

Acknowledgments

This is the end of one journey, and this is the start of another journey. After submitting this dissertation, my five years of graduate research career has formally ended. Looking back to these years of study and research, I realized that the path to doctorate is not just earning a degree, but also a *Sādhana* of life. Only persistence can lead me to the final destination. During these five years of study at this world-class research institute, I'm fortunate to work with so many intelligent people. Many people have contributed to my research career, and I would like to thank all of you sincerely.

First, I would like to thank Professor Paul S. Weiss for his excellent mentorship. I still remember the first-time meeting with him, his easygoing style reduces my nervousness and his insights about science impress me deeply. After joining his lab, I am able to explore different areas of research topics in a diverse group. He always shows supports to my ideas, regardless of its novelty and feasibility, and tries to find resources and people that could help me. In these years of working under Paul, one important philosophy I have learned is to work as a team, as everyone can offer unique skills and perspectives. Another beneficial habit I have learned from Paul is to focus on details, even it is as small as a punctuation. I would also like to thank Professor Anne A. Andrews, who is an outstanding scientist in neuroscience. I really appreciate her guidance and efforts towards several projects that I am involved. I also want to thank my committee members: Profesor Xiangfeng Duan, Professor Yu Huang, and Professor William M. Gelbart.

Secondly, I would like to thank my excellent colleagues: Dr. Xiaobin Xu, Dr. Steven Jonas, Chuanzhen Zhao, Wenfei Liu, Dr. Liane Slaughter, Dr. Huan Cao, Dr. Naihao Chiang, Dr. Sara Rahimnejad, Natcha Wattanatorn, Diana Yugay, Logan Stewart, Kevin Cheung, Jason Belling, and all other members from our lab. Also, I want to acknowledge the efforts contributed from our collaborators: Professor Hsian-Rong Tseng from University of California, Los Angeles, Professor Chad A. Mirkin from Northwestern University, Professor Cengiz Ozkan, and Professor Mihri Ozkan from University of California, Riverside.

Thirdly, I would like to thank the help from all staffs in the Chemistry and Biochemistry Department, California Nanosystems Institute (CNSI), and Nanolab. In addition, I want to thank the funding sources and agencies, including the National Science Foundation (NSF), the U.S. Department of Energy, the Air Force Office of Scientific Research, Alex's Lemonade, and Hyundai Hope on Wheels, that make our research possible.

Lastly, I really want to say "thank you" from the bottom of my heart to all my family members for their generous support and understanding. Words are far from enough to express my gratitude to my family. Even during the toughest time in my graduate career, they are still on my side and encourage me to overcome the challenges. I want to thank my parents, Lu Yang and Xiuying Hu, and my brother, Zhen Yang for 29 years of company. I also want to thank my in-laws, Aoliang Yan and Jianhua Tang, for giving me the chance to take care of their daughter, Yiran Yan, who is the best wife and strongest mother in the world.

In the end, I want to leave the most important place for my son, Charles Yang. You are the most beautiful creation of my life (more coming soon…). Well, also thank you for waking me up several times every night!

Chapter 2 is adapted from the following publication:

Xu, X.[#]; **Yang, Q.**[#]; Cheung, K. M.; Zhao, C.; Wattanatorn, N.; Belling, J. N.; Abendroth, J. M.; Slaughter, L. S.; Mirkin, C. A.; Andrews, A. M.; Weiss, P. S. Polymer-Pen Chemical Lift-Off Lithography. *Nano Lett.* **2017**, *17*, 3302–3311.

X. Xu and Q. Yang contributed equally to this work. The experiments were designed by X. Xu, Q. Yang, and P. S. Weiss. Data were collected and analyzed by X. Xu, Q. Yang, K. M. Cheung, C. Zhao, N. Wattanatorn, J. N. Belling, P. S. Weiss, and A. M. Andrews. Figures were prepared by X. Xu and Q. Yang. The manuscript was written by X. Xu, Q. Yang, P. S. Weiss, and A. M. Andrews with assistance from all other authors. We acknowledge the financial supports from the National Science Foundation Grant CMMI-1636136, the CSC-UCLA scholarship, the Royal Thai Government Fellowship, the Merkin Family Foundation Postdoctoral Fellowship, and the Air Force Office of Scientific Research under Awards FA9550-12-1-0141 and FA9550-16-1-0150.

Chapter 4 is adapted from the following publication:

Zhao, C.; Xu, X.; **Yang, Q.**; Man, T.; Jonas, S. J.; Schwartz, J. J.; Andrews, A. M.; Weiss, P. S. Self-Collapse Lithography. *Nano Lett.* **2017**, *17*, 5035–5042.

The experiments were designed by C. Zhao, X. Xu, and P. S. Weiss. Data were collected and analyzed by C. Zhao, X. Xu, Q. Yang, T. Man, P. S. Weiss, and A. M. Andrews. Figures were prepared by C. Zhao, X. Xu, and J. J. Schwartz. The manuscript was written by C. Zhao, X. Xu, S. J. Jonas, J. J. Schwartz, P. S. Weiss, and A. M. Andrews with assistance from all other authors. We acknowledge the financial supports from the National Science Foundation Grant CMMI-1636136, the CSC-UCLA scholarship, the Eli and Edythe Broad Center of Regenerative Medicine and Stem Cell Research at UCLA Training Program through its Clinical Fellowship Training Award Program, and the UCLA Children's Discovery and Innovation Institute's (CDI) Fellows Research Support Award.

Chapter 5 is adapted from the following publication:

Xu, X.; **Yang, Q.**; Wattanatorn, N.; Zhao, C.; Chiang, N.; Jonas, S. J.; Weiss, P. S. Multiple-Patterning Nanosphere Lithography for Fabricating Periodic Three-Dimensional Hierarchical Nanostructures. *ACS Nano* **2017**, *11*, 10384-10391.

The experiments were designed and conducted by all X. Xu, Q. Yang, N. Wattanatorn, and C. Zhao. The data were collected and analyzed by all authors. X. Xu and N. Chiang designed and carried out the simulations. The manuscript was written and edited by all authors. We gratefully acknowledge the financial supports from the National Science Foundation grant CMMI-1636136, CSC-UCLA scholarship, the Royal Thai Government Fellowship, the Eli and Edythe Broad Center of Regenerative Medicine and Stem Cell Research at UCLA Training Program through its Clinical Fellowship Training Award Program, the Young Investigator Award funds from the Hyundai Hope on Wheels Foundation, the Alex's Lemonade Stand

Foundation, and the David Geffen School of Medicine and Eli and Edythe Broad Center of Regenerative Medicine and Stem Cell Research at UCLA for seed funding.

Biographical Sketch

Qing Yang attended University of Illinois, Urbana-Champaign in 2009 as an undergraduate in the Chemistry Department. Besides finishing the required courses with excellent grades, he also participated in two research groups as an undergraduate researcher. He joined Professor John A. Rogers group for fabrication of flexible/stretchable electronic devices using nanofabrication techniques. He also conducted research in Professor Prashant K. Jain group. He synthesized high-quality CdS or CdSe nanocrystals and performed cation exchange to explore new classes of nanomaterials. He also studied the kinetics of galvanic replacement of Ag nanospheres with Au^{3+}. He received several awards and honors during his undergraduate career, including Summer Research Fellowship, Glenn Rhodes Wilson Fellowship, John Gieseking Scholarship, and Dean's list. In 2013, he received his *Bachelor of Science* degree in Chemistry.

In 2013, he decided to go to University of California, Los Angeles to start his graduate research career. He joined Professor Paul S. Weiss research group from Department of Chemistry and Biochemistry. His graduate researches involved: (1) development of a high-throughput nanoscale patterning technique known as "Polymer-Pen Chemical Lift-off Lithography"; (2) use multiple patterning strategy on polystyrene (PS) nanosphere arrays to generate hierarchical silicon nanostructures; (3) development of silicon nanospear, nanoneedle and nanovolcano arrays for high throughput, high efficiency intracellular delivery while maintaining high cell viability; He will receive his *Ph.D.* degree in Chemistry (Materials and Nanoscience specialization) after submitting this thesis in the September of 2018.

Publications

1. Smith, J. G.; **Yang, Q.**; Jain, P. K. Identification of a Critical Intermediate in Galvanic Exchange Reactions by Single-Nanoparticle-Resolved Kinetics, *Angew. Chem. Int. Ed.* 2014, 53, 2867–2872.
2. Xu, X.[#]; **Yang, Q.**[#]; Cheung, K. M.; Zhao, C.; Wattanatorn, N.; Belling, J. N.; Abendroth, J. M.; Slaughter, L. S.; Mirkin, C. A.; Andrews, A. M.; Weiss, P. S. Polymer-Pen Chemical Lift-Off Lithography. *Nano Lett.* **2017**, *17*, 3302–3311.
3. Zhao, C.; Xu, X.; **Yang, Q.**; Man, T.; Jonas, S. J.; Schwartz, J. J.; Andrews, A. M.; Weiss, P. S. Self-Collapse Lithography. *Nano Lett.* **2017**, *17*, 5035–5042.
4. Xu, X.; **Yang, Q.**; Wattanatorn, N.; Zhao, C.; Chiang, N.; Jonas, S. J.; Weiss, P. S. Multiple-Patterning Nanosphere Lithography for Fabricating Periodic Three-Dimensional Hierarchical Nanostructures. *ACS Nano* **2017**, *11*, 10384-10391.
5. Slaughter, L. S.; Cheung, K. M.; Kaappa, S.; Cao, H. H.; **Yang, Q.**; Young, T. D.; Serino, A. C.; Malola, S.; Olson, J. M.; Link, S.; Häkkinen, H.; Andrews, A. M.; Weiss, P. S. Patterning of Supported Gold Monolayers *via* Chemical Lift-Off Lithography. *Beilstein J. Nanotechnol.* **2017,** *8*, 2648–2661.
6. Xu, X.; Hou, S.; Wattanatorn, N.; Wang, F.; **Yang, Q.**; Zhao, C.; Yu, X.; Tseng, H.-R.; Jonas, S. J.; Weiss, P. S. Precision-Guided Nanospears for Targeted and High-Throughput Intracellular Gene Delivery. *ACS Nano* **2018,** *12*, 4503–4511.
7. Zhao, C.; Xu, X.; Bae, S.-H.; **Yang, Q.**; Liu, W.; Belling, J. N.; Cheung, K. M.; Rim, Y. S.; Yang, Y.; Andrews, A. M.; Weiss, P. S. Large-Area, Ultrathin Metal-Oxide Semiconductor Nanoribbon Arrays Fabricated by Chemical Lift-Off Lithography. *Nano Lett.* **2018**, Article ASAP.

Chapter 1

Lithography is the Path to the Nanoscale World

1.1 State-of-the-Art Lithography Techniques

In 2000, President *Bill Clinton* announced the establishment of the National Nanotechnology Initiative (NNI), which involves more than 20 federal departments and independent agencies working together to understand and to control materials at the nanoscale.[1] Reducing the dimensions of materials to the nanometer scale significantly improves their performance, and generates unique properties. Over the past 20 years, the application of nanotechnology to diverse materials has opened up new and exciting opportunities in many fields, including integrated circuits (ICs),[2-10] data storage,[11-13] displays,[14-16] flexible and wearable electronics,[17-24] solar cells,[25-29] lithium-ion battery (LIB),[30-47] supercapacitors,[48-54] sensing/diagnostics,[55-69] gene/drug delivery,[70-82] and tissue engineering.[71,83,84]

The development of nanotechnology relies on the ability to fabricate nanoscale materials, structures, devices, and systems with controlled dimensions and properties. The semiconductor manufacturing market, for example, is currently on the order of $500 billion per annum.[7] Increasingly sophisticated nanofabrication techniques are the major driving force in miniaturizing the functional components and building up the structural hierarchy. In 2014, Intel's fifth-generation transistors were commercialized with a minimum feature size of 14 nm, which was well beyond the diffraction limit.[3] Within the semiconductor industry, the most advanced lithography techniques can fabricate transistors with sub-20-nm features in full-scale production. However, the high cost (over $50 million per tool and over $5 million per mask sets[85]) and complex protocols make them impractical for use by research laboratories and small companies. Therefore, my graduate research aims to elaborate alternative lithography approaches that can create nanoscale patterns and nanostructures with merits of low cost, high throughput, scalability, and nanometer-scale control.

In the next few sections of this chapter, I discuss the mainstream lithography techniques that are frequently used in research laboratories. They can be categorized into two main approaches: parallel replication and direct writing. Sections **1.1.1** and **1.1.2** discuss conventional photolithography and soft lithography, two representative parallel replication techniques. The throughputs of these two approaches are high, but their resolution is limited by light diffraction or molecular diffusion. Diffraction limits the resolution of conventional photolithography to approximately half of the illuminating wavelength.[4] The lateral diffusion of ink molecules in soft lithography results in poor pattern fidelity with a resolution limit of ~100 nm.[86] I introduce electron-beam lithography (EBL) and scanning probe lithography (SPL) as two direct-write patterning approaches in section **1.1.3**. Direct-write patterning is a maskless technique that can write software-designed patterns with dimensions as low as 5 nm,[87] but it suffers from low throughput and high cost. Reducing expenses and simplifying the process while maintaining nanometer-scale resolution remains an unsolved problem.

Second, I introduce two novel lithography techniques that form the basis of the lithography approaches developed in later chapters. The first technique is chemical lift-off lithography (CLL), which uses oxygen-plasma-activated polydimethylsiloxane (PDMS) stamps to remove molecules in the contact area selectively (**section 1.2**);[86] this strategy produces high-throughput and fidelity chemical patterns in a straightforward manner. The second technique is nanosphere lithography (NSL), which uses hexagonally close-packed nanospheres (*e.g.*, polystyrene and SiO_2) as lithography masks to pattern underlying substrates (**section 1.3**).[88-91] By patterning the nanosphere multiple times, we can fabricate a series of periodic three-dimensional nanostructures with fully controlled parameters.

1.1.1 Conventional Photolithography and Beyond

Photolithography, as the primary fabrication workhorse of the semiconductor industry, is a top-down process that utilizes ultraviolet (UV) light to replicate patterns from photomask to photoresist. In this technique, light-sensitive polymers, known as photoresists, are spin-coated onto target substrates, followed by a dehydration bake (also called soft bake). Exposure of photoresists to UV light through photomasks transfers patterns by changing the photoresist solubility in the exposed regions. There are two types of photoresists: positive and negative tones. In the former, the exposed regions can be dissolved, while they will remain when the unexposed areas are dissolved in the latter. Following the above treatment, the substrates are baked again (known as a post-exposure bake) and then immersed in the developing solvent to remove the exposed or unexposed regions of photoresists, creating the same or complementary patterns thereof on the substrates. The patterns are further transferred to underlying substrates *via* deposition (*e.g.*, of metals and oxides) or etching of the open regions. There are three common configurations of photolithography: contact printing, proximity printing, and projection.[87] The most common form of photolithography in research laboratories is contact printing, where photomasks are placed in hard contact with substrates, and UV radiation at 365 nm (known as the *i*-line) is used to expose the photoresist. In general, contact printing and proximity printing can be used to generate resist patterns at the micron scale. Projection printing utilizes a radiation at 193 nm and optical lens systems to reduce the feature size to 37 nm.[4,87]

More advanced photolithography techniques have been developed, including liquid immersion, multiple patterning, short wavelength X-ray, and extreme ultraviolet (EUV) photolithography, to push the resolution limits below 10 nm. While these methods can produce large-area, nanometer-scale patterning, they are accessible only to a few major semiconductor

companies due to complex processes and great costs involved. The initial investments required are prohibitively high for research institutes, start-ups, and biotechnology companies. Moreover, current photolithography techniques are only suitable for planar and hard substrates such as silicon and silicon dioxide wafers, with limited applicability to flexible and nonplanar electronics.

1.1.2 Benchtop Lithography Approach: Soft Lithography

Soft lithography, a set of benchtop patterning techniques developed by Professor George Whitesides and others, is often adopted as an alternative approach to conventional photolithography in many areas.[92-101] Soft and flexible elastomeric stamps, molds, and conformable photomasks are used to transfer patterns onto target substrates at high throughput addressing large areas.[93] The most commonly used elastomeric material is the polydimethylsiloxane stamp, which can be reused many times without degradation.[94] One advantage of soft lithography is that it can pattern various types of materials or structures on curved, nonplanar, and flexible substrates at micro- or nanoscale resolution.[93,95,102,103] A series of techniques based on soft lithography has been developed, including microcontact printing (μCP),[94,104-108] replica molding (REM),[109] microtransfer molding,[110] solvent-assisted micromolding,[111] microdisplacement printing,[112,113] microcontact insertion printing,[114] and phase-shift edge lithography.[115,116]

Among these techniques, microcontact printing has been broadly adopted in many applications as a straightforward, inexpensive approach for fabricating microscale features over large areas.[94] This technique involves two major parts: (1) fabrication of masters/stamps and (2) use of the stamps to transfer patterns onto target substrates. Part (1) employs one of two primary techniques, photolithography or electron-beam lithography, to fabricate masters. While the former can fabricate large-area masters, resolution is limited to approximately half of the wavelength due to light diffraction. Alternatively, EBL can write small features, but it is slow and expensive. After fabrication of masters, PDMS pre-polymers are cast over the masters and cured. The PDMS stamps are then peeled off the masters and ready for use. In part (2), the stamps are first “inked” with alkanethiol molecules, proteins, nanoparticles, or DNA molecules.

They are subsequently brought into conformal contact with target substrates, and the “inks” are transferred onto the contact regions. When alkanethiol molecules are used, they form well-ordered self-assembled monolayers (SAMs) on noble metal surfaces. The SAMs can serve as “molecular resists” against different wet etchants, enabling patterns to be transferred reproducibly onto underlying substrates.[117-119] The function of the resists is limited by pinhole defects that give developer access to the substrate.[120-123]

There are, however, two major drawbacks to this technique. First, the fabrication of masters relies on either conventional photolithography, which is high throughput but limited in resolution, or e-beam lithography, which produces masters with sub-micron features but is expensive and low throughput. Second, the resolution of patterns created by μCP is limited by lateral diffusion of low-molecular-weight molecules across the substrate surface, causing poor pattern fidelity. The field emission scanning electron microscopy (FESEM) image in **Figure 1.1** presents a pattern of 11-mercaptoundecanoic acid (MUDA) SAMs on a gold substrate.[124] In these data, at a primary electron beam energy of 1 kV, the darker regions surrounded the squares correspond to the lateral diffused MUDA molecules along the edges; they have lower mass coverage compared to the square regions. Regions with more ordered packing emit more secondary electrons, resulting in higher intensity in FESEM.

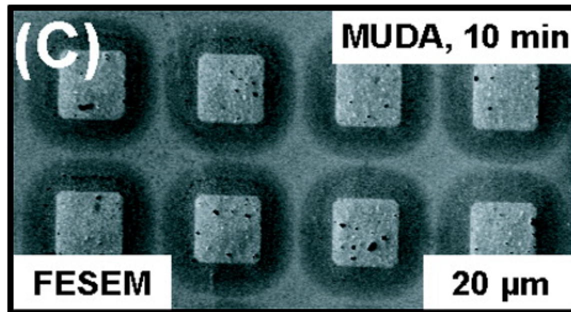

Figure 1.1. Field emission scanning electron microscopy (FESEM) image of patterned 11-mercaptoundecanoic acid (MUDA) SAMs on a gold substrate. The figure is reprinted from reference 124 with permission.

1.1.3 Direct-Write Lithography Approaches: Electron-Beam Lithography and Scanning Probe Lithography

Electron-beam lithography is a maskless, direct-writing technique that uses a high energy electron beam to pattern electron-sensitive polymers. The resolution is limited by the electron beam spot size, which can be as low as 5 nm. In the general procedure, electron-sensitive polymers are spin-coated onto target substrates, and the electron beam exposes the polymers in a programmed spot-by-spot process. Subsequent development of the polymers dissolves the exposed regions. As writing time increases exponentially with decreasing feature size, EBL is intrinsically expensive and slow, taking hours to write one chip pattern. The lack of throughput limits its application primarily to research or mask production.

Scanning probe lithography is sometimes coupled with atomic force microscopy (AFM) to "write" patterns directly onto target substrates *via* mechanical, chemical, and thermal methods.[125] Techniques that utilize SPL include dip-pen nanolithography,[126] nanoshaving,[127] and nanografting.[128] While these methods can produce high-resolution features (<100 nm), their time-consuming writing process and high costs preclude them from use in large-scale manufacturing.

1.2 Chemical Lift-Off Lithography

Self-assembled monolayers[129,130] are formed by spontaneous adsorption and organization of amphiphilic organic molecules on metal substrates (**Figure 1.2**). They are usually prepared by immersing the substrates into solutions containing amphiphilic organic molecules. One of the most widely studied systems is the long-chain alkanethiols on gold surfaces, where the molecules are chemisorbed onto the surface and form ordered monolayer films. The strong affinity between the thiol head group and the gold surface leads to the assembly process, and the van der Waals interactions between alkyl chains maximize the packing efficiency of molecules. The terminal group on the SAM molecule determines the property and functionality of the surface.

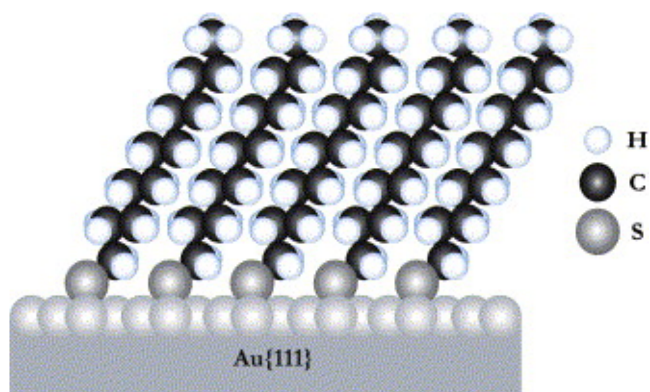

Figure 1.2. Schematic diagram of alkanethiol molecules self-assembled on a noble metal substrate. The figure is reprinted from reference 129 with permission.

We utilized the well-ordered property of SAM molecules to prevent the problem of lateral diffusion in microcontact printing. Instead of using elastomer stamps to print "ink" molecules onto the target substrate, a subtractive patterning process is applied, where SAM molecules are removed only from the contact region between the PDMS stamp and the substrate. This technique is known as "chemical lift-off lithography,[86] and **Figure 1.3** illustrates the process of this technique. The gold substrates are first coated with self-assembled monolayers of

hydroxyl-terminated alkanethiol molecules. Upon treatment with oxygen plasma, siloxyl groups are generated on the PDMS surface, making the stamp hydrophilic. When this PDMS stamp is brought into contact with hydroxyl-terminated SAM molecules on the gold substrate, a condensation reaction occurs between the siloxyl and hydroxyl groups, forming a Si-O-C linkage. After a few hours, the stamp is peeled off the substrate, removing the SAM molecules in the contact regions. The high fidelity chemical patterns observed indicate the elimination of lateral diffusion. We attribute this result to the well-ordered nature of SAMs, strong intermolecular interactions between the hydrophilic SAM molecules, and a diffusion barrier created by the Au step edges.[86]

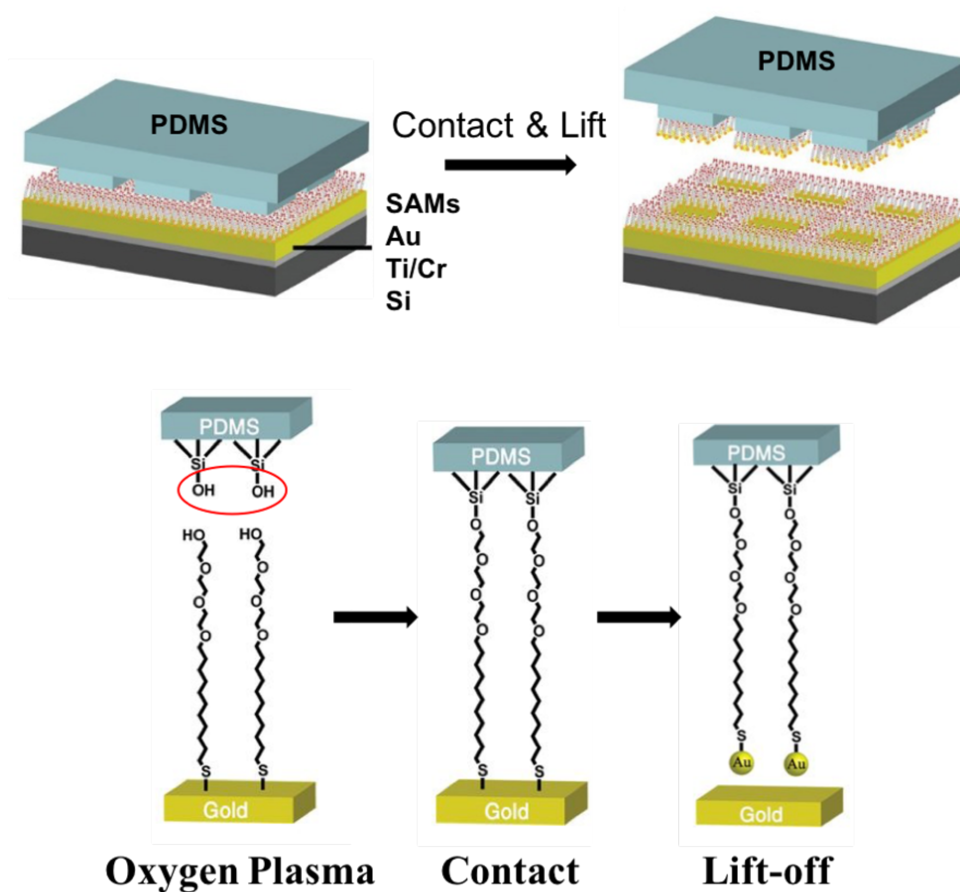

Figure 1.3. Schematic diagram illustrating the process of chemical lift-off lithography. The figure is reprinted from reference 86 with permission.

Moreover, we found that gold atoms are also removed from the substrate upon desorption of alkanethiol molecules. The presence of gold species is confirmed by the following X-ray photoelectron spectroscopy (XPS) measurement of the PDMS substrate (**Figure 1.4**). When the experiment was performed using the oxygen-plasma-activated PDMS stamp, two peaks appeared on the XPS spectrum; the binding energies at 80 and 84 eV are characteristic of gold $4f_{5/2}$ and $4f_{7/2}$ transitions. Without oxygen plasma treatment, no gold peaks were observed. Furthermore, only hydroxyl-terminated SAMs can be lifted-off by activated PDMS stamps, while

methyl-terminated SAMs remain intact, which is further evidence of chemical reactions at the interface.

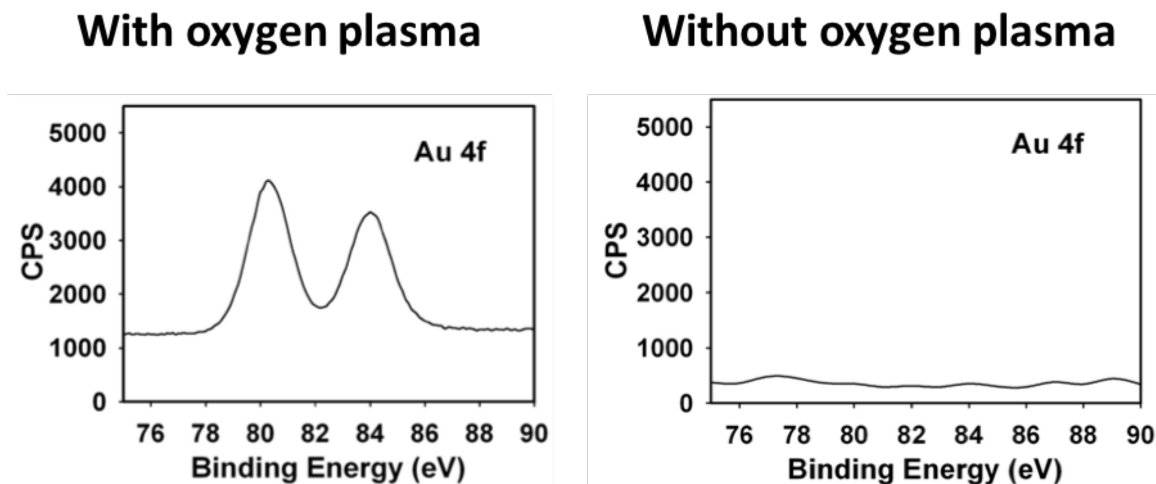

Figure 1.4. X-ray photoelectron spectroscopy measurements on PDMS stamps after CLL. The binding energies at 80 and 84 eV are characteristic of gold $4f_{5/2}$ and $4f_{7/2}$ transitions. Oxygen plasma is required for lift-off of SAM molecules. The figure is modified from reference 86 with permission.

We have demonstrated that CLL is a versatile technique for patterning both gold substrates and flat PDMS stamps (**Figure 1.5**).[131] On the gold side, after lift-off, the remaining SAM molecules in the non-lift-off regions act as resists for etching of exposed gold regions, and gold structures were fabricated (top). On the other side, when alkanethiol molecules are moved, gold atoms are also removed from the substrate. As a result, we can pattern featureless PDMS stamps with different geometries of organogold species. We characterized the patterned PDMS stamps with AFM (middle) and variable-pressure SEM (bottom).

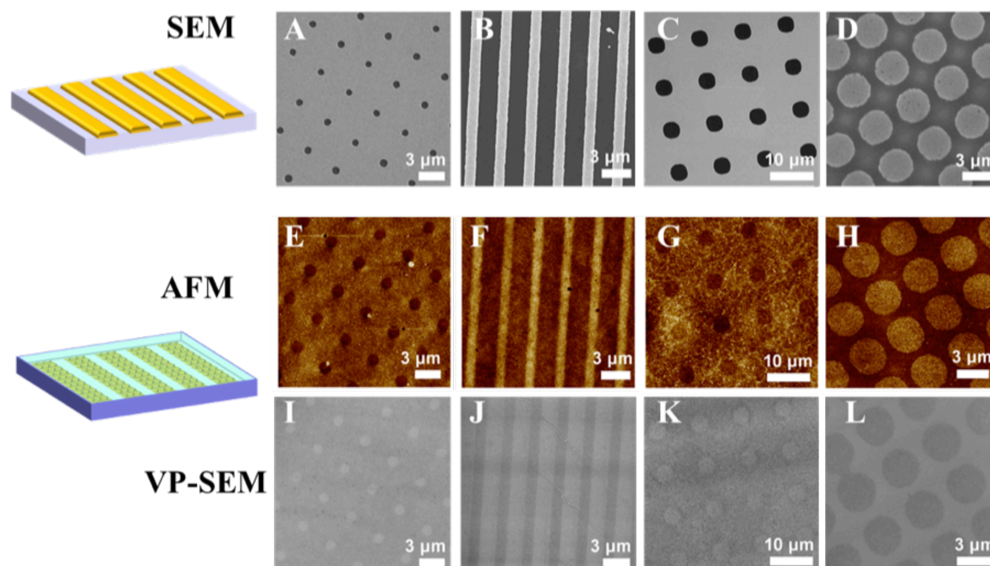

Figure 1.5. Chemical lift-off lithography can be used to pattern gold substrates as well as PDMS stamps. Scanning electron microscopy (SEM), atomic force microscopy (AFM), and variable-pressure SEM were used to characterize the materials. The figure is reprinted from reference 131 with permission.

Hence, we have developed many applications using CLL as the patterning tool. For example, we fabricate high-performance field-effect transistors (FET) for dopamine sensing down to picomolar (pM) concentrations (**Figure 1.6a**),[58,132] functional bio-substrates with reduced DNA-substrate interactions and improved DNA hybridization efficiencies (**Figure 1.6b**),[133] and spin-filtering substrates with the DNA probes acting as spin filters **(Figure 1.6c)**.[134]

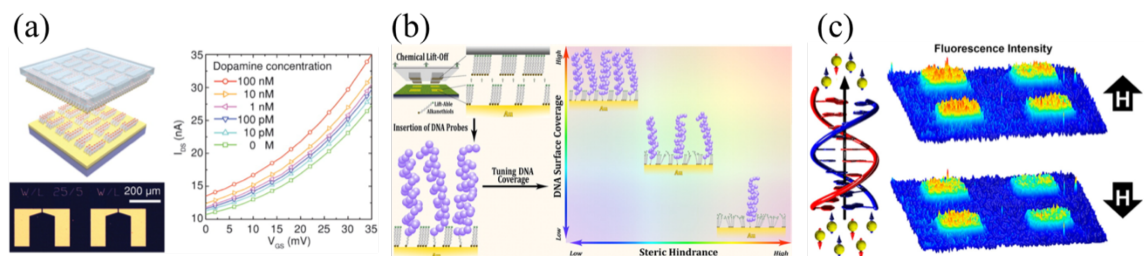

Figure 1.6. Applications of chemical lift-off lithography: (a) field-effect transistors (FET) based biosensor, (b) functional bio-substrates with improved DNA hybridization efficiencies, and (c) spin-filtering substrates. The figures are adapted from references 58, 133, 134 with permissions.

1.3 Nanosphere Lithography

Nanosphere lithography (NSL)[88-90] is a facile, versatile, and inexpensive nanofabrication tool that employs close-packed monolayers (or bilayers, trilayers, and other more complex arrangements) of nanospheres, such as polystyrene and SiO_2, to serve as masks for patterning underlying substrates. The sphere size defines the periodicity/pitch distance between features. One advantage of NSL is that the nanosphere dimensions range from less than 100 nm to hundreds of microns. This technique generally involves two steps: the first step is assembling the nanospheres into hexagonally close-packed arrangements, and the second step is patterning the underlying substrates *via* deposition or etching. Nanosphere lithography is highly scalable and, through the use of an automatic dispensing system, wafer-scale production can be achieved with a rate of 3000 wafers/hour.[135]

Over the years, various strategies have been developed to assemble the nanospheres into high-quality monolayers.[91] In my research projects, I use the *Langmuir-Blodgett* method (see the experimental setup in **Figure 1.7**), which assembles the polystyrene spheres into close-packed arrangement at the water-air interface, and then they are transferred onto target substrates. Before use, the polystyrene (PS) spheres are sonicated for least 30 minutes to ensure there are no aggregates. The silicon substrates are pre-cleaned by sonication, and oxygen plasma is used to increase the surface hydrophilicity. The polystyrene spheres are then slowly added to the water/air interface through a tilted glass slide. By carefully removing the water, the high-quality monolayers are transferred to the silicon wafers underneath (see **Figure S5.1** for example).

Figure 1.7. Experimental setup to prepare high-quality polystyrene monolayers *via* the *Langmuir-Blodgett* method.

Following the preparation of the monolayers, there are two directions to pattern the underlying substrates: deposition or etching. In either case, oxygen plasma is first used to tailor the sphere size. The concentric shrinkage of the PS spheres allows precise reduction of the nanosphere diameter without changing the pitch distance. In the case of deposition, depending on the goal of fabrication, the etching time should be carefully adjusted. For example, after oxygen plasma etching, noble metals can be deposited for the fabrication of biosensors based on the localized surface plasmon resonance (LSPR) effect.[136] Less oxygen plasma etching time

produces bowtie structures (see **Figure 1.8a** for silver bowtie arrays). Increasing the etching time produces a continuous metal film, and nanohole arrays are fabricated after removing the PS spheres (see **Figure 1.8b** for gold nanohole arrays). Dry etching is another option, and it can be used to fabricate three-dimensional (3D) nanostructures. **Figure 1.8c** illustrates the production of silicon nanopillars after dry etching. In our recent work, we have extended the capability of nanosphere lithography to fabricate more complicated 3D nanostructures by introducing the multiple-patterning concept.

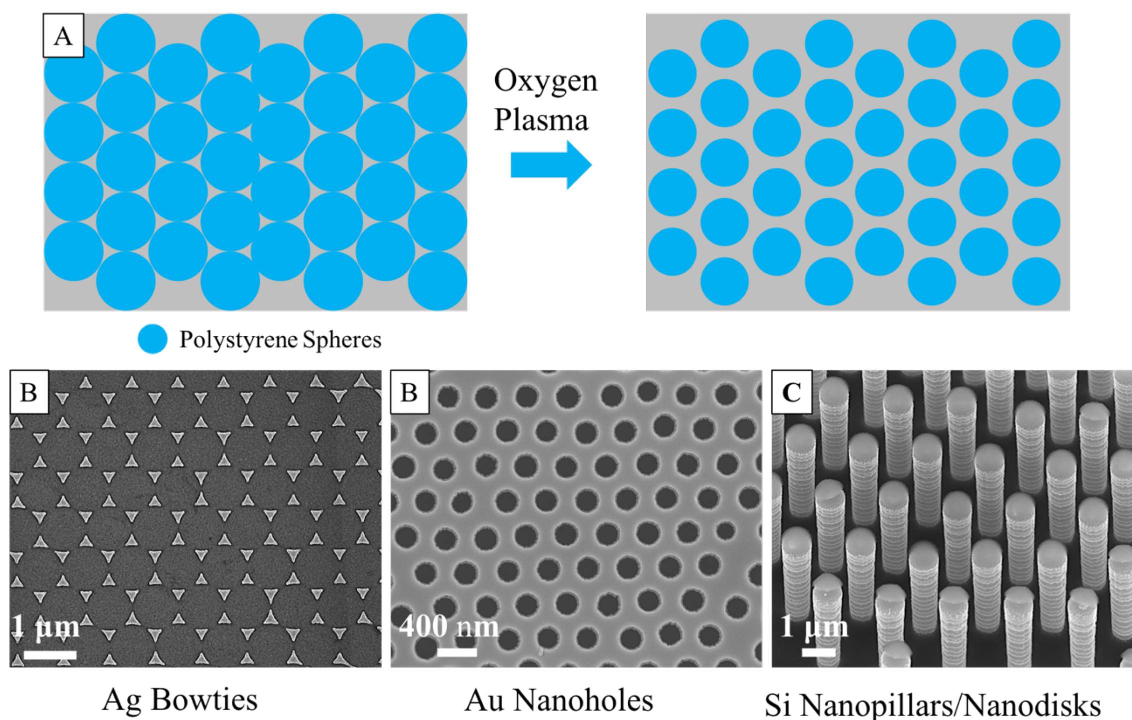

Figure 1.8. Nanosphere lithography can be used to fabricate a variety of nanostructures through single-step patterning (deposition or etching). In either case, oxygen plasma is first used to reduce the sphere size (A). For example, we can fabricate (B) silver bowties, (C) gold nanoholes, and (D) Si nanopillars.

1.4 Conclusions and Dissertation Overview

While the continuous invention and refinement of lithographic techniques are improving current technologies and enabling new applications, current approaches are still insufficient for all our demands (nanometer-scale precision, high throughput, high reproducibility, and low cost). Therefore, my graduate work has been focusing on the development of several lithographic techniques to fabricate nanoscale chemical patterns and 3D hierarchical nanostructures.

Chapters 2, **3**, and **4** discuss two chemical patterning techniques based on chemical lift-off lithography. **Chapter 2**, introduces polymer-pen chemical lift-off lithography, in which we combine chemical lift-off lithography and large areas of polymer pens with nanoscale tips. Through the use of the stamp support system and height gradients, we obtained chemical patterns with linewidths ranging from sub-50 nm to sub-500 nm with sub-20 nm increments. **Chapter 3** demonstrates our ability to tune the feature size by controlling the compression distance. By adding external force, we were able to fabricate more complex hollow patterns at the sub-micron scale, which were difficult to obtain otherwise. The following gold etching with the remaining SAM molecules as the masks yielded arrays of gold nanorings. **Chapter 4** explores self-collapse lithography, in which we utilize the soft, flexible nature of PDMS stamps to create roof collapse, resulting in removal of SAM molecules from the contact area. With this technique, chemical patterns with feature sizes from ~2 μm to below 30 nm were obtained by decreasing stamp relief heights from 1 μm to 50 nm. Likewise, the Young's modulus of the stamp can also be used to adjust the feature size.

Chapter 5 introduces how we apply the multiple patterning strategy to nanosphere lithography and fabricate a series of 3D hierarchical nanostructures with fully tunable dimensions. This approach allows the fabrication of silicon nanotubes with nanometer-scale

control over all dimensions (outer and inner diameters, height, hole-depth, and pitch distance). In **Chapter 6**, we adapt the multiple-patterning strategy and fabricate volcano-shaped nanostructures known as “nanovolcanos.” The sub-20-nm sharp features of these structures enable cell membranes penetration with minimal disruption on cell functions. The holes of the nanovolcanos can contain high payloads of biomolecular cargos to be delivered once cell membranes have been penetrated. We expect this platform to be applicable to delivering therapeutic payloads and to offer solutions to clinical problems.

1.5 References

1. Doemeny, L.; Cheng, H. N.; Grob Schmidt, D.; Geraci, C. L. *Nanotechnology: Delivering on the Promise Volume 1*. ACS Symposium Series 1220; American Chemical Society: Washington, DC, **2016**; Chapter 1.

2. Liddle, J. A.; Gallatin, G. M. Nanomanufacturing: A Perspective. *ACS Nano* **2016,** *10*, 2995–3014.

3. Neisser, M.; Wurm, S. ITRS Lithography Roadmap: 2015 Challenges. *Adv. Opt. Technol.* **2015,** *4*, 235–240.

4. Gates, B. D.; Xu, Q.; Stewart, M.; Ryan, D.; Willson, C. G.; Whitesides, G. M. New Approaches to Nanofabrication: Molding, Printing, and Other Techniques. *Chem. Rev.* **2005,** *105*, 1171–1196.

5. Zeng, M.; Xiao, Y.; Liu, J.; Yang, K.; Fu, L. Exploring Two-Dimensional Materials Toward the Next-Generation Circuits: From Monomer Design to Assembly Control. *Chem. Rev.* **2018,** *118*, 6236–6296.

6. Xiang, D.; Wang, X.; Jia, C.; Lee, T.; Guo, X. Molecular-Scale Electronics: From Concept to Function. *Chem. Rev.* **2016,** *116*, 4318–4440.

7. Kagan, C. R.; Fernandez, L. E.; Gogotsi, Y.; Hammond, P. T.; Hersam, M. C.; Nel, A. E.; Penner, R. M.; Willson, C. G.; Weiss, P. S. Nano Day: Celebrating the Next Decade of Nanoscience and Nanotechnology. *ACS Nano* **2016,** *10*, 9093–9103.

8. Tsai, H.; Pitera, J. W.; Miyazoe, H.; Bangsaruntip, S.; Engelmann, S. U.; Liu, C.-C.; Cheng, J. Y.; Bucchignano, J. J.; Klaus, D. P.; Joseph, E. A.; Sanders, D. P.; Colburn, M. E.; Guillorn, M. A. Two-Dimensional Pattern Formation Using Graphoepitaxy of PS-b-PMMA

Block Copolymers for Advanced FinFET Device and Circuit Fabrication. *ACS Nano* **2014,** *8*, 5227–5232.

9. Cheong, L. L.; Paul, P.; Holzner, F.; Despont, M.; Coady, D. J.; Hedrick, J. L.; Allen, R.; Knoll, A. W.; Duerig, U. Thermal Probe Maskless Lithography for 27.5 nm Half-Pitch Si Technology. *Nano Lett.* **2013,** *13*, 4485–4491.

10. Cao, Q.; Kim, H.-s.; Pimparkar, N.; Kulkarni, J. P.; Wang, C.; Shim, M.; Roy, K.; Alam, M. A.; Rogers, J. A. Medium-Scale Carbon Nanotube Thin-Film Integrated Circuits on Flexible Plastic Substrates. *Nature* **2008,** *454*, 495–500.

11. Wuttig, M.; Yamada, N. Phase-Change Materials for Rewriteable Data Storage. *Nat. Mater.* **2007,** *6*, 824–832.

12. Chappert, C.; Fert, A.; Van Dau, F. N. The Emergence of Spin Electronics in Data Storage. *Nat. Mater.* **2007,** *6*, 813–823.

13. Liu, Y.; Weiss, D. N.; Li, J. Rapid Nanoimprinting and Excellent Piezoresponse of Polymeric Ferroelectric Nanostructures. *ACS Nano* **2010,** *4*, 83–90.

14. Lee, T. W.; Jeon, S.; Maria, J.; Zaumseil, J.; Hsu, J. W. P.; Rogers, J. A. Soft-Contact Optical Lithography Using Transparent Elastomeric Stamps and Application to Nanopatterned Organic Light-Emitting Devices. *Adv. Fun. Mater.* **2005,** *15*, 1435–1439.

15. Kim, T.-H.; Cho, K.-S.; Lee, E. K.; Lee, S. J.; Chae, J.; Kim, J. W.; Kim, D. H.; Kwon, J.-Y.; Amaratunga, G.; Lee, S. Y.; Choi, B. L.; Kuk, Y.; Kim, J. M.; Kim, K. Full-Colour Quantum Dot Displays Fabricated by Transfer Printing. *Nat. Photonics* **2011,** *5*, 176–182.

16. Wu, J.; Agrawal, M.; Becerril, H. A.; Bao, Z.; Liu, Z.; Chen, Y.; Peumans, P. Organic Light-Emitting Diodes on Solution-Processed Graphene Transparent Electrodes. *ACS Nano* **2010,** *4*, 43–48.

17. Ray, W. J.; Joseph, W. Wearable Electrochemical Sensors and Biosensors: A Review. *Electroanalysis* **2013,** *25*, 29–46.

18. Polavarapu, L.; Liz-Marzan, L. M. Towards Low-Cost Flexible Substrates for Nanoplasmonic Sensing. *Phys. Chem. Chem. Phys.* **2013,** *15*, 5288–5300.

19. Rim, Y. S.; Bae, S.-H.; Chen, H.; Yang, J. L.; Kim, J.; Andrews, A. M.; Weiss, P. S.; Yang, Y.; Tseng, H.-R. Printable Ultrathin Metal Oxide Semiconductor-Based Conformal Biosensors. *ACS Nano* **2015,** *9*, 12174–12181.

20. Pang, C.; Lee, C.; Suh, K.-Y. Recent Advances in Flexible Sensors for Wearable and Implantable Devices. *J. Appl. Polym. Sci.* **2013,** *130*, 1429–1441.

21. Kim, D.-H.; Lu, N.; Ma, R.; Kim, Y.-S.; Kim, R.-H.; Wang, S.; Wu, J.; Won, S. M.; Tao, H.; Islam, A.; Yu, K. J.; Kim, T.-i.; Chowdhury, R.; Ying, M.; Xu, L.; Li, M.; Chung, H.-J.; Keum, H.; McCormick, M.; Liu, P.; Zhang, Y.-W.; Omenetto, F. G.; Huang, Y.; Coleman, T.; Rogers, J. A. Epidermal Electronics. *Science* **2011,** *333*, 838–843.

22. Rogers, J. A.; Someya, T.; Huang, Y. Materials and Mechanics for Stretchable Electronics. *Science* **2010,** *327*, 1603–1607.

23. Ko, H. C.; Stoykovich, M. P.; Song, J.; Malyarchuk, V.; Choi, W. M.; Yu, C.-J.; Geddes Iii, J. B.; Xiao, J.; Wang, S.; Huang, Y.; Rogers, J. A. A Hemispherical Electronic Eye Camera Based on Compressible Silicon Optoelectronics. *Nature* **2008,** *454*, 748–753.

24. Du, K.; Wathuthanthri, I.; Liu, Y.; Xu, W.; Choi, C.-H. Wafer-Scale Pattern Transfer of Metal Nanostructures on Polydimethylsiloxane (PDMS) Substrates *via* Holographic Nanopatterns. *ACS Appl. Mater. Interfaces* **2012,** *4*, 5505–5514.

25. Ramsurn, H.; Gupta, R. B. Nanotechnology in Solar and Biofuels. *ACS Sustainable Chem. Eng.* **2013,** *1*, 779–797.

26. Zhang, J.; Song, T.; Shen, X.; Yu, X.; Lee, S.-T.; Sun, B. A 12%-Efficient Upgraded Metallurgical Grade Silicon–Organic Heterojunction Solar Cell Achieved by a Self-Purifying Process. *ACS Nano* **2014,** *8*, 11369–11376.

27. Etgar, L.; Zhang, W.; Gabriel, S.; Hickey, S. G.; Nazeeruddin, M. K.; Eychmüller, A.; Liu, B.; Grätzel, M. High Efficiency Quantum Dot Heterojunction Solar Cell Using Anatase (001) TiO_2 Nanosheets. *Adv. Mater.* **2012,** *24*, 2202–2206.

28. Garnett, E.; Yang, P. Light Trapping in Silicon Nanowire Solar Cells. *Nano Lett.* **2010,** *10*, 1082–1087.

29. Chen, C.-C.; Dou, L.; Zhu, R.; Chung, C.-H.; Song, T.-B.; Zheng, Y. B.; Hawks, S.; Li, G.; Weiss, P. S.; Yang, Y. Visibly Transparent Polymer Solar Cells Produced by Solution Processing. *ACS Nano* **2012,** *6*, 7185–7190.

30. Kim, Y. Y.; Kim, H. J.; Jeong, J. H.; Lee, J.; Choi, J. H.; Jung, J. Y.; Lee, J. H.; Cheng, H.; Lee, K. W.; Choi, D. G. Facile Fabrication of Silicon Nanotube Arrays and Their Application in Lithium-Ion Batteries. *Adv. Eng. Mater.* **2016,** *18*, 1349–1353.

31. Lu, Z.; Wong, T.; Ng, T.-W.; Wang, C. Facile Synthesis of Carbon Decorated Silicon Nanotube Arrays as Anode Material for High-Performance Lithium-Ion Batteries. *RSC Adv.* **2014,** *4*, 2440–2446.

32. Zhao, C.; Li, Q.; Wan, W.; Li, J.; Li, J.; Zhou, H.; Xu, D. Coaxial Carbon-Silicon-Carbon Nanotube Arrays in Porous Anodic Aluminum Oxide Templates as Anodes for Lithium Ion Batteries. *J. Mater. Chem.* **2012,** *22*, 12193–12197.

33. Park, M.-H.; Kim, M. G.; Joo, J.; Kim, K.; Kim, J.; Ahn, S.; Cui, Y.; Cho, J. Silicon Nanotube Battery Anodes. *Nano Lett.* **2009,** *9*, 3844–3847.

34. Song, T.; Xia, J.; Lee, J.-H.; Lee, D. H.; Kwon, M.-S.; Choi, J.-M.; Wu, J.; Doo, S. K.; Chang, H.; Park, W. I.; Zang, D. S.; Kim, H.; Huang, Y.; Hwang, K.-C.; Rogers, J. A.; Paik, U. Arrays of Sealed Silicon Nanotubes As Anodes for Lithium Ion Batteries. *Nano Lett.* **2010,** *10*, 1710–1716.

35. Chan, C. K.; Patel, R. N.; O'Connell, M. J.; Korgel, B. A.; Cui, Y. Solution-Grown Silicon Nanowires for Lithium-Ion Battery Anodes. *ACS Nano* **2010,** *4*, 1443–1450.

36. Wang, B.; Li, X.; Zhang, X.; Luo, B.; Jin, M.; Liang, M.; Dayeh, S. A.; Picraux, S. T.; Zhi, L. Adaptable Silicon–Carbon Nanocables Sandwiched between Reduced Graphene Oxide Sheets as Lithium Ion Battery Anodes. *ACS Nano* **2013,** *7*, 1437–1445.

37. Ge, M.; Lu, Y.; Ercius, P.; Rong, J.; Fang, X.; Mecklenburg, M.; Zhou, C. Large-Scale Fabrication, 3D Tomography, and Lithium-Ion Battery Application of Porous Silicon. *Nano Lett.* **2014,** *14*, 261–268.

38. Ge, M.; Rong, J.; Fang, X.; Zhou, C. Porous Doped Silicon Nanowires for Lithium Ion Battery Anode with Long Cycle Life. *Nano Lett.* **2012,** *12*, 2318–2323.

39. Kim, H.; Cho, J. Superior Lithium Electroactive Mesoporous Si@Carbon Core−Shell Nanowires for Lithium Battery Anode Material. *Nano Lett.* **2008,** *8*, 3688–3691.

40. Liu, B.; Soares, P.; Checkles, C.; Zhao, Y.; Yu, G. Three-Dimensional Hierarchical Ternary Nanostructures for High-Performance Li-Ion Battery Anodes. *Nano Lett.* **2013,** *13*, 3414–3419.

41. Liu, N.; Wu, H.; McDowell, M. T.; Yao, Y.; Wang, C.; Cui, Y. A Yolk-Shell Design for Stabilized and Scalable Li-Ion Battery Alloy Anodes. *Nano Lett.* **2012,** *12*, 3315–3321.

42. Yao, Y.; McDowell, M. T.; Ryu, I.; Wu, H.; Liu, N.; Hu, L.; Nix, W. D.; Cui, Y. Interconnected Silicon Hollow Nanospheres for Lithium-Ion Battery Anodes with Long Cycle Life. *Nano Lett.* **2011,** *11*, 2949–2954.

43. Wu, H.; Chan, G.; Choi, J. W.; Ryu, I.; Yao, Y.; McDowell, M. T.; Lee, S. W.; Jackson, A.; Yang, Y.; Hu, L.; Cui, Y. Stable Cycling of Double-Walled Silicon Nanotube Battery Anodes Through Solid-Electrolyte Interphase Control. *Nat. Nanotechnol.* **2012,** *7*, 310–315.

44. Li, X.; Gu, M.; Hu, S.; Kennard, R.; Yan, P.; Chen, X.; Wang, C.; Sailor, M. J.; Zhang, J.-G.; Liu, J. Mesoporous Silicon Sponge as An Anti-Pulverization Structure for High-Performance Lithium-Ion Battery Anodes. *Nat. Commun.* **2014,** *5*, 4105.

45. Wu, H.; Yu, G.; Pan, L.; Liu, N.; McDowell, M. T.; Bao, Z.; Cui, Y. Stable Li-Ion Battery Anodes by *In-Situ* Polymerization of Conducting Hydrogel to Conformally Coat Silicon Nanoparticles. *Nat. Commun.* **2013,** *4*, 1943.

46. Chan, C. K.; Peng, H.; Liu, G.; McIlwrath, K.; Zhang, X. F.; Huggins, R. A.; Cui, Y. High-Performance Lithium Battery Anodes Using Silicon Nanowires. *Nat. Nanotechnol.* **2007,** *3*, 31–35.

47. Liu, N.; Lu, Z.; Zhao, J.; McDowell, M. T.; Lee, H.-W.; Zhao, W.; Cui, Y. A Pomegranate-Inspired Nanoscale Design for Large-Volume-Change Lithium Battery Anodes. *Nat. Nanotechnol.* **2014,** *9*, 187–192.

48. Down, M.; Banks, C. E. Freestanding Three-Dimensional Graphene Macroporous Supercapacitor. *ACS Appl. Energy Mater.* **2018,** *1*, 891–899.

49. Ke, F.-S.; Wu, Y.-S.; Deng, H. Metal-Organic Frameworks for Lithium Ion Batteries and Supercapacitors. *J. Solid State Chem.* **2015,** *223*, 109–121.

50. Li, W.; Xu, X.; Liu, C.; Tekell, M. C.; Ning, J.; Guo, J.; Zhang, J.; Fan, D. Ultralight and Binder-Free All-Solid-State Flexible Supercapacitors for Powering Wearable Strain Sensors. *Adv. Fun. Mater.* **2017,** *27*, 1702738.

51. Liu, C.; Li, C.; Ahmed, K.; Wang, W.; Lee, I.; Zaera, F.; Ozkan, C. S.; Ozkan, M. Scalable, Binderless, and Carbonless Hierarchical Ni Nanodendrite Foam Decorated with Hydrous Ruthenium Dioxide for 1.6 V Symmetric Supercapacitors. *Adv. Mater. Interfaces* **2016,** *3*, 1500503.

52. Liu, C.; Li, F.; Ma, L.-P.; Cheng, H.-M. Advanced Materials for Energy Storage. *Adv. Mater.* **2010,** *22*, 28–62.

53. Wang, K.; Zhang, X.; Li, C.; Zhang, H.; Sun, X.; Xu, N.; Ma, Y. Flexible Solid-State Supercapacitors Based on A Conducting Polymer Hydrogel with Enhanced Electrochemical Performance. *J. Mater. Chem. A* **2014,** *2*, 19726–19732.

54. Wang, W.; Guo, S.; Penchev, M.; Ruiz, I.; Bozhilov, K. N.; Yan, D.; Ozkan, M.; Ozkan, C. S. Three Dimensional Few Layer Graphene and Carbon Nanotube Foam Architectures for High Fidelity Supercapacitors. *Nano Energy* **2013,** *2*, 294–303.

55. Stewart, M. E.; Anderton, C. R.; Thompson, L. B.; Maria, J.; Gray, S. K.; Rogers, J. A.; Nuzzo, R. G. Nanostructured Plasmonic Sensors. *Chem. Rev.* **2008,** *108*, 494–521.

56. Peng, F.; Su, Y.; Zhong, Y.; Fan, C.; Lee, S.-T.; He, Y. Silicon Nanomaterials Platform for Bioimaging, Biosensing, and Cancer Therapy. *Acc. Chem. Res.* **2014,** *47*, 612–623.

57. Xu, X.; Kim, K.; Li, H.; Fan, D. L. Ordered Arrays of Raman Nanosensors for Ultrasensitive and Location Predictable Biochemical Detection. *Adv. Mater.* **2012,** *24*, 5457–5463.

58. Kim, J.; Rim, Y. S.; Chen, H.; Cao, H. H.; Nakatsuka, N.; Hinton, H. L.; Zhao, C.; Andrews, A. M.; Yang, Y.; Weiss, P. S. Fabrication of High-Performance Ultrathin In_2O_3 Film Field-Effect Transistors and Biosensors Using Chemical Lift-Off Lithography. *ACS Nano* **2015,** *9*, 4572–4582.

59. Michalet, X.; Pinaud, F. F.; Bentolila, L. A.; Tsay, J. M.; Doose, S.; Li, J. J.; Sundaresan, G.; Wu, A. M.; Gambhir, S. S.; Weiss, S. Quantum Dots for Live Cells, *in Vivo* Imaging, and Diagnostics. *Science* **2005,** *307*, 538–544.

60. Jain, P. K.; Huang, X.; El-Sayed, I. H.; El-Sayed, M. A. Noble Metals on the Nanoscale: Optical and Photothermal Properties and Some Applications in Imaging, Sensing, Biology, and Medicine. *Acc. Chem. Res.* **2008,** *41*, 1578–1586.

61. Lin, Z. C.; Xie, C.; Osakada, Y.; Cui, Y.; Cui, B. Iridium Oxide Nanotube Electrodes for Sensitive and Prolonged Intracellular Measurement of Action Potentials. *Nat. Commun.* **2014,** *5*, 3206.

62. Chen, X.; Kis, A.; Zettl, A.; Bertozzi, C. R. A Cell Nanoinjector Based on Carbon Nanotubes. *Proc. Natl. Acad. Sci.* **2007,** *104*, 8218–8222.

63. Na, Y.-R.; Kim, S. Y.; Gaublomme, J. T.; Shalek, A. K.; Jorgolli, M.; Park, H.; Yang, E. G. Probing Enzymatic Activity inside Living Cells Using a Nanowire–Cell "Sandwich" Assay. *Nano Lett.* **2013,** *13*, 153–158.

64. Hou, S.; Choi, J.-s.; Garcia, M. A.; Xing, Y.; Chen, K.-J.; Chen, Y.-M.; Jiang, Z. K.; Ro, T.; Wu, L.; Stout, D. B.; Tomlinson, J. S.; Wang, H.; Chen, K.; Tseng, H.-R.; Lin, W.-Y. Pretargeted Positron Emission Tomography Imaging That Employs Supramolecular Nanoparticles with *in Vivo* Bioorthogonal Chemistry. *ACS Nano* **2016,** *10*, 1417–1424.

65. Duan, X.; Gao, R.; Xie, P.; Cohen-Karni, T.; Qing, Q.; Choe, H. S.; Tian, B.; Jiang, X.; Lieber, C. M. Intracellular Recordings of Action Potentials by An Extracellular Nanoscale Field-Effect Transistor. *Nat. Nanotechnol.* **2012,** *7*, 174–179.

66. Choi, J.-s.; Zhu, Y.; Li, H.; Peyda, P.; Nguyen, T. T.; Shen, M. Y.; Yang, Y. M.; Zhu, J.; Liu, M.; Lee, M. M.; Sun, S.-S.; Yang, Y.; Yu, H.-h.; Chen, K.; Chuang, G. S.; Tseng, H.-R. Cross-Linked Fluorescent Supramolecular Nanoparticles as Finite Tattoo Pigments with Controllable Intradermal Retention Times. *ACS Nano* **2017,** *11*, 153–162.

67. Chiappini, C.; Martinez, J. O.; De Rosa, E.; Almeida, C. S.; Tasciotti, E.; Stevens, M. M. Biodegradable Nanoneedles for Localized Delivery of Nanoparticles *in Vivo*: Exploring the Biointerface. *ACS Nano* **2015,** *9*, 5500–5509.

68. Chiappini, C. Nanoneedle-Based Sensing in Biological Systems. *ACS Sens.* **2017,** *2*, 1086–1102.

69. Cao, Y.; Hjort, M.; Chen, H.; Birey, F.; Leal-Ortiz, S. A.; Han, C. M.; Santiago, J. G.; Paşca, S. P.; Wu, J. C.; Melosh, N. A. Nondestructive Nanostraw Intracellular Sampling for Longitudinal Cell Monitoring. *Proc. Natl. Acad. Sci.* **2017,** *114*, 1866–1874.

70. Farokhzad, O. C.; Langer, R. Impact of Nanotechnology on Drug Delivery. *ACS Nano* **2009,** *3*, 16–20.

71. Shi, J.; Votruba, A. R.; Farokhzad, O. C.; Langer, R. Nanotechnology in Drug Delivery and Tissue Engineering: From Discovery to Applications. *Nano Lett.* **2010,** *10*, 3223–3230.

72. Chiappini, C.; De Rosa, E.; Martinez, J. O.; Liu, X.; Steele, J.; Stevens, M. M.; Tasciotti, E. Biodegradable Silicon Nanoneedles Delivering Nucleic Acids Intracellularly Induce Localized i*n Vivo* Neovascularization. *Nat. Mater.* **2015,** *14*, 532–539.

73. Sharei, A.; Zoldan, J.; Adamo, A.; Sim, W. Y.; Cho, N.; Jackson, E.; Mao, S.; Schneider, S.; Han, M.-J.; Lytton-Jean, A.; Basto, P. A.; Jhunjhunwala, S.; Lee, J.; Heller, D. A.; Kang, J. W.; Hartoularos, G. C.; Kim, K.-S.; Anderson, D. G.; Langer, R.; Jensen, K. F. A Vector-Free Microfluidic Platform for Intracellular Delivery. *Proc. Natl. Acad. Sci.* **2013,** *110*, 2082–2087.

74. Hasani-Sadrabadi, M. M.; Taranejoo, S.; Dashtimoghadam, E.; Bahlakeh, G.; Majedi, F. S.; VanDersarl, J. J.; Janmaleki, M.; Sharifi, F.; Bertsch, A.; Hourigan, K.; Tayebi, L.; Renaud, P.; Jacob, K. I. Microfluidic Manipulation of Core/Shell Nanoparticles for Oral Delivery of Chemotherapeutics: A New Treatment Approach for Colorectal Cancer. *Adv. Mater.* **2016,** *28*, 4134–4141.

75. Fox, C. B.; Cao, Y.; Nemeth, C. L.; Chirra, H. D.; Chevalier, R. W.; Xu, A. M.; Melosh, N. A.; Desai, T. A. Fabrication of Sealed Nanostraw Microdevices for Oral Drug Delivery. *ACS Nano* **2016,** *10*, 5873–5881.

76. Thomas, C. E.; Ehrhardt, A.; Kay, M. A. Progress and Problems with The Use of Viral Vectors for Gene Therapy. *Nat. Rev. Genet.* **2003,** *4*, 346–358.

77. Yin, H.; Kanasty, R. L.; Eltoukhy, A. A.; Vegas, A. J.; Dorkin, J. R.; Anderson, D. G. Non-Viral Vectors for Gene-Based Therapy. *Nat. Rev. Genet.* **2014,** *15*, 541–555.

78. Tebas, P.; Stein, D.; Tang, W. W.; Frank, I.; Wang, S. Q.; Lee, G.; Spratt, S. K.; Surosky, R. T.; Giedlin, M. A.; Nichol, G.; Holmes, M. C.; Gregory, P. D.; Ando, D. G.; Kalos, M.; Collman, R. G.; Binder-Scholl, G.; Plesa, G.; Hwang, W.-T.; Levine, B. L.; June, C. H. Gene Editing of CCR5 in Autologous CD4 T Cells of Persons Infected with HIV. *N. Engl. J. Med.* **2014,** *370*, 901–910.

79. Kay, M. A. State-of-The-Art Gene-Based Therapies: The Road Ahead. *Nat. Rev. Genet.* **2011,** *12*, 316–328.

80. Stewart, M. P.; Sharei, A.; Ding, X.; Sahay, G.; Langer, R.; Jensen, K. F. *In Vitro* and e*x Vivo* Strategies for Intracellular Delivery. *Nature* **2016,** *538*, 183–192.

81. Kim, W.; Ng, J. K.; Kunitake, M. E.; Conklin, B. R.; Yang, P. Interfacing Silicon Nanowires with Mammalian Cells. *J. Am. Chem. Soc.* **2007,** *129*, 7228–7229.

82. Elnathan, R.; Delalat, B.; Brodoceanu, D.; Alhmoud, H.; Harding, F. J.; Buehler, K.; Nelson, A.; Isa, L.; Kraus, T.; Voelcker, N. H. Maximizing Transfection Efficiency of Vertically Aligned Silicon Nanowire Arrays. *Adv. Fun. Mater.* **2015,** *25*, 7215–7225.

83. Goldberg, M.; Langer, R.; Jia, X. Nanostructured Materials for Applications in Drug Delivery and Tissue Engineering. *J. Biomater. Sci. Polym. Ed.* **2007,** *18*, 241–268.

84. Zhang, L.; Webster, T. J. Nanotechnology and Nanomaterials: Promises for Improved Tissue Regeneration. *Nano Today* **2009,** *4*, 66–80.

85. Pan, L.; Park, Y.; Xiong, Y.; Ulin-Avila, E.; Wang, Y.; Zeng, L.; Xiong, S.; Rho, J.; Sun, C.; Bogy, D. B.; Zhang, X. Maskless Plasmonic Lithography at 22 nm Resolution. *Sci. Rep.* **2011,** *1*, 175.

86. Liao, W. S.; Cheunkar, S.; Cao, H. H.; Bednar, H. R.; Weiss, P. S.; Andrews, A. M. Subtractive Patterning *via* Chemical Lift-Off Lithography. *Science* **2012,** *337*, 1517–1521.

87. Pimpin, A. S., W. Review on Micro- and Nanolithography Techniques and Their Applications. *Eng. J.* **2011,** *16*, 37–56.

88. Haynes, C. L.; Van Duyne, R. P. Nanosphere Lithography: A Versatile Nanofabrication Tool for Studies of Size-Dependent Nanoparticle Optics. *J. Phys. Chem. B* **2001,** *105*, 5599–5611.

89. Jensen, T. R.; Malinsky, M. D.; Haynes, C. L.; Van Duyne, R. P. Nanosphere Lithography: Tunable Localized Surface Plasmon Resonance Spectra of Silver Nanoparticles. *J. Phys. Chem. B* **2000,** *104*, 10549–10556.

90. Hulteen, J. C.; Van Duyne, R. P. Nanosphere Lithography: A Materials General Fabrication Process for Periodic Particle Array Surfaces. *J. Vac. Sci. Technol. A* **1995,** *13*, 1553–1558.

91. Colson, P.; Henrist, C.; Cloots, R. Nanosphere Lithography: A Powerful Method for the Controlled Manufacturing of Nanomaterials. *J. Nanomater.* **2013,** *2013*, 1–19.

92. Xia, Y.; Whitesides, G. M. Soft Lithography. *Annu. Rev. Mater. Sci.* **1998,** *28*, 153–184.

93. Rogers, J. A.; Nuzzo, R. G. Recent Progress in Soft Lithography. *Mater. Today* **2005,** *8*, 50–56.

94. Qin, D.; Xia, Y.; Whitesides, G. M. Soft Lithography for Micro- and Nanoscale Patterning. *Nat. Protoc.* **2010,** *5*, 491–502.

95. Wolfe, D. B.; Qin, D.; Whitesides, G. M. Rapid Prototyping of Microstructures by Soft Lithography for Biotechnology. *Methods Mol. Biol.* **2010,** *583*, 81–107.

96. Meitl, M. A.; Zhu, Z.-T.; Kumar, V.; Lee, K. J.; Feng, X.; Huang, Y. Y.; Adesida, I.; Nuzzo, R. G.; Rogers, J. A. Transfer Printing by Kinetic Control of Adhesion to An Elastomeric Stamp. *Nat. Mater.* **2005,** *5*, 33–38.

97. Briseno, A. L.; Mannsfeld, S. C. B.; Ling, M. M.; Liu, S.; Tseng, R. J.; Reese, C.; Roberts, M. E.; Yang, Y.; Wudl, F.; Bao, Z. Patterning Organic Single-Crystal Transistor Arrays. *Nature* **2006,** *444*, 913–917.

98. LaFratta, C. N.; Li, L.; Fourkas, J. T. Soft-Lithographic Replication of 3D Microstructures with Closed Loops. *Proc. Natl. Acad. Sci.* **2006,** *103*, 8589–8594.

99. Lipomi, D. J.; Kats, M. A.; Kim, P.; Kang, S. H.; Aizenberg, J.; Capasso, F.; Whitesides, G. M. Fabrication and Replication of Arrays of Single- or Multicomponent Nanostructures by Replica Molding and Mechanical Sectioning. *ACS Nano* **2010,** *4*, 4017–4026.

100. Moonen, P. F.; Yakimets, I.; Huskens, J. Fabrication of Transistors on Flexible Substrates: from Mass-Printing to High-Resolution Alternative Lithography Strategies. *Adv. Mater.* **2012,** *24*, 5526–5541.

101. Rodrigue, H.; Bhandari, B.; Wang, W.; Ahn, S.-H. 3D Soft Lithography: A Fabrication Process for Thermocurable Polymers. *J. Mater. Process. Technol.* **2015,** *217*, 302–309.

102. Whitesides, G. M.; Ostuni, E.; Takayama, S.; Jiang, X.; Ingber, D. E. Soft Lithography in Biology and Biochemistry. *Annu. Rev. Biomed. Eng.* **2001,** *3*, 335–373.

103. Kane, R. S.; Takayama, S.; Ostuni, E.; Ingber, D. E.; Whitesides, G. M. Patterning Proteins and Cells Using Soft Lithography. *Biomaterials* **1999,** *20*, 2363–2376.

104. Jackman, R. J.; Wilbur, J. L.; Whitesides, G. M. Fabrication of Submicrometer Features on Curved Substrates by Microcontact Printing. *Science* **1995,** *269*, 664–666.

105. Gunawan, C. A.; Ge, M. C.; Zhao, C. Robust and Versatile Ionic Liquid Microarrays Achieved by Microcontact Printing. *Nat. Commun.* **2014,** *5*, 3744.

106. Jeon, N. L.; Nuzzo, R. G.; Xia, Y. N.; Mrksich, M.; Whitesides, G. M. Patterned Self-Assembled Monolayers Formed by Microcontact Printing Direct Selective Metalization by Chemical-Vapor-Deposition on Planar and Nonplanar Substrates. *Langmuir* **1995,** *11*, 3024–3026.

107. Gassensmith, J. J.; Erne, P. M.; Paxton, W. F.; Frasconi, M.; Donakowski, M. D.; Stoddart, J. F. Patterned Assembly of Quantum Dots onto Surfaces Modified with Click Microcontact Printing. *Adv. Mater.* **2013,** *25*, 223–226.

108. Xia, Y.; Qin, D.; Whitesides, G. M. Microcontact Printing with A Cylindrical Rolling Stamp: A Practical Step Toward Automatic Manufacturing of Patterns with Submicrometer-Sized Features. *Adv. Mater.* **1996,** *8*, 1015–1017.

109. Xia, Y.; Kim, E.; Zhao, X.-M.; Rogers, J. A.; Prentiss, M.; Whitesides, G. M. Complex Optical Surfaces Formed by Replica Molding Against Elastomeric Masters. *Science* **1996,** *273*, 347–349.

110. Zhao, X.-M.; Xia, Y.; Whitesides, G. M. Fabrication of Three-Dimensional Micro-Structures: Microtransfer Molding. *Adv. Mater.* **1996,** *8*, 837–840.

111. King, E.; Xia, Y.; Zhao, X.-M.; Whitesides, G., M. Solvent-Assisted Microcontact Molding: A Convenient Method for Fabricating Three-Dimensional Structures on Surfaces of Polymers. *Adv. Mater.* **2004,** *9*, 651–654.

112. Dameron, A. A.; Hampton, J. R.; Gillmor, S. D.; Hohman, J. N.; Weiss, P. S. Enhanced Molecular Patterning *via* Microdisplacement Printing. *J. Vac. Sci. Technol. B* **2005,** *23*, 2929–2932.

113. Dameron, A. A.; Hampton, J. R.; Smith, R. K.; Mullen, T. J.; Gillmor, S. D.; Weiss, P. S. Microdisplacement Printing. *Nano Lett.* **2005,** *5*, 1834–1837.

114. Mullen, T. J.; Srinivasan, C.; Hohman, J. N.; Gillmor, S. D.; Shuster, M. J.; Horn, M. W.; Andrews, A. M.; Weiss, P. S. Microcontact Insertion Printing. *Appl. Phys. Lett.* **2007,** *90*, 063114.

115. Guder, F.; Yang, Y.; Kruger, M.; Stevens, G. B.; Zacharias, M. Atomic Layer Deposition on Phase-Shift Lithography Generated Photoresist Patterns for 1D Nanochannel Fabrication. *ACS Appl. Mater. Interfaces* **2010,** *2*, 3473–3478.

116. Subannajui, K.; Guder, F.; Zacharias, M. Bringing Order to the World of Nanowire Devices by Phase Shift Lithography. *Nano Lett.* **2011,** *11*, 3513–3518.

117. Xia, Y.; Zhao, X.-M.; Kim, E.; Whitesides, G. M. A Selective Etching Solution for Use with Patterned Self-Assembled Monolayers of Alkanethiolates on Gold. *Chem. Mater.* **1995,** *7*, 2332–2337.

118. Tiberio, R. C.; Craighead, H. G.; Lercel, M.; Lau, T.; Sheen, C. W.; Allara, D. L. Self‐Assembled Monolayer Electron Beam Resist on GaAs. *Appl. Phys. Lett.* **1993,** *62*, 476‐478.

119. Lercel, M. J.; Craighead, H. G.; Parikh, A. N.; Seshadri, K.; Allara, D. L. Plasma Etching with Self‐Assembled Monolayer Masks for Nanostructure Fabrication. *J. Vac. Sci. Technol. A* **1996,** *14*, 1844‐1849.

120. Hatzor, A.; Weiss, P. S. Molecular Rulers for Scaling Down Nanostructures. *Science* **2001,** *291*, 1019–1020.

121. Saavedra, H. M.; Barbu, C. M.; Dameron, A. A.; Mullen, T. J.; Crespi, V. H.; Weiss, P. S. 1-Adamantanethiolate Monolayer Displacement Kinetics Follow a Universal Form. *J. Am. Chem. Soc.* **2007,** *129*, 10741–10746.

122. Saavedra, H. M.; Thompson, C. M.; Hohman, J. N.; Crespi, V. H.; Weiss, P. S. Reversible Lability by *in Situ* Reaction of Self-Assembled Monolayers. *J. Am. Chem. Soc.* **2009,** *131*, 2252–2259.

123. Héctor, M. S.; Thomas, J. M.; Pengpeng, Z.; Daniel, C. D.; Shelley, A. C.; Paul, S. W. Hybrid Strategies in Nanolithography. *Rep. Prog. Phys.* **2010,** *73*, 036501.

124. Srinivasan, C.; Mullen, T. J.; Hohman, J. N.; Anderson, M. E.; Dameron, A. A.; Andrews, A. M.; Dickey, E. C.; Horn, M. W.; Weiss, P. S. Scanning Electron Microscopy of Nanoscale Chemical Patterns. *ACS Nano* **2007,** *1*, 191–201.

125. Garcia, R.; Knoll, A. W.; Riedo, E. Advanced Scanning Probe Lithography. *Nat. Nanotechnol.* **2014,** *9*, 577–587.

126. Piner, R. D.; Zhu, J.; Xu, F.; Hong, S.; Mirkin, C. A. "Dip-Pen" Nanolithography. *Science* **1999,** *283*, 661–663.

127. Xu, S.; Liu, G.-Y. Nanometer-Scale Fabrication by Simultaneous Nanoshaving and Molecular Self-Assembly. *Langmuir* **1997,** *13*, 127–129.

128. Luis, G. R.; Jian, L. Atomic Force Microscope Nanolithography: Dip-Pen, Nanoshaving, Nanografting, Tapping Mode, Electrochemical and Thermal Nanolithography. *J. Phys. Condens. Matter.* **2009,** *21*, 483001.

129. Smith, R. K.; Lewis, P. A.; Weiss, P. S. Patterning Self-Assembled Monolayers. *Prog. Surf. Sci.* **2004,** *75*, 1–68.

130. Schreiber, F. Structure and Growth of Self-Assembling Monolayers. *Prog. Surf. Sci.* **2000,** *65*, 151–257.

131. Slaughter, L. S.; Cheung, K. M.; Kaappa, S.; Cao, H. H.; Yang, Q.; Young, T. D.; Serino, A. C.; Malola, S.; Olson, J. M.; Link, S.; Häkkinen, H.; Andrews, A. M.; Weiss, P. S. Patterning of Supported Gold Monolayers *via* Chemical Lift-Off Lithography. *Beilstein J. Nanotechnol.* **2017,** *8*, 2648–2661.

132. Nakatsuka, N.; Yang, K.-A.; Abendroth, J. M.; Cheung, K. M.; Xu, X.; Yang, H.; Zhao, C.; Zhu, B.; Rim, Y. S.; Yang, Y.; Weiss, P. S.; Stojanovic, M. N.; Andrews, A. M. Aptamer-Field-Effect Transistors Overcome Debye Length Limitations for Small-Molecule Sensing. *Science* **2018,** *In Press*.

133. Cao, H. H.; Nakatsuka, N.; Serino, A. C.; Liao, W.-S.; Cheunkar, S.; Yang, H.; Weiss, P. S.; Andrews, A. M. Controlled DNA Patterning by Chemical Lift-Off Lithography: Matrix Matters. *ACS Nano* **2015,** *9*, 11439–11454.

134. Abendroth, J. M.; Nakatsuka, N.; Ye, M.; Kim, D.; Fullerton, E. E.; Andrews, A. M.; Weiss, P. S. Analyzing Spin Selectivity in DNA-Mediated Charge Transfer *via* Fluorescence Microscopy. *ACS Nano* **2017,** *11*, 7516–7526.

135. Gao, P.; He, J.; Zhou, S.; Yang, X.; Li, S.; Sheng, J.; Wang, D.; Yu, T.; Ye, J.; Cui, Y. Large-Area Nanosphere Self-Assembly by a Micro-Propulsive Injection Method for High Throughput Periodic Surface Nanotexturing. *Nano Lett.* **2015,** *15*, 4591–4598.

136. Haes, A. J.; Hall, W. P.; Chang, L.; Klein, W. L.; Van Duyne, R. P. A Localized Surface Plasmon Resonance Biosensor: First Steps Toward an Assay for Alzheimer's Disease. *Nano Lett.* **2004,** *4*, 1029–1034.

Chapter 2

Polymer-Pen Chemical Lift-Off Lithography

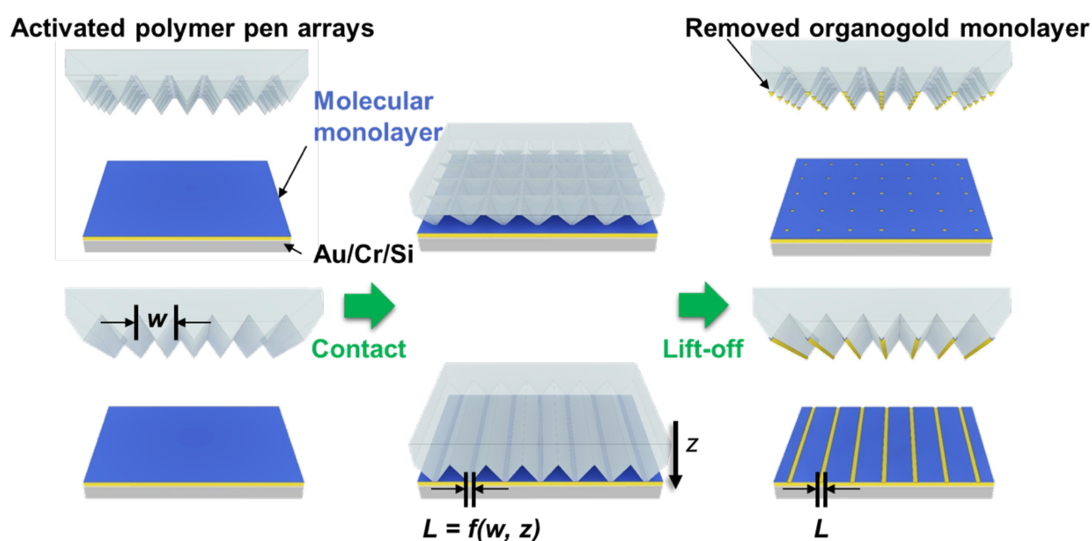

The information in this chapter was published in

Nano Lett. **2017**, *17*, 3302–3311 and has been reproduced here.

Authors: Xu, X.[#]; **Yang, Q.[#]**; Cheung, K. M.; Zhao, C.; Wattanatorn, N.; Belling, J. N.; Abendroth, J. M.; Slaughter, L. S.; Mirkin, C. A.; Andrews, A. M.; Weiss, P. S.

([#]indicates equal contribution)

2.1 Abstract

We designed and fabricated large arrays of polymer pens having sub-20-nm tips to perform chemical lift-off lithography (CLL). As such, we developed a hybrid patterning strategy called polymer-pen chemical lift-off lithography (PPCLL). We demonstrated PPCLL patterning using pyramidal and v-shaped polymer-pen arrays. Associated simulations revealed a nanometer-scale quadratic relationship between contact linewidths of the polymer pens and two other variables: polymer-pen base linewidths and vertical compression distances. We devised a stamp support system consisting of interspersed arrays of flat-tipped polymer pens that are taller than all other sharp-tipped polymer pens. These supports partially or fully offset stamp weights thereby also serving as a leveling system. We investigated a series of v-shaped polymer pens with known height differences to control relative vertical positions of each polymer pen precisely at the sub-20-nm scale mimicking a high-precision scanning stage. In doing so, we obtained linear-array patterns of alkanethiols with sub-50-nm to sub-500-nm linewidths and minimum sub-20-nm linewidth tunable increments. The CLL pattern linewidths were in agreement with those predicted by simulations. Our results suggest that through informed design of a stamp support system and tuning of polymer-pen base widths, throughput can be increased by eliminating the need for a scanning stage system in PPCLL without sacrificing precision. To demonstrate functional microarrays patterned by PPCLL, we inserted probe DNA into PPCLL patterns and observed hybridization by complementary target sequences.

2.2 Introduction

Substantial progress has been made in chemical patterning methods to push resolution from micron to nanometer scales for applications in electronics,[1-7] optics,[8,9] energy,[10,11] and biology,[12,13] *e.g.*, integrated circuits,[14-16] displays,[17-19] ultra-sensitive biosensors,[20-25] nanomotors,[26] biomolecule micro-/nano-arrays,[27-31] wearable sensors,[32-35] and other advanced metamaterials.[36] Nano- and microfabrication are dominated by patterning methods based on energetic beams, such as light, electrons, ions, and X-rays. Conventional photolithography can be used to fabricate structures over large areas, however, resolution is limited and costs of the masks are high. Advanced lithography techniques, such as liquid immersion/multiple patterning photolithography,[37,38] X-ray lithography,[39,40] or extreme ultraviolet photolithography[41-43] can push resolution to nanometer scales but availability is limited due to high set-up and maintenance costs. Direct-write techniques, such as electron-beam lithography (EBL)[44-50] and focused ion-beam lithography (FIB)[51,52] are used to generate nanoscale patterns, but time-consuming serial writing processes limit their throughput.[53]

Without using energetic beams, microcontact printing (μCP) is a high-throughput, straightforward molecular printing technique for chemical patterning at the micro- and nanometer scales.[54,55] Microcontact printing involves elastomeric stamps with molecular "inks" such as organic molecules, proteins, or DNA that enables ink transfer to planar or curved substrates composed of metals, glass, or polymers to produce patterns. Organic ink molecules, such as alkanethiols, serve as molecular resists in successive wet etching steps to transfer patterns to underlying substrates, *e.g.*, metals.[56,57] Nonetheless, ink molecules are known to diffuse laterally beyond the contact areas during printing, resulting in resolution limited to ~100 nm for μCP.[58-60]

We have developed strategies to minimize or to eliminate lateral diffusion of ink molecules *via* modified μCP methods.[61-66] For example, microdisplacement printing[67,68] and microcontact insertion printing[59,69] are used to print molecules on alkanethiol self-assembled monolayer (SAM) -modified substrates through displacement or insertion processes, respectively. The SAMs in the unpatterned regions prevent ink molecules from diffusing beyond the contact areas.[59,70] We also developed a "subtractive" stamping process called chemical lift-off lithography (CLL),[60,71] in which oxygen plasma-activated polydimethylsiloxane (PDMS) stamps selectively remove hydroxyl- (-OH) (or other sufficiently reactive groups such as amine-) terminated alkanethiols only in the contact areas with high pattern fidelity and without observable lateral diffusion. The remaining SAM molecules in the non-lift-off regions act as resists for selective etching of exposed gold in the patterned regions. High-fidelity chemical patterns with linewidths as narrow as 40 ± 2 nm were achieved using CLL, with features reaching 20 nm *via* double patterning[60] and even 5 nm (corresponding to patterns *ca.* ten molecules across).[71] However, for CLL, like μCP, the fabrication of masters with nanometer-scale resolution relies on low-throughput, high-cost EBL/FIB limiting applicability.

Dip-pen lithography can write chemical patterns directly on substrates at sub-50 nm resolution by using atomic force microscopy with tip-coated molecular "inks", e.g., alkanethiols, but again, throughput is low due to time-consuming serial writing.[72] Polymer-pen lithography (PPL)[73-77] combines high-resolution dip-pen lithography[72,78] and μCP by using a scanning stage equipped with massively parallel polymer-pen arrays (with sub-80 nm tip diameters) to write patterns with ink molecules directly at ~100 nm resolution with high throughput.[73] Reusable masters for producing polymer pens are fabricated by conventional photolithography at micron-scale resolution *via* anisotropic etching of Si(100).[73] The use of a scanning stage enables

nanometer-scale control of polymer pens in the *x, y,* and *z* planes. Another advantage of PPL is that feature sizes can be tuned from 80 nm to >10 μm by varying dwell times and vertical pen compression in a single stamp.[76] However, lateral diffusion of ink molecules persists limiting the resolution of PPL similar to issues with μCP.

2.3 Materials and Methods

Materials. Prime quality 4″ Si(100) wafers (P/B, 1-10 ohm-cm) were purchased from University Wafer Inc. (Boston, MA, USA). 11-Mercapto-1-undecanol was purchased from Sigma-Aldrich (St. Louis, MO, USA). Sylgard 184® silicone elastomer kit was purchased from Ellsworth Adhesives (Germantown, WI, USA). The 32-mer DNA molecules thiolated at the 5′ end (5′-/5ThioMC6-D/GAC TGA CCT CGG ACG CGA CTG ACC TCG GAC GA-3′ with molecular weight 10148.8 g/mol and melting temperature 70.1 °C) and Alexa 488 fluorophore-labeled complementary DNA (5′-/5Alex488N/TCG TCC GAG GTC AGT CGC GTC CGA GGT CAG TC-3′ with molecular weight 10529.0 g/mol and melting temperature 70.1 °C) were purchased from Integrated DNA Technologies (Coralville, IA, USA). The DNA stock solutions were diluted to 1 μM with TE buffer (10 mM Tris and 0.1 mM EDTA). The ZEP 520A e-beam resist, SPR700-1.2 photoresist, MF-26A developer, and 30 wt% potassium hydroxide (KOH) solutions were obtained from the Integrated Systems Nanofabrication Cleanroom (ISNC) at UCLA.

Characterization. Scanning electron microscopy (SEM) images were taken using a Zeiss Supra 40VP scanning electron microscope (SEM). The polydimethylsiloxane (PDMS) stamps were made conductive by sputtering 5-nm Au for SEM imaging. ImageJ (https://imagej.nih.gov/ij/) was used to quantify the dimensions of the micro/nanostructures and chemical patterns in the SEM images. Surface roughness was characterized using a Bruker Dimension Icon Scanning Probe Microscope.

Fabrication of Si masters and PDMS stamps was shown in Scheme S2.1. Growth of SiO_2 on Si(100) (Step 1): a 500-nm-thick SiO_2 film was thermally grown on piranha-cleaned Si(100) wafers. The SiO_2/Si wafers are also available for purchase elsewhere. Photolithography

(Step 2): the pattern in the photomask was designed using AutoCAD software (Autodesk, Inc.). Photomasks for fabricating a Si master comprised of a 2D array of squares or lines whose linewidths are >1 μm were fabricated by conventional photolithography. The designed linewidths are equal to the base linewidths of the polymer pens. Positive photoresist SPR700-1.2 was spin-coated on the SiO_2/Si wafer surface, followed by a 90 sec soft bake at 90 °C on a hotplate. A Karl Suss contact aligner was used to expose the photoresist on the wafer selectively with the pattern from photomask with an optimal exposure time of 16.5 sec (UV wavelength = 365 nm, intensity = 8.5 mW/cm^2). The exposed wafer was baked post-exposure at 110 °C for 90 seconds, immersed in MF-26A developer for 1 min (development), rinsed with deionized water, and blown dry with N_2 gas. Electron-beam lithography (Step 2): for proof of concept for PPCLL, we designed a line array pattern with a series of linewidths in sequence from 3500 nm to 4000 nm, as listed in **Table 2.1**, with neighbor center-to-center distances of 14 μm. Between each two neighboring lines, we inserted a line with 6 μm linewidth, which served as the pattern for the support elements. All of the lines have the same 200 μm length. Positive electron-beam resist ZEP 520A was spin-coated (3000 RPM, 30 sec) on a (2 cm × 2 cm) Si(100) wafer with a 500-nm-thick SiO_2 coating. The edge of the Si(100) wafer was pre-cut to be parallel to the Si<110> direction. A pre-bake was performed at 180 °C for 2 min. An electron-beam writer (Vistec EBPG 5000+ ES) was used to write the designed patterns on the substrate with repeated line arrays with an overall area of 1 cm × 1 cm. One min development in ZED-N50 was used to expose the SiO_2 with pattern. Reactive ion etching (RIE) of SiO_2 (Step 3): after patterning by photolithography or EBL, the exposed SiO_2 was selectively etched by RIE (Oxford 80 Plus) using a gas mixture of CHF_3 (25-sccm) and Ar (25 sccm) at 35 mTorr. Anisotropic etching of Si(100) (Step 4): The anisotropic etching took place in a mixture of 4:1 KOH (30%) and

isopropanol at 75 °C with variable times depending on the feature sizes. SiO_2 and resist removal (Step 5)**:** the fabrication of the Si master was completed by removing the remaining SiO_2 and resist in a 25% HF solution for 5 min. Preparation and removal of PDMS stamps (Steps 6-7): a 10:1 mass ratio of Sylgard® 184 elastomer silicone elastomer base and curing agent were thoroughly mixed and then degassed in a vacuum desiccator. This mixture was poured onto the Si master and cured overnight at 65 °C. After curing, PDMS stamps were carefully removed from the Si master.

Surface functionalization of Au/Cr/Si substrate for PPCLL**:** The 5-nm Cr and 100-nm Au films were deposited on clean silicon wafers in a CHA Solution E-Beam Evaporator at high vacuum (10^{-8} Torr) with evaporation rates of 0.1 nm/s. the Cr/Au/Si wafers were annealed in a hydrogen flame for 5-10 sec to create Au(111) surfaces and then immersed into 0.5 mM an 11-mercapto-1-undecanol ethanolic solution overnight for SAM formation on the Au surface.

Activation of PDMS stamps**:** Clean PDMS stamps were treated in oxygen plasma (Harrick Plasma, Ithaca, NY) for 40 seconds at a power of 18 W and a pressure of 10 Psi to generate hydrophilic surfaces.

DNA insertion and fluorescence microscopy**:** DNA was inserted into lifted-off areas as previously reported. Substrates after PPCLL were incubated in a 1 μm solution of thiolated DNA in 0.01 M PBS (pH = 7.4) for ~17 h to insert the DNA into the lifted-off areas. The substrates were then rinsed with deionized water and blown dry with N_2 gas. The inserted DNA was hybridized by incubating the substrates with a 1 μm solution of Alexa 488-labeled complementary DNA in 0.01 M PBS (pH = 7.4) for 30 min. Samples were imaged using an inverted fluorescence microscope (Axio Observer.D1, Carl Zeiss MicroImaging, Inc.,

Thornwood, NY, USA) with excitation and emission wavelengths of 470 ± 20 nm and 525 ± 25 nm, respectively.

2.4. Results and Discussions

To advance feature resolution in chemical patterning in highly multiplexed and facile directions, we developed a hybrid method termed polymer-pen chemical lift-off lithography (PPCLL) that combines the advantages of PPL (massively parallel polymer pens with nanometer-scale tips for high-throughput patterning and feature size tunability by controlling vertical compression distances) and CLL (high-fidelity patterning without lateral diffusion) to enable large-area, low-cost, and sub-20-nm resolution patterning capabilities simultaneously. Fabrication of polymer pens with nanometer-sized tip diameters is described (**Scheme S2.1**). Films of 500-nm-thick SiO_2 were grown on 4" Si(100) wafers *via* thermal oxidation, followed by spin coating with photoresist (SPR700-1.2). Conventional photolithography was then used to create micron-scale square or line array patterns on photoresist-coated SiO_2/Si(100) wafers. The linewidths of the masters govern the *base* linewidths of the polymer pens. Overall areas are 1.5 cm × 1.5 cm for each square or line array pattern. It is critical to align edge axes of the square/line features on each photomask such that they are parallel with the primary flat edge of each Si(100) wafer, which is parallel to the <110> direction of Si(100). Imperfect alignment resulted in blunt pen tips.

Next, reactive ion-etching (RIE) was used to etch exposed SiO_2 selectively to reveal the underlying Si(100). Subsequently, a solution with a 4:1 ratio of 30% KOH and isopropanol was used to etch Si(100) wafers anisotropically to generate recessed pyramidal or v-shaped structure arrays having base dimensions matched to the designed patterns in the photomasks.[77] The Si master fabrication was completed by removing remaining SiO_2 in 25% HF solution for 5 min. Finally, PDMS stamps containing arrays of polymer pens were produced from the masters. Both

the masters and stamps can be reused many times. (Experimental details are provided in Materials and Methods.)

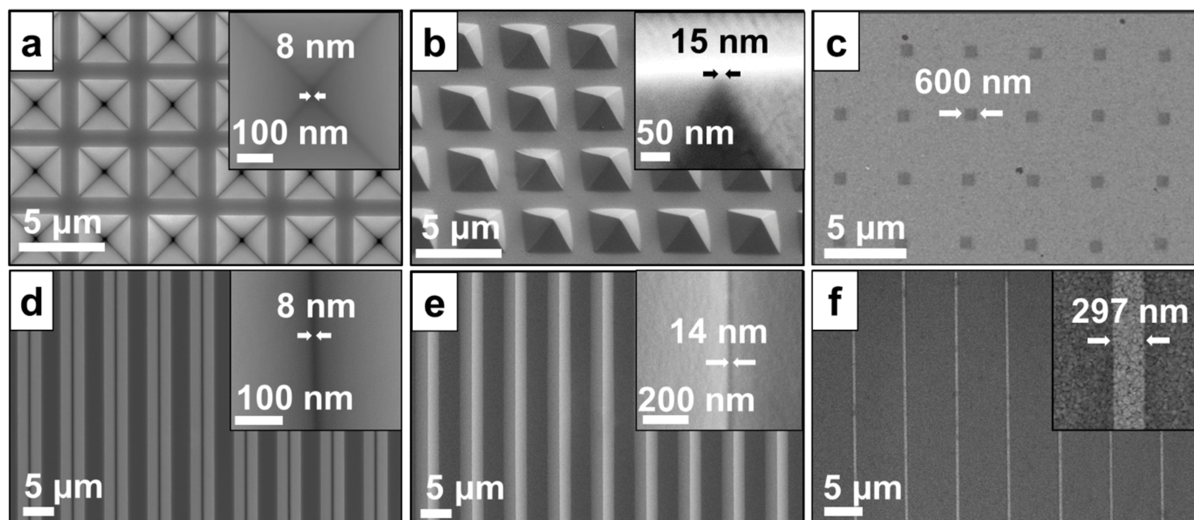

Figure 2.1. Scanning electron microscopy (SEM) images of: (a) Si master with recessed pyramidal structures having base linewidths of 3 μm and a periodicity of 4 μm; (b) polydimethylsiloxane (PDMS) stamp with pyramidal polymer-pen arrays replicated from the master in (a); (c) polymer-pen chemical lift-off lithography (PPCLL) pattern produced using the stamp in (b) without external compression; (d) Si master with recessed v-shaped structures with base linewidths of 3.8 μm and a periodicity of 7 μm; (e) PDMS stamp with v-shaped polymer pen arrays replicated from the master in (d); (f) typical PPCLL pattern produced using the stamp in (b) without external compression. (Insets: high magnification SEM images) (The images (c) and (f) are processed to visualize the patterns better; the unprocessed images are shown in Figure S2.3).

As shown in the scanning electron microscopy (SEM) images in **Figure 2.1**, high-quality Si masters containing large arrays of recessed pyramidal or v-shaped structures and stamps containing large arrays of protruding pyramidal/v-shaped polymer pens were fabricated using

this method. The recessed pyramids or v-shaped structures of the masters had typical tip diameters d_{tip} of 8 nm, whereas protruding pyramids and v-shaped polymer pens had average measured tip diameters d_{tip} of 19 ± 2 nm and 15 ± 2 nm, respectively. Typical polymer pen tips with d_{tip} of 15 nm and 14 nm are shown in the insets of **Figure 2.1**. The larger tip diameters of the features on the PDMS stamps compared to those of the masters were likely due to tip-rounding effects caused by the high surface tension of PDMS when it is applied to the masters (and before curing).[79] The sub-20-nm tip-diameters d_{tip} of the polymer pens are comparable to the smallest features fabricated using EBL,[48] however, polymer pens produced by the method described above avoid EBL and thus, the need to produce each set of pens serially. Average tip diameters of the polymer pens fabricated here are smaller than most reported polymer pens (usually >50 nm),[73] because the square or narrow rectangular features on the photomasks have small widths (<6 μm) and their edges were perfectly aligned to Si<110> directions to allow Si{111} facets to converge into sharp points or sharp lines during the anisotropic etching of Si(100).

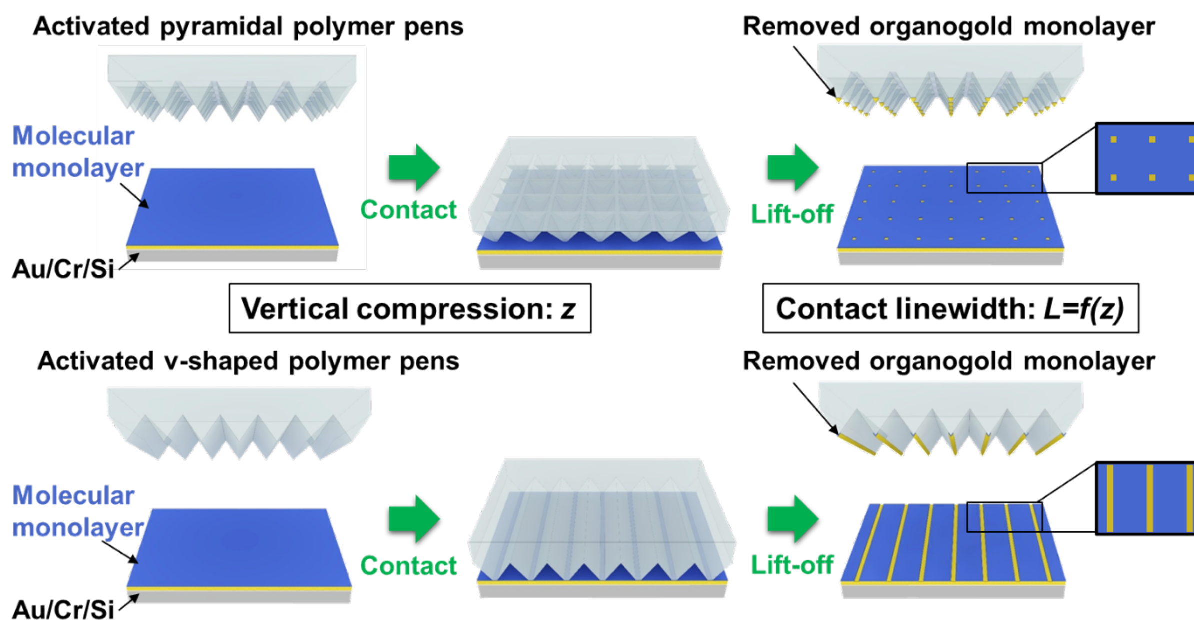

Scheme 2.1. Schematic illustrations of polymer-pen chemical lift-off lithography (PPCLL) using pyramidal (top) and v-shaped (bottom) polymer pen arrays. In both cases, in the first step, hydroxyl-terminated alkanethiol molecules form self-assembled monolayers (SAMs) on Au/Cr/Si substrates. The polydimethylsiloxane (PDMS) stamps carrying the polymer-pen arrays are then activated with oxygen plasma treatment. In the second step, an activated PDMS stamp is brought into conformal contact with the SAM on a Au/Cr/Si substrate using a known vertical compression distance. Condensation reactions occur between the hydroxyl-terminated SAM molecules and the activated PDMS stamp to form strong covalent bonds. In the third step, the PDMS stamp is lifted off of the substrate, removing a portion of SAM molecules (~70%) together with Au adatoms from the contact areas to produce a complementary pattern on the substrate and an organogold monolayer on the stamp in the regions of contact. The contact/feature linewidth (*L*) is controlled by the vertical compression distance (*z*) of the stamp during contact *via* the relationship *L* = *f(z)*.

As-fabricated PDMS stamps with polymer pen arrays were used in PPCLL as illustrated in **Scheme 2.1**. Step 1: a 40-sec O_2 plasma treatment generated hydrophilic siloxy (Si-OH) groups on PDMS stamp surfaces containing pyramidal/v-shaped polymer pens. This step is called "activation".[80] Step 2: activated PDMS stamps were brought into conformal contact with Au/Cr/Si substrates (Au: 100 nm over Cr: 5 nm) functionalized with hydroxyl-terminated alkanethiol SAM molecules. 11-Mercapto-1-undecanol SAM molecules were used throughout this study, but alkanethiols with other backbones, chain lengths, and terminal functional groups can be used.[31,60] A condensation reaction occurs between Si-OH groups on activated PDMS stamps and the terminal hydroxyl groups of the self-assembled alkanethiol molecules to form covalent bonds, *i.e.*, Si-O-SAM thereby enabling lift-off.[60] Step 3: the PDMS stamps were removed to lift-off SAM molecules only in the contact areas producing complementary patterns of SAMs on the Au/Cr/Si substrates. Note that in this lift-off process, a layer of Au adatoms is removed along with the lifted SAM molecules. We hypothesize that this occurs because weaker Au-Au bonds in the top layer of the substrate surfaces are preferentially broken during lift-off, rather than the Au-S bonds between the substrate and alkanethiols.[60]

As previously reported,[76,77] deformation of polymer pens and thus, the areas contacted by each pen can be controlled in PPL by compressing the polymer pens onto the substrates using a scanning stage with vertical compression-distance control. For example, square features can be obtained with linewidths ranging from 500-2000 nm by controlled vertical compression with sub-micron increments.[76] However, time-dependent lateral diffusion results in larger feature sizes than actual contact areas in PPL. By contrast, in PPCLL, patterned features and contact areas are *identical* in size. If the vertical compression distance is controlled at the

nanometer-scale, then presumably contact areas can be correspondingly controlled. However, in practice, nanometer-scale differences in deformation and contact areas are challenging.

Alternately, computational simulations can be used to predict deformation at the nanometer scale. Here, we simulated compression of v-shaped polymer pens, in addition to the more well-studied pyramidal polymer pens.[76,81] Zheng *et al.* simulated deformation of pyramidal polymer pens and found that contact radii increased linearly with vertical compression distances from sub-100-nm to sub-micron with nanometer-scale resolution.[81] To simulate the vertical compression-distance dependent deformation of v-shaped polymer pens at the nanometer scale, we constructed a 2D *Mooney-Rivlin* model using a finite-element method *via* ANSYS software (Ansys Inc., Canonsburg, PA). We simulated vertical compression distances (z) from 0 nm to 560 nm with a minimum step size in z of 2 nm for v-shaped polymer pens having a base linewidth (w) = 4000 nm and a tip diameter of 22 nm. An element size of 8 nm was used to model polymer-pen tips (from the tip to 400 nm in height). For the remainder of the polymer-pen height, an element size of 40 nm was used.

The initial contact was set to occur at a vertical compression distance of $z = 10$ nm. As shown in **Figure 2.2**, as z increased, the v-shaped polymer pen tips flattened and the contact linewidths (L) increased. After fitting, we found a quadratic dependence between z and L at $w = 4000$ nm:

$$L = f(z) = a + bz + cz^2 \qquad \textbf{Eq. (2.1)}$$

where $a = 0$ nm, $b = 0.444$, $c = 5.72 \times 10^{-4}$ nm^{-1}, $z > 10$ nm, with L in nm. According to **Eq. (2.1)**, we can precisely and robustly control the feature size by controlling z. Note, that the standard deviation of the difference between the simulation results and fitted curve is only

1.4 nm, and can be further reduced by decreasing the element size and step size in the simulations. Therefore, **Eq. (2.1)** accurately represents the relationship between *z* and *L*.

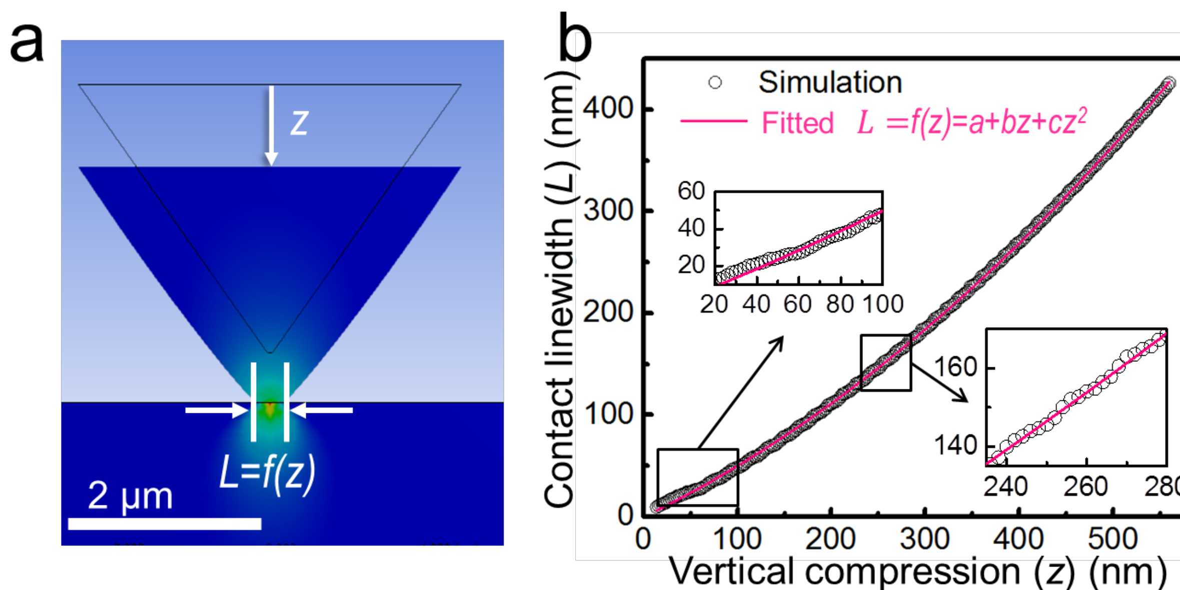

Figure 2.2. (a) Simulation: cross-sectional view of a v-shaped polymer pen (base linewidth: 4-µm) vertically compressed onto a rigid Au surface with a vertical compression distance of *z* and a resulting contact linewidth of $L = f(z)$. (b) Simulation results: increasing the vertical compression distance *z* leads to increased contact linewidth (*L*). The relationship between vertical compression distance *z* and *L* is fitted using the quadratic equation $L = f(z) = a + bz + cz^2$, where *a*, *b*, and *c* are constants.

The above simulations demonstrate that feature-size resolution can be tuned at the nanometer scale in PPCLL. However, in practical experiments, resolution is affected by the following additional factors: (a) precision of vertical compression distance, which relies solely on the resolution of the scanning stage – typically, a piezoelectric stage has a resolution <1 nm; and (b) surface smoothness of the polymer pens and substrates. As shown in **Figure S2.1**, atomic force microscopy characterization shows that the surfaces used here have an arithmetic average

roughness (R_a) of 0.4 ± 0.1 nm for a recessed structure in the master and 1.1 ± 0.1 nm for a polymer pen. The value of R_a for the Au/Cr/Si substrate is ~1 nm (data not shown).

The integration of a piezoelectric scanning stage[75,77] and a high-quality leveling technique into PPCLL, such as an optical- or force-feedback leveling system, would enable an ultimate theoretical resolution of <2 nm to be reached.[75] Without using these advanced equipment-intensive techniques, we nevertheless demonstrate nanometer-scale feature size control in PPCLL by designing and implementing a support-arm array system and polymer pen arrays with height gradients, as described in the following experiments and simulations.

In the first experiment, activated PDMS stamps containing large arrays (3750 × 3750 and 1 × 2150) of pyramidal (w = 3 μm, period = 4 μm) or v-shaped polymer pens (w = 3.8 μm, period = 7 μm) were placed on substrates without external compression. Stamps conformally contacted substrates without the need for a leveling system. The contact time was set to 4-6 h to ensure high-quality pattern transfer. Our previous CLL work showed features could be transferred with contact times as short as 1 min; however, shorter contact times resulted in poorer features after wet etching.

The PPCLL patterns were imaged by SEM. The different intensities observed in SEM images were due to different chemical components on the surfaces.[59] As shown in **Figure 2.1c,f**, a square-dot array pattern (~600 nm linewidth) and a line-array pattern (~300 nm linewidth) were achieved. Moreover, the lateral diffusion of ink molecules was avoided in PPCLL, otherwise much enlarged features would have been observed after such long contact times.[59,76] The periodicities of the dot/line arrays were consistent with the stamp patterns. The enlarged feature sizes, compared to the original 20 nm tip diameters, was the result of polymer pen deformation caused by the weight of the stamps, which increased the contact linewidth to

>20 nm. However, features were still 1-2 orders of magnitude smaller than the base linewidths of the polymer pens in the photomask. Without using sophisticated fabrication techniques, we achieved sub-micron feature scales over large areas simply by this “contact & lift” process. Our results demonstrate that PPCLL is an economical and high-throughput method for producing sub-micron features over large areas.

We learned from the first set of experiments that the stamp weight deforms the tips such that no leveling is necessary. The height of each pyramidal/v-shaped polymer pen (h) is determined by its base linewidth (w) using the equation: $h = \frac{w}{2} \cdot \tan\theta = \frac{w}{\sqrt{2}}$, here θ is the angle between the Si(100) and Si(111) facets. Thus, polymer pens with a series of different base linewidths (w_i) have different heights (h_i) by design. As illustrated in **Figure 2.3a**, the distances ($D_i = D_0 - h_i$) from the tip of each polymer pen to the surface are different, where the subscript i ($i > 0$) is used to distinguish different polymer pens, and D_0 ($D_0 > h_i$) is the initial vertical distance from the base of the polymer pens to the surface of each substrate before contact. Under conformal contact, all of the polymer pens have the same initial vertical compression distance, z. However, upon initial contact with the substrate and due to their height differences, each polymer pen has a *different* effective vertical compression distance, $z_i' = z - D_i$. Contact only occurs when $z_i' > 0$, *i.e.*, $z > D_i$. Each contacted polymer pen has a contact linewidth, $L = f(z_i')$. We hypothesize that this process would be similar to vertical compression distances in PPCLL controlled using a piezoelectric scanning stage system.

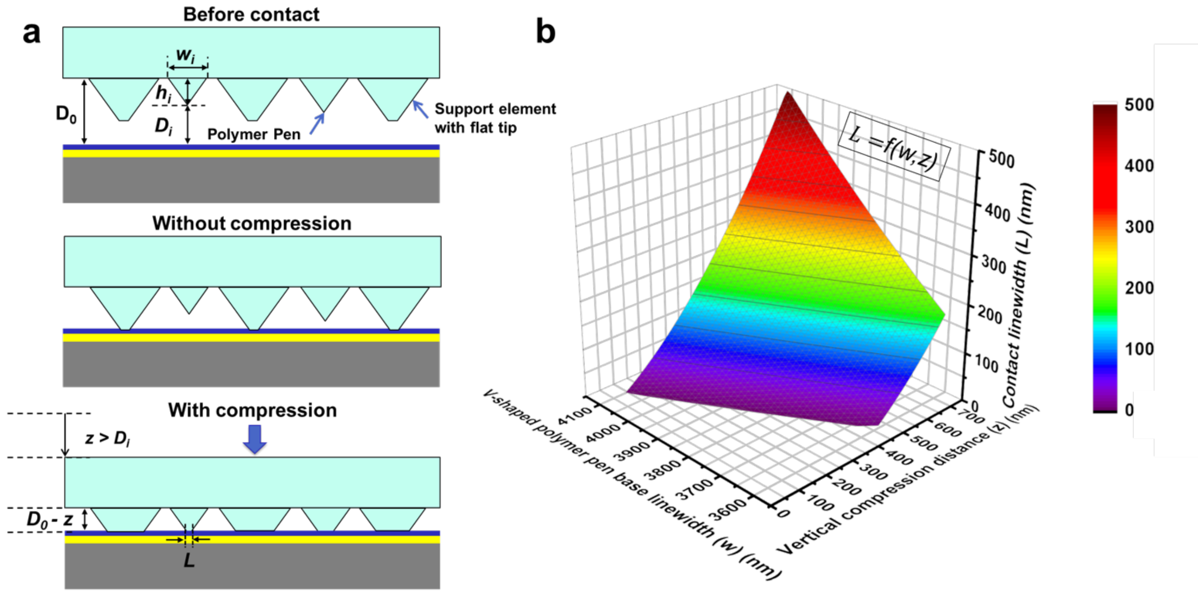

Figure 2.3. (a) Illustration of a polydimethylsiloxane (PDMS) stamp used in polymer-pen chemical lift-off lithography (PPCLL) having support elements (taller v-shaped polymer pens with flat tips) interleaved with v-shaped polymer pens (sharp tips with designed base linewidths w_i): before contact, after placement on a substrate but with no vertical compression, and after vertical compression. Here, D_0 ($D_0 > h_i$) is the initial vertical distance from the base of the polymer pens to the surface of each substrate before contact; h_i is the height of a polymer pen; D_i is distance from the polymer pen tip to the substrate, $D_i = D_0 - h_i$; z is the vertical compression distance and L is resulting contact linewidth. (b) Simulation of results where v-shaped polymer pen base linewidths (w) and vertical compression distances (z) were varied to control contact-dependent linewidths (L), *i.e.*, $L = f(w, z)$.

To test this hypothesis, we added the base linewidth w as another variable in our simulations, in addition to the vertical compression distance z, *i.e.*, $L = f(w, z)$. In this simulation, we designed a series of w values ranging from 3500 nm to 4000 nm in increments of 25 nm. The

initial vertical distance from the base of all of the v-shaped polymer pens to the surfaces of substrates was set at D_0 = 3000 nm, which is a reasonable distance to keep all of the v-shaped polymer pens from contacting the substrates. Then, vertical compression distances *z*, ranging from 0 nm to 700 nm with a step size of 5 nm, were applied in the contact simulation between each v-shaped polymer pen and the substrate. After fitting the simulation results for all of the polymer pens with $L = f(z)$, we derived a series of fitted curves. We plotted and connected all the fitted curves in the same 3D space to form a curved surface. The curved surface was well fit by:

$$L = f(z, w) = a + bz + cw + dzw + ez^2 + fw^2 \qquad \textbf{Eq. (2.2)}$$

where a = 2783, b = -2.786, c = -1.602, $d = 7.572 \times 10^{-4}$, $e = 5.729 \times 10^{-4}$, $f = 2.232 \times 10^{-4}$ (the fitted curved surface is plotted in **Figure 2.3b**). The **Eq. (2.2)** is a universal equation wherein we can design and control desired contact linewidths *L* either through *w* or *z*. Furthermore, when *z* is fixed, *w* becomes the only variable influencing *L*. Under these conditions, **Eq. (2.2)** is reduced to:

$$L = f(w) = a'' + b''w + c''w^2 \quad \textbf{Eq. (2.3)}$$

Based on the above simulation results, in the second experiment, we added two components in PPCLL, *i.e*., a stamp support system and polymer pens with height gradients. The supporting elements are taller polymer pens with flat tips (obtained by incomplete anisotropic etching of Si(100)) distributed between the polymer pens used for pattering, as illustrated in **Figure 2.3a**. Here, the support elements have fixed base linewidths of 6 μm (**Figure 2.4a**). These support elements serve as weight-bearing pillars to support the stamp[56] and the flat tips further serve as a low-cost leveling system. Properly designed support elements can either keep the patterning-purpose polymer-pen arrays away from the substrate by fully cancelling the weight of the stamp or they can control the degree of tip deformation of the patterning-purpose polymer

pens by partially offsetting the stamp weights. The support elements can also be integrated into other PPL designs as an initial contact indicator to estimate how much extra vertical compression distance or force is needed to obtain desired contact areas.[75,77]

For the second component, a series of v-shaped polymer pen arrays was designed with base linewidths from 3500 to 4000 nm, as listed in **Table 2.1**. The support elements were designed with linewidth increments of 25, 50, and 100 nm. For the 25-nm increment (shown in bold in **Table 2.1**), the corresponding height increment of the polymer pens was $\frac{25\ nm}{\sqrt{2}} = 18\ nm$. As shown in **Figure 2.4a,** the v-shaped polymer pens were separated by the support elements. Electron-beam lithography was used to produce base linewidths with small increments (25 nm to 100 nm) for proof-of-concept purposes (details of EBL are in Materials and Methods). The differences between the designed base linewidths (w_{design}) and the measured base linewidths ($w_{measured}$) of the v-shaped polymer pens were 100 nm, as listed in **Table 2.1**.

Using this stamp design, a PPCLL experiment *without* an extra compression force beyond the weight of the stamp was performed. As seen in the SEM image in **Figure 2.4**, v-shaped polymer pens with larger base linewidths generated larger PPCLL feature linewidths, which indicated larger contact areas, as expected. A full set of SEM images are shown in **Figure S2.4**. As listed in **Table 2.1**, we obtained a series of linewidths of 31 ± 4 nm, 48 ± 4 nm, 67 ± 4 nm, 81 ± 7 nm, 101 ± 7 nm, and 120 ± 5 nm, 134 ± 7 nm, 141 ± 5 nm, 156 ± 8 nm, 169 ± 8 nm, 202 ± 5 nm, 223 ± 9 nm, 248 ± 6 nm, and 309 ± 9 nm. Among these, the smallest linewidth was 31 ± 4 nm. For w_{design} from 3550 to 3750 nm, the designed base linewidth increment Δw_{design} was fixed at 25 nm resulting in an average measured base linewidth increment of $\Delta w_{measured}$ = 26 ± 6 nm, and an average calculated height increment of $\Delta h_{calculated}$ = 18 ± 4 nm based on $\Delta w_{measured}$ increment (shown in bold in **Table 2.1**). Such small increments resulted in

average measured pattern linewidth increments $\Delta L_{measured}$ at the sub-20-nm scale, 15 ± 4 nm. Both the sub-40-nm linewidth and the sub-20-nm linewidth increments are comparable to the critical dimensions and resolutions of many vacuum-based nanolithography techniques.[44-52]

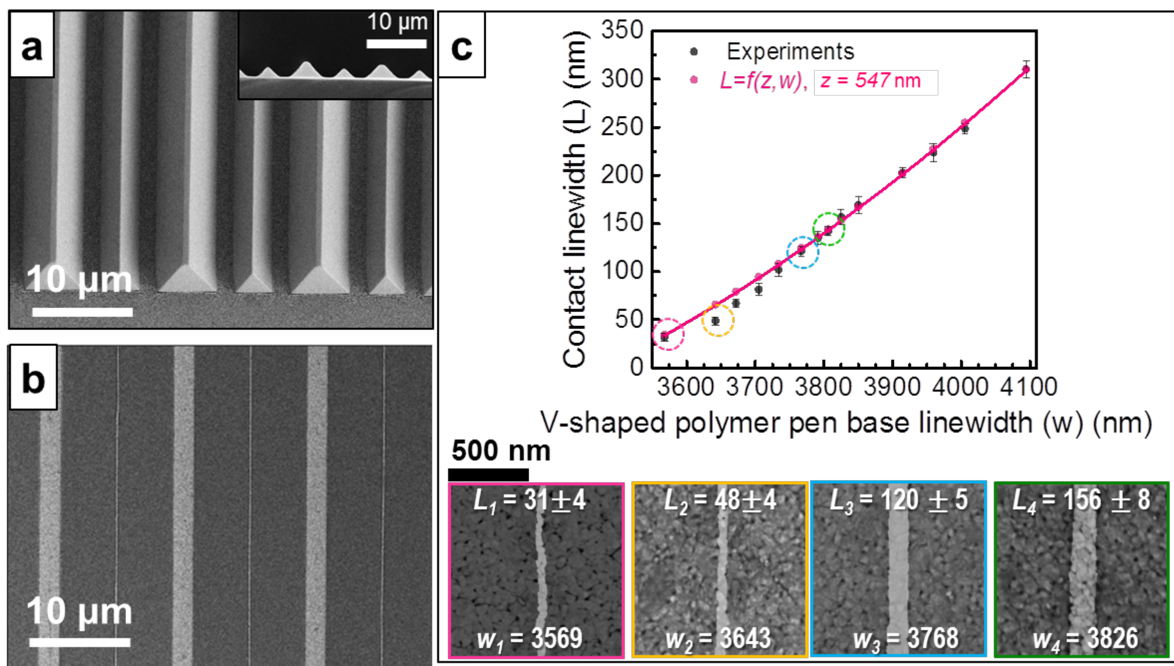

Figure 2.4. (a) A scanning electron microscope (SEM) image of a polymer-pen array having designed height gradients and a stamp support system; Inset: cross-sectional view to show height differences. (b) A SEM image of a polymer-pen chemical lift-off lithography (PPCLL) pattern produced by the stamp in (a). (c) A plot of experimental and simulation results of the relationship between the linewidths of the PPCLL patterns and the v-shaped polymer pen base linewidths. Below are four SEM images of typical PPCLL patterned lines corresponding to the four data points circled in different colors. Note, L_1, L_2, L_3, and L_4 are measured linewidths; w_1, w_2, w_3, and w_4 are the corresponding base linewidths in nm. (The images (b) and insets of (c) are processed to visualize the patterns better; the unprocessed images are shown in Figures S2.3 and S2.4.)

Table 2.1. Measured and simulated patterning results of polymer-pen chemical lift-off lithography using stamp support elements and v-shaped polymer pens over a series of designed base linewidths. All values are in nm.

w_{design}	$w_{measured}$	$L_{measured}$	$L_{simulated}$	Δw_{design}	$\Delta w_{measured}$	$\Delta h_{calculated}$	$\Delta L_{measured}$
3500	3569	31 ± 4	34	-	-	-	-
3550	3643	48 ± 4	65	50	74	52	17
3575	3673	67 ± 4	79	**25**	**30**	**21**	**18**
3600	3706	81 ± 7	94	**25**	**33**	**23**	**14**
3625	3735	101 ± 7	108	**25**	**29**	**21**	**20**
3650	3768	120 ± 5	124	**25**	**33**	**23**	**19**
3675	3792	134 ± 7	136	**25**	**24**	**17**	**14**
3700	3807	141 ± 5	143	**25**	**15**	**11**	**7**
3725	3826	156 ± 8	153	**25**	**19**	**13**	**15**
3750	3851	169 ± 8	166	**25**	**25**	**18**	**13**
3800	3915	202 ± 5	201	50	64	45	33
3850	3960	223 ± 9	227	50	45	32	21
3900	4006	248 ± 6	254	50	46	32	25
4000	4095	309 ± 9	309	100	89	63	61

Footnote: w_{design} is the designed base linewidth of the v-shaped polymer pens; $w_{measured}$ is the measured linewidth of each PPCLL line pattern; $L_{simulated}$ is the simulated contact linewidth based on **Eq. (2.3)** $L = f(w, z)$, for $w = w_{measured}$ and z = 547 nm;Δw_{design}, $\Delta w_{measured}$, and $\Delta L_{measured}$ are the increments corresponding to w_{desgin}, $w_{measured}$, and $L_{measured}$;$\Delta h_{calculated}$ is the height increment of v-shaped polymer pen calculated from$\Delta h_{calculated} = \frac{1}{\sqrt{2}}\Delta w_{measured}$.

Next, we compared the measured results with the universal equation **Eq. (2.2)** from the simulation results. The measured feature linewidths $L_{measured}$ and the measured base linewidths $w_{measured}$ of the corresponding v-shaped polymer pens are plotted in **Figure 2.4c**. To calculate the corresponding vertical compression distance z in **Eq. (2.2)**, we first applied the largest measured $w_{measured}$ = 4095 nm and $L_{measured}$ = 309 nm in **Eq. (2.2)** to get z = 547 nm. Then, by fixing z at 547 nm, we obtained **Eq. (2.3)**, where a'' = 1431 nm, b'' = -1.188, and c'' = 2.232 × 10^{-4} nm^{-1}. We plotted **Eq. (2.3)** in **Figure 2.4c** and found that the calculated data fit the experimental data well. Based on $w_{measured}$, we calculated $L_{simulated}$. The almost negligible differences (~5 nm average) between the $L_{measured}$ and $L_{simulated}$ could be due to imperfect estimates of the PDMS properties used in the simulations.

To visualize the fabricated patterns, to test the applicability of PPCLL, and to demonstrate the potential for biological patterning applications, DNA hybridization experiments were performed. We have demonstrated that CLL can be used to produce DNA patterns with high hybridization efficiencies.[7] Using PPCLL to pattern DNA in a similar fashion represents an economical and high-throughput avenue for fabricating functional DNA micro/nano arrays.[7,23,60,82] As shown in the scheme in **Figure 2.5a**, SAM molecules were removed from the contacted regions by PPCLL and thiolated single-stranded DNA molecules were inserted into the patterned regions through Au-S bonding.

Single-stranded patterned DNA was hybridized with fluorescently labeled complementary DNA enabling visualization of the chemical lift-off patterns *via* fluorescence microscopy. In **Figure 2.5b**, an image of a PPCLL pattern is shown illustrating regions (lines of varying widths) of patterned, hybridized DNA. The patterns are consistent with SEM data, which provides additional confirmation that PPCLL has indeed occurred. The DNA hybridization

experiments show that PPCLL can be used to pattern biomolecules that retain functionality, *i.e.*, hybridization in this case. Being able to adjust pattern sizes and to create large-area substrates with binding sites and bioactive species illustrates that PPCLL might be used to fabricate biological devices, such as, biosensors, nucleotide arrays, and selective capture substrates. (Experimental details are provided in Materials and Methods.)

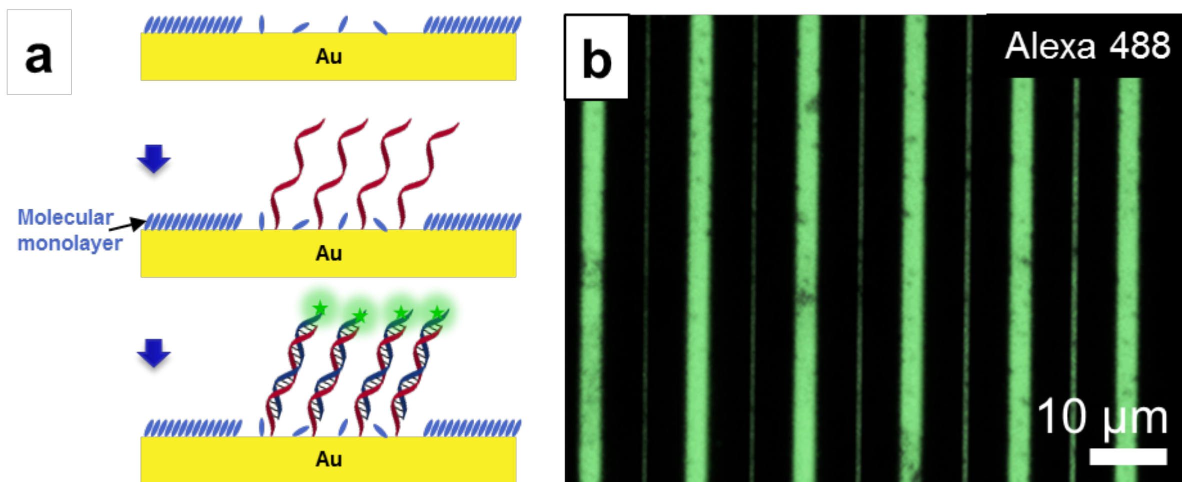

Figure 2.5. (a) After polymer-pen chemical lift-off lithography (PPCLL) patterning, thiolated DNA molecules are inserted into the patterned regions and fluorescently labeled complementary target DNA is hybridized on the substrate. (b) A typical fluorescence microscopy image after hybridization. (False color (green) is used to enhance pattern image.)

2.5 Conclusions and Prospects

In summary, we demonstrated and tested PPCLL through simulation and experiments. Polymer-pen chemical lift-off lithography offers high pattern fidelity, low-cost, large-area, nanometer-scale resolution patterning capabilities by combining the advantages of polymer-pen lithography and chemical lift-off lithography. Through the use of stamp support elements and polymer pens with designed size gradients, we demonstrated sub-40-nm feature patterning and sub-20-nm feature linewidth increments without a piezoelectric scanning stage or a leveling system used in many conventional nanolithography techniques. Nonetheless, we plan to couple PPCLL with a piezoelectric scanning stage system to realize higher resolution patterning. Polymer-pen chemical lift-off lithography is a promising nanofabrication technique for a broad range of applications in electronics, optics, energy, and biology.

2.6 Supplementary Materials

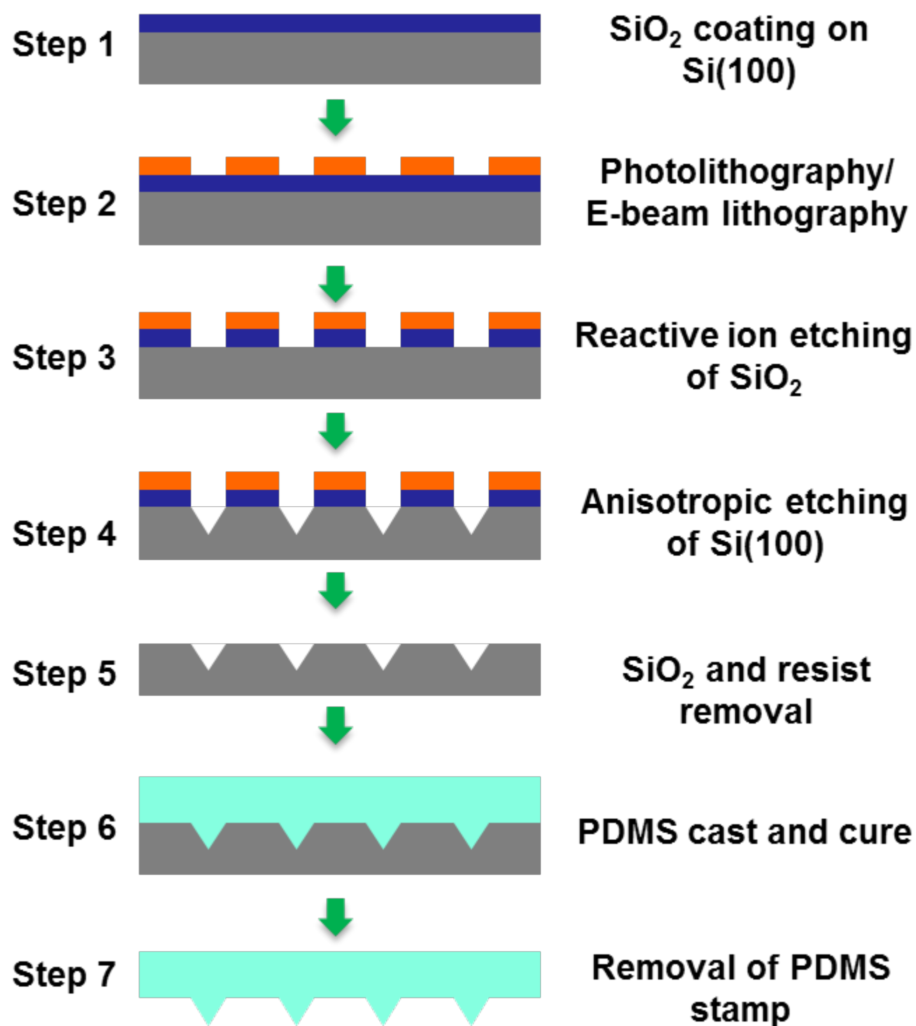

Scheme S2.1. The fabrication scheme of silicon masters and polydimethylsiloxane (PDMS) stamps.

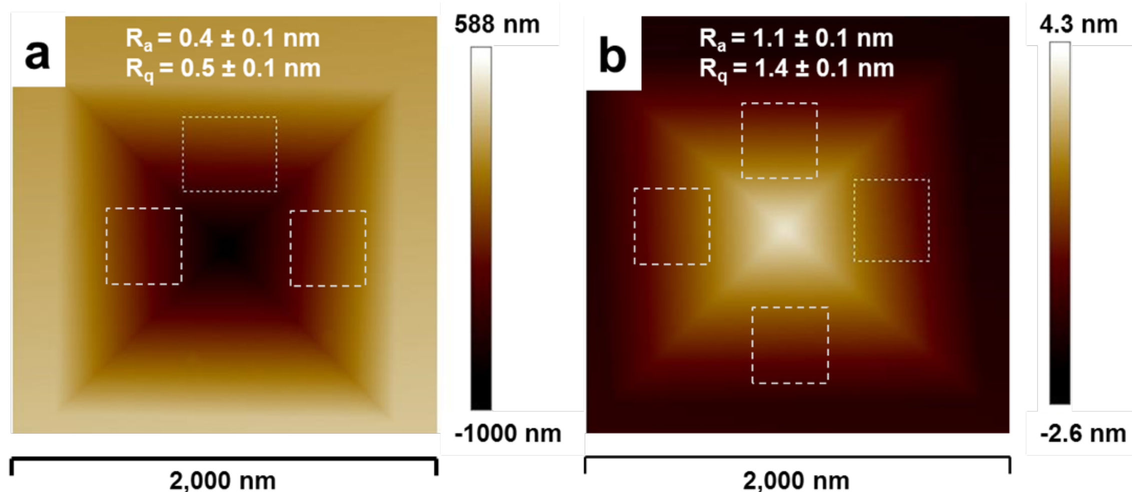

Figure S2.1. Atomic force microscope (AFM) height images of (a) inverted pyramid on a silicon master and (b) protruding pyramid on a polydimethylsiloxane (PDMS) stamp. The AFM data were collected using a Bruker Dimension Icon Scanning Probe Microscope. Surface roughness was measured inside the square dashed-line areas for each image using the instrument software, Nanoscope Analysis. The R_a is the arithmetic average of absolute values and R_q is the root mean square of the data points.

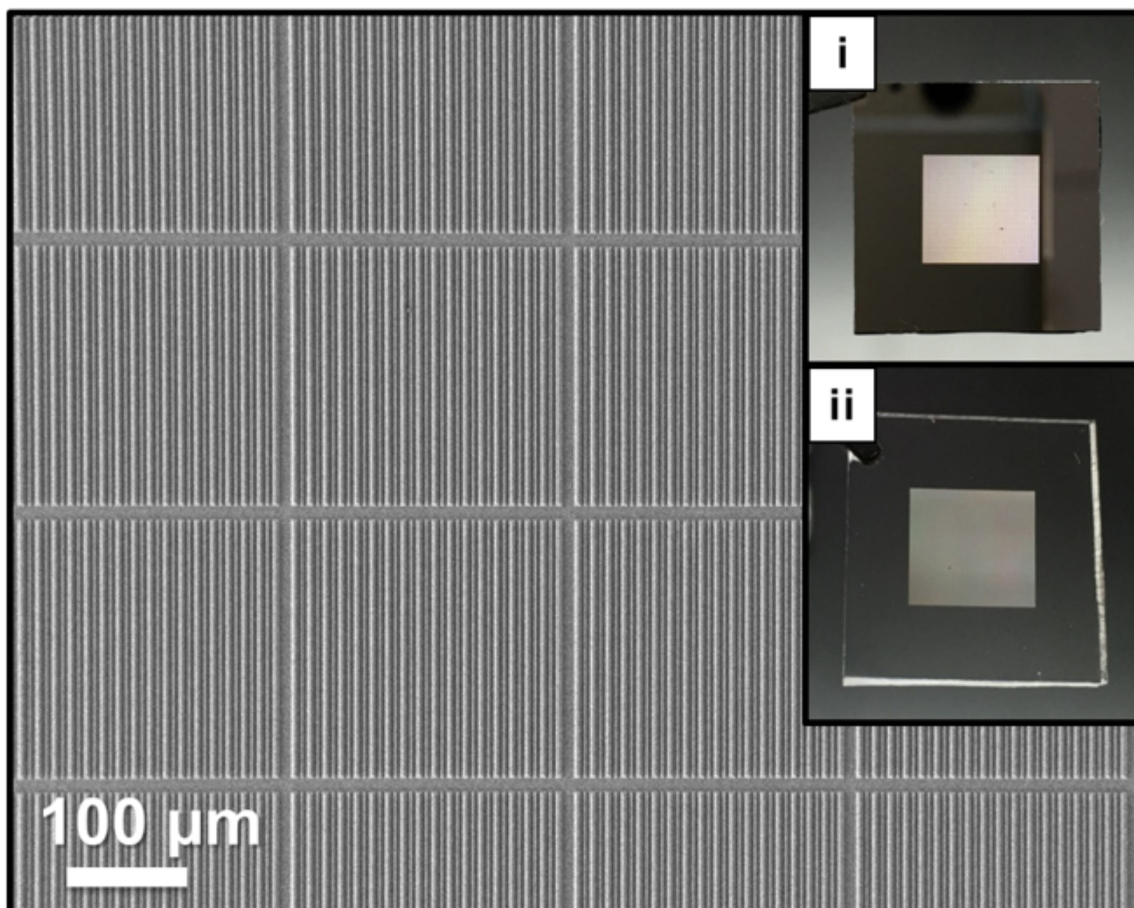

Figure S2.2. A scanning electron microscope image of a polydimethylsiloxane (PDMS) stamp with gradient arrays. Insets: photographs of (i) a silicon master and (ii) a PDMS stamp.

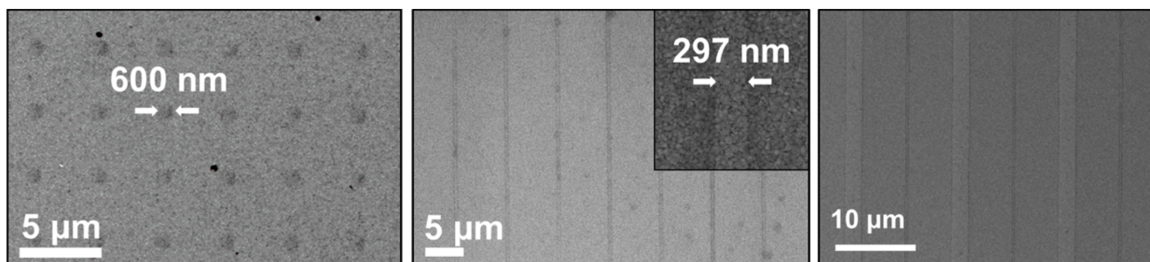

Figure S2.3. Unprocessed images of Figures 2.1c, 2.1f, and 2.4b.

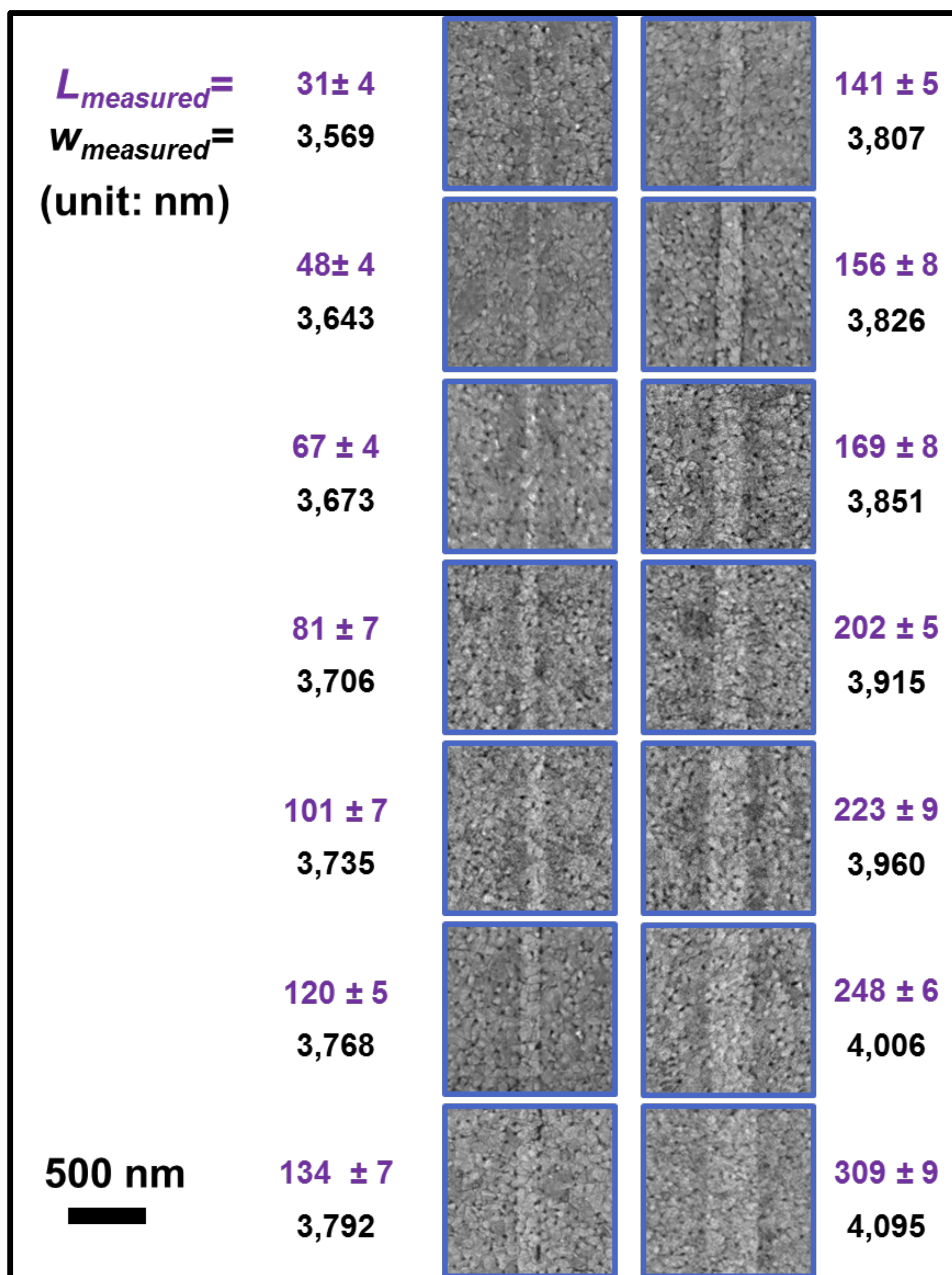

Figure S2.4. A full set of scanning electron microscope images of line patterns with a series of different linewidths ($L_{measured}$) patterned from a series of corresponding v-shaped polymer pens with linewidths ($w_{measured}$) as listed in Table 2.1.

2.7 References

(1) Jeon, H.-J.; Kim, K. H.; Baek, Y.-K.; Kim, D. W.; Jung, H.-T. New Top-Down Approach for Fabricating High-Aspect-Ratio Complex Nanostructures with 10 nm Scale Features. *Nano Lett.* **2010**, *10*, 3604–3610.

(2) Pires, D.; Hedrick, J. L.; De Silva, A.; Frommer, J.; Gotsmann, B.; Wolf, H.; Despont, M.; Duerig, U.; Knoll, A. W. Nanoscale Three-Dimensional Patterning of Molecular Resists by Scanning Probes. *Science* **2010**, *328*, 732–735.

(3) Carlson, A.; Bowen, A. M.; Huang, Y.; Nuzzo, R. G.; Rogers, J. A. Transfer Printing Techniques for Materials Assembly and Micro/Nanodevice Fabrication. *Adv. Mater.* **2012**, *24*, 5284–5318.

(4) Smith, J. T.; Franklin, A. D.; Farmer, D. B.; Dimitrakopoulos, C. D. Reducing Contact Resistance in Graphene Devices through Contact Area Patterning. *ACS Nano* **2013**, *7*, 3661–3667.

(5) Priolo, F.; Gregorkiewicz, T.; Galli, M.; Krauss, T. F. Silicon Nanostructures for Photonics and Photovoltaics. *Nat. Nanotechnol.* **2014**, *9*, 19–32.

(6) Tsai, H.; Pitera, J. W.; Miyazoe, H.; Bangsaruntip, S.; Engelmann, S. U.; Liu, C.-C.; Cheng, J. Y.; Bucchignano, J. J.; Klaus, D. P.; Joseph, E. A.; Sanders, D. P.; Colburn, M. E.; Guillorn, M. A. Two-Dimensional Pattern Formation Using Graphoepitaxy of PS-b-PMMA Block Copolymers for Advanced Finfet Device and Circuit Fabrication. *ACS Nano* **2014**, *8*, 5227–5232.

(7) Kim, J.; Rim, Y. S.; Chen, H.; Cao, H. H.; Nakatsuka, N.; Hinton, H. L.; Zhao, C.; Andrews, A. M.; Yang, Y.; Weiss, P. S. Fabrication of High-Performance Ultrathin In_2O_3 Film

Field-Effect Transistors and Biosensors Using Chemical Lift-Off Lithography. *ACS Nano* **2015**, *9*, 4572–4582.

(8) Ozbay, E. Plasmonics: Merging Photonics and Electronics at Nanoscale Dimensions. *Science* **2006**, *311*, 189–193.

(9) Henzie, J.; Lee, M. H.; Odom, T. W. Multiscale Patterning of Plasmonic Metamaterials. *Nat. Nanotechnol.* **2007**, *2*, 549–554.

(10) Kung, S.-C.; Van Der Veer, W. E.; Yang, F.; Donavan, K. C.; Penner, R. M. 20 Ms Photocurrent Response from Lithographically Patterned Nanocrystalline Cadmium Selenide Nanowires. *Nano Lett.* **2010**, *10*, 1481–1485.

(11) Fan, F.-R.; Lin, L.; Zhu, G.; Wu, W.; Zhang, R.; Wang, Z. L. Transparent Triboelectric Nanogenerators and Self-Powered Pressure Sensors Based on Micropatterned Plastic Films. *Nano Lett.* **2012**, *12*, 3109–3114.

(12) Ul-Haq, E.; Patole, S.; Moxey, M.; Amstad, E.; Vasilev, C.; Hunter, C. N.; Leggett, G. J.; Spencer, N. D.; Williams, N. H. Photocatalytic Nanolithography of Self-Assembled Monolayers and Proteins. *ACS Nano* **2013**, *7*, 7610–7618.

(13) Moxey, M.; Johnson, A.; El-Zubir, O.; Cartron, M.; Dinachali, S. S.; Hunter, C. N.; Saifullah, M. S. M.; Chong, K. S. L.; Leggett, G. J. Fabrication of Self-Cleaning, Reusable Titania Templates for Nanometer and Micrometer Scale Protein Patterning. *ACS Nano* **2015**, *9*, 6262–6270.

(14) Cao, Q.; Kim, H.-S.; Pimparkar, N.; Kulkarni, J. P.; Wang, C.; Shim, M.; Roy, K.; Alam, M. A.; Rogers, J. A. Medium-Scale Carbon Nanotube Thin-Film Integrated Circuits on Flexible Plastic Substrates. *Nature* **2008**, *454*, 495–500.

(15) Hwang, J. K.; Cho, S.; Dang, J. M.; Kwak, E. B.; Song, K.; Moon, J.; Sung, M. M. Direct Nanoprinting by Liquid-Bridge-Mediated Nanotransfer Moulding. *Nat. Nanotechnol.* **2010**, *5*, 742–748.

(16) Cheong, L. L.; Paul, P.; Holzner, F.; Despont, M.; Coady, D. J.; Hedrick, J. L.; Allen, R.; Knoll, A. W.; Duerig, U. Thermal Probe Maskless Lithography for 27.5 nm Half-Pitch Si Technology. *Nano Lett.* **2013**, *13*, 4485–4491.

(17) Kim, T.-H.; Cho, K.-S.; Lee, E. K.; Lee, S. J.; Chae, J.; Kim, J. W.; Kim, D. H.; Kwon, J.-Y.; Amaratunga, G.; Lee, S. Y.; Choi, B. L.; Kuk, Y.; Kim, J. M.; Kim, K. Full-Colour Quantum Dot Displays Fabricated by Transfer Printing. *Nat. Photon.* **2011**, *5*, 176–182.

(18) Jiang, M.; Kurvits, J. A.; Lu, Y.; Nurmikko, A. V.; Zia, R. Reusable Inorganic Templates for Electrostatic Self-Assembly of Individual Quantum Dots, Nanodiamonds, and Lanthanide-Doped Nanoparticles. *Nano Lett.* **2015**, *15*, 5010–5016.

(19) Xie, W.; Gomes, R.; Aubert, T.; Bisschop, S.; Zhu, Y.; Hens, Z.; Brainis, E.; Van Thourhout, D. Nanoscale and Single-Dot Patterning of Colloidal Quantum Dots. *Nano Lett.* **2015**, *15*, 7481–7487.

(20) Liang, X.; Morton, K. J.; Austin, R. H.; Chou, S. Y. Single Sub-20 nm Wide, Centimeter-Long Nanofluidic Channel Fabricated by Novel Nanoimprint Mold Fabrication and Direct Imprinting. *Nano Lett.* **2007**, *7*, 3774–3780.

(21) Stewart, M. E.; Anderton, C. R.; Thompson, L. B.; Maria, J.; Gray, S. K.; Rogers, J. A.; Nuzzo, R. G. Nanostructured Plasmonic Sensors. *Chem. Rev.* **2008**, *108*, 494–521.

(22) Xu, X. B.; Kim, K.; Li, H. F.; Fan, D. L. Ordered Arrays of Raman Nanosensors for Ultrasensitive and Location Predictable Biochemical Detection. *Adv. Mater.* **2012**, *24*, 5457–5463.

(23) Scheible, M. B.; Pardatscher, G.; Kuzyk, A.; Simmel, F. C. Single Molecule Characterization of DNA Binding and Strand Displacement Reactions on Lithographic DNA Origami Microarrays. *Nano Lett.* **2014**, *14*, 1627–1633.

(24) Rim, Y. S.; Bae, S.-H.; Chen, H.; Yang, J. L.; Kim, J.; Andrews, A. M.; Weiss, P. S.; Yang, Y.; Tseng, H.-R. Printable Ultrathin Metal Oxide Semiconductor-Based Conformal Biosensors. *ACS Nano* **2015**, *9*, 12174–12181.

(25) Xu, X. B.; Kim, K.; Fan, D. L. Tunable Release of Multiplex Biochemicals by Plasmonically Active Rotary Nanomotors. *Angew. Chem. Int. Ed.* **2015**, *54*, 2525–2529.

(26) Kim, K.; Guo, J. H.; Xu, X. B.; Fan, D. L. Micromotors with Step-Motor Characteristics by Controlled Magnetic Interactions among Assembled Components. *ACS Nano* **2015**, *9*, 548–554.

(27) Brown, P. O.; Botstein, D. Exploring the New World of the Genome with DNA Microarrays. *Nat. Genet.* **1999**, *21*, 33–37.

(28) Pollack, J. R.; Perou, C. M.; Alizadeh, A. A.; Eisen, M. B.; Pergamenschikov, A.; Williams, C. F.; Jeffrey, S. S.; Botstein, D.; Brown, P. O. Genome-Wide Analysis of DNA Copy-Number Changes Using Cdna Microarrays. *Nat. Genet.* **1999**, *23*, 41–46.

(29) Lickwar, C. R.; Mueller, F.; Hanlon, S. E.; Mcnally, J. G.; Lieb, J. D. Genome-Wide Protein-DNA Binding Dynamics Suggest a Molecular Clutch for Transcription Factor Function. *Nature* **2012**, *484*, 251–255.

(30) Loven, J.; Orlando, D. A.; Sigova, A. A.; Lin, C. Y.; Rahl, P. B.; Burge, C. B.; Levens, D. L.; Lee, T. I.; Young, R. A. Revisiting Global Gene Expression Analysis. *Cell* **2012**, *151*, 476–482.

(31) Cao, H. H.; Nakatsuka, N.; Serino, A. C.; Liao, W. S.; Cheunkar, S.; Yang, H.; Weiss, P. S.; Andrews, A. M. Controlled DNA Patterning by Chemical Lift-Off Lithography: Matrix Matters. *ACS Nano* **2015**, *9*, 11439–11454.

(32) Ko, H. C.; Stoykovich, M. P.; Song, J.; Malyarchuk, V.; Choi, W. M.; Yu, C.-J.; Geddes Iii, J. B.; Xiao, J.; Wang, S.; Huang, Y.; Rogers, J. A. A Hemispherical Electronic Eye Camera Based on Compressible Silicon Optoelectronics. *Nature* **2008**, *454*, 748–753.

(33) Rogers, J. A.; Someya, T.; Huang, Y. Materials and Mechanics for Stretchable Electronics. *Science* **2010**, *327*, 1603–1607.

(34) Windmiller, J. R.; Wang, J. Wearable Electrochemical Sensors and Biosensors: A Review. *Electroanal.* **2013**, *25*, 29–46.

(35) Pang, C.; Lee, C.; Suh, K.-Y. Recent Advances in Flexible Sensors for Wearable and Implantable Devices. *J. Appl. Polym. Sci.* **2013**, *130*, 1429–1441.

(36) Kim, J.; Rim, Y. S.; Liu, Y.; Serino, A. C.; Thomas, J. C.; Chen, H.; Yang, Y.; Weiss, P. S. Interface Control in Organic Electronics Using Mixed Monolayers of Carboranethiol Isomers. *Nano Lett.* **2014**, *14*, 2946–2951.

(37) Switkes, M.; Rothschild, M. Immersion Lithography at 157 nm. *J. Vac. Sci. Technol. B Microelectron. Nanometer Struct.* **2001**, *19*, 2353.

(38) Mason, M. E.; Ghaida, R. S.; Agarwal, K. B.; Liebmann, L. W.; Nassif, S. R.; Gupta, P. A Novel Methodology for Triple/Multiple-Patterning Layout Decomposition. *Proc. SPIE* **2012**, *8327*, 83270M.

(39) Han, S. H.; Doherty, C. M.; Marmiroli, B.; Jo, H. J.; Buso, D.; Patelli, A.; Schiavuta, P.; Innocenzi, P.; Lee, Y. M.; Thornton, A. W.; Hill, A. J.; Falcaro, P. Simultaneous

Microfabrication and Tuning of the Permselective Properties in Microporous Polymers Using X-Ray Lithography. *Small* **2013**, *9*, 2277–2282.

(40) Miszta, K.; Greullet, F.; Marras, S.; Prato, M.; Toma, A.; Arciniegas, M.; Manna, L.; Krahne, R. Nanocrystal Film Patterning by Inhibiting Cation Exchange *via* Electron-Beam or X-Ray Lithography. *Nano Lett.* **2014**, *14*, 2116–2122.

(41) Chang, S. W.; Ayothi, R.; Bratton, D.; Yang, D.; Felix, N.; Cao, H. B.; Deng, H.; Ober, C. K. Sub-50 nm Feature Sizes Using Positive Tone Molecular Glass Resists for EUV Lithography. *J. Mater. Chem.* **2006**, *16*, 1470–1474.

(42) Langner, A.; Paivanranta, B.; Terhalle, B.; Ekinci, Y. Fabrication of Quasiperiodic Nanostructures with EUV Interference Lithography. *Nanotechnology* **2012**, *23*, 105303.

(43) Frommhold, A.; Mcclelland, A.; Yang, D. X.; Palmer, R. E.; Roth, J.; Ekinci, Y.; Rosamund, M. C.; Robinson, A. P. G. Towards 11 nm Half-Pitch Resolution for a Negative-Tone Chemically Amplified Molecular Resist Platform for EUV Lithography. *Proc. SPIE* **2015**, *9425*, 942504.

(44) Cumming, D. R. S.; Thoms, S.; Weaver, J. M. R.; Beaumont, S. P. 3 nm NiCr Wires Made Using Electron Beam Lithography and PMMA Resist. *Microelectron. Eng.* **1996**, *30*, 423–425.

(45) Hu, W. C.; Sarveswaran, K.; Lieberman, M.; Bernstein, G. H. Sub-10 nm Electron Beam Lithography Using Cold Development of Poly(Methylmethacrylate). *J. Vac. Sci. Technol. B* **2004**, *22*, 1711–1716.

(46) Chen, S.; Svedendahl, M.; Antosiewicz, T. J.; Kall, M. Plasmon-Enhanced Enzyme-Linked Immunosorbent Assay on Large Arrays of Individual Particles Made by Electron Beam Lithography. *ACS Nano* **2013**, *7*, 8824–8832.

(47) Kim, S.; Marelli, B.; Brenckle, M. A.; Mitropoulos, A. N.; Gil, E. S.; Tsioris, K.; Tao, H.; Kaplan, D. L.; Omenetto, F. G. All-Water-Based Electron-Beam Lithography Using Silk as a Resist. *Nat. Nanotechnol.* **2014**, *9*, 306–310.

(48) Manfrinato, V. R.; Wen, J. G.; Zhang, L. H.; Yang, Y. J.; Hobbs, R. G.; Baker, B.; Su, D.; Zakharov, D.; Zaluzec, N. J.; Miller, D. J.; Stach, E. A.; Berggren, K. K. Determining the Resolution Limits of Electron-Beam Lithography: Direct Measurement of the Point-Spread Function. *Nano Lett.* **2014**, *14*, 4406–4412.

(49) Bat, E.; Lee, J.; Lau, U. Y.; Maynard, H. D. Trehalose Glycopolymer Resists Allow Direct Writing of Protein Patterns by Electron-Beam Lithography. *Nat. Commun.* **2015**, *6*, 6654.

(50) Gschrey, M.; Thoma, A.; Schnauber, P.; Seifried, M.; Schmidt, R.; Wohlfeil, B.; Kruger, L.; Schulze, J. H.; Heindel, T.; Burger, S.; Schmidt, F.; Strittmatter, A.; Rodt, S.; Reitzenstein, S. Highly Indistinguishable Photons from Deterministic Quantum-Dot Microlenses Utilizing Three-Dimensional in Situ Electron-Beam Lithography. *Nat. Commun.* **2015**, *6*, 7662.

(51) Volkert, C. A.; Minor, A. M. Focused Ion Beam Microscopy and Micromachining. *MRS Bull.* **2007**, *32*, 389–395.

(52) Kalhor, N.; Boden, S. A.; Mizuta, H. Sub-10 nm Patterning by Focused He-Ion Beam Milling for Fabrication of Downscaled Graphene Nano Devices. *Microelectron. Eng.* **2014**, *114*, 70–77.

(53) Pan, L.; Park, Y.; Xiong, Y.; Ulin-Avila, E.; Wang, Y.; Zeng, L.; Xiong, S.; Rho, J.; Sun, C.; Bogy, D. B.; Zhang, X. Maskless Plasmonic Lithography at 22 nm Resolution. *Sci. Rep.* **2011**, *1*, 175.

(54) Kumar, A.; Whitesides, G. M. Features of Gold Having Micrometer to Centimeter Dimensions Can Be Formed through a Combination of Stamping with an Elastomeric Stamp and an Alkanethiol ‘‘Ink’’ Followed by Chemical Etching. *Appl. Phys. Lett.* **1993**, *63*, 2002.

(55) Qin, D.; Xia, Y.; Whitesides, G. M. Soft Lithography for Micro- and Nanoscale Patterning. *Nat. Protoc.* **2010**, *5*, 491–502.

(56) Xia, Y.; Whitesides, G. M. Soft Lithography. *Angew. Chem. Int. Ed.* **1998**, *37*, 550–575.

(57) Xia, Y.; Zhao, X.-M.; Kim, E.; Whitesides, G. M. A Selective Etching Solution for Use with Patterned Self-Assembled Monolayers of Alkanethiolates on Gold. *Chem. Mater.* **1995**, *7*, 2332–2337.

(58) Delamarche, E.; Schmid, H.; Bietsch, A.; Larsen, N. B.; Rothuizen, H.; Michel, B.; Biebuyck, H. Transport Mechanisms of Alkanethiols During Microcontact Printing on Gold. *J. Phys. Chem. B* **1998**, *102*, 3324–3334.

(59) Srinivasan, C.; Mullen, T. J.; Hohman, J. N.; Anderson, M. E.; Dameron, A. A.; Andrews, A. M.; Dickey, E. C.; Horn, M. W.; Weiss, P. S. Scanning Electron Microscopy of Nanoscale Chemical Patterns. *ACS Nano* **2007**, *1*, 191–201.

(60) Liao, W.-S.; Cheunkar, S.; Cao, H. H.; Bednar, H. R.; Weiss, P. S.; Andrews, A. M. Subtractive Patterning *via* Chemical Lift-Off Lithography. *Science* **2012**, *337*, 1517–1521.

(61) Xu, S.; Liu, G.-Y. Nanometer-Scale Fabrication by Simultaneous Nanoshaving and Molecular Self-Assembly. *Langmuir* **1997**, *13*, 127–129.

(62) Xu, S.; Miller, S.; Laibinis, P. E.; Liu, G.-Y. Fabrication of Nanometer Scale Patterns within Self-Assembled Monolayers by Nanografting. *Langmuir* **1999**, *15*, 7244–7251.

(63) Li, X.-M.; Péter, M.; Huskens, J.; Reinhoudt, D. N. Catalytic Microcontact Printing without Ink. *Nano Lett.* **2003**, *3*, 1449–1453.

(64) Mclellan, J. M.; Geissler, M.; Xia, Y. Edge Spreading Lithography and Its Application to the Fabrication of Mesoscopic Gold and Silver Rings. *J. Am. Chem. Soc.* **2004**, *126*, 10830–10831.

(65) Sullivan, T. P.; Van Poll, M. L.; Dankers, P. Y. W.; Huck, W. T. S. Forced Peptide Synthesis in Nanoscale Confinement under Elastomeric Stamps. *Angew. Chem. Int. Ed.* **2004**, *43*, 4190–4193.

(66) Wendeln, C.; Ravoo, B. J. Surface Patterning by Microcontact Chemistry. *Langmuir* **2012**, *28*, 5527–5538.

(67) Dameron, A. A.; Hampton, J. R.; Smith, R. K.; Mullen, T. J.; Gillmor, S. D.; Weiss, P. S. Microdisplacement Printing. *Nano Lett.* **2005**, *5*, 1834–1837.

(68) Saavedra, H. M.; Mullen, T. J.; Zhang, P. P.; Dewey, D. C.; Claridge, S. A.; Weiss, P. S. Hybrid Strategies in Nanolithography. *Rep. Prog. Phys.* **2010**, *73*, 036501.

(69) Shuster, M. J.; Vaish, A.; Cao, H. H.; Guttentag, A. I.; Mcmanigle, J. E.; Gibb, A. L.; Martinez, M. M.; Nezarati, R. M.; Hinds, J. M.; Liao, W. S.; Weiss, P. S.; Andrews, A. M. Patterning Small-Molecule Biocapture Surfaces: Microcontact Insertion Printing Vs. Photolithography. *Chem. Commun.* **2011**, *47*, 10641–10643.

(70) Claridge, S. A.; Liao, W. S.; Thomas, J. C.; Zhao, Y.; Cao, H. H.; Cheunkar, S.; Serino, A. C.; Andrews, A. M.; Weiss, P. S. From the Bottom Up: Dimensional Control and Characterization in Molecular Monolayers. *Chem. Soc. Rev.* **2013**, *42*, 2725–2745.

(71) Andrews, A. M.; Liao, W.-S.; Weiss, P. S. Double-Sided Opportunities Using Chemical Lift-Off Lithography. *Acc. Chem. Res.* **2016**, *49*, 1449–1457.

(72) Piner, R. D.; Zhu, J.; Xu, F.; Hong, S.; Mirkin, C. A. "Dip-Pen" Nanolithography. *Science* **1999**, *283*, 661–663.

(73) Huo, F.; Zheng, Z.; Zheng, G.; Giam, L. R.; Zhang, H.; Mirkin, C. A. Polymer Pen Lithography. *Science* **2008**, *321*, 1658–1660.

(74) Zheng, Z.; Daniel, W. L.; Giam, L. R.; Huo, F.; Senesi, A. J.; Zheng, G.; Mirkin, C. A. Multiplexed Protein Arrays Enabled by Polymer Pen Lithography: Addressing the Inking Challenge. *Angew. Chem. Int. Ed.* **2009**, *48*, 7626–7629.

(75) Liao, X.; Braunschweig, A. B.; Mirkin, C. A. "Force-Feedback" Leveling of Massively Parallel Arrays in Polymer Pen Lithography. *Nano Lett.* **2010**, *10*, 1335–1340.

(76) Liao, X.; Braunschweig, A. B.; Zheng, Z.; Mirkin, C. A. Force- and Time-Dependent Feature Size and Shape Control in Molecular Printing *via* Polymer-Pen Lithography. *Small* **2010**, *6*, 1082–1086.

(77) Eichelsdoerfer, D. J.; Liao, X.; Cabezas, M. D.; Morris, W.; Radha, B.; Brown, K. A.; Giam, L. R.; Braunschweig, A. B.; Mirkin, C. A. Large-Area Molecular Patterning with Polymer Pen Lithography. *Nat. Protoc.* **2013**, *8*, 2548–2560.

(78) Demers, L. M.; Ginger, D. S.; Park, S. J.; Li, Z.; Chung, S. W.; Mirkin, C. A. Direct Patterning of Modified Oligonucleotides on Metals and Insulators by Dip-Pen Nanolithography. *Science* **2002**, *296*, 1836–1838.

(79) Odom, T. W.; Love, J. C.; Wolfe, D. B.; Paul, K. E.; Whitesides, G. M. Improved Pattern Transfer in Soft Lithography Using Composite Stamps. *Langmuir* **2002**, *18*, 5314–5320.

(80) Vaish, A.; Shuster, M. J.; Cheunkar, S.; Weiss, P. S.; Andrews, A. M. Tuning Stamp Surface Energy for Soft Lithography of Polar Molecules to Fabricate Bioactive Small-Molecule Microarrays. *Small* **2011**, *7*, 1471–1479.

(81) Xie, Z.; Shen, Y.; Zhou, X.; Yang, Y.; Tang, Q.; Miao, Q.; Su, J.; Wu, H.; Zheng, Z. Polymer Pen Lithography Using Dual-Elastomer Tip Arrays. *Small* **2012**, *8*, 2664–2669.

(82) Noh, H.; Hung, A. M.; Choi, C.; Lee, J. H.; Kim, J.-Y.; Jin, S.; Cha, J. N. 50 nm DNA Nanoarrays Generated from Uniform Oligonucleotide Films. *ACS Nano* **2009**, *3*, 2376–2382.

Chapter 3

Deformation-Controlled Chemical Patterning *via* External Force Using Polymer-Pen Chemical Lift-Off Lithography

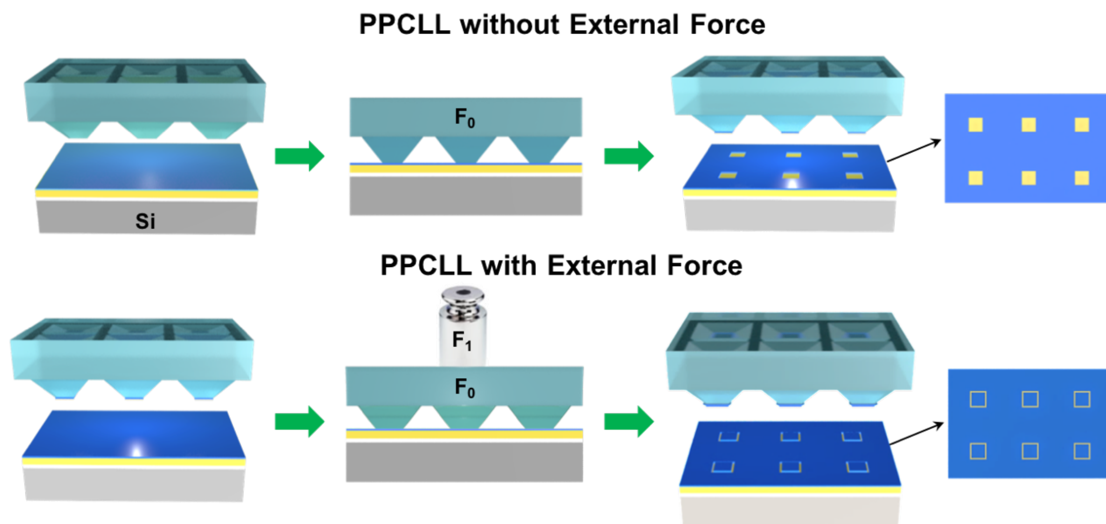

3.1 Abstract

Polymer-pen chemical lift-off lithography (PPCLL) combines the advantages of polymer pen lithography (large-area polymer pens with nanometer-scale tips) and chemical lift-off lithography (high-fidelity patterning without lateral diffusion) to provide large-area chemical patterning. Polymer pen arrays are used to pattern self-assembled monolayer (SAM) molecules on gold substrates. By adjusting the relative polymer pen heights, we tuned the feature size of chemical patterns at nanoscale resolution (**Chapter 2**). The universal equation (**Eq. 2.2**) correlated the feature size L with two variables, base linewidth w and vertical compression distance z. In this work, we first demonstrate our ability to tune feature size by controlling the compression distance z. Through the addition of an external force to compress the polymer pens, we extend the ability of PPCLL to generate more complex hollow patterns, which are difficult to obtain otherwise, *via* a "subtraction" process between consecutive deformation-controlled contact and lift processes. Selective gold etching using the SAM patterns as masks readily produced arrays of gold nanorings over large areas.

3.2 Introduction

The development of novel lithographic techniques is of great interest, as they enable new opportunities and applications. Significant progress has been made in improving fabrication skills within the fields of electronics,[1-6] optics,[7-10] energy,[11-13] and biology.[14-21] While conventional photolithography remains the dominant top-down approach for scalable microfabrication, in its simplest form optical diffraction limits its critical resolution to approximately half of the wavelength. There are three common setups of photolithography: contact printing, proximity printing, and projection printing. Contact printing is the most common approach in research laboratories and can straightforwardly be used to generate resist patterns at the micron scale. In a projection printing system, feature size can scaled down to a few tens of nanometers by using a shorter wavelength (193 nm) and optical lens system.[22,23] Other techniques, such as electron-beam lithography (EBL)[24-30] and focused ion-beam lithography (FIB),[31,32] can generate sub-micron features, but time-consuming serial writing processes and high costs restrict their throughput and accessibility.[33]

Microcontact printing (μCP) was developed as an alternative to conventional photolithography, because of its ability to print "ink" molecules economically, high throughput, and straightforwardly over large areas.[34-36] In μCP, "ink" molecules, such as alkanethiols, DNA, and proteins, are first coated onto polymeric stamps and then directly printed onto substrates *via* conformal contact. The chemical patterns (*e.g.,* alkanethiols) can subsequently serve as resists in successive wet etching steps to transfer patterns onto underlying substrates.[36,37] However, the "ink" molecules are known to diffuse laterally beyond the contact areas during the printing process, resulting in poor pattern fidelity. In addition, experimental conditions, including time, pressure, temperature, and humidity, need to be strictly controlled for consistent results.[38-40]

Alkanethiol molecules can form well-ordered self-assembled monolayers (SAMs) on gold surfaces. Our previous work has revealed that pre-assembled SAMs can prevent diffusion of "added" alkanethiol molecules beyond the contact areas.[39] Based on this discovery, modified μCP strategies *via* displacement[41,42] and insertion[39,43] of alkanethiol molecules have been developed to increase pattern fidelity by minimizing the lateral diffusion of ink molecules. Recently, our group has developed a subtractive chemical patterning process called chemical lift-off lithography (CLL).[44,45] Activated polymeric stamps selectively remove alkanethiol molecules with reactive terminal groups (such as -OH, -COOH, or -NH_2) in the contact regions. Pattern dissolution is prevented by pre-formed, well-ordered SAMs, strong intermolecular interactions between hydrophilic SAM molecules, and a diffusion barrier created by the Au step edges during lift-off. While high-fidelity patterns with features down to 20 nm have been obtained *via* CLL,[44,45] large-area fabrication of nanoscale silicon masters and stamps remains a challenge.

Nanoscale mechanical deformation of polymer stamps can be realized *via* approaches such as proper instrumentation (*e.g.,* piezoelectric stages),[40,46,47] stamp design,[19] or even self-collapse of soft structures.[48] Theoretically, the resolution obtained through these deformation-based approaches can readily surpass the limit of conventional photolithography and reach sub-5-nm resolution or even smaller.[19,48] Previous PPCLL research (**Chapter 2**) combined nanoscale polymer-pen arrays with high-fidelity chemical lift-off lithography and successfully obtained molecular patterns with tunable feature size through proper design of the polymer pen base linewidths.[19] The arrays, fabricated *via* conventional photolithography and anisotropic Si etching, have tips smaller than 20 nm in diameter. By fabricating a series of v-shaped polymer pens with designed base linewidth increments, we controlled the compression

distances and contact areas under the same compression, producing large-area square and line patterns with sub-50-nm linewidth and sub-20-nm tunability.

This chapter describes a modified version of PPCLL known as deformation-controlled polymer-pen chemical lift-off lithography (DC-PPCLL). We adjusted the compression distance z to achieve more complex hollow patterns at sub-micron level, which are difficult to obtain with conventional microcontact printing techniques. In the modified procedure, we performed multiple contact and lift steps; polymer pen tips were completely filled with lifted alkanethiol molecules and therefore deactivated for the following process. External force was applied to increase compression distance and to introduce additional contact area between the polymer pens and SAM-modified gold substrates by increasing tip deformation. Condensation reactions occurred in the newly added contact areas around the tips, while the original tip-contact region remains intact. The molecules in the newly added (ring-like) regions were removed after the lift-off process. As a result, we fabricated sub-micron, hollow chemical patterns. Following selective gold etching, large arrays of hollow gold nanorings were obtained. This strategy provides a straightforward solution for fabrication large-area nanoring production, which has potential applications in optical devices and biosensors.

3.3 Materials and Methods

Materials. Iron(III) nitrate nonahydrate (≥99.95%, trace metal basis), thiourea (ACS reagent, ≥99.0%), and 11-mercapto-1-undecanol (99%) were purchased from Sigma-Aldrich (St. Louis, MO, USA). Tridecafluoro-1,1,2,2-tetrahydrooctyl-1-trichlorosilane (TFOCS) was purchased from Gelest, Inc. (Morrisville, PA, USA). Prime quality Si(100) wafers (100 mm, P/B, 1-10 ohm-cm) were purchased from University Wafer, Inc. (Boston, MA, USA). Sylgard 184® silicone elastomer kit was purchased from Ellsworth Adhesives (Germantown, WI, USA). The gold and chromium targets, SPR700-1.2 photoresist, MF-26A developer, isopropanol, 30 wt% potassium hydroxide (KOH) solution, and hydrofluoric acid (48%) were obtained and used from the Integrated Systems Nanofabrication Cleanroom (ISNC) at UCLA.

Characterization. **A** Zeiss Supra 40VP scanning electron microscope (SEM) was used to take the SEM images. The water contact angle was characterized using a custom-built system with an Appro® B/W camera (model: BV-7105EN). A thin layer of gold was sputtered onto the polydimethylsiloxane (PDMS) stamps in order to make them sufficiently conductive for SEM imaging. The dimensions of micro/nanostructures and chemical patterns in the SEM images were measured using ImageJ software (https://imagej.nih.gov/ij/). A Zeiss Axiotech optical microscope was used to monitor the Au etching process.

Fabrication of truncated Si masters and PDMS stamps. The detailed fabrication process was illustrated in **Scheme S2.1** and **Section 2.3**. Anisotropic etching of Si(100) was performed in a mixture of 4:1 KOH (30%) and isopropanol at 75 °C with variable times. After fabrication of truncated pyramids on silicon masters, they were placed in a vacuum desiccator with a few drops of tridecafluoro-1,1,2,2-tetrahydrooctyl-1-trichlorosilane (TFOCS) in a petri dish. The substrates were kept under vacuum conditions for 40 minutes to allow the evaporation and deposition of

TFOCS on the silicon surface. The Sylgard® 184 elastomer silicone elastomer base and curing agent (10:1 mass ratio) were thoroughly mixed and degassed in a vacuum desiccator. Then, the mixture was poured onto the TFOCS-modified Si masters and cured overnight at 65 °C. After curing, PDMS stamps were carefully peeled off the Si master.

Surface functionalization of Au/Cr/Si substrates. The 10-nm Cr and 30-nm Au films were evaporated using a CHA Solution E-Beam Evaporator at high vacuum (10^{-8} Torr) with evaporation rates of 0.1 nm/s. The Au/Cr/Si wafers were annealed in a hydrogen flame and then immersed into 0.5 mM 11-mercapto-1-undecanol ethanolic solution overnight for the formation of self-assembled monolayers on the Au surfaces.

Oxygen Plasma Activation of PDMS stamps. Clean PDMS stamps were treated in oxygen plasma (Harrick Plasma, Ithaca, NY) for 40 seconds at a power of 18 W and a pressure of 10 psi to generate hydrophilic surfaces.

Contact and Lift with Polymer-Pen Elastomer Stamps. (1) Single contact and lift: after oxygen plasma activation, a pair of tweezers was used to place the PDMS stamp on SAM-modified substrate carefully. In some experiments, metal blocks with different weights were placed on top of PDMS stamps to increase the compression distance. For stamp removal, the substrate was held with one pair of tweezers, and another pair of tweezers was used to lift the stamp. (2) Multiple contacts and lifts: the general procedures were the same as single contact and lift. After 30 minutes, the stamp was transferred to a new SAM-modified substrate without re-activating the PDMS stamp. The process was repeated four times and, for the fifth repetition, metal blocks with different weights (20 – 300 g) were placed on top of PDMS stamp to increase the compression distance, as well as the contact area.

Gold Etching. The gold etchant was made by mixing 20 mM iron nitrate and 30 mM thiourea in 1:1 volume ratio. After chemical patterning, the gold substrates were immersed into a freshly-prepared gold etchant, and the etching process was monitored by the Zeiss Axiotech optical microscope. Etching was stopped when clear gold patterns were observed. The substrates were then rinsed with plenty of DI water and dried with a nitrogen gun.

3.4 Results and Discussions

The fabrication of silicon molds and PDMS stamps are similar to procedures that have been previously reported with PPCLL (see **Section 2.3** for experimental details). We first used conventional photolithography to pattern photoresists into square hole arrays (15 µm in diameter) on a 4-inch SiO_2/Si(100) wafer. Note that the square features on the photomask were set to align with the flat edge of the Si(100) wafer, which is parallel to Si<110>. The exposed SiO_2 was then etched *via* reactive-ion etching (RIE) to reveal the underlying Si(100). Subsequently, a mixture of 30% KOH and isopropanol (volume ratio 4:1) was used to etch the Si(100) anisotropically. Incomplete Si(100) etching resulted in recessed pyramids, and the tip sizes were determined by the etching time.[49] Residual photoresists and SiO_2 were removed with acetone and hydrofluoric acid, respectively. The resulting silicon master was cleaned and silanized with TFOCS. Finally, PDMS stamps containing flat-tip polymer-pens arrays were replicated from the Si masters.

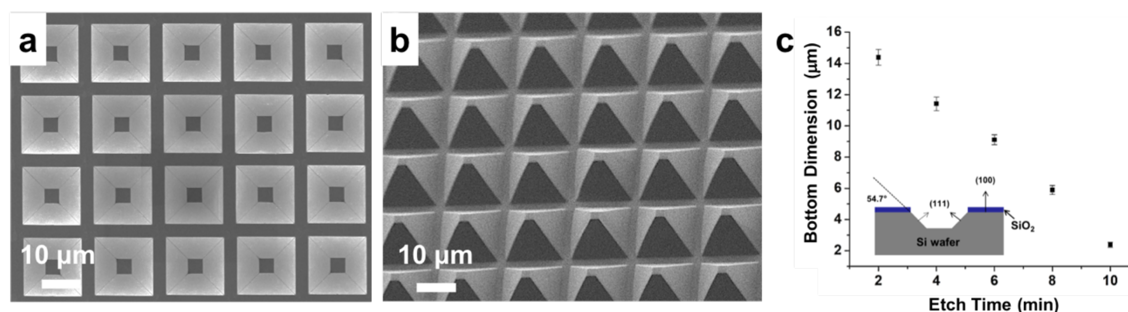

Figure 3.1. (a,b) Scanning electron microscopy (SEM) images of silicon masters and PDMS stamps consist of flat-tip pyramid arrays (base linewidth = 15.2 ± 0.1 µm, tip = 3.6 ± 0.1 µm). (c) The change of tip dimensions over silicon etching time. Inset: illustration of the anisotropic etching of Si(100) to generate recessed silicon pyramids. Note: image (b) was taken at a 30° relative to the surface normal.

The obtained Si masters and PDMS stamps containing large arrays of flat-tip pyramid structures are shown in scanning electron microscopy (SEM) images in **Figure 3.1a,b**. The recessed pyramids in the Si master had a base linewidth of 15.2 ± 0.1 μm and an average tip size of 3.6 ± 0.1 μm. The tip dimensions of Si pyramids determined the feature sizes of chemical patterns without further compression, which was adjustable from microns (flat tips) to sub-20 nm (sharp tips) through increasing the Si etching time (**Figure 3.1c**). For the 15-micron feature size patterns, pyramid tips with diameters from 15 to 2 μm correspond to silicon etching time from 0 to 10 min. The anisotropic etching of silicon is a result of significant etch rate differences between crystalline planes. For Si(100), the etch rate on Si{100} planes is about 200 times faster than that on Si{111} due to the latter's higher atomic density.

Basic patterning procedures were similar to those in PPCLL (see **Scheme 2.1** for more details). First, PDMS stamps were treated with 40 seconds of oxygen plasma to generate hydrophilic siloxy (Si-OH) groups on the surface. The activated PDMS stamps were then brought into conformal contact with the Au/Cr/Si substrates, which were pre-functionalized with 11-mercapto-1-undecanol alkanethiol molecules. Condensation reaction between siloxy groups on PDMS surface and hydroxyl groups from alkanethiol molecules formed covalent bonds (Si-O-SAM) that were strong enough to lift off the SAM molecules. Finally, the PDMS stamps were peeled off the substrates, removing SAM molecules only in the contact areas and producing complementary chemical patterns.

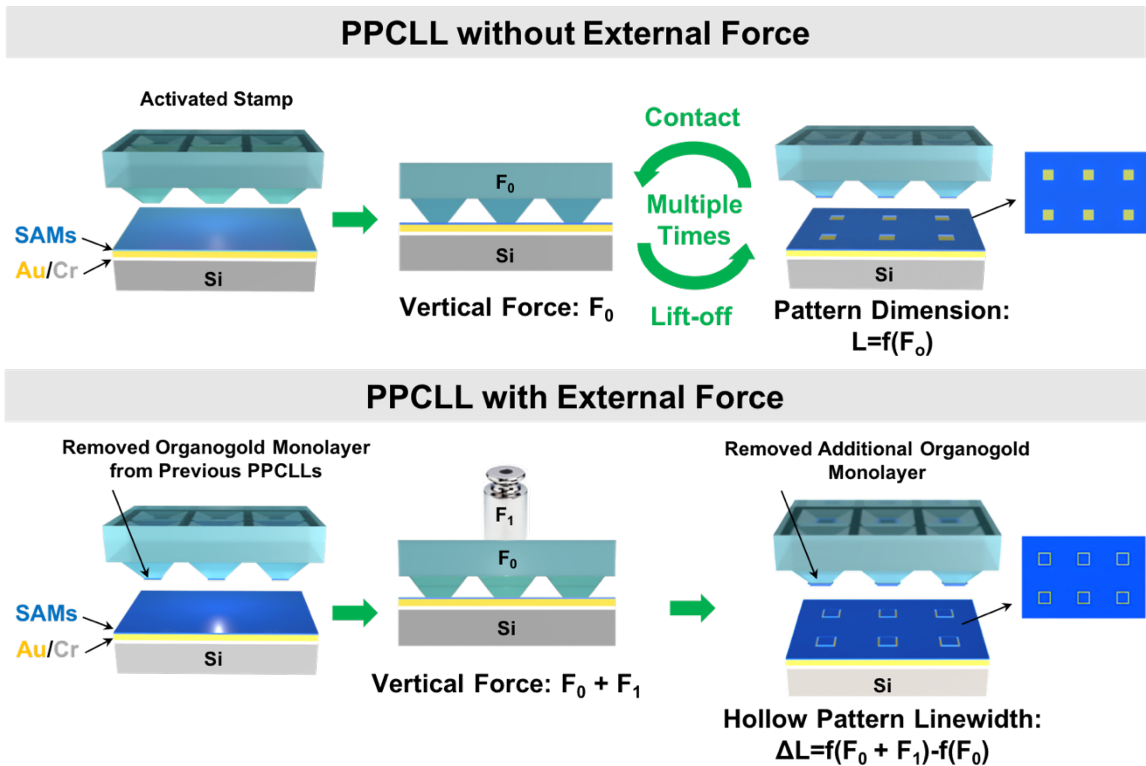

Figure 3.2. Schematic illustrations of deformation-controlled polymer-pen chemical lift-off lithography (PPCLL) with and without external force. Polymer-pen chemical lift-off lithography without external force: the oxygen-plasma-activated PDMS stamp was brought into conformal contact with the SAM-coated Au/Cr/Si substrate and compressed only by its weight F_0. The stamp was then lifted-off to remove a layer of organogold monolayer from the contact areas, leaving complementary square arrays on the gold surface. The square size (*L*) can be expressed as $L = f(F_0)$. After multiple cycles of PPCLL without external force, the tip areas of the stamp are fully "deactivated". Polymer-pen chemical lift-off lithography with external force: tip-deactivated stamp was brought into contact with a fresh SAM-coated Au/Cr/Si substrate with external stress of F_1. After chemical lift-off, a hollow pattern with feature thickness of $\Delta L=1/2\ (f(F_0+F_1)-f(F_0))$ was created.

As illustrated in **Figure 3.2**, DC-PPCLL contains two key steps: (1) PPCLL(s) without external force, and (2) PPCLL with external force. In the first step, the contact and lift experiments were performed without external force. The only compression force involved during contact came from the stamp's own weight $\mathbf{F_0}$. After 30 minutes, the polymer pens were lifted-off from the substrate with organogold monolayers removed from the contact areas, forming a square pattern with size $L_0 = f(F_0)$. This process was repeated multiple times with new SAM-coated Au/Cr/Si substrates to deactivate the tip-contact area. For the second part, a tip-deactivated stamp was brought into contact with a fresh SAM-coated Au/Cr/Si substrate with an external stress of F_1, which further deformed the polymer pens and introduced new contact areas around the tips. After lift-off, hollow rings with a thickness of $\Delta L=1/2(f(F_1+F_0)-f(F_0))$ were obtained. Through DC-PPCLL, nanoscale features can be generated from micron-scale tips, which is rarely reported in soft lithography. One special property of chemical lift-off lithography is that condensation reactions only occur at the contact regions between the stamp and the substrate. As a result, DC-PPCLL produces hollow chemical patterns by fully deactivating the stamp tip (no lift-off in the tip-contact area) and increasing compression (introducing new contact area) afterwards. While lengthening the contact time (*e.g.*, overnight) could increase the lift-off yield in the tip areas, the overall stamp reactivity also decreased over time, because of the gradual decrease in Si-OH density of the stamp. To maximize the tip-area lift-off yields while preserving reactivity, we proposed to performing multiple cycles of PPCLLs with reduced time, which was expected to cover the tip areas completely with lifted-off molecules.

The reactivity of PDMS stamps depends on the density of the Si-OH groups generated through oxygen plasma treatment on the stamp surface. This density can be characterized by the hydrophilicity of the flat stamp, which is determined by the water contact angle experiment. As

illustrated in **Figure S3.1**, the water contact angle had a value θ = 97° before oxygen plasma "activation" of the PDMS stamp, indicating a hydrophobic stamp. Immediately after activation, the water contact angle became θ = 30°, which suggested the generation of high-density Si-OH groups on the surface. Surprisingly, we discovered that this hydrophilicity could be maintained for an extended period of time before reverting to the hydrophobic state. Two hours later, the water contact angle was θ = 42°, and even after 16 hours, the stamp was still not restored to its initial hydrophobicity (water contact angle θ = 62°). The extended period of hydrophilicity enabled performing multiple contact and lift experiments without sacrificing the stamp reactivity.

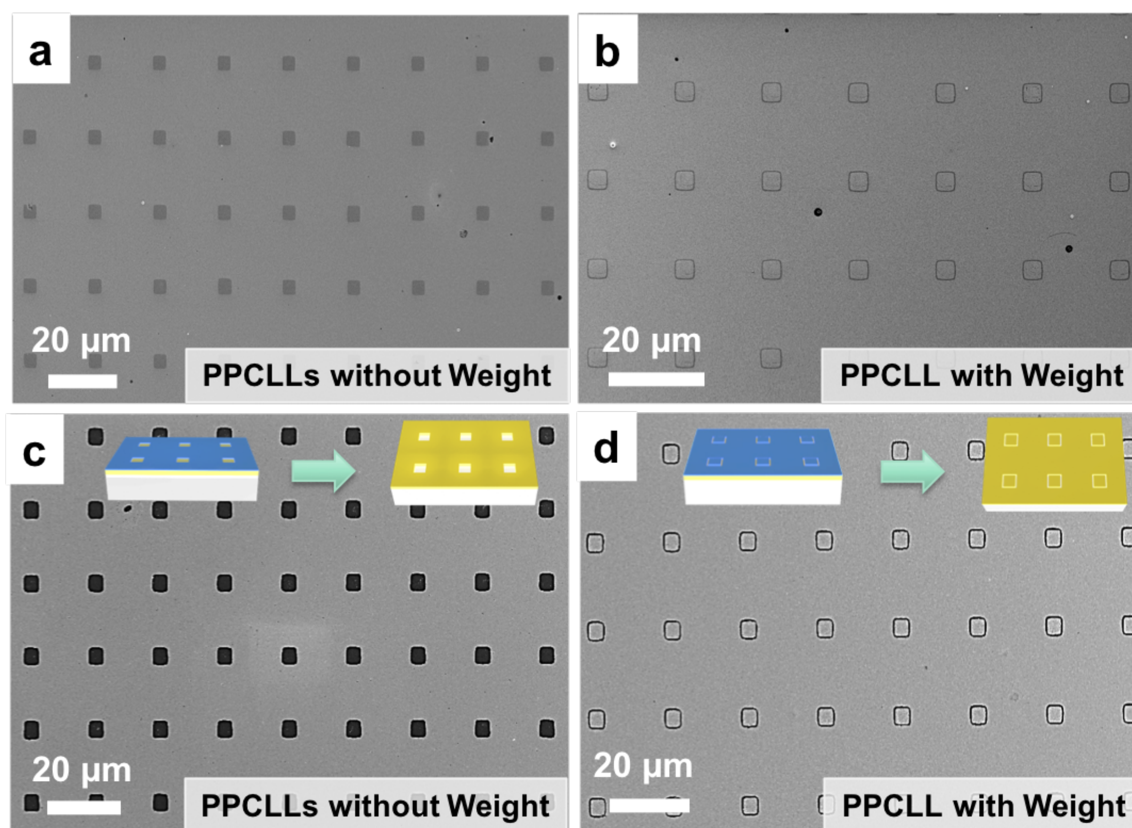

Figure 3.3. (a) Scanning electron microscopy (SEM) images of square chemical pattern fabricated by polymer-pen chemical lift-off lithography (PPCLL) without external weight. (c) After selective Au etching, Au square holes were observed. The dimension of chemical

patterns was identical to the tip size, but the Au square holes were slightly larger due to lateral etch. (b,d) SEM images of hollow chemical pattern fabricated by deformation-controlled polymer-pen chemical lift-off lithography (DC-PPCLL) and hollow Au rings after etching.

To test this concept for complex hollow pattern fabrication, we purposely used polymer pens with flat tips (with a base linewidth of 15.2 ± 0.1 μm and a tip size of 3.6 ± 0.1 μm), since larger contact areas provided better registry between the stamps and substrates. After performing PPCLL without external weight, we observed square chemical patterns in SEM (**Figure 3.3a**); the chemical pattern had a diameter of 3.7 ± 0.0 μm, which was consistent with the tip size. Arrays of square holes with 3.8 ± 0.1 μm in diameter were obtained after selective Au etching (**Figure 3.3c**). After fully deactivating the tip area, we performed PPCLL with external weight; the SEM image in **Figure 3.3b** revealed a hollow chemical pattern with a ring diameter of 247 ± 31 nm. The inner diameter was consistent with the tip size. We further verified that the observed chemical pattern was due to the removal of SAM molecules by performing subsequent Au etching. As illustrated in in **Figure 3.3d**, hollow Au rings with diameters of 365 ± 35 nm were fabricated. The ring thickness was slightly larger than the chemical pattern size, which was likely due to lateral etching of Au over time. To examine the effects of the polymer pen tip "deactivation" process on nanoring fabrication, we performed etching experiments with varying numbers of PPCLLs without weight. The corresponding SEM images in **Figure S3.2** indicated that increasing the number of PPCLLs reduced the number of defects, thereby improving the quality of the center gold regions. This result was consistent with our previous studies, which calculated that the lift-off yield was about 70%.[18,44] Therefore, one contact and lift process was not sufficient to deactivate the tip areas completely. Multiple rounds of contact and lift were used

to optimize nanoring fabrication. As a result, we were able to fabricate large areas of hollow Au nanorings (**Figure S3.3**). Hollow metal nanorings have been demonstrated in optics-related applications, such as optical trapping and filtering.[50]

3.5 Conclusions and Prospects

In summary, we were able to fabricate large areas of hollow gold nanorings using deformation-controlled polymer-pen chemical lift-off lithography. The average ring size was at the sub-micron scale (365 ± 35 nm). One special property of chemical lift-off lithography is that the contact area is equal to the feature size, which allows us to “deactivate” the tip area of the polymer pens selectively *via* multiple contacts and lifts. External force was added to increase the compression distance z and introduce new contact area between the polymer pens and SAM-modified gold substrates. By creating a reactivity difference between the tip area and surrounding regions, we can control the lift-off yield in different areas and successfully fabricate complex hollow ring structures at sub-micron scales. Future work includes correlating simulation results with experimental findings to provide guidance for more precise tuning of nanoring size.

3.6 Supplementary Materials

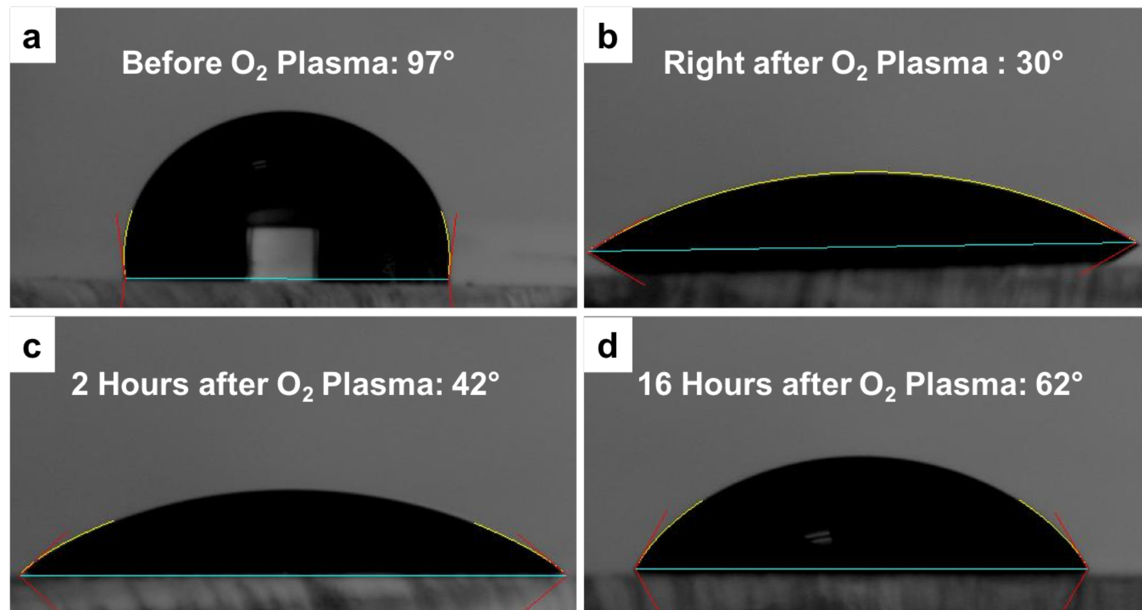

Figure S3.1. Water contact angle measurement of the polydimethylsiloxane (PDMS) stamp before and after oxygen plasma treatment.

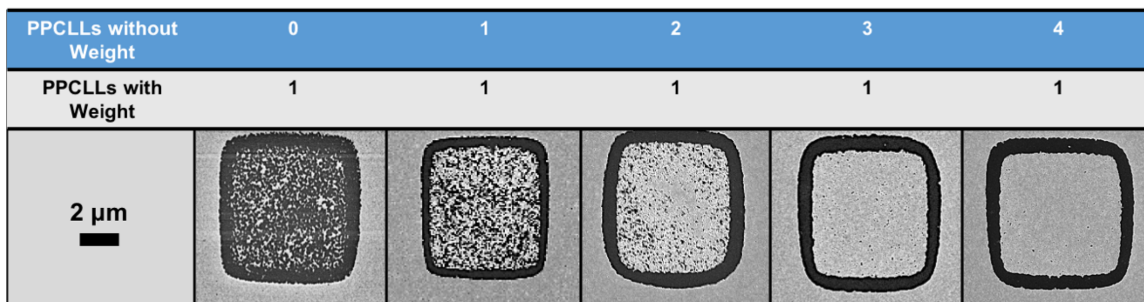

Figure S3.2. Scanning electron microscopy (SEM) images of Au nanorings with different numbers of polymer-pen chemical lift-off lithography (PPCLL) without external weight. The number of defects in the central gold regions decreased with increased number of "deactivations" steps.

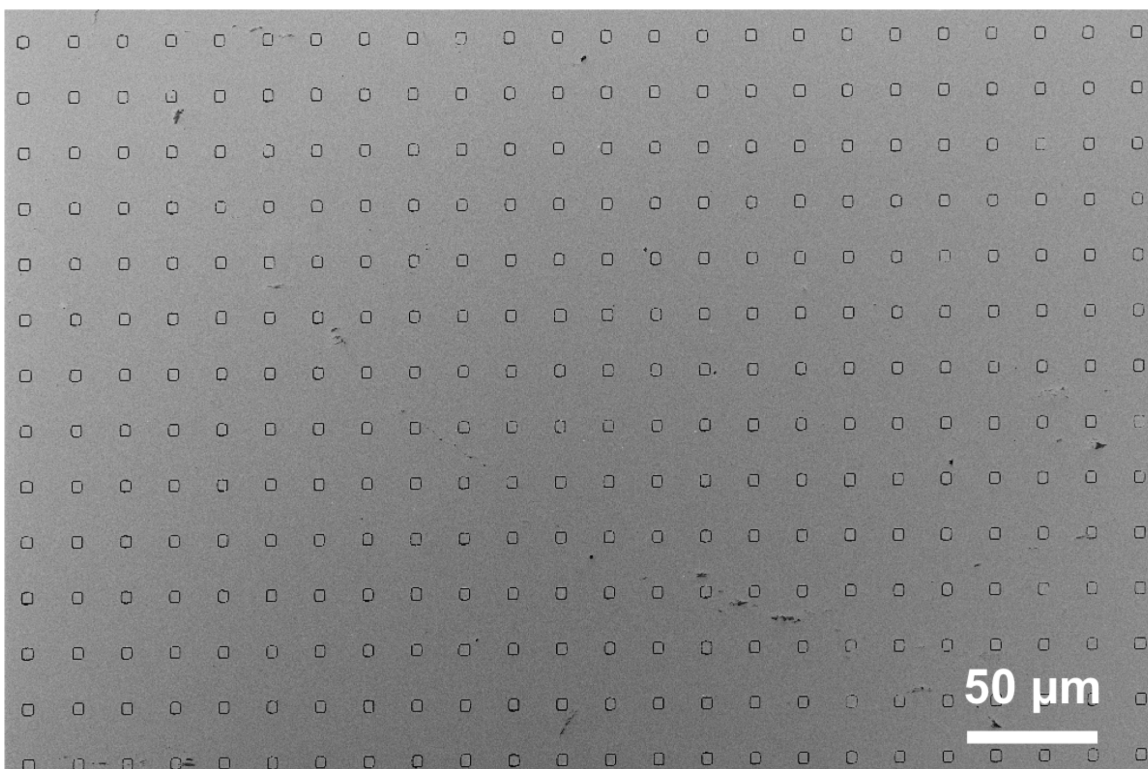

Figure S3.3. Scanning electron microscopy (SEM) image of hollow Au nanorings over a large area after selective etching.

3.7 References

1. Carlson, A.; Bowen, A. M.; Huang, Y.; Nuzzo, R. G.; Rogers, J. A. Transfer Printing Techniques for Materials Assembly and Micro/Nanodevice Fabrication. *Adv. Mater.* **2012,** *24*, 5284–5318.

2. Smith, J. T.; Franklin, A. D.; Farmer, D. B.; Dimitrakopoulos, C. D. Reducing Contact Resistance in Graphene Devices through Contact Area Patterning. *ACS Nano* **2013,** *7*, 3661–3667.

3. Tsai, H.; Pitera, J. W.; Miyazoe, H.; Bangsaruntip, S.; Engelmann, S. U.; Liu, C.-C.; Cheng, J. Y.; Bucchignano, J. J.; Klaus, D. P.; Joseph, E. A.; Sanders, D. P.; Colburn, M. E.; Guillorn, M. A. Two-Dimensional Pattern Formation Using Graphoepitaxy of PS-b-PMMA Block Copolymers for Advanced FinFET Device and Circuit Fabrication. *ACS Nano* **2014,** *8*, 5227–5232.

4. Xu, X.; Kim, K.; Fan, D. Tunable Release of Multiplex Biochemicals by Plasmonically Active Rotary Nanomotors. *Angew. Chem. Int. Ed.* **2015,** *54*, 2525–2529.

5. Kim, J.; Rim, Y. S.; Chen, H.; Cao, H. H.; Nakatsuka, N.; Hinton, H. L.; Zhao, C.; Andrews, A. M.; Yang, Y.; Weiss, P. S. Fabrication of High-Performance Ultrathin In_2O_3 Film Field-Effect Transistors and Biosensors Using Chemical Lift-Off Lithography. *ACS Nano* **2015,** *9*, 4572–4582.

6. Chen, S.; Bomer, J. G.; van der Wiel, W. G.; Carlen, E. T.; van den Berg, A. Top-Down Fabrication of Sub-30 nm Monocrystalline Silicon Nanowires Using Conventional Microfabrication. *ACS Nano* **2009,** *3*, 3485–3492.

7. Ozbay, E. Plasmonics: Merging Photonics and Electronics at Nanoscale Dimensions. *Science* **2006,** *311*, 189–193.

8. Henzie, J.; Lee, M. H.; Odom, T. W. Multiscale Patterning of Plasmonic Metamaterials. *Nat. Nanotechnol.* **2007,** *2*, 549–554.

9. Nordlander, P. The Ring: A Leitmotif in Plasmonics. *ACS Nano* **2009,** *3*, 488–492.

10. Priolo, F.; Gregorkiewicz, T.; Galli, M.; Krauss, T. F. Silicon Nanostructures for Photonics and Photovoltaics. *Nat. Nanotechnol.* **2014,** *9*, 19–32.

11. Kung, S.-C.; van der Veer, W. E.; Yang, F.; Donavan, K. C.; Penner, R. M. 20 μs Photocurrent Response from Lithographically Patterned Nanocrystalline Cadmium Selenide Nanowires. *Nano Lett.* **2010,** *10*, 1481–1485.

12. Fan, F.-R.; Lin, L.; Zhu, G.; Wu, W.; Zhang, R.; Wang, Z. L. Transparent Triboelectric Nanogenerators and Self-Powered Pressure Sensors Based on Micropatterned Plastic Films. *Nano Lett.* **2012,** *12*, 3109–3114.

13. Ge, M.; Rong, J.; Fang, X.; Zhou, C. Porous Doped Silicon Nanowires for Lithium Ion Battery Anode with Long Cycle Life. *Nano Lett.* **2012,** *12*, 2318–2323.

14. Ul-Haq, E.; Patole, S.; Moxey, M.; Amstad, E.; Vasilev, C.; Hunter, C. N.; Leggett, G. J.; Spencer, N. D.; Williams, N. H. Photocatalytic Nanolithography of Self-Assembled Monolayers and Proteins. *ACS Nano* **2013,** *7*, 7610–7618.

15. Moxey, M.; Johnson, A.; El-Zubir, O.; Cartron, M.; Dinachali, S. S.; Hunter, C. N.; Saifullah, M. S. M.; Chong, K. S. L.; Leggett, G. J. Fabrication of Self-Cleaning, Reusable Titania Templates for Nanometer and Micrometer Scale Protein Patterning. *ACS Nano* **2015,** *9*, 6262–6270.

16. Xu, X.; Hou, S.; Wattanatorn, N.; Wang, F.; Yang, Q.; Zhao, C.; Yu, X.; Tseng, H.-R.; Jonas, S. J.; Weiss, P. S. Precision-Guided Nanospears for Targeted and High-Throughput Intracellular Gene Delivery. *ACS Nano* **2018,** *12*, 4503–4511.

17. Cao, H. H.; Nakatsuka, N.; Deshayes, S.; Abendroth, J. M.; Yang, H.; Weiss, P. S.; Kasko, A. M.; Andrews, A. M. Small-Molecule Patterning *via* Prefunctionalized Alkanethiols. *Chem. Mater.* **2018,** *30*, 4017–4030.

18. Cao, H. H.; Nakatsuka, N.; Liao, W.-S.; Serino, A. C.; Cheunkar, S.; Yang, H.; Weiss, P. S.; Andrews, A. M. Advancing Biocapture Substrates *via* Chemical Lift-Off Lithography. *Chem. Mater.* **2017,** *29*, 6829–6839.

19. Xu, X.; Yang, Q.; Cheung, K. M.; Zhao, C.; Wattanatorn, N.; Belling, J. N.; Abendroth, J. M.; Slaughter, L. S.; Mirkin, C. A.; Andrews, A. M.; Weiss, P. S. Polymer-Pen Chemical Lift-Off Lithography. *Nano Lett.* **2017,** *17*, 3302–3311.

20. Zheng, Z.; Daniel, W. L.; Giam, L. R.; Huo, F.; Senesi, A. J.; Zheng, G.; Mirkin, C. A. Multiplexed Protein Arrays Enabled by Polymer Pen Lithography: Addressing the Inking Challenge. *Angew. Chem. Int. Ed.* **2009,** *48*, 7626–7629.

21. Sullivan, T. P.; van Poll, M. L.; Dankers, P. Y. W.; Huck, W. T. S. Forced Peptide Synthesis in Nanoscale Confinement under Elastomeric Stamps. *Angew. Chem. Int. Ed.* **2004,** *43*, 4190–4193.

22. Pimpin, A. S., W. Review on Micro- and Nanolithography Techniques and Their Applications. *Eng. J.* **2011,** *16*, 37–56.

23. Gates, B. D.; Xu, Q.; Stewart, M.; Ryan, D.; Willson, C. G.; Whitesides, G. M. New Approaches to Nanofabrication: Molding, Printing, and Other Techniques. *Chem. Rev.* **2005,** *105*, 1171–1196.

24. Cumming, D. R. S.; Thoms, S.; Weaver, J. M. R.; Beaumont, S. P. 3 nm NiCr wires made using electron beam lithography and PMMA resist. *Microelectron. Eng.* **1996,** *30*, 423–425.

25. Hu, W. C.; Sarveswaran, K.; Lieberman, M.; Bernstein, G. H. Sub-10 nm Electron Beam Lithography Using Cold Development of Poly(methylmethacrylate). *J. Vac. Sci. Technol. B* **2004,** *22*, 1711–1716.

26. Chen, S.; Svedendahl, M.; Antosiewicz, T. J.; Kall, M. Plasmon-Enhanced Enzyme-Linked Immunosorbent Assay on Large Arrays of Individual Particles Made by Electron Beam Lithography. *ACS Nano* **2013,** *7*, 8824–8832.

27. Kim, S.; Marelli, B.; Brenckle, M. A.; Mitropoulos, A. N.; Gil, E. S.; Tsioris, K.; Tao, H.; Kaplan, D. L.; Omenetto, F. G. All-Water-Based Electron-Beam Lithography Using Silk as A resist. *Nat. Nanotechnol.* **2014,** *9*, 306–310.

28. Manfrinato, V. R.; Wen, J. G.; Zhang, L. H.; Yang, Y. J.; Hobbs, R. G.; Baker, B.; Su, D.; Zakharov, D.; Zaluzec, N. J.; Miller, D. J.; Stach, E. A.; Berggren, K. K. Determining the Resolution Limits of Electron-Beam Lithography: Direct Measurement of the Point-Spread Function. *Nano Lett.* **2014,** *14*, 4406–4412.

29. Bat, E.; Lee, J.; Lau, U. Y.; Maynard, H. D. Trehalose Glycopolymer Resists Allow Direct Writing of Protein Patterns by Electron-Beam Lithography. *Nat. Commun.* **2015,** *6*, 6654.

30. Gschrey, M.; Thoma, A.; Schnauber, P.; Seifried, M.; Schmidt, R.; Wohlfeil, B.; Kruger, L.; Schulze, J. H.; Heindel, T.; Burger, S.; Schmidt, F.; Strittmatter, A.; Rodt, S.; Reitzenstein, S. Highly Indistinguishable Photons From Deterministic Quantum-Dot Microlenses Utilizing Three-Dimensional *in Situ* Electron-Beam Lithography. *Nat. Commun.* **2015,** *6*, 7662.

31. Volkert, C. A.; Minor, A. M. Focused Ion Beam Microscopy and Micromachining. *MRS Bull.* **2007,** *32*, 389–395.

32. Kalhor, N.; Boden, S. A.; Mizuta, H. Sub-10 nm Patterning by Focused He-Ion Beam Milling for Fabrication of Downscaled Graphene Nano Devices. *Microelectron. Eng.* **2014,** *114*, 70–77.

33. Pan, L.; Park, Y.; Xiong, Y.; Ulin-Avila, E.; Wang, Y.; Zeng, L.; Xiong, S.; Rho, J.; Sun, C.; Bogy, D. B.; Zhang, X. Maskless Plasmonic Lithography at 22 nm Resolution. *Sci. Rep.* **2011,** *1*, 175.

34. Kumar, A.; Whitesides, G. M. Features of Gold Having Micrometer to Centimeter Dimensions Can Be Formed Through A Combination of Stamping with An Elastomeric Stamp and An Alkanethiol ''Ink'' Followed by Chemical Etching. *Appl. Phys. Lett.* **1993,** *63*, 2002–2004.

35. Qin, D.; Xia, Y.; Whitesides, G. M. Soft Lithography for Micro- and Nanoscale Patterning. *Nat. Protoc.* **2010,** *5*, 491–502.

36. Xia, Y.; Whitesides, G. M. Soft Lithography. *Angew. Chem. Int. Ed.* **1998,** *37*, 550–575.

37. Xia, Y.; Zhao, X.-M.; Kim, E.; Whitesides, G. M. A Selective Etching Solution for Use with Patterned Self-Assembled Monolayers of Alkanethiolates on Gold. *Chem. Mater.* **1995,** *7*, 2332–2337.

38. Delamarche, E.; Schmid, H.; Bietsch, A.; Larsen, N. B.; Rothuizen, H.; Michel, B.; Biebuyck, H. Transport Mechanisms of Alkanethiols During Microcontact Printing on Gold. *J. Phys. Chem. B* **1998,** *102*, 3324–3334.

39. Srinivasan, C.; Mullen, T. J.; Hohman, J. N.; Anderson, M. E.; Dameron, A. A.; Andrews, A. M.; Dickey, E. C.; Horn, M. W.; Weiss, P. S. Scanning Electron Microscopy of Nanoscale Chemical Patterns. *ACS Nano* **2007,** *1*, 191–201.

40. Huo, F.; Zheng, Z.; Zheng, G.; Giam, L. R.; Zhang, H.; Mirkin, C. A. Polymer Pen Lithography. *Science* **2008,** *321*, 1658–1660.

41. Dameron, A. A.; Hampton, J. R.; Smith, R. K.; Mullen, T. J.; Gillmor, S. D.; Weiss, P. S. Microdisplacement Printing. *Nano Lett.* **2005,** *5*, 1834–1837.

42. Saavedra, H. M.; Mullen, T. J.; Zhang, P. P.; Dewey, D. C.; Claridge, S. A.; Weiss, P. S. Hybrid Strategies in Nanolithography. *Rep. Prog. Phys.* **2010,** *73*, 036501.

43. Shuster, M. J.; Vaish, A.; Cao, H. H.; Guttentag, A. I.; McManigle, J. E.; Gibb, A. L.; Martinez, M. M.; Nezarati, R. M.; Hinds, J. M.; Liao, W. S.; Weiss, P. S.; Andrews, A. M. Patterning Small-Molecule Biocapture Surfaces: Microcontact Insertion Printing *vs.* Photolithography. *Chem. Commun.* **2011,** *47*, 10641–10643.

44. Liao, W.-S.; Cheunkar, S.; Cao, H. H.; Bednar, H. R.; Weiss, P. S.; Andrews, A. M. Subtractive Patterning *via* Chemical Lift-Off Lithography. *Science* **2012,** *337*, 1517–1521.

45. Andrews, A. M.; Liao, W.-S.; Weiss, P. S. Double-Sided Opportunities Using Chemical Lift-Off Lithography. *Acc. Chem. Res.* **2016,** *49*, 1449–1457.

46. Liao, X.; Braunschweig, A. B.; Zheng, Z.; Mirkin, C. A. Force- and Time-Dependent Feature Size and Shape Control in Molecular Printing *via* Polymer-Pen Lithography. *Small* **2010,** *6*, 1082–1086.

47. Liao, X.; Braunschweig, A. B.; Mirkin, C. A. "Force-Feedback" Leveling of Massively Parallel Arrays in Polymer Pen Lithography. *Nano Lett.* **2010,** *10*, 1335–1340.

48. Zhao, C.; Xu, X.; Yang, Q.; Man, T.; Jonas, S. J.; Schwartz, J. J.; Andrews, A. M.; Weiss, P. S. Self-Collapse Lithography. *Nano Lett.* **2017,** *17*, 5035–5042.

49. Eichelsdoerfer, D. J.; Liao, X.; Cabezas, M. D.; Morris, W.; Radha, B.; Brown, K. A.; Giam, L. R.; Braunschweig, A. B.; Mirkin, C. A. Large-Area Molecular Patterning with Polymer Pen Lithography. *Nat. Protoc.* **2013,** *8*, 2548–2560.

50. Yoo, D.; Gurunatha, K. L.; Choi, H.-K.; Mohr, D. A.; Ertsgaard, C. T.; Gordon, R.; Oh, S.-H. Low-Power Optical Trapping of Nanoparticles and Proteins with Resonant Coaxial Nanoaperture Using 10 nm Gap. *Nano Lett.* **2018,** *18*, 3637–3642.

Chapter 4

Self-Collapse Lithography

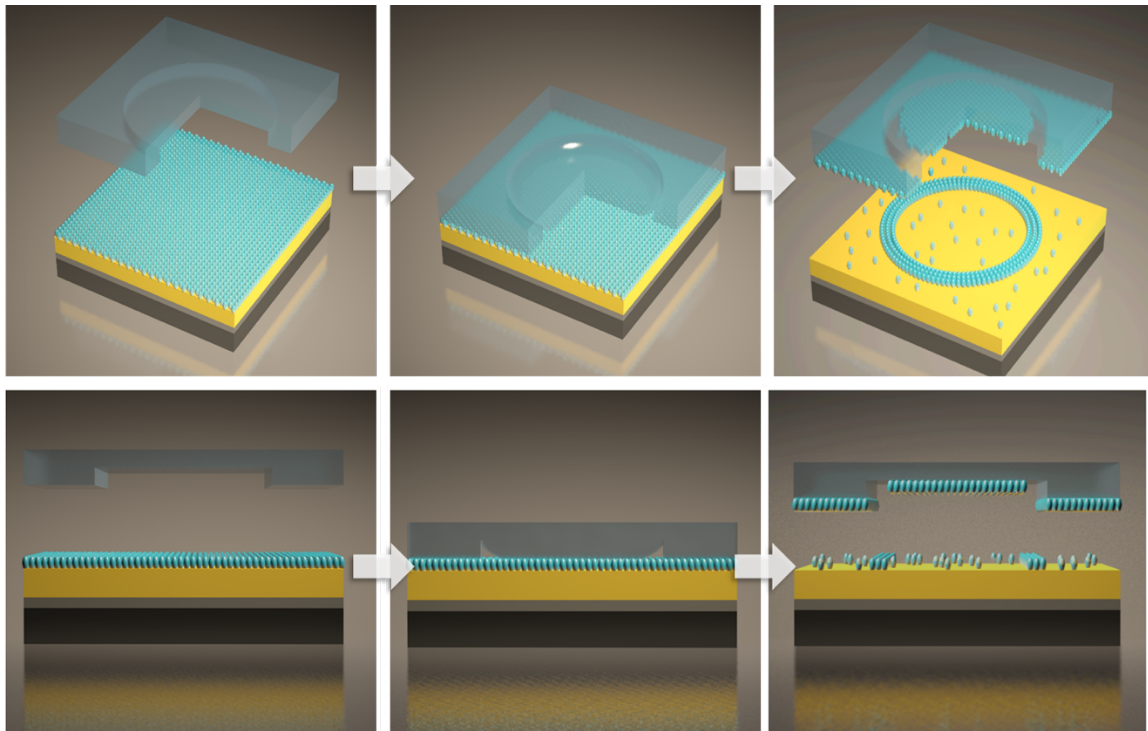

The information in this chapter was published in

Nano Lett. **2017**, *17*, 5035–5042 and has been reproduced here.

Authors: Zhao, C.; Xu, X.; **Yang, Q.**; Man, T.; Jonas, S. J.; Schwartz, J. J.; Andrews, A. M.; Weiss, P. S.

4.1 Abstract

We report a facile, high-throughput soft lithography process that utilizes nanoscale channels formed naturally at the edges of microscale relief features on soft, elastomeric stamps. Upon contact with self-assembled monolayer (SAM) functionalized substrates, the roof of the stamp collapses, resulting in the selective removal of SAM molecules *via* a chemical lift-off process. With this technique, which we call self-collapse lithography (SCL), sub-30-nm patterns were achieved readily using masters with microscale features prepared by conventional photolithography. The feature sizes of the chemical patterns can be varied continuously from ~2 μm to below 30 nm by decreasing stamp relief heights from 1 μm to 50 nm. Likewise, for fixed relief heights, reducing the stamp Young's modulus from ~2.0 to ~0.8 MPa resulted in shrinking the features of resulting patterns from ~400 to ~100 nm. The self-collapse mechanism was studied using finite element simulation methods to model the competition between adhesion and restoring stresses during patterning. These results correlate well with the experimental data and reveal the relationship between the linewidths, channel heights, and Young's moduli of the stamps. In addition, SCL was applied to pattern two-dimensional arrays of circles and squares. These chemical patterns served as resists during etching processes to transfer patterns to the underlying materials (*e.g.,* gold nanostructures). This work provides new insights into the natural propensity of elastomeric stamps to self-collapse and demonstrates a means of exploiting this behavior to achieve patterning *via* nanoscale chemical lift-off lithography.

4.2 Introduction

The rapid development of new and more complex nanoscale technologies, including those in electronics,[1-4] displays and lighting,[5-8] nanofluidics,[9,10] wearable and flexible sensors,[3,11-13] ultrasensitive biosensors,[14-17] and medical devices[18-21] is transforming modern life. To meet demands for further advances in these areas, needs must be met for economical and high-throughput molecular patterning techniques to enable efficient nanofabrication. Conventional photolithography methods cannot achieve robust nanoscale patterns as their resolutions are limited by optical and/or UV light sources and are prohibitively slow for large-area patterning. Additionally, current costs of state-of-the-art nanolithography tools, including parallel approaches (*e.g.,* extreme ultraviolet patterning,[22] and X-ray patterning[23]) and direct-write methods (*e.g.*, electron-beam lithography,[24,25] focused ion-beam milling,[26] and scanning probe lithography[27,28]), require highly specialized equipment and significant infrastructural investments that limit availability outside of large corporations, and academic and government research centers.

Several molecular patterning strategies have been developed as economical and accessible alternatives to conventional nanofabrication methods, including soft lithographic microcontact printing (μCP),[29-32] replica molding,[33,34] nanoimprint lithography,[35] polymer pen lithography,[36-40] nanotransfer printing,[41] decal transfer printing,[42] and nanoskiving.[43] The most widely utilized of these methods, μCP, achieves micro- and nanoscale patterning of molecular "inks" (*e.g.,* alkanethiols[29-32] or biomolecules[44-46]) *via* stamps replica-molded from masters prepared by conventional photolithography. Some molecular inks (*e.g.,* alkanethiols) have been shown to serve as etch resists that enable the transfer of the desired patterns into the underlying substrates.[14,47]

The quality of the final patterns produced *via* μCP is limited by a variety of factors, including diffusion of molecular inks and/or the deformation of stamp features.[31,32,48] For example, lateral diffusion of ink molecules on surfaces results in enlarged features with lower contrast that can, in some cases, results in the complete loss of the transferred pattern.[31] This effect becomes even more significant when patterning sub-μm features, and often limits the resolution of μCP to ~100 nm. Several modified μCP approaches have been developed by our group to minimize or to eliminate lateral diffusion of ink molecules.[49-52] Microdisplacement printing[50,53] and microcontact insertion printing[49,54,55] were invented to print molecules on alkanethiol self-assembled monolayer (SAM) modified substrates through displacement or insertion processes, respectively. The SAMs in the unpatterned regions prevent ink molecules from diffusing beyond the contact areas.[54,56] We also developed a subtractive molecular patterning method called chemical lift-off lithography (CLL) that effectively eliminates ink-molecule diffusion and is capable of high-fidelity patterning down to 20-nm linewidths.[14,52,57] Further refinements of CLL have achieved feature sizes down to ~5 nm.[51]

In addition to lateral diffusion, the accuracy of transferred patterns can also be affected adversely by deformations of stamps upon physical contact with substrates during μCP (*e.g.,* mechanical sagging, sliding, and/or compression of stamp features).[32,58-60] For example, when an external load is applied to a polydimethylsiloxane (PDMS) stamp, the relief features sag causing the roof of the stamp to collapse and to contact the substrate. Recent studies demonstrated that this roof-collapse phenomenon could occur spontaneously even without the application of an external load when the aspect ratio of the stamp features was engineered to be sufficiently large.[58-60] This "self-collapsing" behavior occurs due to the adhesion force between the stamp and substrate. Several groups, including Rogers, Huang, and coworkers have

investigated stamp designs that minimize self-collapse, which include tailoring feature aspect ratios, adhesion energy, and Young's modulus.[40,61-63] While seen initially as a disadvantage for pattern reproduction, other groups, including Erickson and colleagues have harnessed self-collapse for the fabrication of 60 nm nanofluidic channels from microchannels under controlled loads.[64,65] We have also exploited this phenomenon for precise control of patterns using polymer-pen arrays and integral supporting structures.[40] However, to the best of our knowledge, self-collapse has not been specifically exploited for nanolithography.

Here, we report control of self-collapse behavior of PDMS stamps precisely at the nanoscale when integrated with CLL to establish a new nanolithography method—self-collapse lithography (SCL). Using SCL, we achieve sub-30 nm features by tailoring the dimensions of the stamp features, as well as the stiffness of the PDMS.

4.3 Materials and Methods

Materials. Prime quality 4″ Si(100) wafers (P/B, 1-10 Ω-cm) were purchased from University Wafer Inc. (Boston, MA, USA). Sylgard 184® silicone elastomer kits (lot # 0008823745) were purchased from Ellsworth Adhesives (Germantown, WI, USA). All other chemicals were purchased from Sigma-Aldrich (St. Louis, MO, USA) and used as received. The SPR 700-1.2 photoresist and MF-26A developer were obtained from the Integrated Systems Nanofabrication Cleanroom (ISNC) at UCLA.

Characterization. Scanning electron microscopy (SEM) images were obtained using a Zeiss Supra 40VP scanning electron microscope with an Inlens SE Detector (Inlens secondary electron detector). Optical images were taken with a Zeiss Axiotech optical microscope.

Growth of SiO_2 on Si (100). A 1-μm SiO_2 film was thermally grown on Si(100) wafers. If needed, SiO_2/Si wafers are also available for purchase elsewhere.

Photolithography. Photomasks were designed using the AutoCAD software suite (Autodesk, Inc.) with patterns consisting of two-dimensional (2D) arrays of lines, circles, or squares. The linewidths of the feature investigated here were >2 μm and thus, were fabricated by conventional photolithography. Positive photoresist SPR700-1.2 was spin-coated on SiO_2/Si wafer surfaces, followed by a 90-sec soft bake at 90 °C on a hotplate. A Karl Suss contact aligner was used to expose the photoresist on the wafer with the pattern from a photomask with an optimal exposure time of 16.5 sec (UV wavelength = 365 nm, intensity = 8.5 mW/cm^2). Each exposed wafer was post-exposure baked at 110 °C for 90 sec, immersed in MF-26A developer for 1 min, rinsed with deionized water, and blown dry with N_2 gas.

Reactive ion etching (RIE) of SiO_2. After patterning by photolithography, the exposed SiO_2 was selectively etched by RIE (Oxford 80 Plus) with a gas mixture of CHF_3 (25 sccm) and Ar (25 sccm) at 35 mTorr. Channel heights were tuned by varying the etch times. A Dektak profilometer was used to confirm the heights of the etched features. Once the desired channel height was obtained, the remaining photoresist was removed from each surface using a Matrix Asher or dissolved using acetone. The molds were then coated with silane (trichloro(1H,1H,2H,2H-perfluorooctyl)silane) as a release layer.

Preparation of PDMS stamps. The Young's modulus of polydimethylsiloxane (PDMS) was tuned by varying the mass ratio of the Sylgard® 184 elastomer silicone elastomer base and curing agent at 5:1, 10:1, 15:1, or 20:1 ratios. Base and curing agent were thoroughly mixed. The mixture was poured into a petri dish containing the Si masters and then degassed in a vacuum desiccator and cured overnight at 65 °C. Afterwards, PDMS stamps were carefully removed from the Si masters.

Surface functionalization of Au/Ti/Si substrate for self-collapse lithography. The 10-nm Ti and 30-nm Au films were deposited on clean silicon wafers with a CHA Solution E-Beam Evaporator at high vacuum (10^{-8} Torr) at an evaporation rate of 0.1 nm/s. The Au/Ti/Si wafers were annealed in a hydrogen flame for ~10 s to create Au(111) surfaces and then immersed into 1 mM 11-mercapto-1-undecanol ethanolic solution overnight for self-assembled monolayer formation on the Au surfaces.

Activation of PDMS stamps. Clean PDMS stamps were treated in oxygen plasma (Harrick Plasma, Ithaca, NY) for 40 s at a power of 18 W and a pressure of 10 psi to generate hydrophilic surfaces.

Contact and removal of stamps. A pair of tweezers was used to place each PDMS stamp on a substrate without applying a compression force. In the stamp removal process, one pair of tweezers was used to hold the substrate and another pair was used to lift off the stamp. In the future, more precise control can be achieved by coupling the stamp to a scanning stage system.

Estimate of the Young's modulus of PDMS stamps. The Young's modulus of PDMS stamps prepared using a 10:1 ratio (X:Y) of Sylgard 184 pre-polymer base (X) and curing agent (Y) is approximately 1.75 MPa (cured at 65 °C). The Young's moduli of PDMS cast from different ratios of X:Y were estimated based on previously reported values,[66,67] where stamps used in the present study were 2.0 MPa (5:1), 1.15 MPa (15:1), and 0.85 MPa (20:1).

Error analyses. The errors in linewidths were based on 10 measurements of the patterned molecules on three different PDMS stamps. The three PDMS stamps were prepared using one silicon master for a fixed height. The errors in the heights originate from the RIE process and were determined by five measurements at different locations on the same substrate. The errors in heights were determined to be 100 ± 15 nm, 200 ± 10 nm, 300 ± 20 nm, 400 ± 25 nm, 500 ± 10 nm for heights under 500 nm. The errors in widths were determined to be within 10%, measured over five lines on the same substrate, which is not critical for this study, as described in the manuscript.

Wet etching. After PDMS stamps were lifted-off from SAM-modified substrates, each substrate was immersed into an aqueous solution of 20 mM iron nitrate and 30 mM thiourea to etch Au films selectively.[14] The etching rate was ~1 nm/min and the samples were put into the etching solution for 30 min. After 30 min of etching, the substrates were rinsed with DI water and blown dry with a N_2 gun.

4.4. Results and Discussions

A typical SCL process is illustrated in **Figure 4.1**. Step 1, a Au (30 nm)/Ti (10 nm)/Si substrate is immersed into a hydroxyl-terminated alkanethiol solution (1 mM 11-mercapto-1-undecanol in ethanol) for ~12 h to form a self-assembled monolayer (SAM) on the Au surface. Next, a PDMS stamp with the desired pattern is "activated" by exposure to oxygen plasma for 40 s, which generates hydrophilic silanol (—Si-OH) groups on the stamp surface. Step 2, an activated stamp is placed in conformal contact with the SAM-functionalized Au surface without an externally applied load. The Au surface is flame annealed before functionalization. The surface roughness is ~1 nm, which is necessary for the subsequent high-resolution chemical patterning. Self-collapse of the stamp's recessed features occurs spontaneously due to adhesion forces between the PDMS and the SAM on the Au surface. As the self-collapsing regions of the stamp, as well as the stamp protruding features contact the surface, covalent bonds form *via* condensation reactions between the -OH moieties of the SAM and the silanol groups of the activated PDMS stamp[47]. Upon lifting the PDMS stamp off the substrate (Step 3), alkanethiol molecules are removed selectively from the Au surface in the stamp-contact regions, leaving intact SAMs in the non-contacted areas. As observed in CLL, Au atoms are also removed during lift-off as the Au-S bonds between alkanethiol adsorbates and Au surface atoms are stronger than Au-Au bonds at the surface of the substrate.[51,52] Note that as discovered in our previous work and shown in **Figure 4.1c,f**, not all of the molecules in the contact regions are removed in the CCL process (and the remaining molecules can form a matrix for controlled chemical patterning).[57]

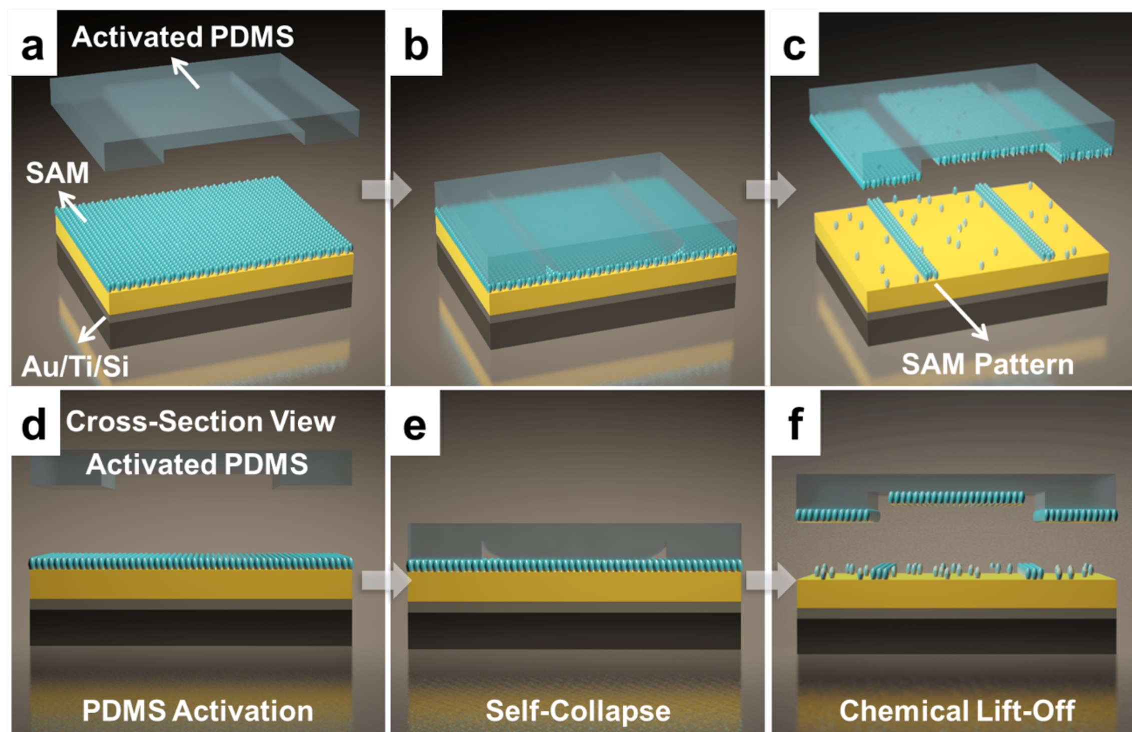

Figure 4.1. Schematic illustration of self-collapse lithography (SCL). (a,d) Hydroxyl-terminated alkanethiols form a self-assembled monolayer (SAM) on the surface of an Au/Ti-coated Si substrate. A polydimethylsiloxane (PDMS) stamp is activated by oxygen plasma treatment. (b,e) The activated stamp is brought into conformal contact with the SAM-coated Au surface without externally applied forces. (c,f) The chemical lift-off process removes the SAM from regions of the functionalized surface in direct contact with the stamp, thereby producing a pattern from molecules remaining in non-contacted regions.[57]

For self-collapse to occur, the aspect ratios (channel width/height) of stamp features and Young's modulus must satisfy specific criteria.[61] We assembled stamps with recessed channels having widths and heights configured to collapse at desired locations, resulting in controlled, reproducible patterns. Scanning electron microscope (SEM) images, as seen in **Figure 4.2**,

demonstrate the removal of SAMs in regions that were in conformal contact with the stamps. Due to stamp self-collapse, narrow structures with linewidths much smaller than the original channel dimensions were observed on the SCL-patterned surface. In **Figures 4.2a**,**b**, arrays of lines ~170 nm wide were produced *via* SCL using PDMS stamps with 6 µm wide channels and 300 nm channel heights. The patterned lines were straight and continuous for tens of micrometers, corresponding to the edges of the original microscale channel. Despite one side of the line being determined by the edge of the stamp contact and the other side being determined by the collapsed polymer, no significant differences in the two sides of the patterned features were observed in these and other patterns.

Table 4.1. Gap linewidths (*L*) produced using stamps with different channel heights (*h*) and channel widths (*w*), with a fixed Young's modulus (*E* = 1.75 MPa).

h	*L*	*w*
50 nm	27 ± 5 nm	1 µm
100 nm	48 ± 6 nm	4 µm
200 nm	78 ± 6 nm	6 µm
300 nm	168 ± 12 nm	6 µm
400 nm	235 ± 17 nm	10 µm
400 nm	227 ± 19 nm	20 µm
500 nm	411 ± 9 nm	20 µm
700 nm	872 ± 82 nm	20 µm
1 µm	1710 ± 98 nm	80 µm

We identified a set of basic design rules that govern SCL to understand the effects of key parameters on the final patterns. It has previously been reported that for reproducible self-collapse to occur, the channel width needs to be larger than a threshold value fixed for each value of the Young's modulus of the stamps, where the potential energy for the collapse is employed to determine the threshold.[61] The aspect ratios (channel width/height) of the stamp features were engineered to be sufficiently large to enable self-collapse.[61] We denote stamp features as follows: channel width as ***w***, channel height as ***h***, and the non-collapsed gap linewidth as ***L*** (**Figure 4.2c**). We first examined the dependence of ***L*** on ***h***. Stamps with discrete values of ***h***, within the range of 50 (*w* = 1 µm) to 400 nm (*w* = 10 µm), produced patterned lines with ***L*** values of 27 ± 5, 48 ± 6, 78 ± 6, 168 ± 12, and 235 ± 17 nm, respectively, as shown in

Figure 4.2d and reported in **Table 4.1**. The channel width for each height is highlighted in the table. Note that when ***w*** is larger than this threshold value, at fixed ***h***, changes in ***w*** have little influence on ***L***,[61] in agreement with our experimental results. For example, we obtained similar values of ***L*** at 235 or 227 nm for different values ***w*** at 10 or 20 µm, respectively, with ***h*** fixed at 400 nm.[61,63] We kept the thickness of PDMS stamps the same (5 mm) in all experiments, and the influence of gravity was neglected in this study. Note that the applied external force and the thickness of the PDMS could also be used to control ***L***, *e.g.*, larger widths can be achieved by applying external stress, which is currently under investigation.

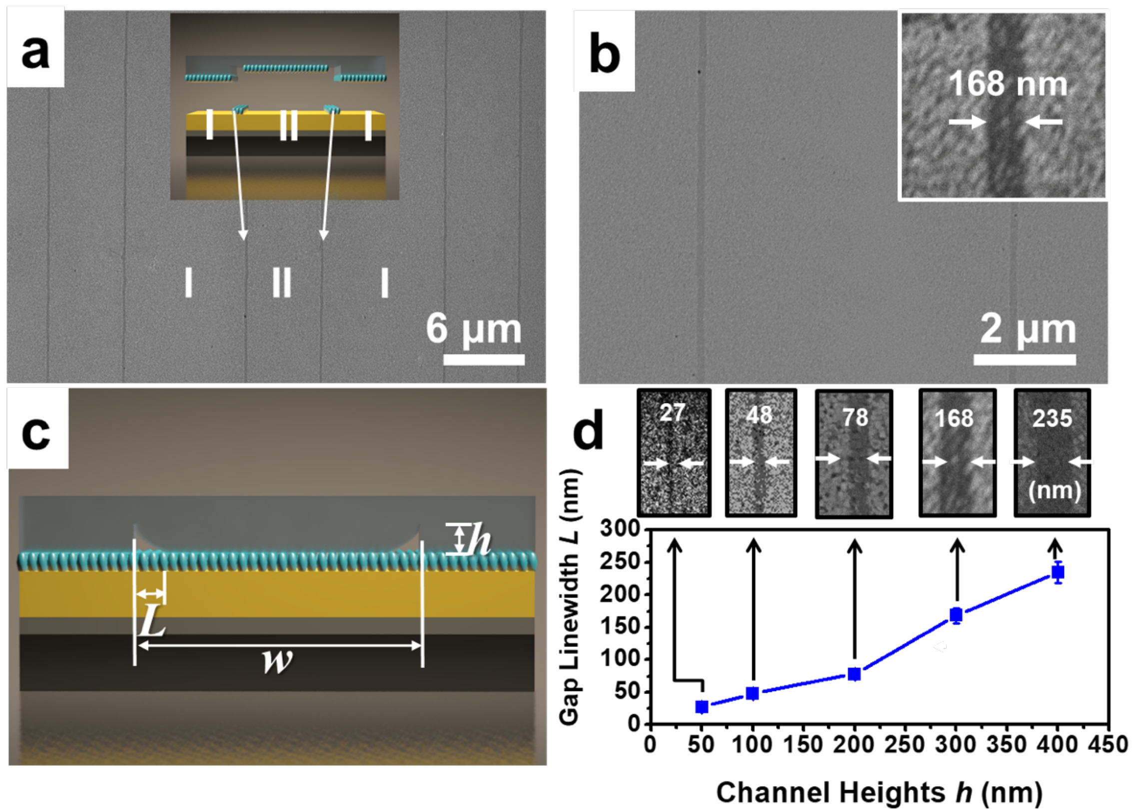

Figure 4.2. (a, b) Scanning electron microscope (SEM) images of linear arrays with sub-200 nm linewidths created by self-collapse lithography using a stamp with microchannel features (6 µm channel width, 300 nm channel height). (c) Schematic

illustration of a collapsed stamp (*L*: gap linewidth; *w*: channel width; and *h*: channel height). (d) Plot of gap linewidths *L* obtained using different channel heights *h* with a fixed Young's modulus of 1.75 MPa. The channel width for each data point is listed in Table 4.1. Insets correspond to a representative SEM image for each data point.

Next, we investigated the relationship between ***L*** and the Young's modulus (***E)*** of stamps. The PDMS stamps were prepared using different ratios (X:Y) of Sylgard 184 pre-polymer base (X) and curing agent (Y) to control the relationship with the patterned linewidths. Values of ***E*** were estimated based on previous reports with details included in the Supporting Information.[66-68] Stamps with ***E*** ranging from 0.85 to 2.0 MPa were molded from a master with relief channel heights fixed at 400 nm. When these stamps were utilized for SCL, ***L*** was found to decrease proportionally with decreasing ***E*** (**Table 4.2**). These results indicate that SCL patterns can be fine-tuned by varying stamp stiffness, *i.e.*, a smaller *L* can be achieved by using softer stamps.

Table 4.2. Gap linewidths (*L*) produced using stamps with different Young's moduli (*E*), and a fixed channel height (*h* = 400 nm) and width (*w* = 10 µm).

E	***L***
2.0 MPa	366 ± 12 nm
1.15 MPa	165 ± 16 nm
1.75 MPa	235 ± 17 nm
0.85 MPa	100 ± 17 nm

A key distinction between SCL and other soft lithographic strategies is that nanoscale patterns are generated from the deformation of micron-scale features on stamps molded from conventional photolithographically prepared masters. The self-collapse process transfers the two-dimensional pattern of the stamp features to the surface while avoiding scaling issues that limit conventional lithographic methods. In principle, the scale over which stamp patterns are reduced is limited only by the precision to which masters can be fabricated and the degree of control over stamp stiffness.

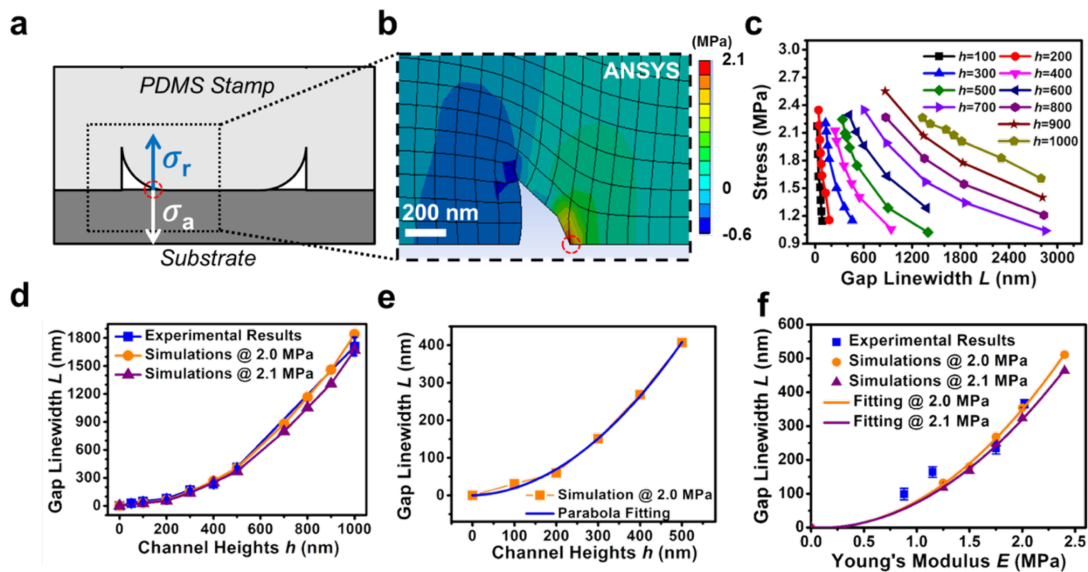

Figure 4.3. (a) Schematic illustration of the self-collapse model used in finite element analysis (FEA) simulations, where σ_r represents the restoring stress and σ_a denotes the adhesion stress between the PDMS stamp and the substrate. (b) A typical FEA simulation result illustrating the stress distribution on a self-collapse stamp (only the restoring stresses normal to the substrate are depicted). (c) Relationships between simulated stresses and gap sizes *L* at different channel heights *h*. (d) Experimentally measured gap widths and channel heights (squares) plotted with simulated values (circles, triangles) using Young's moduli

(E) of 2.0 and 2.1 MPa. (e) Simulated gap linewidths plotted as a function of channel height with a parabolic fit. (f) Plots of simulated and experimental results showing variations in gap linewidths at different values of E.

Adhesion forces between the stamp and the underlying substrate drive the self-collapse of recessed elastomer features. Previously, this process has been approximated using a classic crack growth model (*i.e.,* crack growth stops when the required work equals the adhesion energy) by Huang *et al*.[61,63] Here, we examined the self-collapse process more directly by modeling stress distributions along the gap ($\boldsymbol{L}$) between collapsed regions and the edges of the original features. Two stresses compete at the edges of the gap: an elastic restoring force ($\boldsymbol{\sigma_r}$) and an adhesion force ($\boldsymbol{\sigma_a}$), both acting normal to the substrate. Interactions between $\boldsymbol{\sigma_r}$ and $\boldsymbol{\sigma_a}$ can be used to predict $\boldsymbol{L}$ during SCL (**Figure 4.3a**). The adhesion force acts to collapse the top of the channel, pulling it toward the substrate surface, while the restoring force acts to retain the shape of the channel, pulling it away from the substrate. At equilibrium ($\boldsymbol{\sigma_r} = \boldsymbol{\sigma_a}$), a stable gap ($\boldsymbol{L}$) is formed between the collapsed top and edges of the channel.

Finite element analysis (FEA) simulations were carried out using the ANSYS software suite (Ansys Inc. Student version 16.0, Canonsburg, PA) to model the distributions of mechanical stress within a stamp with minimum mesh sizes fixed at 100 nm (**Figure 4.3b**). We employed an inverse method to simulate the mechanism of self-collapse, where the roofs of simulated channels of specified widths were displaced toward their corresponding substrates by an amount equal to the channel height, $\boldsymbol{h}$. By varying the widths of the simulated channel roof, we obtained a series of restoring stresses along the gap edges and their corresponding gap linewidths, $\boldsymbol{L}$. In this way, we simulated the collapse of stamps configured with different channel

heights to obtain an approximate relationship between the restoring stress and gap width at different channel heights.

As illustrated in **Figure 4.3c**, increases in stamp channel heights result in increases in the resulting gap linewidths as less of each channel's roof makes contact with the substrate surface at fixed stress. A comparison of the results from our FEA simulations at adhesion stresses of 2.0 and 2.1 MPa with those obtained from SCL experiments are shown in **Figure 4.3d.** There is excellent agreement between simulated responses and experimental data, indicating that our stress-balance model correlates well and is predictive of the self-collapse phenomenon. Moreover, the simulation results can be used to predict the line widths of patterns with smaller features. Fitting a parabolic function to the 2.0 MPa curve (**Figure 4.3e**):

$$L = f(h) = ah + bh^2 \qquad \textbf{Eq. (4.1)}$$

we determined the fitting constants $a = 0.038\ \mathrm{nm}^{-1}$ and $b = 0.00156\ \mathrm{nm}^{-2}$. Using **Eq. (4.1)**, we can estimate the $\boldsymbol{L}$ of a pattern produced with any $\boldsymbol{h}$ at stable collapse regions, which enables the manipulation of SCL-generated patterns *via* strategic design of stamp features. For example, to achieve a linewidth of 100 nm, a stamp with channel heights of $\boldsymbol{h} \approx 242$ nm is needed, according to **Eq. (4.1)**. With proper design and optimization, we estimate that SCL will be able to produce linewidths as small as 5 nm (corresponding to patterns about 10 molecules across).[40,51]

In addition to channel height, our studies demonstrate how the mechanical stiffness of PDMS affects linewidths of the final pattern. We modeled the behavior of stamps using different ratios (X:Y) of Sylgard 184 pre-polymer base (X) and curing agent (Y) to determine the relationship with the pattern linewidth. Simulation results of stress and $\boldsymbol{L}$, at a fixed channel

height of 400 nm, are shown in **Figure S4.1** using different values of ***E***: 2.0 MPa (5:1), 1.75 MPa (10:1), 1.15 MPa (15:1) and 0.85 MPa (20:1). Analyses of these data were used to visualize the relationship between ***E*** and ***L*** (**Figure 4.3f**). A trend emerges showing that a decrease in ***E*** (*i.e.,* as the PDMS stamp becomes softer) results in smaller values of ***L*** when patterning using stamps with identical channel heights. Therefore, stamps derived from a single master may be used to generate a range of feature sizes by varying ***E.***

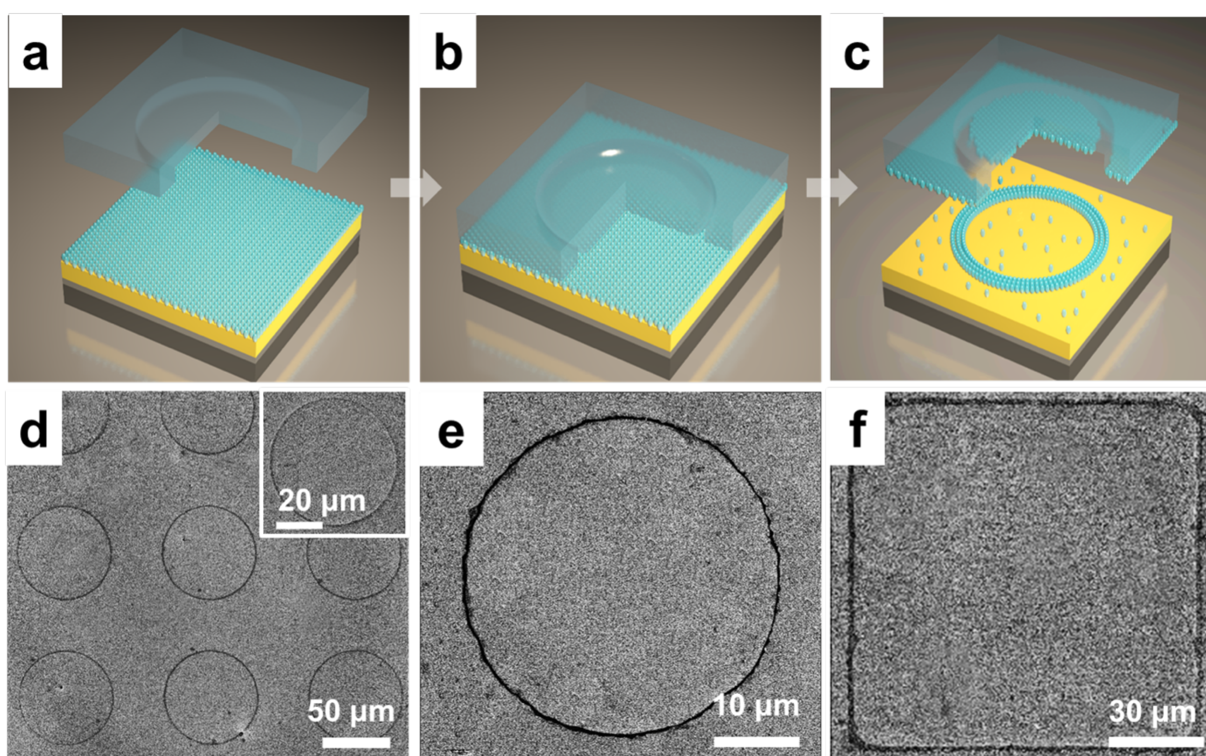

Figure 4.4. (a–c) Schematic illustrations of a ring chemical pattern fabricated *via* self-collapse lithography (SCL). (a) Hydroxyl-terminated alkanethiols form a self-assembled monolayer (SAM) on the surface of an Au/Ti-coated Si substrate. (b) A stamp with recessed circular features is activated by oxygen plasma and then placed into conformal contact with the functionalized Au surface, without an external force. The

central portions of the recessed features on the stamp contact the underlying SAM in smaller circular regions due to self-collapse. (c) The chemical lift-off process removes the SAM in direct contact with the polydimethlysiloxane (PDMS) surfaces from the Au substrate, leaving raised (dark), ring-like SAM patterns behind. (d–f) Contrast enhanced SEM images of (d) ring patterns (*L* ~1.71 µm), patterned by SCL with a stamp with recessed circles (50 µm in diameter and 1 µm in height), (e) a ring pattern (*L* ~235 nm) patterned using recessed circles (40 µm in diameter and 400 nm in height), and (f) raised (dark) squares (*L* ~1.71 µm) patterned with recessed square structures (100 µm on each edge and 1 µm in height).

To demonstrate the versatility of SCL, we produced a variety of patterns, including arrays of circle and square features from PDMS stamps comprised of micron-scale, recessed circular or square features, as illustrated in **Figures 4.4** and 4.**5**. Nanoscale patterning of other shapes can be similarly achieved by careful design of the stamp mold. To date, we have produced robust arrays of ~250 nm linewidth circular rings *via* SCL from stamps comprised of circular holes with diameters ~40 µm and heights ~400 nm (**Figure 4.4e**). By deconstructing these patterns into component lines and angular elements, it is possible to extend SCL further to achieve more complex pattern configurations, such those needed for circuits for nanoelectronics.

The chemical patterns produced *via* SCL can be utilized as templates for selectively patterning a variety of materials, including metals and biomolecules. For example, the intact SAM that remains on a gold substrate following SCL can resist selective chemical etching, enabling the creation of Au nanostructures, including large-area arrays of Au micro-/nano-rings, wires, or square structures (**Figure 4.5)**. We used atomic force microscopy for depth analysis to

image the SAM patterns by CLL, and, in our previous work, wet etching processed samples.[52] Nanostructures of other materials such as silver and copper can be fabricated similarly. As demonstrated by our prior work in developing CLL, SCL may also be applied to pattern biomolecules at the nanoscale.[40,51,52,57,69]

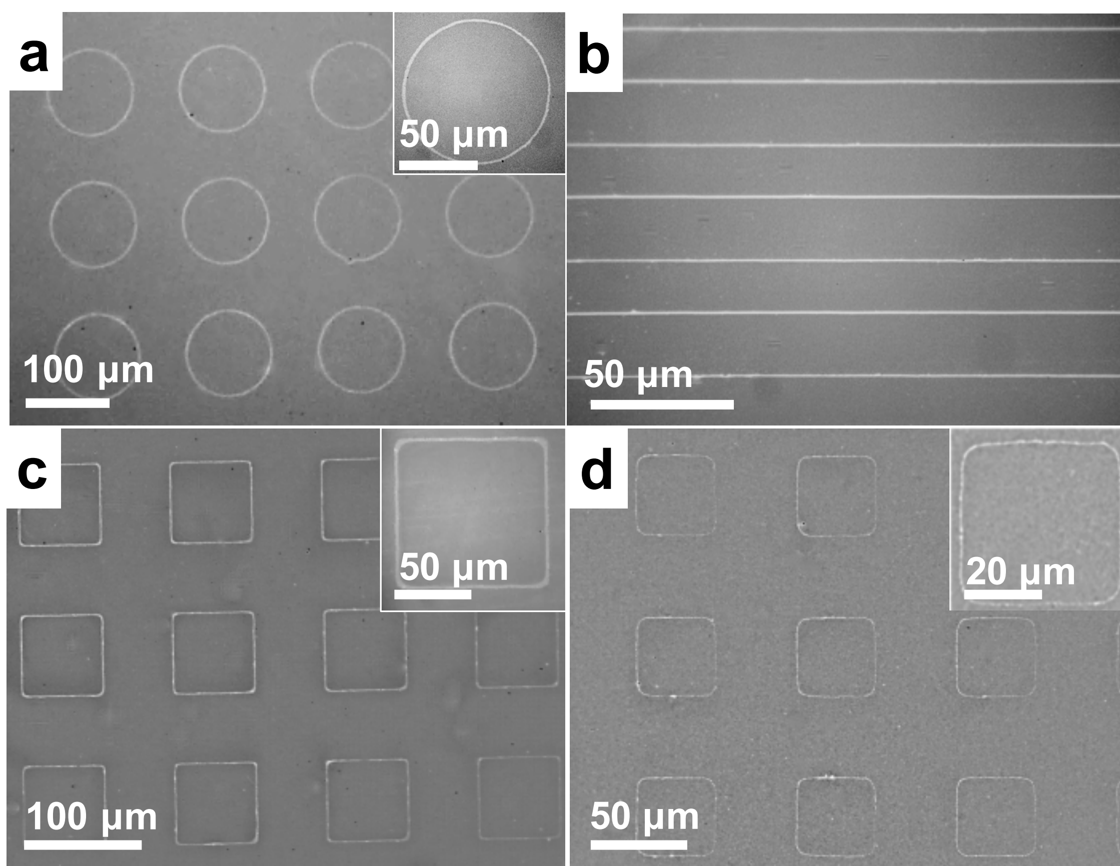

Figure 4.5. Optical microscope images of Au micro/nanostructures fabricated by self-collapse lithography (SCL) followed by selective etching. (a) The Au rings with linewidths of 1.71 μm were fabricated using stamps patterned with 100-μm-diameter circles recessed by 1 μm. (b) Here, Au lines 870 nm wide were fabricated using stamps possessing recessed linear features that were 40 μm wide and 700 nm deep. (c) Sub-2 μm Au squares fabricated using stamps patterned with recessed square features that were

100 µm on an edge and 1 µm in height. (d) Sub-250 nm Au squares fabricated using stamps with recessed squares that were 40 µm in width and 400 nm in height.

4.5 Conclusions and Prospects

In summary, SCL represents a facile and robust nanolithography technique to achieve sub-30 nm resolution by exploiting the elasticity of PDMS structures and natural stamp-substrate adhesion forces. A wide range of shapes and feature sizes can be patterned by strategically designing stamp feature dimensions (*e.g.,* height/width) and/or Young's modulus. Importantly, this soft-lithographic approach can be used as a complement or alternative to slow and expensive direct-writing processes (*e.g.*, electron-beam lithography). The SCL technique provides new insight into how a previously undesirable characteristic of soft lithography can be exploited, *via* CLL, to yield nanoscale patterns. Finite element model simulations suggest a straightforward mechanism for the self-collapse process through the competition between restoring and adhesion stresses along the gap edge produced between the protruding and collapsed stamp features. Results from these simulations correlate well with experimental data and elucidate design rules for using controlled self-collapse to generate complex patterns at the nanoscale that can be applied broadly to applications in nanoelectronics, biosensing, energy storage, and catalysis.

4.6 Supplementary Materials

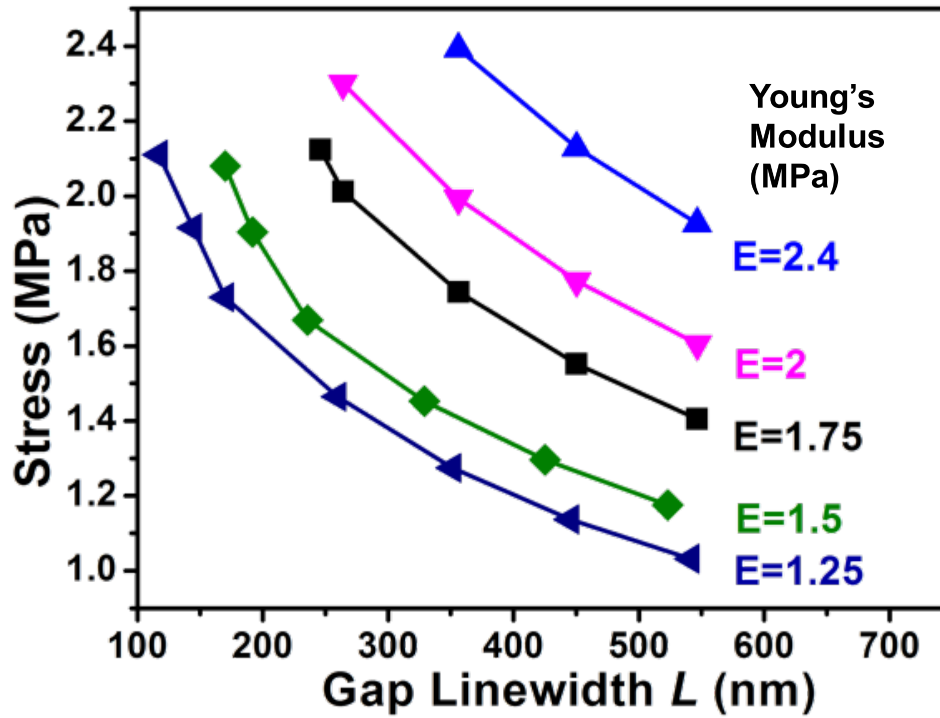

Figure S4.1. Plots of simulation results at different Young's moduli. The relationships between stress at the critical point and gap linewidths at a 400-nm channel height are shown.

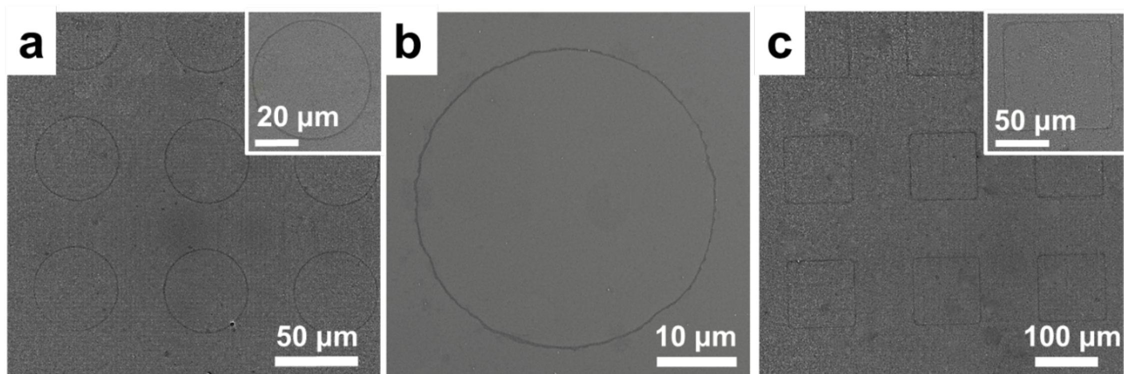

Figure S4.2. Scanning electron microscope (SEM) images of (a) ring patterns (L ~1.71 µm) patterned by a stamp with recessed circles (50 µm diameter and 1 µm height). (b) A ring pattern (L ~235 nm) by a stamp with recessed circles (40 µm diameter and 400 nm height), (c) hollow squares (L ~1.71 µm) by a stamp with recessed square structures (100 µm length and 1 µm height).

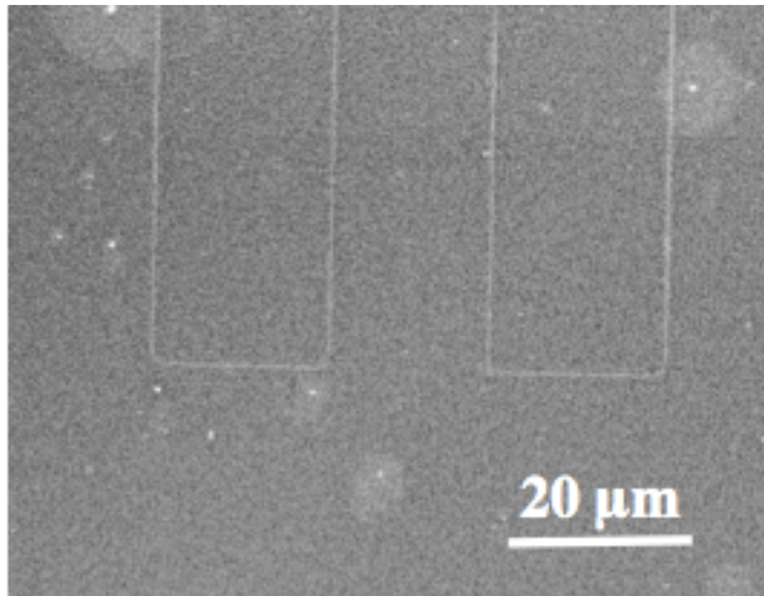

Figure S4.3. Scanning electron microscope (SEM) images of line patterns at the corners with a stamp height of 500 nm.

4.7 References

1. Yan, H.; Chen, Z.; Zheng, Y.; Newman, C.; Quinn, J. R.; Dotz, F.; Kastler, M.; Facchetti, A. A High-Mobility Electron-Transporting Polymer for Printed Transistors. *Nature* **2009,** *457*, 679–686.

2. Jeon, H.-J.; Kim, K. H.; Baek, Y.-K.; Kim, D. W.; Jung, H.-T. New Top-Down Approach for Fabricating High-Aspect-Ratio Complex Nanostructures with 10 nm Scale Features. *Nano Lett.* **2010,** *10*, 3604–3610.

3. Kim, D.-H.; Lu, N.; Ma, R.; Kim, Y.-S.; Kim, R.-H.; Wang, S.; Wu, J.; Won, S. M.; Tao, H.; Islam, A.; Yu, K. J.; Kim, T.-i.; Chowdhury, R.; Ying, M.; Xu, L.; Li, M.; Chung, H.-J.; Keum, H.; McCormick, M.; Liu, P.; Zhang, Y.-W.; Omenetto, F. G.; Huang, Y.; Coleman, T.; Rogers, J. A. Epidermal Electronics. *Science* **2011,** *333*, 838–843.

4. Tsai, H.; Pitera, J. W.; Miyazoe, H.; Bangsaruntip, S.; Engelmann, S. U.; Liu, C.-C.; Cheng, J. Y.; Bucchignano, J. J.; Klaus, D. P.; Joseph, E. A.; Sanders, D. P.; Colburn, M. E.; Guillorn, M. A. Two-Dimensional Pattern Formation Using Graphoepitaxy of PS-b-PMMA Block Copolymers for Advanced FinFET Device and Circuit Fabrication. *ACS Nano* **2014,** *8*, 5227–5232.

5. Kim, T.-H.; Cho, K.-S.; Lee, E. K.; Lee, S. J.; Chae, J.; Kim, J. W.; Kim, D. H.; Kwon, J.-Y.; Amaratunga, G.; Lee, S. Y.; Choi, B. L.; Kuk, Y.; Kim, J. M.; Kim, K. Full-Colour Quantum Dot Displays Fabricated by Transfer Printing. *Nat. Photonics* **2011,** *5*, 176–182.

6. Kim, B. H.; Onses, M. S.; Lim, J. B.; Nam, S.; Oh, N.; Kim, H.; Yu, K. J.; Lee, J. W.; Kim, J.-H.; Kang, S.-K.; Lee, C. H.; Lee, J.; Shin, J. H.; Kim, N. H.; Leal, C.; Shim, M.; Rogers, J. A. High-Resolution Patterns of Quantum Dots Formed by Electrohydrodynamic Jet Printing for Light-Emitting Diodes. *Nano Lett.* **2015,** *15*, 969–973.

7. Kim, B. H.; Nam, S.; Oh, N.; Cho, S.-Y.; Yu, K. J.; Lee, C. H.; Zhang, J.; Deshpande, K.; Trefonas, P.; Kim, J.-H.; Lee, J.; Shin, J. H.; Yu, Y.; Lim, J. B.; Won, S. M.; Cho, Y. K.; Kim, N. H.; Seo, K. J.; Lee, H.; Kim, T.-I.; Shim, M.; Rogers, J. A. Multilayer Transfer Printing for Pixelated, Multicolor Quantum Dot Light-Emitting Diodes. *ACS Nano* **2016,** *10*, 4920–4925.

8. Park, J.-S.; Kyhm, J.; Kim, H. H.; Jeong, S.; Kang, J.; Lee, S.-E.; Lee, K.-T.; Park, K.; Barange, N.; Han, J.; Song, J. D.; Choi, W. K.; Han, I. K. Alternative Patterning Process for Realization of Large-Area, Full-Color, Active Quantum Dot Display. *Nano Lett.* **2016,** *16*, 6946–6953.

9. Whitesides, G. M. The Origins and the Future of Microfluidics. *Nature* **2006,** *442*, 368–373.

10. Liang, X.; Morton, K. J.; Austin, R. H.; Chou, S. Y. Single Sub-20 nm Wide, Centimeter-Long Nanofluidic Channel Fabricated by Novel Nanoimprint Mold Fabrication and Direct Imprinting. *Nano Lett.* **2007,** *7*, 3774–3780.

11. Rogers, J. A.; Someya, T.; Huang, Y. Materials and Mechanics for Stretchable Electronics. *Science* **2010,** *327*, 1603–1607.

12. Gao, W.; Emaminejad, S.; Nyein, H. Y. Y.; Challa, S.; Chen, K.; Peck, A.; Fahad, H. M.; Ota, H.; Shiraki, H.; Kiriya, D.; Lien, D.-H.; Brooks, G. A.; Davis, R. W.; Javey, A. Fully Integrated Wearable Sensor Arrays for Multiplexed *in Situ* Perspiration Analysis. *Nature* **2016,** *529*, 509–514.

13. Xu, J.; Wang, S.; Wang, G.-J. N.; Zhu, C.; Luo, S.; Jin, L.; Gu, X.; Chen, S.; Feig, V. R.; To, J. W. F.; Rondeau-Gagné, S.; Park, J.; Schroeder, B. C.; Lu, C.; Oh, J. Y.; Wang, Y.; Kim, Y.-H.; Yan, H.; Sinclair, R.; Zhou, D.; Xue, G.; Murmann, B.; Linder, C.; Cai, W.; Tok, J. B. H.;

Chung, J. W.; Bao, Z. Highly Stretchable Polymer Semiconductor Films Through the Nanoconfinement Effect. *Science* **2017,** *355*, 59–64.

14. Kim, J.; Rim, Y. S.; Chen, H.; Cao, H. H.; Nakatsuka, N.; Hinton, H. L.; Zhao, C.; Andrews, A. M.; Yang, Y.; Weiss, P. S. Fabrication of High-Performance Ultrathin In_2O_3 Film Field-Effect Transistors and Biosensors Using Chemical Lift-Off Lithography. *ACS Nano* **2015,** *9*, 4572–4582.

15. Rim, Y. S.; Bae, S.-H.; Chen, H.; Yang, J. L.; Kim, J.; Andrews, A. M.; Weiss, P. S.; Yang, Y.; Tseng, H.-R. Printable Ultrathin Metal Oxide Semiconductor-Based Conformal Biosensors. *ACS Nano* **2015,** *9*, 12174–12181.

16. Limaj, O.; Etezadi, D.; Wittenberg, N. J.; Rodrigo, D.; Yoo, D.; Oh, S.-H.; Altug, H. Infrared Plasmonic Biosensor for Real-Time and Label-Free Monitoring of Lipid Membranes. *Nano Lett.* **2016,** *16*, 1502–1508.

17. Liu, Q.; Aroonyadet, N.; Song, Y.; Wang, X.; Cao, X.; Liu, Y.; Cong, S.; Wu, F.; Thompson, M. E.; Zhou, C. Highly Sensitive and Quick Detection of Acute Myocardial Infarction Biomarkers Using In_2O_3 Nanoribbon Biosensors Fabricated Using Shadow Masks. *ACS Nano* **2016,** *10*, 10117–10125.

18. Hochbaum, A. I.; Aizenberg, J. Bacteria Pattern Spontaneously on Periodic Nanostructure Arrays. *Nano Lett.* **2010,** *10*, 3717–3721.

19. Ul-Haq, E.; Patole, S.; Moxey, M.; Amstad, E.; Vasilev, C.; Hunter, C. N.; Leggett, G. J.; Spencer, N. D.; Williams, N. H. Photocatalytic Nanolithography of Self-Assembled Monolayers and Proteins. *ACS Nano* **2013,** *7*, 7610–7618.

20. Chiappini, C.; De Rosa, E.; Martinez, J. O.; Liu, X.; Steele, J.; Stevens, M. M.; Tasciotti, E. Biodegradable Silicon Nanoneedles Delivering Nucleic Acids Intracellularly Induce Localized *in Vivo* Neovascularization. *Nat. Mater.* **2015,** *14*, 532–539.

21. Moxey, M.; Johnson, A.; El-Zubir, O.; Cartron, M.; Dinachali, S. S.; Hunter, C. N.; Saifullah, M. S. M.; Chong, K. S. L.; Leggett, G. J. Fabrication of Self-Cleaning, Reusable Titania Templates for Nanometer and Micrometer Scale Protein Patterning. *ACS Nano* **2015,** *9*, 6262–6270.

22. Wagner, C.; Harned, N. EUV Lithography: Lithography Gets Extreme. *Nat. Photonics* **2010,** *4*, 24–26.

23. Miszta, K.; Greullet, F.; Marras, S.; Prato, M.; Toma, A.; Arciniegas, M.; Manna, L.; Krahne, R. Nanocrystal Film Patterning by Inhibiting Cation Exchange *via* Electron-Beam or X-Ray Lithography. *Nano Lett.* **2014,** *14*, 2116–2122.

24. Manfrinato, V. R.; Wen, J.; Zhang, L.; Yang, Y.; Hobbs, R. G.; Baker, B.; Su, D.; Zakharov, D.; Zaluzec, N. J.; Miller, D. J.; Stach, E. A.; Berggren, K. K. Determining the Resolution Limits of Electron-Beam Lithography: Direct Measurement of the Point-Spread Function. *Nano Lett.* **2014,** *14*, 4406–4412.

25. Bat, E.; Lee, J.; Lau, U. Y.; Maynard, H. D. Trehalose Glycopolymer Resists Allow Direct Writing of Protein Patterns by Electron-Beam Lithography. *Nat. Commun.* **2015,** *6*, 6654.

26. Volkert, C. A.; Minor, A. M. Focused Ion Beam Microscopy and Micromachining. *MRS Bull.* **2011,** *32*, 389–399.

27. Xu, S.; Liu, G. Y. Nanometer-Scale Fabrication by Simultaneous Nanoshaving and Molecular Self-Assembly. *Langmuir* **1997,** *13*, 127–129.

28. Piner, R. D.; Zhu, J.; Xu, F.; Hong, S. H.; Mirkin, C. A. "Dip-Pen" Nanolithography. *Science* **1999,** *283*, 661–663.

29. Kumar, A.; Whitesides, G. M. Features of Gold Having Micrometer to Centimeter Dimensions Can Be Formed Through a Combination of Stamping with An Elastomeric Stamp and An Alkanethiol ‘‘Ink’’ Followed by Chemical Etching. *Appl. Phys. Lett.* **1993,** *63*, 2002–2004.

30. Xia, Y.; Whitesides, G. M. Soft Lithography. *Angew. Chem. Int. Ed.* **1998,** *37*, 550–575.

31. Srinivasan, C.; Mullen, T. J.; Hohman, J. N.; Anderson, M. E.; Dameron, A. A.; Andrews, A. M.; Dickey, E. C.; Horn, M. W.; Weiss, P. S. Scanning Electron Microscopy of Nanoscale Chemical Patterns. *ACS Nano* **2007,** *1*, 191–201.

32. Qin, D.; Xia, Y.; Whitesides, G. M. Soft Lithography for Micro- and Nanoscale Patterning. *Nat. Protoc.* **2010,** *5*, 491–502.

33. Xia, Y. N.; McClelland, J. J.; Gupta, R.; Qin, D.; Zhao, X. M.; Sohn, L. L.; Celotta, R. J.; Whitesides, G. M. Replica Molding Using Polymeric Materials: A Practical Step Toward Nanomanufacturing. *Adv. Mater.* **1997,** *9*, 147–149.

34. Tian, C.; Kim, H.; Sun, W.; Kim, Y.; Yin, P.; Liu, H. DNA Nanostructures-Mediated Molecular Imprinting Lithography. *ACS Nano* **2017,** *11*, 227–238.

35. Chou, S. Y.; Krauss, P. R.; Renstrom, P. J. Imprint Lithography with 25-Nanometer Resolution. *Science* **1996,** *272*, 85–87.

36. Huo, F.; Zheng, Z.; Zheng, G.; Giam, L. R.; Zhang, H.; Mirkin, C. A. Polymer Pen Lithography. *Science* **2008,** *321*, 1658–1660.

37. Shim, W.; Braunschweig, A. B.; Liao, X.; Chai, J.; Lim, J. K.; Zheng, G.; Mirkin, C. A. Hard-Tip, Soft-Spring Lithography. *Nature* **2011,** *469*, 516–520.

38. Zhong, X.; Bailey, N. A.; Schesing, K. B.; Bian, S.; Campos, L. M.; Braunschweig, A. B. Materials for the Preparation of Polymer Pen Lithography Tip Arrays and A Comparison of Their Printing Properties. *J. Polym. Sci. A: Polym. Chem.* **2013,** *51*, 1533–1539.

39. Liao, X.; Huang, Y.-K.; Mirkin, C. A.; Dravid, V. P. High Throughput Synthesis of Multifunctional Oxide Nanostructures within Nanoreactors Defined by Beam Pen Lithography. *ACS Nano* **2017,** *11*, 4439–4444.

40. Xue, Y.; Kang, D.; Ma, Y.; Feng, X.; Rogers, J. A.; Huang, Y. Collapse of Microfluidic Channels/Reservoirs in Thin, Soft Epidermal Devices. *Extreme Mech. Lett.* **2017**, 18–23.

41. Jeon, S.; Menard, E.; Park, J. U.; Maria, J.; Meitl, M.; Zaumseil, J.; Rogers, J. A. Three-Dimensional Nanofabrication with Rubber Stamps and Conformable Photomasks. *Adv. Mater.* **2004,** *16*, 1369–1373.

42. Childs, W. R.; Nuzzo, R. G. Decal Transfer Microlithography: A New Soft-Lithographic Patterning Method. *J. Am. Chem. Soc.* **2002,** *124*, 13583–13596.

43. Xu, Q. B.; Rioux, R. M.; Dickey, M. D.; Whitesides, G. M. Nanoskiving: A New Method to Produce Arrays of Nanostructures. *Acc. Chem. Res.* **2008,** *41*, 1566–1577.

44. James, C. D.; Davis, R. C.; Kam, L.; Craighead, H. G.; Isaacson, M.; Turner, J. N.; Shain, W. Patterned Protein Layers on Solid Substrates by Thin Stamp Microcontact Printing. *Langmuir* **1998,** *14*, 741–744.

45. Bernard, A.; Renault, J. P.; Michel, B.; Bosshard, H. R.; Delamarche, E. Microcontact Printing of Proteins. *Adv. Mater.* **2000,** *12*, 1067–1070.

46. Vaish, A.; Shuster, M. J.; Cheunkar, S.; Weiss, P. S.; Andrews, A. M. Tuning Stamp Surface Energy for Soft Lithography of Polar Molecules to Fabricate Bioactive Small-Molecule Microarrays. *Small* **2011,** *7*, 1471–1479.

47. Xia, Y.; Zhao, X.-M.; Kim, E.; Whitesides, G. M. A Selective Etching Solution for Use with Patterned Self-Assembled Monolayers of Alkanethiolates on Gold. *Chem. Mater.* **1995,** *7*, 2332–2337.

48. Delamarche, E.; Schmid, H.; Bietsch, A.; Larsen, N. B.; Rothuizen, H.; Michel, B.; Biebuyck, H. Transport Mechanisms of Alkanethiols During Microcontact Printing on Gold. *J. Phys. Chem. B* **1998,** *102*, 3324–3334.

49. Mullen, T. J.; Srinivasan, C.; Hohman, J. N.; Gillmor, S. D.; Shuster, M. J.; Horn, M. W.; Andrews, A. M.; Weiss, P. S. Microcontact Insertion Printing. *Appl. Phys. Lett.* **2007,** *90*, 063114.

50. Dameron, A. A.; Hampton, J. R.; Smith, R. K.; Mullen, T. J.; Gillmor, S. D.; Weiss, P. S. Microdisplacement Printing. *Nano Lett.* **2005,** *5*, 1834–1837.

51. Andrews, A. M.; Liao, W.-S.; Weiss, P. S. Double-Sided Opportunities Using Chemical Lift-Off Lithography. *Acc. Chem. Res.* **2016,** *49*, 1449–1457.

52. Liao, W.-S.; Cheunkar, S.; Cao, H. H.; Bednar, H. R.; Weiss, P. S.; Andrews, A. M. Subtractive Patterning *via* Chemical Lift-Off Lithography. *Science* **2012,** *337*, 1517–1521.

53. Saavedra, H. M.; Mullen, T. J.; Zhang, P. P.; Dewey, D. C.; Claridge, S. A.; Weiss, P. S. Hybrid Strategies in nanolithography. *Rep. Prog. Phys.* **2010,** *73*, 036501.

54. Srinivasan, C.; Mullen, T. J.; Hohman, J. N.; Anderson, M. E.; Dameron, A. A.; Andrews, A. M.; Dickey, E. C.; Horn, M. W.; Weiss, P. S. Scanning Electron Microscopy of Nanoscale Chemical Patterns. *ACS Nano* **2007,** *1* (3), 191–201.

55. Shuster, M. J.; Vaish, A.; Cao, H. H.; Guttentag, A. I.; McManigle, J. E.; Gibb, A. L.; Martinez, M. M.; Nezarati, R. M.; Hinds, J. M.; Liao, W. S.; Weiss, P. S.; Andrews, A. M.

Patterning Small-Molecule Biocapture Surfaces: Microcontact Insertion Printing *vs.* Photolithography. *Chem. CommUN.* **2011,** *47*, 10641–10643.

56. Claridge, S. A.; Liao, W. S.; Thomas, J. C.; Zhao, Y.; Cao, H. H.; Cheunkar, S.; Serino, A. C.; Andrews, A. M.; Weiss, P. S. From the Bottom Up: Dimensional Control and Characterization in Molecular Monolayers. *Chem. Soc. Rev.* **2013,** *42*, 2725–2745.

57. Cao, H. H.; Nakatsuka, N.; Serino, A. C.; Liao, W.-S.; Cheunkar, S.; Yang, H.; Weiss, P. S.; Andrews, A. M. Controlled DNA Patterning by Chemical Lift-Off Lithography: Matrix Matters. *ACS Nano* **2015,** *9*, 11439–11454.

58. Hui, C. Y.; Jagota, A.; Lin, Y. Y.; Kramer, E. J. Constraints on Microcontact Printing Imposed by Stamp Deformation. *Langmuir* **2002,** *18*, 1394–1407.

59. Sharp, K. G.; Blackman, G. S.; Glassmaker, N. J.; Jagota, A.; Hui, C. Y. Effect of Stamp Deformation on the Quality of Microcontact Printing: Theory and Experiment. *Langmuir* **2004,** *20*, 6430–6438.

60. Hsia, K. J.; Huang, Y.; Menard, E.; Park, J. U.; Zhou, W.; Rogers, J.; Fulton, J. M. Collapse of Stamps for Soft Lithography Due to Interfacial Adhesion. *Appl. Phys. Lett.* **2005,** *86*, 154106.

61. Huang, Y. G. Y.; Zhou, W. X.; Hsia, K. J.; Menard, E.; Park, J. U.; Rogers, J. A.; Alleyne, A. G. Stamp Collapse in Soft Lithography. *Langmuir* **2005,** *21*, 8058–8068.

62. Zhou, W.; Huang, Y.; Menard, E.; Aluru, N. R.; Rogers, J. A.; Alleyne, A. G. Mechanism for Stamp Collapse in Soft Lithography. *Appl. Phys. Lett.* **2005,** *87*, 251925.

63. Xue, Y.; Zhang, Y.; Feng, X.; Kim, S.; Rogers, J. A.; Huang, Y. A Theoretical Model of Reversible Adhesion in Shape Memory Surface Relief Structures and Its Application in Transfer Printing. *J. Mech. Phys. Solids* **2015,** *77*, 27–42.

64. Huh, D.; Mills, K. L.; Zhu, X.; Burns, M. A.; Thouless, M. D.; Takayama, S. Tuneable Elastomeric Nanochannels for Nanofluidic Manipulation. *Nat. Mater.* **2007,** *6*, 424–428.

65. Park, S. M.; Huh, Y. S.; Craighead, H. G.; Erickson, D. A Method for Nanofluidic Device Prototyping Using Elastomeric Collapse. *Proc. Natl. Acad. Sci.* **2009,** *106*, 15549–15554.

66. Armani, D.; Liu, C.; Aluru, N. Re-Configurable Fluid Circuits by PDMS Elastomer Micromachining. *Proc. IEEE MEMS99* **1999**, 222–227.

67. Carrillo, F.; Gupta, S.; Balooch, M.; Marshall, S. J.; Marshall, G. W.; Pruitt, L.; Puttlitz, C. M. Nanoindentation of Polydimethylsiloxane Elastomers: Effect of Crosslinking, Work of Adhesion, and Fluid Environment on Elastic Modulus. *J. Mater. Res.* **2011,** *20*, 2820–2830.

68. Johnston, I. D.; McCluskey, D. K.; Tan, C. K. L.; Tracey, M. C. Mechanical Characterization of Bulk Sylgard 184 for Microfluidics and Microengineering. *J. Micromech. Microeng.* **2014,** *24*, 035017.

69. Cao, H. H.; Nakatsuka, N.; Liao, W.-S.; Serino, A. C.; Cheunkar, S.; Yang, H.; Weiss, P. S.; Andrews, A. M. Advancing Biocapture Substrates *via* Chemical Lift-Off Lithography. *Chem. Mater.* **2017,** *29*, 6829–6839.

Chapter 5

Multiple-Patterning Nanosphere Lithography for Fabricating Periodic Three-Dimensional Hierarchical Nanostructures

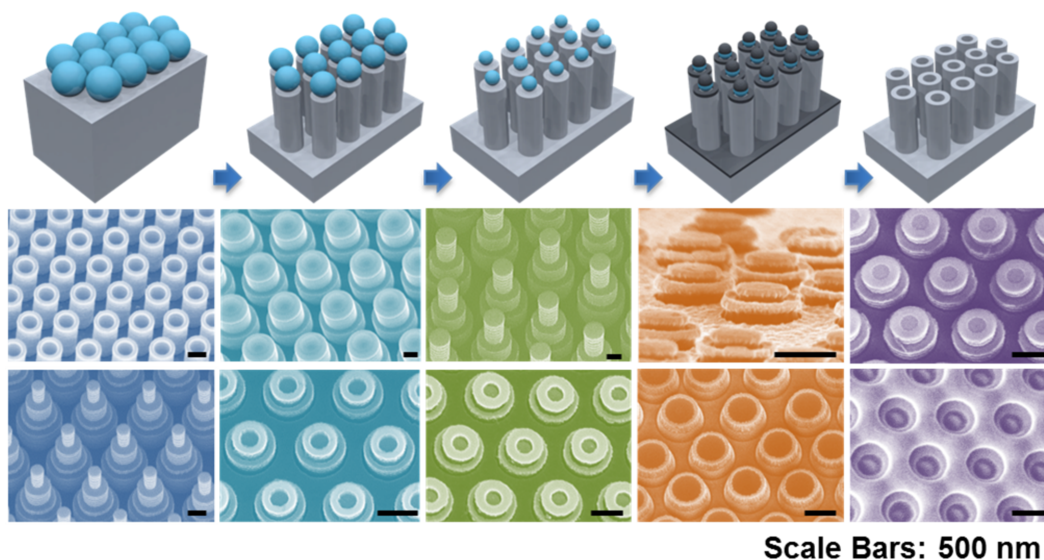

The information in this chapter was published in

ACS Nano **2017**, *11*, 10384-10391 and has been reproduced here.

Authors: Xu, X.; **Yang, Q.**; Wattanatorn, N.; Zhao, C.; Chiang, N.; Jonas, S. J.; Weiss, P. S.

5.1 Abstract

While three-dimensional (3D) configurable hierarchical nanostructures have wide ranging applications in electronics, biology, and optics, finding scalable approaches remains a challenge. We report a robust and general strategy called multiple-patterning nanosphere lithography (MP-NSL) for the fabrication of periodic 3D hierarchical nanostructures in a highly scalable and tunable manner. This nanofabrication technique exploits the selected and repeated etching of polymer nanospheres that serve as resists and that can be shaped in parallel for each processing step. The application of MP-NSL enables the fabrication of periodic, vertically aligned Si nanotubes at the wafer scale with nanometer-scale control in three dimensions including outer/inner diameters, heights/hole-depths, and pitches. The MP-NSL method was utilized to construct 3D periodic hierarchical hybrid nanostructures such as multilevel solid/hollow nanotowers where the height and diameter of each level of each structure can be configured precisely as well as 3D concentric plasmonic nanodisk/nanorings with tunable optical properties on a variety of substrates.

5.2 Introduction

Periodic semiconductor nanostructures, such as pyramids, holes, wires, pillars, tubes, and cones are increasingly applied in the design of solar cells, biosensors, biomaterials, and drug-delivery systems due to their superior optical/electrical properties, biocompatibility, and mechanical properties.[1-10] In particular, periodic single-crystalline silicon (Si) nanotubes[11] assembled *via* electron-beam lithography and nanoimprint lithography demonstrate better light conversion efficiency than other structures in hybrid solar cells, while their biocompatibility[12] and tubular structures also suggest their tantalizing potential as tools to enable improved studies of cellular mechanics,[13-15] circulating tumor cell capture/release,[16] and intracellular biochemical delivery.[17,18] However, despite this interest and their broad applicability, the deployment of periodic Si-nanotube-based devices with controlled dimensions has been limited by the lack of simple and scalable fabrication approaches for these structures.

Current strategies for the fabrication of periodic Si nanostructures, including nanopillars, nanocones, and nanoholes, involve nanosphere lithography,[19-25] because of its low cost, simplicity, and high throughput compared to conventional nanolithographic methods including electron-beam lithography and focused ion beam milling. Nanosphere lithography employs periodic arrays of self-assembled close-packed mono-/bilayer nanospheres (*e.g.,* polystyrene, SiO_2, and others) as masks to pattern underlying substrate materials.[19] However, the fabrication of periodic Si nanotubes with precise dimensional control over large areas remains challenging due primarily to the nanosphere template being used only once during processing. This "*one-time* use" approach restricts traditional nanosphere lithography techniques in that only the outer diameter of Si nanotubes can be defined fully. For example, previous attempts to generate

nanoring-like masks for Si nanotube fabrication lacked suitable control over dimensions (such as tube thickness), quality, and reproducibility.

In this work, we propose and demonstrate a nanosphere lithography strategy named multiple-patterning nanosphere lithography (MP-NSL), which circumvents the limitations of traditional one-time use methods by adopting a multiple use template concept. The MP-NSL method achieves wafer-scale fabrication of periodic Si nanotubes while enabling independent control over all structural dimensions during fabrication including inner/outer tube diameters, heights, hole-depths, and pitches. To our knowledge, this degree of versatility and precision has not previously been reported for structures prepared *via* nanosphere lithography. Moreover, our MP-NSL technique represents a powerful three-dimensional (3D) nanolithographic tool for high-throughput fabrication of periodic hierarchical nanoarchitectures, enabling the assembly of multilevel solid/hollow Si nanotowers and 3D concentric plasmonic nanodisk/nanorings.

5.3 Materials and Methods

Materials. Prime quality 4″ Si (100) wafers (P/B, 1-10 ohm-cm resistivity) were purchased from University Wafer (Boston, MA, USA). All polystyrene spheres (1% solids, 400 nm to 2 μm) were purchased from Thermo Fisher Scientific Inc. (Fremont, CA, USA). Sodium dodecyl sulfate (SDS, 98%) was purchased from Sigma-Aldrich (St. Louis, MO, USA). Hydrochloric acid (36.5 to 38.0% w/w) was purchased from Fisher Scientific Inc. (Fair Lawn, NJ, USA). Evaporation materials including gold (99.99%) and nickel (99.995%) were purchased from K. J. Lesker Company (Jefferson Hills, PA, USA).

Morphology characterization. The scanning electron micrographs were taken by a Zeiss Supra 40VP scanning electron microscope. Focused ion beam samples were made and imaged using the Nova 600 SEM/FIB system.

Polystyrene sphere monolayer formation on Si substrates. The polystyrene nanospheres (1% solids) stock dispersion were centrifuged and re-dispersed in water/ethanol mixture (1:1 ratio) with 2-4% solids. A 2 cm × 2 cm Si substrate and a 22 mm × 22 mm glass coverslip were treated in an oxygen plasma (Harrick Plasma, Ithaca, NY) for 1 min to generate hydrophilic surfaces. Next, the Si substrate was put in a 2" petri dish, ~4 mL water was added to immerse the Si substrate fully, and then ~50 μL 1 wt% SDS was added. The polystyrene nanosphere dispersion in water/ethanol was slowly added to the water/air interface through a tilted glass coverslip that was placed against the edge of the petri dish to form close-packed monolayers. Then, the water was removed to transfer the polystyrene nanosphere monolayers to the surface of Si substrate. Finally, the Si substrate was dried in a vacuum desiccator.

Oxygen plasma RIE of polystyrene nanospheres. An Oxford 80 Plus system was used to tailor the size of polystyrene nanospheres. A time-controlled etching process of the polystyrene

nanospheres was carried out under a gas mixture of O_2 (35 sccm) and Ar (10 sccm) at a pressure of 60 mTorr and radio frequency power of 60 W. The polystyrene-nanosphere-coated Si substrate was heated at 120 °C for ~30 s to fix nanospheres on the Si substrate.

Deep reactive ion etching of silicon. (1) Bosch process. An inductively coupled plasma reactive ion etcher (ICP-RIE, Plasma Therm SLR700) was used. It involved alternate cycles of passivation and etching steps. During the passivation step, a flow of 24 sccm C_4F_8 and 12 sccm Ar was used at power of 825 W. During the etching step, a flow of 30 sccm SF_6 and 12 sccm Ar was used at power of 825 W. (2) Single-step dry etching**.** The single-step RIE of silicon was completed in a simultaneous flow of 24 sccm C_4F_8, 21 sccm SF_6, and 5 sccm Ar at a pressure of 12 mTorr with ICP power of 650 W and platen power of 9 W (STS Advanced Oxide Etcher) to achieve silicon pillars/tubes with smooth sidewalls. For both processes, the etching depth of Si was controlled by the etching time.

Fabrication of SiO_2 hierarchical nanostructures. SiO_2/Si (500-nm-thick SiO_2) substrates with polystyrene nanoparticles as the masks were etched by an Oxford 80 Plus using a gas mixture of CHF_3 (25 sccm) and Ar (25 sccm) at 35 mTorr to generate the SiO_2 hierarchical nanostructures.

Pattern replication to PDMS substrates. A 10:1 mass ratio of Sylgard® 184 elastomer silicone elastomer base and curing agent were thoroughly mixed and then degassed in a vacuum desiccator. This mixture was poured onto the Si mold with hierarchical nanostructures and cured overnight at 65 °C. After curing, PDMS stamps were carefully removed from the Si mold.

Metal coating. Desirable substrates were loaded into the vacuum chamber of an electron beam metal evaporator (Kurt J. Lesker Company, Jefferson Hills, PA) and held at a base pressure

of 1×10^{-7} Torr. Ni film was deposited at rate of ~1 Å/s, and Au film was deposited at rate of ~0.5 Å/s.

5.4 Results and Discussions

The process for fabricating periodic Si nanotubes by MP-NSL is illustrated schematically in **Figure 5.1A** with associated scanning electron microscopy (SEM) images of the products from key steps shown in **Figure 5.1B-G**. We fabricated a variety of Si nanotube arrays with different parameters: pitches (400 nm to 2 μm), outer heights (100 nm to 6 μm), inner heights (100 nm to 2 μm), outer diameters (220 nm to 1.3 μm), inner diameters (130 to 1050 nm), and tube thicknesses (sub-50 to 500 nm). Representative SEM images of a selection of Si nanotubes are depicted in **Figure 5.2**. In addition, SEM images of large area, well-ordered nanosphere templates and Si nanotube arrays with the corresponding Fourier transform patterns are shown in **Figures S5.1** and **S5.2**.

The template for MP-NSL consists of a monolayer of polystyrene nanospheres, which is assembled by slowly distributing an aqueous dispersion of the nanospheres drop cast onto a tilted glass slide, as reported elsewhere.[20] The monolayer is then transferred to a 2 cm × 2 cm Si substrate underneath the water/air interface by gently removing the liquid. Note that the pitch of the final Si nanotube arrays is determined by the original diameters of the polystyrene nanosphere template, which can be tailored from several hundred nanometers to several microns depending on their original size. Here, we specifically chose polystyrene nanospheres with diameters of 400 nm, 600 nm, 900 nm, 1 μm, and 2 μm as examples. The assembly of the nanosphere template is highly scalable such that one can easily reach the wafer scale manually and can conceivably reach the square meter scale using automated nanosphere dispensing systems.[26]

Next, the diameters of the polystyrene nanospheres are configured *via* oxygen plasma reactive ion etching (RIE) to define the outer diameter (d_o) of the Si nanotubes. By controlling

the oxygen plasma RIE time, one can tailor the nanosphere diameter precisely without changing the pitch. For instance, a 4-min oxygen plasma RIE can uniformly and precisely etch close-packed polystyrene spheres of 1 μm diameter into ~820 nm diameter nanospheres with identical spacing of ~180 nm, as shown in **Figure 5.1C**. As illustrated in **Figure 5.2D** and **Table 5.1,** the oxygen plasma RIE time and the diameters of polystyrene nanospheres correlate closely and the results are highly reproducible. The diameters of the nanospheres notably decrease faster with increasing oxygen plasma RIE time due to the polymer nanoparticles becoming flatter with a more oblate ellipsoid shape (**Figure S5.4**).[27]

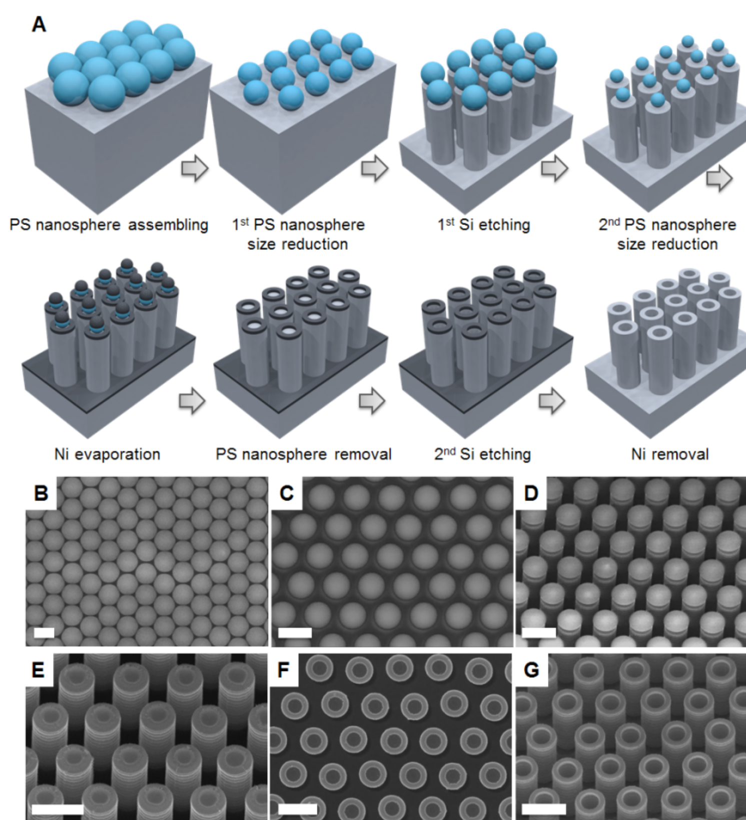

Figure 5.1. Self-aligned multiple-patterning nanosphere lithography (MP-NSL) for Si nanotube arrays. (A) A schematic illustration of the process. Step 1: a monolayer of close-packed polystyrene (PS) nanospheres is formed at a water/air interface, then transferred onto a Si wafer. The size of the nanospheres defines the ultimate pitches (*p*) of

the Si nanotubes. Step 2: oxygen plasma RIE reduces the sphere size and defines the outer diameters (d_o) of Si nanotubes. Step 3: deep reactive ion etching (DRIE) etches Si into nanopillars by using the nanospheres as masks. The outer heights (h_o) of Si nanotubes are controlled by the etch time. Step 4: a second oxygen plasma RIE further reduces the sizes of polymer nanoparticles and defines the inner diameters (d_i) of Si nanotubes. Step 5: Ni is deposited to form Ni nanorings on the Si nanopillars and it functions as a DRIE mask. Step 6: polystyrene nanoparticles are removed by 10 min oxygen plasma etching to expose the center part of the Si nanopillars. Step 7: DRIE is performed again to etch holes and to define the hole depth (h_i). Step 8: Ni is removed by HCl and pristine Si nanotube arrays are obtained. Scanning electron microscope (SEM) images of key intermediates: (B) monolayer of closed-packed polystyrene nanospheres (diameter: 1 µm) formed on a Si wafer; (C) polystyrene nanoparticles on Si wafer after first size reduction; (D) polystyrene nanoparticles on top of periodic Si nanopillar arrays; (E) second size reduction of polystyrene nanoparticles by oxygen plasma (step 4); and (F) Ni nanorings on top of Si nanopillars. The region displayed as dark is Si and the region displayed as bright is Ni. (G) Etching of the inner regions by DRIE to form Si nanotubes (step 7). Images (D, E, G) were taken at a tilt of 30°. Scale bars: 1 µm.

Table 5.1. Controlling size reduction of polystyrene nanospheres by oxygen plasma reactive ion etching (RIE).

Pitch = 1 µm		Pitch = 2 µm	
Etch time	d_o	**Etch time**	d_o
2.5 min	910 ± 4 nm	4 min	1860 ± 9 nm
3 min	900 ± 4 nm	7 min	1630 ± 8 nm
3.5 min	860 ± 6 nm	10 min	1350 ± 10 nm
4 min	820 ± 5 nm	13 min	1160 ± 9 nm
5 min	760 ± 7 nm	15 min	800 ± 10 nm
6 min	610 ± 7 nm	16 min	740 ± 8 nm
7 min	480 ± 5 nm		
8 min	330 ± 6 nm		

Note that enhancing the adhesion between the polystyrene nanospheres and the underlying Si substrate before dry etching helps to prevent the random tilting of the etched polymer nanoparticles, which could lead to asymmetries in the final pillar/nanotube arrays (**Figure S5.5**). The nanospheres were coupled to the Si substrate after the initial oxygen RIE step by heating briefly to 120 °C for ~30 seconds. This treatment does not result in noticeable lateral deformation, but appears to fix the etched polymer nanoparticles to prevent moving or tilting during the subsequent processes.

Methods for etching Si involve either wet-etching strategies such as metal-assisted chemical etching[28] or dry-etching approaches such as RIE.[9] Here, we chose a dry-etching technique, specifically deep reactive ion etching (DRIE), due to its capability for anisotropic etching, high reproducibility, and non-toxicity. The outer heights ($\boldsymbol{h_o}$) and inner hole-depths ($\boldsymbol{h_i}$) of the Si nanotubes are controlled by the DRIE time. Specifically, DRIE *via* the Bosch process, which consists of multiple cycles of passivation and etching, was applied to achieve high-aspect-ratio nanopillars. The alternating cycles of passivation and etching in the Bosch process protects the sidewalls of nanostructures from being etched laterally over large depths. **Figure 5.1D** illustrates a typical array of high-aspect-ratio Si nanopillars produced *via* MP-NSL with polystyrene nanoparticles sitting on their tops (h_o = 2000 nm). The Bosch process typically results in periodic "ripples" on the sidewalls as shown in **Figure 5.2**, which is called the "scalloping effect". As shown in the high-resolution SEM image in **Figure S5.6**, the thickness of the "ripple" is typically ~25 nm. Note that the top surfaces of the silicon nanopillars remain smooth, as they were protected by the PS bead template during etching. However, the "scalloping effect" can be minimized and/or eliminated in MP-NSL by using an optimized Bosch process[29] or cryogenic-DRIE[30] to generate Si nanostructures with smooth sidewalls. In the present study, low-aspect-ratio Si nanostructures with smooth sidewalls were achieved straightforwardly *via* single-step DRIE, which uses C_4F_8 and SF_6 simultaneously as the etching and passivation gases (**Figures 5.2G-H** and **S5.7**).

After the fabrication of Si nanopillars, a second oxygen plasma RIE was applied to reduce the size of the polystyrene nanoparticles sitting on top of the pillars (**Figure 5.1D**). The smaller nanospheres remain centered on the pillars and serve as templates for subsequent etching treatments to obtain nanotubes. Next, a thin layer of nickel (Ni) was deposited *via* electron-beam

evaporation along the exposed Si at the tops of the nanopillars to avoid undesired etching. Nickel was selected as the masking material as it is highly resistant to Si dry etching processes. The thin Ni layer, typically 20 nm, forms Ni nanorings at the top of the nanopillars and also covers the bottom surface of the Si substrate, **Figure 5.1E**. The polymer nanoparticles are subsequently removed with tape to expose the centers of the Si pillars for etching **Figure 5.1F**. The inner-diameters of the Ni nanorings define the inner diameter (d_i) and sidewall thickness ($w = d_o - d_i$) of nanotubes generated after a second round of DRIE. The Ni is then removed *via* a chemical etch treatment (5% HCl) to obtain the final Si nanotube arrays (**Figure 5.1G**).

As illustrated in **Figure 5.3A**, altering the time of the second oxygen plasma RIE step enables the inner diameter d_i and thus the sidewall thickness w of the Si nanotubes to be tuned precisely. As a proof of concept, we fabricated a series of Si nanotubes by using 1 μm and 2 μm polystyrene spheres as masks for MP-NSL. We first fabricated Si nanopillars with diameters of 730 ± 7 nm and 1340 ± 12 nm using the 1 μm and 2 μm polystyrene spheres masks, respectively. Then, we varied the second oxygen plasma RIE time to control the diameter of the polystyrene nanoparticles on top of the Si nanopillars and applied a second DRIE treatment as described above to generate ordered Si nanotubes with different sidewall thicknesses. As shown in the **Tables 5.1** and **5.2**: for Si nanopillars with d_o = 720 nm, a second oxygen plasma RIE time of 3, 3.25, 3.5, 4, and 4.5 min, resulted in sidewall thicknesses of 105 ± 5, 120 ± 4, 150 ± 5, 200 ± 5, and 290 ± 7 nm, respectively, while for 1340 ± 12 nm diameter Si nanopillars, oxygen plasma RIE times of 3-7 min resulted sidewall thicknesses ranging from 120 ± 12 to 420 ± 8 nm. Even smaller sidewall thickness, such as 45 ± 2, 80 ± 2, 100 ± 3 nm, can be achieved by further decreasing the RIE time difference, see **Figure 5.2F-H**. Such high accuracy control over the nanosphere size is comparable to many electron- or ion-beam-based nanolithographies.

Table 5.2. Controlling sidewall thicknesses (*w*) of Si nanotubes by varying the etch time difference between two oxygen plasma reactive ion etching.

Pitch = 1 µm		Pitch = 2 µm	
Etch time	***w***	**Etch time**	***w***
3 min	105 ± 5 nm	3 min	120 ± 12 nm
3.25 min	120 ± 5 nm	4 min	180 ± 7 nm
3.5 min	150 ± 5 nm	5 min	250 ± 8 nm
4 min	200 ± 9 nm	5.5 min	300 ± 8 nm
4.5 min	290 ± 7 nm	6 min	340 ± 9 nm
		7 min	420 ± 8 nm

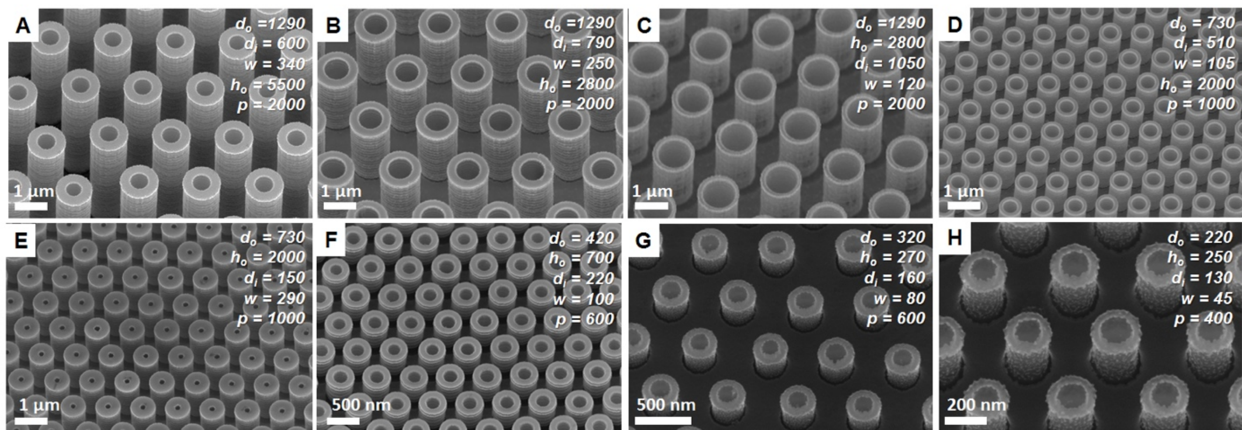

Figure 5.2. (A-H) Scanning electron micrographs (SEM) of representative periodic Si nanotube arrays with different parameters in nm: pitch (p), outer diameter (d_o), inner diameter (d_i), sidewall thickness ($w = (d_o - d_i)/2$), and outer height (h_o). Images were recorded at a tilt of 30°. (Units: nm)

The outer height (h_o) and inner hole depth (h_i) of the Si nanotubes can be controlled independently by varying their respective DRIE times. The SEM cross-sectional images shown in **Figure 5.3F** illustrate three representative Si nanotube arrays with different h_o/h_i ratios, where from left to the right, $h_o > h_i$, $h_o = h_i$ (center), and $h_o < h_i$. The DRIE etching rates used for each h_o and h_i are shown in **Figure 5.3G** and **Table 5.3**. Specifically, an etch rate of 0.66 μm/min was used for h_o while rates of 0.50 μm/min (0-3 min) and 0.18 μm/min (3-8 min) were used for h_i. A slower etch rate is observed for h_i, which is known as "RIE lag", *i.e.*, the etching rate is related to the feature size, and the smaller the feature size, the lower the etching rate.[31]

Table 5.3. Tuning the outer/inner heights (h_o/h_i) of Si nanotubes by controlling the duration of deep reactive ion etching.

Etch time	h_o	Etch time	h_i
1 min	700 ± 25 nm	2 min	1100 ± 20 nm
3 min	2000 ± 28 nm	3 min	1500 ± 25 nm
4 min	2800 ± 32 nm	4 min	1700 ± 30 nm
6 min	4000 ± 38 nm	6 min	2000 ± 20 nm
8 min	5200 ± 50 nm	8 min	2410 ± 28 nm

The robust and rapid fabrication of periodic 3D hierarchical nanostructures is highly desirable for applications in nanophotonics, metamaterials, and biotechnology.[32] Direct writing fabrication strategies based on two-photon,[33] focused ion-beam, or electron-beam[34] techniques have been developed to assemble 3D hierarchical micro-/nanostructures serially, but their

widespread use within these areas has been precluded by low fabrication throughputs and a limited selection of compatible materials.

We find that MP-NSL can serve as a high-throughput 3D nanolithographic tool to fabricate a variety of periodic 3D hierarchical nanostructures. For example, as shown in **Figure 5.4A**, multilevel Si nanopillars or "nanotowers" with two, three, and four levels were fabricated by reducing the polystyrene nanosphere size twice, three, and four times, respectively, with Si etching applied after each size reduction. A high-resolution SEM image (**Figure S5.6**) of multilevel silicon nanotowers shows all the levels have smooth surfaces. The smallest diameters at the apex of the Si nanotowers achieved so far are ~100 nm when using 900 nm nanospheres templates. The sidewall thickness (w) and height (h) of *each* level were controlled individually and precisely by varying the oxygen plasma RIE and DRIE times during processing (**Figure 5.4A**). In principle, there is no limitation to the complexity of the nanostructures generated *via* MP-NSL. Potential applications for these multilevel nanotowers include nanobarcodes[35] and anti-reflective coatings.[36] It is also possible to fabricate hollow Si nanotowers by integrating the etching processes used to generate Si nanotubes above. Moreover, we have applied MP-NSL to pattern similar nanotowers with a wide range of materials, including SiO_2, and have used the nanostructures as a mold for soft materials, such as polydimethylsiloxane (PDMS) (**Figure 5.4A**).[37-39]

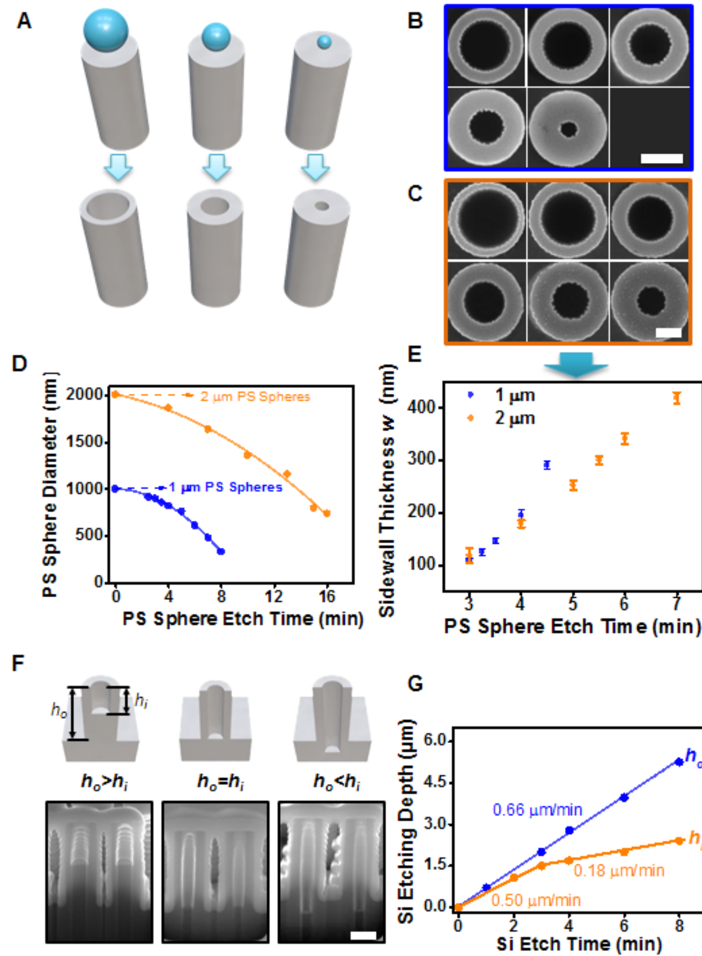

Figure 5.3. (A) Schematic illustration of tuning the outer and inner diameters (d_o and d_i, respectively) of Si nanotubes. (B) Top-view scanning electron microscopy (SEM) images of Si nanotubes fabricated from 1 µm polystyrene nanospheres with $d_o = 730 \pm 7$ nm, and sidewall width ($w=(d_o-d_i)/2$) from 105 ± 5 nm to 290 ± 7 nm (scale bar: 400 nm); (C) Top-view SEM images of Si nanotubes fabricated from 2 µm polystyrene (PS) nanospheres with $d_o = 1340 \pm 12$ nm, and w from 120 ± 12 nm to 420 ± 8 nm (scale bar: 400 nm). (D) Oxygen plasma reactive ion etching (RIE) time dependent size reduction of polystyrene nanoparticles. (E) Oxygen plasma RIE time dependent w corresponding to (B,C) with $d_o = 1340 \pm 12$ nm. (F) Schematic illustrations of independent control of h_o and h_i. From left

to right, $h_o > h_i$, $h_o = h_i$, and $h_o < h_i$. Bottom: SEM images of corresponding Si nanotube cross-sections prepared by focused ion beam milling with Pt (white part) as protection layer (scale bar: 500 nm). (G) Plot of DRIE time dependence of h_o and h_i. Si etch rates were 0.66 µm/min for h_o and 0.50 µm/min (0-3 min)/ 0.18 µm/min (3-8 min) for h_i, respectively.

Plasmonic nanostructures have attracted broad interest, including for potential applications ranging from biosensing and surface-enhanced spectroscopy to optical trapping.[40-46] So far, most plasmonic nanostructures fabricated by nanolithography have been largely two-dimensional. Our 3D nanostructures can further serve as templates for achieving periodic 3D hierarchical plasmonic nanostructures, important for engineering nanophotonics in 3D.[47-49] Simply by evaporating a layer of a plasmonic metal (*e.g.,* gold, silver, aluminum), onto an array of periodic Si/SiO_2/PDMS nanotowers, we obtained periodic 3D plasmonic nanostructures (**Figure 5.4A**). After Au evaporation, high-resolution SEM imaging reveals that each layer of the nanotower structures is smooth (**Figure S5.8**). The dimensions of these Au nanorings and Au nanodisks as well as the relative vertical distances between them are fully tunable with sub-20-nm-scale resolution, which presents the tantalizing possibility to design and to manipulate the optical properties of these periodic 3D plasmonic nanostructures. For example, we evaporated 50 nm of Au on two slightly different two-level Si nanotowers as shown in **Figure 5.4B**, and fully tunable 3D ring/disk plasmonic nanocavities were thereby fabricated. As shown in the reflection spectra of these vertically stacked plasmonic nanostructures, multiple resonant peaks ranged from visible to mid-IR were observed. The reflection spectra agree well with finite-difference-time-domain (FDTD) simulations. The simulation results indicate that multiple peaks and dips result from multimodal plasmonic resonances through hybridization between different plasmonic multipole modes of ring and disk cavities vertically FDTD

simulations of the electric-field and charge distributions are provided in **Figure S5.9**). Slight, intentional geometry differences between the two plasmonic nanostructures (sample i *vs*. sample ii) result in shifts in the reflection spectra due to changes of the resonance (**Figure 5.4B**). Thus, MP-NSL is a tool to design and to fabricate optically tunable 3D plasmonic nanostructures.

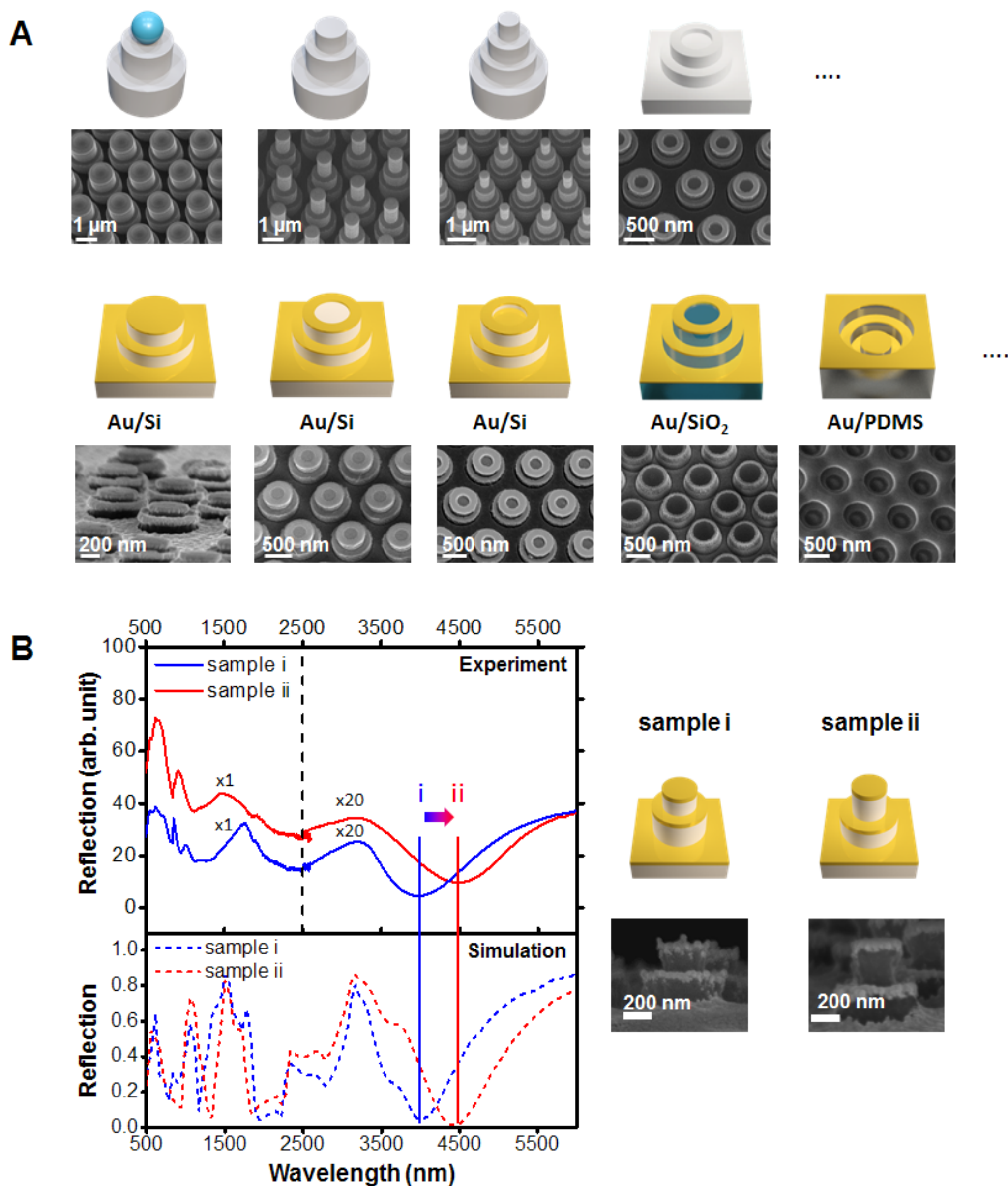

Figure 5.4. (A) By using multiple-patterning nanosphere lithography, a variety of periodic hierarchical nanostructures have been designed and fabricated: Si nanotowers with two

levels, three levels, and four levels with tunable heights (including negative heights for selected levels) and diameters for each level; configurable concentric plasmonic Au nanorings/nanodisk on Si substrates (solid/hollow two-level nanotowers), SiO_2 nanostructures (two-level nanotowers), and flexible polydimethylsiloxane (PDMS) substrates (negatively replicated hollow nanotowers). (B) Reflection visible-infrared spectra of Au/Si nanotowers with different dimensions. Solid lines are the experiment results and dotted lines are corresponding simulation results. (Sample sizes in nm, sample i: p=900, d_1=530, h_1=300, d_2=320, h_2=230, and t_{Au}=50; Sample ii: p=900, d_1=570, h_1=230, d_2=320, h_2=300, and t_{Au}=50). Note that, the spectra (500 to 6000 nm) were collected using two different spectrometers with different ranges (500 to 2500 nm and 2500 to 6000 nm respectively) and stitched together at 2500 nm for comparison to simulations (see detailed description in the supporting information).

5.5 Conclusions and Prospects

Our results suggest that MP-NSL is a promising 3D nanolithographic tool to achieve a variety of periodic 3D hierarchical nanostructures that can be configured to enable applications in nanophotonics, optoelectronics, electronics, metamaterials, and biotechnology. This strategy is compatible with and could be integrated into micro/nanoscale device manufacturing to add components with functions enabled by rationally designed 3D nanostructures. Additionally, by using beads with different physicochemical properties and/or geometries, even greater control can be achieved.

5.6 Supplementary Materials

Characterization of reflection spectra. In the characterization of the reflection spectra of the plasmonic hierarchical nanostructures, we set the incident light and reflected light to be near normal to the substrate, as illustrated on the left. Note that we also used these settings for the finite-difference time-domain (FDTD) optical simulations. In order to obtain the reflection spectra across the wavelength range from 500 to 6000 nm, two spectrophotometers were used. One spectrophotometer measured the reflection spectra from 500 to 2500 nm and other measured the reflection spectra from 2500 to 6000 nm. An UV-3101PC UV-VIS-NIR Spectrophotometer (Shimadzu Co., Japan) with an integrating sphere attachment (ISR-3100) was used to collect the reflection spectra of the plasmonic hierarchical nanostructures within the wavelength range (500 to 2500 nm). The scan rate was set at 1 nm/s. A customized polarization modulation-infrared reflection-adsorption spectroscopy (PM-IRRAS) instrument was used to collect the reflection spectra of the plasmonic hierarchical nanostructures in the range of 2500 to 6000 nm. The scan step size was set at 2 nm with medium scan rate. Due to the differences in sensitivities of the two spectrometers, for comparisons to the simulations, the two segments of the reflection spectra were stitched together as follows. Sample (i): no changes were made to the reflection spectra from 500 to 2500 nm, and the intensity of reflection spectra from 2500 to 6000 nm was multiplied by 20× in order to combine the spectra. Sample (ii): the overall intensity of the reflection spectra obtained from 500 to 2500 nm was increased by 20 (arbitrary units), while the intensity of the reflection spectra from 2500 to 6000 nm was multiplied by 20×. See **Figure S5.9A**.

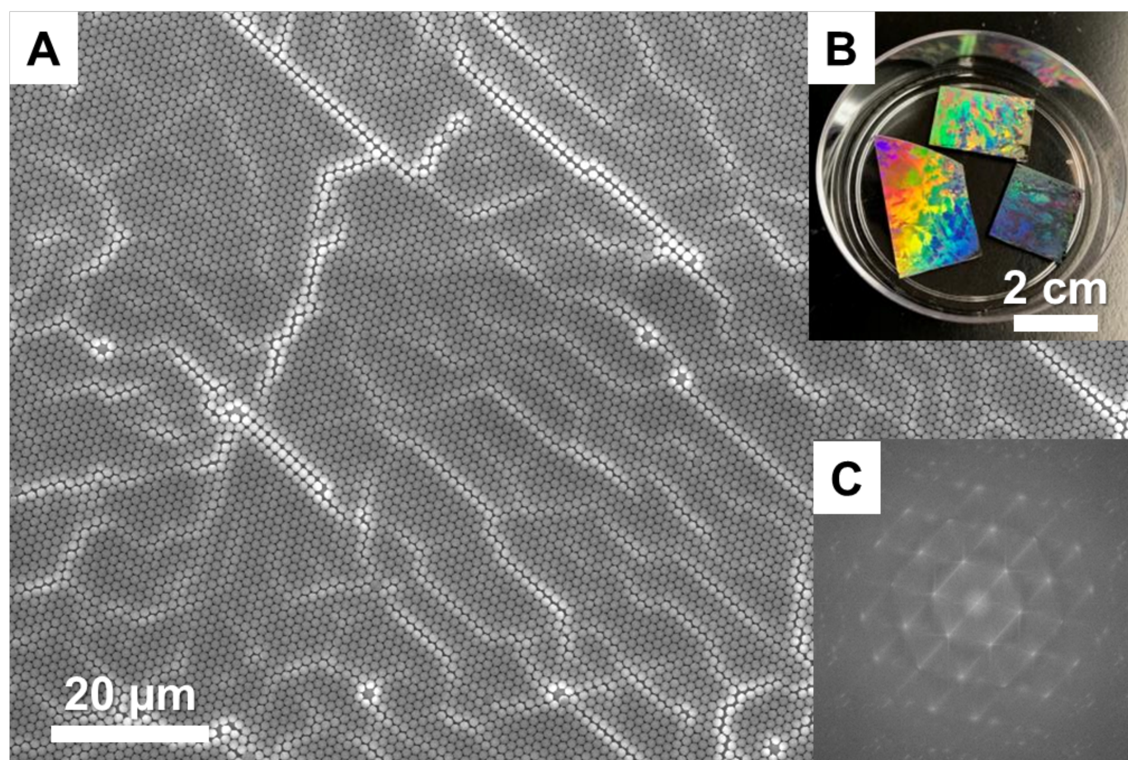

Figure S5.1: (A) A typical scanning electron microscope (SEM) image of close-packed 1 µm polystyrene spheres in micro-scale. (B) A photograph of Si wafers fully covered by close-packed 1 µm polystyrene spheres. The reflected colors indicate the well-ordered configuration of the polystyrene microspheres. (C) The corresponding fast Fourier transform (FFT) of the SEM image.

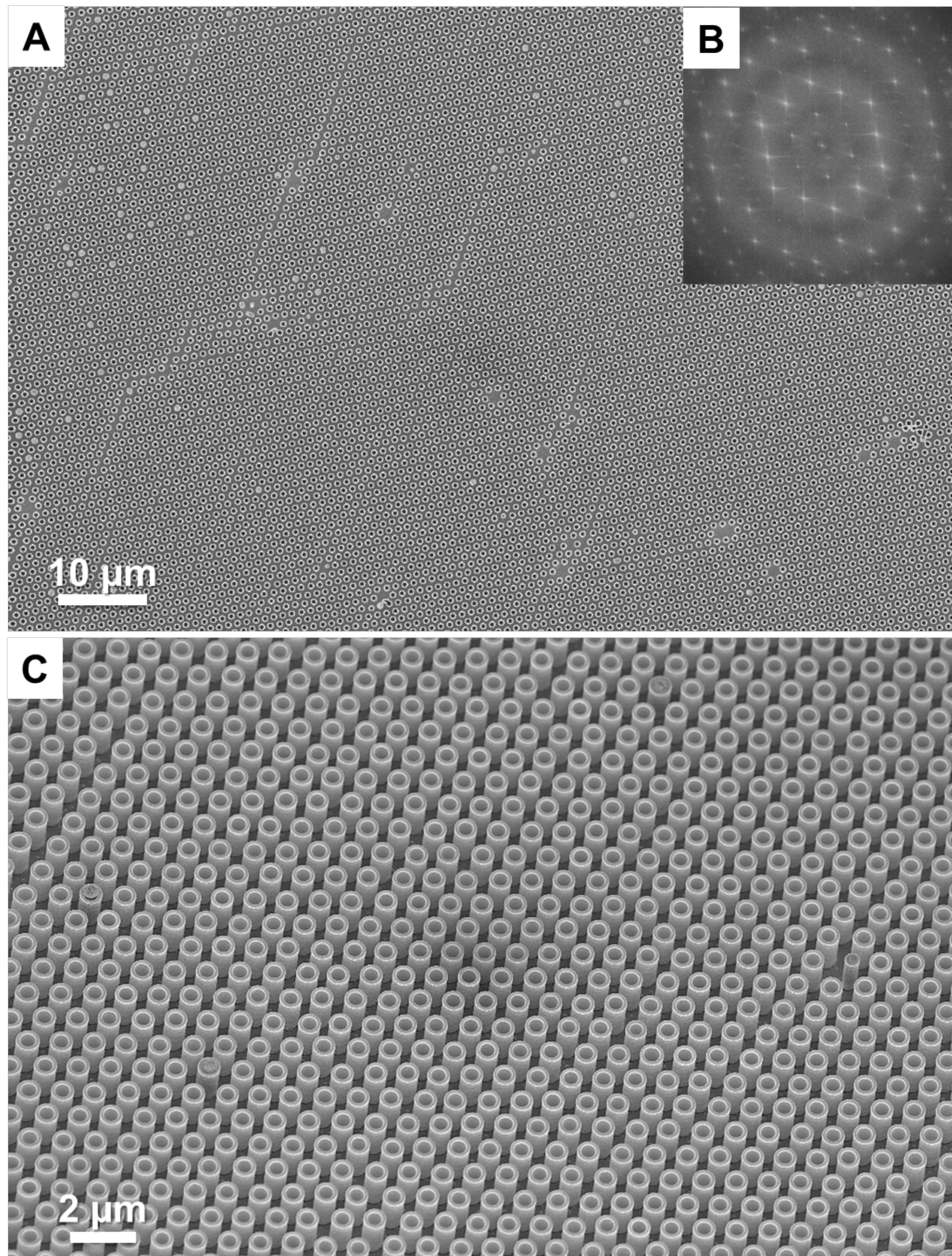

Figure S5.2. (A) A typical scanning electron microscope (SEM) image of a large area of the silicon nanotube arrays. (B) The corresponding fast Fourier transform (FFT) of the image. (C) A typical SEM image of large-area silicon nanotube arrays recorded at a tilt of 30°.

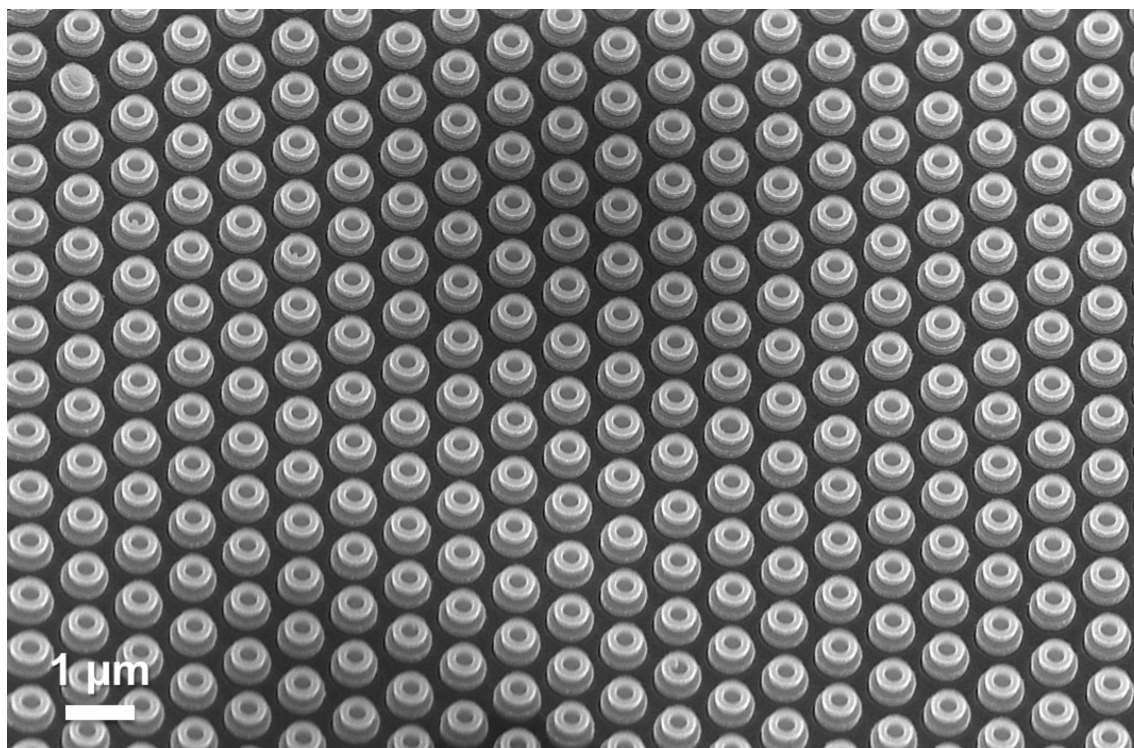

Figure S5.3. A typical scanning electron microscope (SEM) image of a large area of silicon nanostructures recorded at a tilt of 30°.

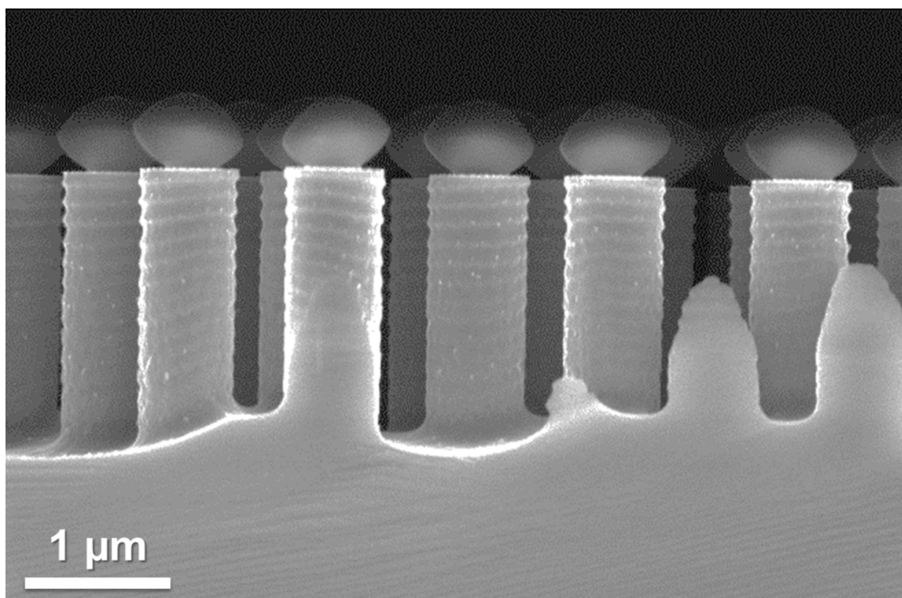

Figure S5.4. A typical scanning electron microscope image of polystyrene nanospheres with oblate ellipsoid shapes after oxygen plasma reactive ion etching.

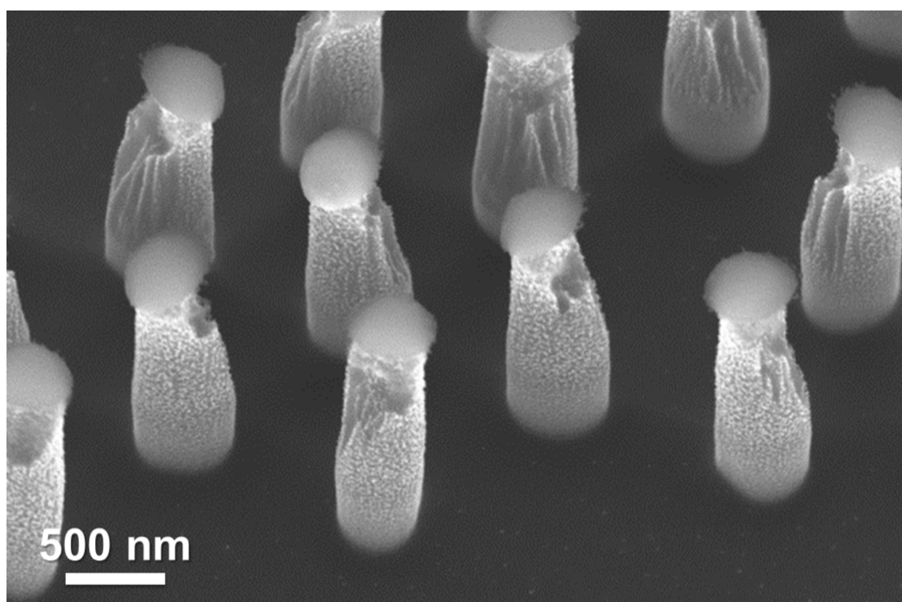

Figure S5.5. Enhancing the adhesion between the polystyrene nanospheres and the underlying silicon substrate before dry etching helps to prevent tilting of the etched polymer nanoparticles, which could lead to asymmetries in the final pillar/nanotube arrays without heating.

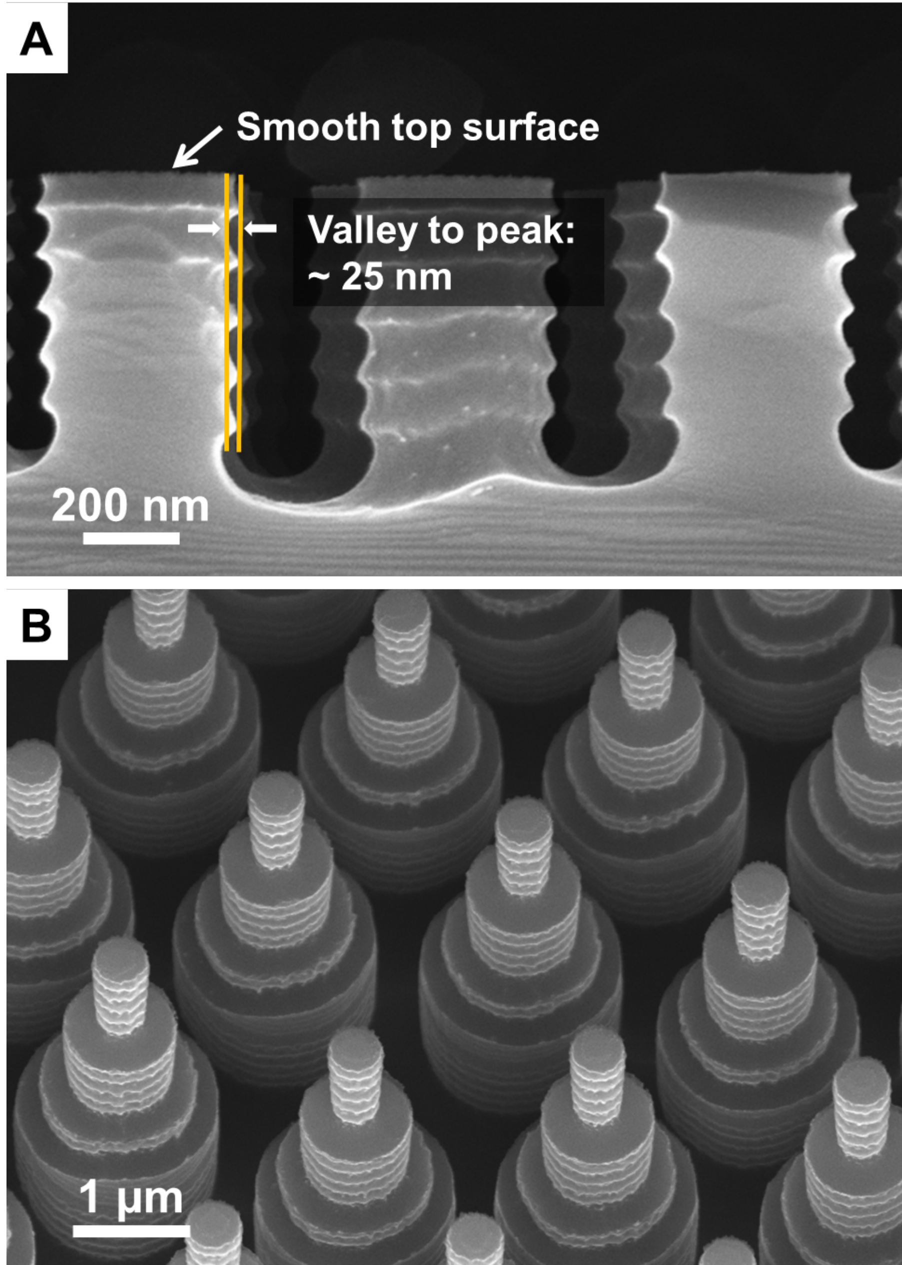

Figure S5.6. (A) A high-resolution scanning electron microscope (SEM) image of silicon nanopillars made *via* the Bosch process. The top surfaces of the silicon nanopillars are smooth. The average distance between valleys and peaks on the sidewall of a silicon nanopillar is ~25 nm. (B) A high-resolution SEM image of four-level silicon nanotowers shows the smooth surfaces on the four levels.

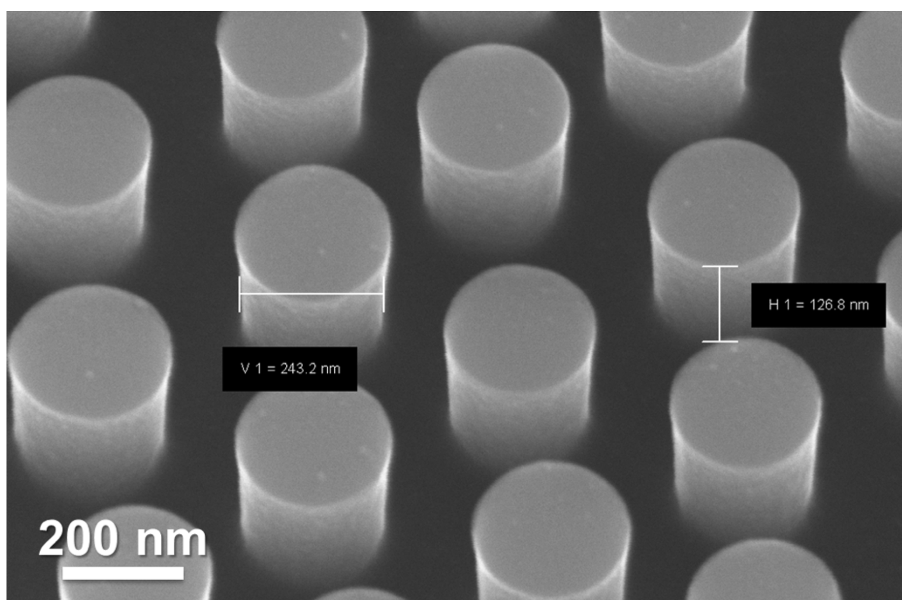

Figure S5.7. A scanning electron microscope (SEM) image of periodic silicon nanopillars with smooth sidewalls fabricated by single-step deep reactive ion etching.

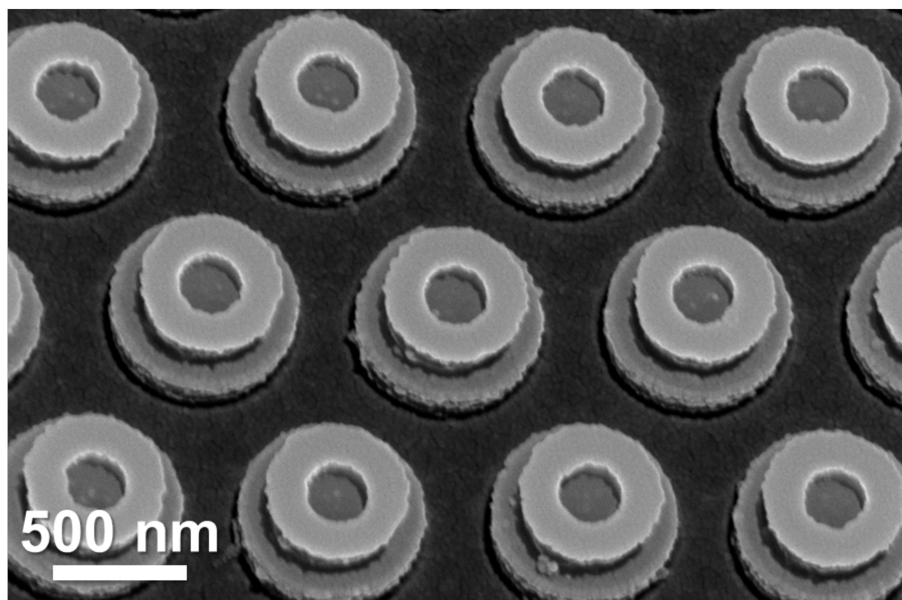

Figure S5.8. A high-resolution scanning electron microscope (SEM) image of 50 nm Au evaporated silicon nanostructures.

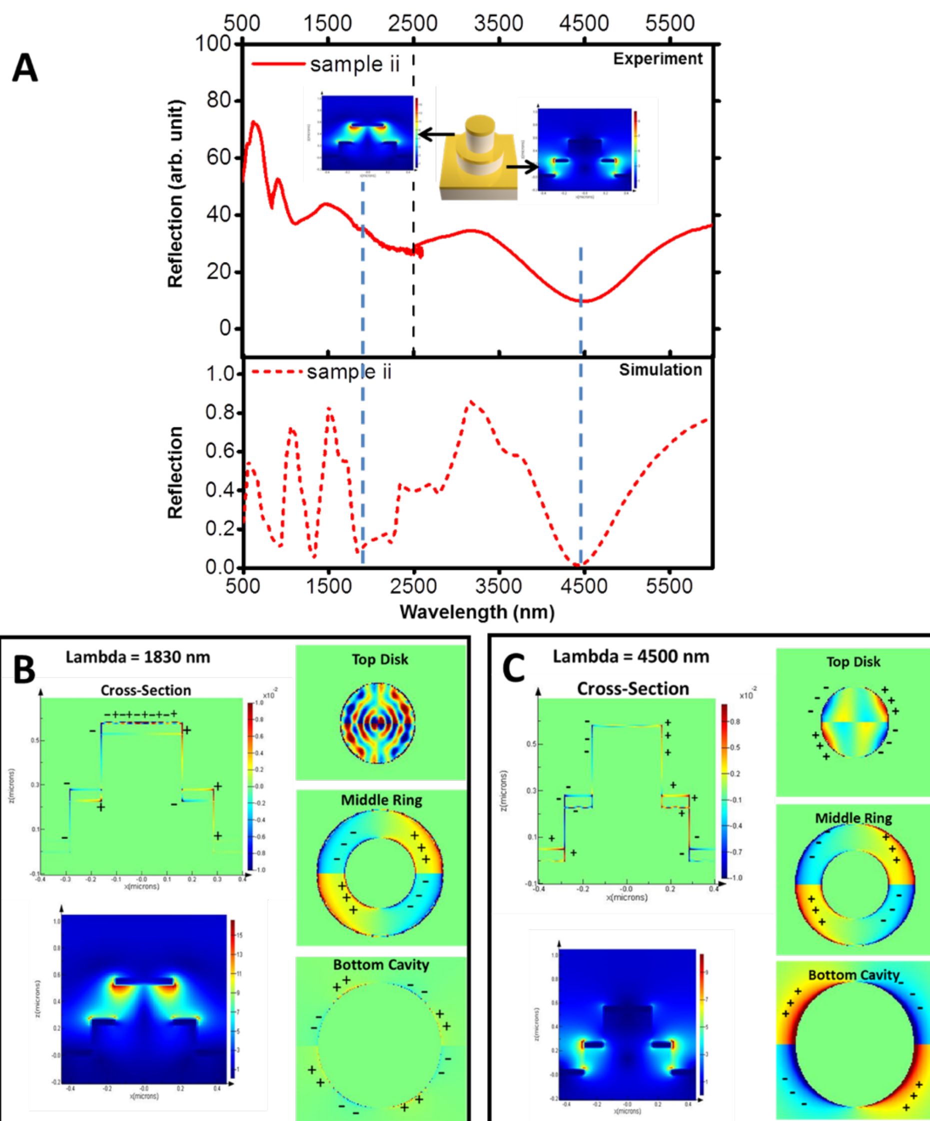

Figure S5.9. (A) The visible-infrared reflectance spectra of sample ii. Insets: simulation results of the electric-field distribution of sample ii under photoexcitation (cross section). (B,C) Simulation of charge distributions on the Au surfaces on different layers of the sample ii at the two major dips (1830 nm and 4500 nm), from which we can see the 1830 nm mode is a combination of different multipole modes from the three layers; while the 4500 nm mode corresponds to the quadrupole modes of all three layers.

5.7 References

(1) Kim, Y. Y.; Kim, H. J.; Jeong, J. H.; Lee, J.; Choi, J. H.; Jung, J. Y.; Lee, J. H.; Cheng, H.; Lee, K. W.; Choi, D. G. Facile Fabrication of Silicon Nanotube Arrays and Their Application in Lithium-Ion Batteries. *Adv. Eng. Mater.* **2016**, *18*, 1349–1353.

(2) Yoo, J.-K.; Kim, J.; Jung, Y. S.; Kang, K. Scalable Fabrication of Silicon Nanotubes and Their Application to Energy Storage. *Adv. Mater.* **2012**, *24*, 5452–5456.

(3) Park, M.-H.; Kim, M. G.; Joo, J.; Kim, K.; Kim, J.; Ahn, S.; Cui, Y.; Cho, J. Silicon Nanotube Battery Anodes. *Nano Lett.* **2009**, *9*, 3844–3847.

(4) Wu, H.; Chan, G.; Choi, J. W.; Ryu, I.; Yao, Y.; Mcdowell, M. T.; Lee, S. W.; Jackson, A.; Yang, Y.; Hu, L.; Cui, Y. Stable Cycling of Double-Walled Silicon Nanotube Battery Anodes through Solid–Electrolyte Interphase Control. *Nat. Nanotechnol.* **2012**, *7*, 310–315.

(5) Xie, C.; Nie, B.; Zeng, L.; Liang, F.-X.; Wang, M.-Z.; Luo, L.; Feng, M.; Yu, Y.; Wu, C.-Y.; Wu, Y.; Yu, S.-H. Core–Shell Heterojunction of Silicon Nanowire Arrays and Carbon Quantum Dots for Photovoltaic Devices and Self-Driven Photodetectors. *ACS Nano* **2014**, *8*, 4015–4022.

(6) Wei, W.-R.; Tsai, M.-L.; Ho, S.-T.; Tai, S.-H.; Ho, C.-R.; Tsai, S.-H.; Liu, C.-W.; Chung, R.-J.; He, J.-H. Above-11%-Efficiency Organic–Inorganic Hybrid Solar Cells with Omnidirectional Harvesting Characteristics by Employing Hierarchical Photon-Trapping Structures. *Nano Lett.* **2013**, *13*, 3658-3663.

(7) Ali, M.; Zhou, F.; Chen, K.; Kotzur, C.; Xiao, C.; Bourgeois, L.; Zhang, X.; Macfarlane, D. R. Nanostructured Photoelectrochemical Solar Cell for Nitrogen Reduction Using Plasmon-Enhanced Black Silicon. *Nat. Commun.* **2016**, *7*, 11335.

(8) Kelzenberg, M. D.; Boettcher, S. W.; Petykiewicz, J. A.; Turner-Evans, D. B.; Putnam, M. C.; Warren, E. L.; Spurgeon, J. M.; Briggs, R. M.; Lewis, N. S.; Atwater, H. A. Enhanced Absorption and Carrier Collection in Si Wire Arrays for Photovoltaic Applications. *Nat. Mater.* **2010**, 9, 239–244.

(9) Garnett, E.; Yang, P. Light Trapping in Silicon Nanowire Solar Cells. *Nano Lett.* **2010**, *10*, 1082–1087.

(10) Xu, X.; Liu, C.; Kim, K.; Fan, D. L. Electric-Driven Rotation of Silicon Nanowires and Silicon Nanowire Motors. *Adv. Funct. Mater.* **2014**, *24*, 4843–4850.

(11) Jeong, H.; Song, H.; Pak, Y.; Kwon, I. K.; Jo, K.; Lee, H.; Jung, G. Y. Enhanced Light Absorption of Silicon Nanotube Arrays for Organic/Inorganic Hybrid Solar Cells. *Adv. Mater.* **2014**, *26*, 3445–3450.

(12) Chiappini, C.; De Rosa, E.; Martinez, J. O.; Liu, X.; Steele, J.; Stevens, M. M.; Tasciotti, E. Biodegradable Silicon Nanoneedles Delivering Nucleic Acids Intracellularly Induce Localized *in Vivo* Neovascularization. *Nat. Mater.* **2015**, *14*, 532–539.

(13) Bucaro, M. A.; Vasquez, Y.; Hatton, B. D.; Aizenberg, J. Fine-Tuning the Degree of Stem Cell Polarization and Alignment on Ordered Arrays of High-Aspect-Ratio Nanopillars. *ACS Nano* **2012**, *6*, 6222–6230.

(14) Polacheck, W. J.; Chen, C. S. Measuring Cell-Generated Forces: A Guide to the Available Tools. *Nat. Methods* **2016**, *13*, 415–423.

(15) Weng, S. N.; Shao, Y.; Chen, W. Q.; Fu, J. P. Mechanosensitive Subcellular Rheostasis Drives Emergent Single-Cell Mechanical Homeostasis. *Nat. Mater.* **2016**, *15*, 961–967.

(16) Green, B. J.; Saberi Safaei, T.; Mepham, A.; Labib, M.; Mohamadi, R. M.; Kelley, S. O. Beyond the Capture of Circulating Tumor Cells: Next-Generation Devices and Materials. *Angew. Chem. Int. Ed.* **2016**, *55*, 1252–1265.

(17) Fox, C. B.; Cao, Y.; Nemeth, C. L.; Chirra, H. D.; Chevalier, R. W.; Xu, A. M.; Melosh, N. A.; Desai, T. A. Fabrication of Sealed Nanostraw Microdevices for Oral Drug Delivery. *ACS Nano* **2016**, *10*, 5873–5881.

(18) Wu, Y.-C.; Wu, T.-H.; Clemens, D. L.; Lee, B.-Y.; Wen, X.; Horwitz, M. A.; Teitell, M. A.; Chiou, P.-Y. Massively Parallel Delivery of Large Cargo into Mammalian Cells with Light Pulses. *Nat. Methods* **2015**, *12*, 439–444.

(19) Hulteen, J. C.; Van Duyne, R. P. Nanosphere Lithography: A Materials General Fabrication Process for Periodic Particle Array Surfaces. *J. Vac. Sci. Technol. A* **1995**, *13*, 1553–1558.

(20) Chen, K.; Rajeeva, B. B.; Wu, Z.; Rukavina, M.; Dao, T. D.; Ishii, S.; Aono, M.; Nagao, T.; Zheng, Y. Moiré Nanosphere Lithography. *ACS Nano* **2015**, *9*, 6031–6040.

(21) Kosiorek, A.; Kandulski, W.; Glaczynska, H.; Giersig, M. Fabrication of Nanoscale Rings, Dots, and Rods by Combining Shadow Nanosphere Lithography and Annealed Polystyrene Nanosphere Masks. *Small* **2005**, *1*, 439–444.

(22) Haynes, C. L.; Van Duyne, R. P. Nanosphere Lithography: A Versatile Nanofabrication Tool for Studies of Size-Dependent Nanoparticle Optics. *J. Phys. Chem. B* **2001**, *105*, 5599–5611.

(23) Huang, Z.; Fang, H.; Zhu, J. Fabrication of Silicon Nanowire Arrays with Controlled Diameter, Length, and Density. *Adv. Mater.* **2007**, *19*, 744–748.

(24) Jeong, S.; Mcgehee, M. D.; Cui, Y. All-Back-Contact Ultra-Thin Silicon Nanocone Solar Cells with 13.7% Power Conversion Efficiency. *Nat. Commun.* **2013**, *4*, 2950.

(25) Jeong, S.; Garnett, E. C.; Wang, S.; Yu, Z.; Fan, S.; Brongersma, M. L.; Mcgehee, M. D.; Cui, Y. Hybrid Silicon Nanocone–Polymer Solar Cells. *Nano Lett.* **2012**, *12*, 2971–2976.

(26) Gao, P. Q.; He, J.; Zhou, S. Q.; Yang, X.; Li, S. Z.; Sheng, J.; Wang, D.; Yu, T. B.; Ye, J. C.; Cui, Y. Large-Area Nanosphere Self-Assembly by a Micro-Propulsive Injection Method for High Throughput Periodic Surface Nanotexturing. *Nano Lett.* **2015**, *15*, 4591–4598.

(27) Zhang, J.; Li, Y.; Zhang, X.; Yang, B. Colloidal Self-Assembly Meets Nanofabrication: From Two-Dimensional Colloidal Crystals to Nanostructure Arrays. *Adv. Mater.* **2010**, *22*, 4249–4269.

(28) Ge, M.; Rong, J.; Fang, X.; Zhou, C. Porous Doped Silicon Nanowires for Lithium Ion Battery Anode with Long Cycle Life. *Nano Lett.* **2012**, *12*, 2318–2323.

(29) Morton, K. J.; Nieberg, G.; Bai, S.; Chou, S. Y. Wafer-Scale Patterning of Sub-40 nm Diameter and High Aspect Ratio (>50:1) Silicon Pillar Arrays by Nanoimprint and Etching. *Nanotechnology* **2008**, *19*, 345301.

(30) Li, Z.; Chen, Y.; Zhu, X.; Zheng, M.; Dong, F.; Chen, P.; Xu, L.; Chu, W.; Duan, H. Fabrication of Single-Crystal Silicon Nanotubes with Sub-10 nm Walls Using Cryogenic Inductively Coupled Plasma Reactive Ion Etching. *Nanotechnology* **2016**, *27*, 365302.

(31) Chung, C.-K. Geometrical Pattern Effect on Silicon Deep Etching by an Inductively Coupled Plasma System. *J. Micromech. Microeng.* **2004**, *14*, 656–662.

(32) Fan, Z.; Razavi, H.; Do, J.-W.; Moriwaki, A.; Ergen, O.; Chueh, Y.-L.; Leu, P. W.; Ho, J. C.; Takahashi, T.; Reichertz, L. A.; Neale, S.; Yu, K.; Wu, M.; Ager, J. W.; Javey, A. Three-Dimensional Nanopillar-Array Photovoltaics on Low-Cost and Flexible Substrates. *Nat. Mater.* **2009**, *8*, 648–653.

(33) Perry, J. W.; Cumpston, B. H.; Ananthavel, S. P.; Barlow, S.; Dyer, D. L.; Ehrlich, J. E.; Erskine, L. L.; Heikal, A. A.; Kuebler, S. M.; Lee, I. Y. S.; Mccord-Maughon, D.; Qin, J.; Röckel, H.; Rumi, M.; Wu, X.-L.; Marder, S. R. Two-Photon Polymerization Initiators for Three-Dimensional Optical Data Storage and Microfabrication. *Nature* **1999**, *398*, 51–54.

(34) Yamazaki, K.; Yamaguchi, H. Flexible Nanofabrication in Three-Dimensional Electron-Beam Lithography Enhanced by Suppression of Proximity Effect. *Appl. Phys. Expr.* **2008**, *1*, 097001.

(35) Qin, L.; Banholzer, M. J.; Millstone, J. E.; Mirkin, C. A. Nanodisk Codes. *Nano Lett.* **2007**, *7*, 3849–3853.

(36) Raut, H. K.; Ganesh, V. A.; Nair, A. S.; Ramakrishna, S. Anti-Reflective Coatings: A Critical, in-Depth Review. *Energy Environ. Sci.* **2011**, *4*, 3779–3804.

(37) Cao, H. H.; Nakatsuka, N.; Liao, W.-S.; Serino, A. C.; Cheunkar, S.; Yang, H.; Weiss, P. S.; Andrews, A. M. Advancing Biocapture Substrates *via* Chemical Lift-Off Lithography. *Chem. Mater.* **2017**, *29*, 6829–6839.

(38) Xu, X.; Yang, Q.; Cheung, K. M.; Zhao, C.; Wattanatorn, N.; Belling, J. N.; Abendroth, J. M.; Slaughter, L. S.; Mirkin, C. A.; Andrews, A. M.; Weiss, P. S. Polymer-Pen Chemical Lift-Off Lithography. *Nano Lett.* **2017**, *17*, 3302–3311.

(39) Liao, W.-S.; Cheunkar, S.; Cao, H. H.; Bednar, H. R.; Weiss, P. S.; Andrews, A. M. Subtractive Patterning *via* Chemical Lift-Off Lithography. *Science* **2012**, *337*, 1517–1521.

(40) Brolo, A. G. Plasmonics for Future Biosensors. *Nat. Photonics* **2012**, *6*, 709–713.

(41) Juan, M. L.; Righini, M.; Quidant, R. Plasmon Nano-Optical Tweezers. *Nat. Photonics* **2011**, *5*, 349–356.

(42) Lu, Y. J.; Kim, J.; Chen, H. Y.; Wu, C.; Dabidian, N.; Sanders, C. E.; Wang, C. Y.; Lu, M. Y.; Li, B. H.; Qiu, X.; Chang, W. H.; Chen, L. J.; Shvets, G.; Shih, C. K.; Gwo, S. Plasmonic Nanolaser Using Epitaxially Grown Silver Film. *Science* **2012**, *337*, 450–453.

(43) Nie, S. Probing Single Molecules and Single Nanoparticles by Surface-Enhanced Raman Scattering. *Science* **1997**, *275*, 1102–1106.

(44) Rodrigo, D.; Limaj, O.; Janner, D.; Etezadi, D.; Garcia De Abajo, F. J.; Pruneri, V.; Altug, H. Mid-Infrared Plasmonic Biosensing with Graphene. *Science* **2015**, *349*, 165–168.

(45) Xu, X.; Li, H.; Hasan, D.; Ruoff, R. S.; Wang, A. X.; Fan, D. L. Near-Field Enhanced Plasmonic-Magnetic Bifunctional Nanotubes for Single Cell Bioanalysis. *Adv. Funct. Mater.* **2013**, *23*, 4332–4338.

(46) Zheng, Y. B.; Payton, J. L.; Chung, C.-H.; Liu, R.; Cheunkar, S.; Pathem, B. K.; Yang, Y.; Jensen, L.; Weiss, P. S. Surface-Enhanced Raman Spectroscopy to Probe Reversibly Photoswitchable Azobenzene in Controlled Nanoscale Environments. *Nano Lett.* **2011**, *11*, 3447–3452.

(47) Kuzyk, A.; Schreiber, R.; Zhang, H.; Govorov, A. O.; Liedl, T.; Liu, N. Reconfigurable 3D Plasmonic Metamolecules. *Nat. Mater.* **2014**, *13*, 862-866.

(48) Frank, B.; Yin, X.; Schäferling, M.; Zhao, J.; Hein, S. M.; Braun, P. V.; Giessen, H. Large-Area 3D Chiral Plasmonic Structures. *ACS Nano* **2013**, *7*, 6321-6329.

(49) De Angelis, F.; Malerba, M.; Patrini, M.; Miele, E.; Das, G.; Toma, A.; Zaccaria, R. P.; Di Fabrizio, E. 3D Hollow Nanostructures as Building Blocks for Multifunctional Plasmonics. *Nano Lett.* **2013**, *13*, 3553-3558.

Chapter 6

Fabrication of Silicon Nanovolcanos and Their Applications in Direct Gene Delivery with High Efficiency and Cell Viability

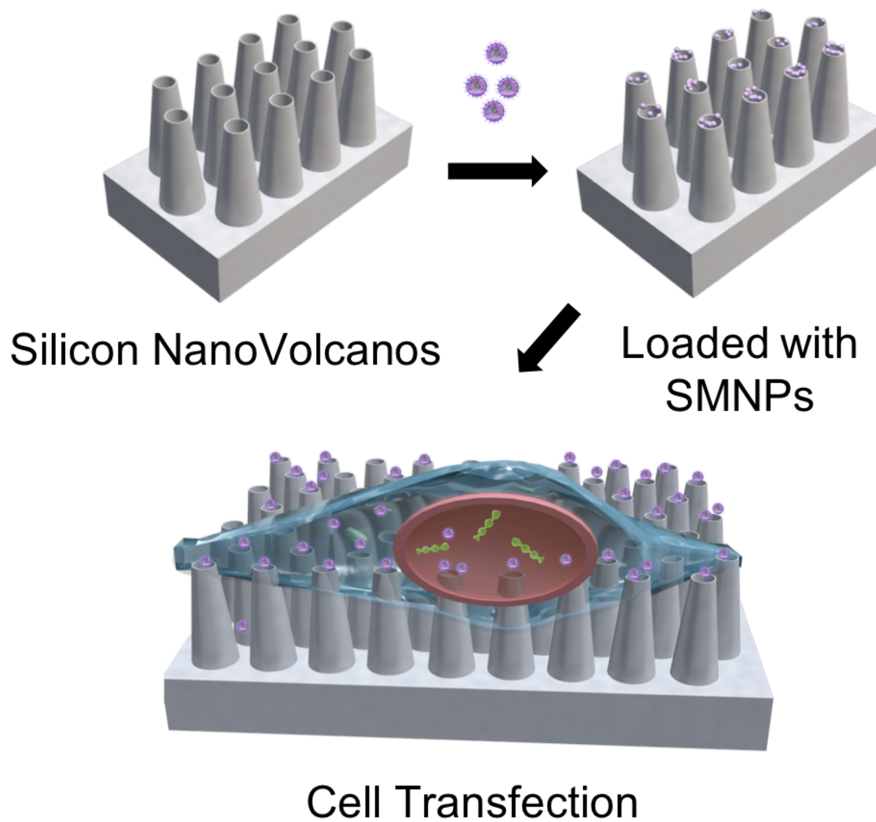

6.1 Abstract

Membrane-disruptive nanostructures are promising candidates for delivering exogenous materials with high throughput, efficiency, and cell viability. Here, we fabricate a silicon nanovolcano platform that could penetrate cell membranes and deliver genetic materials intracellularly, *i.e.*, to cell nuclei for gene transfer. By adopting a multiple-patterning nanosphere lithography strategy, we are able to fabricate mechanically stable volcano-shaped nanostructures with controllable heights, hole diameters/depths, and pitches. The sub-20-nm sharp features of nanovolcanos enable penetration of cell membranes and minimize disruption of cell functions. Biomolecular payloads containing the gene-editing packages are assembled and encapsulated into supramolecular nanoparticles. The holes (calderas) of the nanovolcanos can contain high payloads of biomolecular cargos that are readily accessed once cell membranes are penetrated. Enhanced green fluorescent protein (eGFP) plasmid and small interfering RNA (siRNA) were used as proof-of-concept studies for intracellular delivery. With advances in ease of fabrication, fully tunable dimensions, and high parallelism, silicon nanovolcanos could provide a versatile platform for a wide range of fundamental and clinical applications.

6.2 Introduction

High-efficiency intracellular delivery of exogenous species, such as DNA,[1-9] small interfering RNA (siRNA),[10-14] proteins,[15-19] peptides,[20] and other small particles,[21-26] can provide robust and powerful platforms for broad applications, including intracellular imaging/sensing,[27-33] gene editing,[34-38] delivery of membrane-impermeable drugs,[17,39,40] immunotherapy,[10,37,41] and regenerative medicine.[35,42,43] Among these efforts, viral-based intracellular approaches have had encouraging results in gene delivery with high efficiency and specificity because viruses are highly evolved biological machines that can enter cells without assistance and then release genetic materials.[44] However, the loading capacity, immune response, safety concerns, and high cost associated with viral-based approaches have impeded their application in advanced clinical stages. To overcome the limitations of viral vectors, attention is shifting to the development of non-viral intracellular strategies. For example, cell membrane disruption-mediated approaches use mechanical,[2,16,45] electrical,[4,46] or photothermal[17,47,48] methods to generate transient pores in cell membranes,[49] which can be utilized to deliver diverse materials into many cell types. Compared to electroporation and thermal processes, direct physical penetration *via* sharp nanostructures preloaded with biomolecular cargos is less destructive. Nanostructures with sharp features including nanowires,[1,6,8,20,50] nanostraws,[2,4,51,52] nanoneedles,[3,6-7,9,23,24] nanopyramids,[53,54] and nanomotors[28,31,53,55-64] are ideal candidates to pierce membranes and to release cargos into the cell's cytoplasm. Developing a platform with universal cargo delivery, high efficiency, and high throughput with minimal cell disruption and scalability remains a critical long-term challenge.[49]

Here, we fabricated silicon nanovolcano arrays that will be used to deliver biomolecular cargos with high efficiency while maintaining high cell viability. Silicon nanovolcano structures

with fully tunable parameters (pitch, height, rim diameter, and hole depth) and sub-20-nm sharp rim edges were fabricated using our recently developed multiple-patterning nanosphere lithography (MP-NSL).[65] These nanovolcanos were further combined with supramolecular nanoparticles[66,67] to promote delivery efficiency. As shown in **Figure 6.1**, nanovolcanos have three key advantages to ensure the intracellular delivery with high efficiency: (1) the volcano-shape nanostructure offers mechanical stability during cell penetration. With preserved structural integrity, multiple and long-term use without reduced efficiency are possible. (2) The sub-20-nm scale sharp rims of nanovolcanos yield higher penetration efficiencies into cell membranes[68] with minimal influence on cell viability.[9] (3) The dimensions of nanovolcanos, including hole diameter/depth, are fully tunable. Thus, the maximum payload of biomolecular cargos in each nanovolcano can be controlled. Once the nanovolcanos penetrate through the cell membrane, the preloaded biomolecular cargos can be readily accessed by the cells.

6.3 Materials and Methods

Materials. Prime quality 4″ Si (100) wafers (*p*-type/B-doped, 1-10 ohm·cm) were purchased from University Wafer Inc. (Boston, MA, USA). Polystyrene spheres were purchased from Thermo Fisher Scientific Inc. (Fremont, CA, USA). Dimethyl sulfoxide (DMSO), sodium dodecyl sulfate (≥98.5%), (3-aminopropyl)triethoxysilane (99%), and 1-adamantane isocyanate (97%) were purchased from Sigma-Aldrich (St. Louis, MO, USA). Hydrochloric acid (36.5 to 38.0% w/w) was purchased from Fisher Scientific Inc. (Fair Lawn, NJ, USA). The sputtering target nickel (99.995%) was purchased from Kurt J. Lesker Company (Jefferson Hills, PA, USA). Lipofectamine® 2000 and Silencer^{TM} GFP (eGFP) siRNA were purchased from Thermo Fisher Scientific Inc. (Fremont, CA, USA). Cyclodextrin-grafted polyethyleneimine (CD-PEI), adamantane-grafted polyamidoamine dendrimer (Ad-PAMAM), adamantane-grafted poly(ethylene glycol) (Ad-PEG), enhanced green fluorescent protein (eGFP) plasmid were prepared and purified following previous method. The U87 glioblastoma cells were purchased from American Type Culture Collection (ATCC). Dulbecco's modified Eagle's medium (DMEM) was purchased from Invitrogen (Carlsbad, CA, USA).

Fabrication of silicon nanovolcanos. The polystyrene spheres were assembled into close-packed monolayers and transferred to silicon substrates following reported method.[65] Oxygen plasma (Oxford Plasmalab 80 Plus, Oxford Instruments, Abingdon, UK) was then applied to reduce the size of spheres. The etching conditions were 35 sccm of O_2 and 10 sccm of Ar at a radio frequency (RF) power of 60 W and pressure of 60 mTorr. Single-step deep reactive ion etching (STS Advanced Oxide Etcher) was performed with 23 sccm of C_4F_8, 27 sccm of SF_6, and 5 sccm of Ar at inductively coupled plasma power of 650 W, platen power of 9 W, and pressure of 12 mTorr to achieve cone-shape structure. Nickel film was deposited *via*

electron-beam evaporator (Kurt J. Lesker Company) at rate of 1 Å/s. Then, the polystyrene spheres were removed by Scotch tape. A second single-step DRIE was performed to etch holes. For both silicon etching processes, nanovolcano height and hole depth can be independently controlled by etching time. Finally, nickel was removed by immersing the substrates into concentrated hydrochloric acid solution.

Preparation of supramolecular nanoparticles (SMNPs). A centrifuge tube containing 600 μL nuclease-free water, 2.0 μL DMSO solution containing 3.96 μg Ad-PAMAM, 10.56 μg Ad-PEG, 9.0 μg CD-PEI, and the reported amounts of nuclei acids (eGFP plasmid or siRNA) were added and vortexed vigorously.

Surface functionalization of silicon nanovolcanos. In a vacuum desiccator, 20 μL of (3-aminopropyl)triethoxysilane was added to a petri dish containing silicon nanovolcano substrates and let the substrates stay under vacuum conditions for 40 min. Then the substrates were immersed into 1-adamantane isocyanate in DMSO solution (1.0 mM) for 2 h. The post-modified substrates were washed three times with DMSO to remove excess 1-adamantane isocyanate.

Scanning electron microscopy (SEM) and focused ion beam (FIB). SEM images were recorded using a Zeiss Supra 40VP scanning electron microscope. Cross-sectional samples were prepared and imaged using a Nova 600 SEM/FIB system.

Dynamic light scattering (DLS) measurements. DLS measurements were performed using a Zetasizer Nano instrument (Malvern Instruments Ltd., United Kingdom) equipped with a 10 mW helium-neon laser (λ = 632.8 nm) and a thermoelectric temperature controller.

6.4. Results and Discussions

The fabrication process for the silicon nanovolcanos by MP-NSL is shown in **Figure 6.1a**. (See **Figure S6.2** for the full process). Nanosphere lithography employs close-packed nanospheres/microspheres as lithography masks to pattern underlying substrates,[69-72] which is highly scalable.[73] By applying the multiple patterning strategy, we can fabricate complex three-dimensional nanostructures such as nanotubes, nanotowers with fully tunable dimensions. In a typical fabrication sequence, polystyrene (PS) microspheres are first assembled into close-packed monolayers at the water/air interface as previously described.[65] Then, the monolayers are transferred to silicon substrates and oxygen plasma etching is used to reduce the sphere size. Single-step deep reactive ion etching (DRIE) etches silicon with high uniformity and reproducibility. In this process, C_4F_8 and SF_6 are simultaneously introduced as passivation and etching gases. The ratio between two gases can be adjusted to achieve truncated cones. With a fixed flow rate of SF_6, increasing or decreasing C_4F_8 results in truncated cones with larger or smaller rims, which will thereby determine the hole diameter of nanovolcanos (see **Table 6.1**: #1 *vs* #2 and **Figure S6.3**). Subsequently, the PS particles centered on top of the truncated cones serve as masks for metal deposition. A thin film of nickel (~15 nm) is deposited as a protecting layer since nickel is highly resistant to dry etching processes. Polystyrene spheres are then removed by adhesive tape to expose the apex of truncated cones for hole etching. The hole depth is independently controlled *via* a second single DRIE step. Finally, the nickel film is removed by immersing substrates into hydrochloric acid. (The fabrication details are provided in Materials and Methods). A representative scanning electron microscopy (SEM) image of silicon nanovolcanos is shown in **Figure 6.1b**. The typical height of nanovolcanos used in this work is 3.0 ± 0.1 μm with hole diameters of 610 ± 20 nm. Moreover, we are able to fabricate

nanovolcanos with fully tunable parameters: pitch distances (1, 2, and 5 μm), heights (from ~1.6 to ~4.7 μm), and hole diameters (from ~600 nm to ~1.6 μm), which are summarized in **Table 6.1** and **Figure S6.4**.

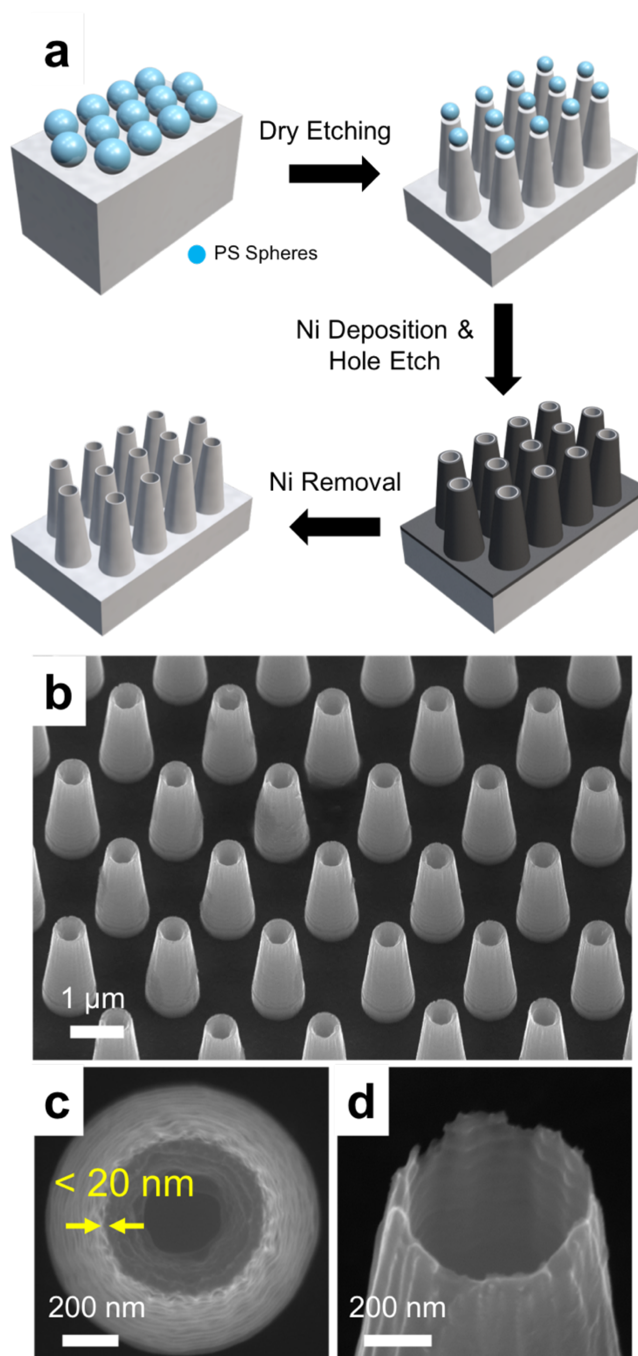

Figure 6.1. (a) Schematic of the nanovolcano fabrication process. An array of polystyrene

(PS) spheres is first assembled on a silicon wafer, which is then exposed to oxygen plasma to reduce the sphere size. Single-step dry etching of the silicon defines the cone-shape structure. Next, a thin layer of nickel is deposited to serve as a protective layer prior to removal of the polystyrene spheres. Hole-depth can be controlled independently *via* a second drying etching step. The nickel layer is removed by immersing substrates into hydrochloric acid. Scanning electron micrographs of representative (b) silicon nanovolcanos with hole diameters of 610 ± 20 nm and height of 3.0 ± 0.1 µm. (c, d) Top and side views of a typical nanovolcano: edge width is generally less than 20 nm. Note: for (b) and (d), images were taken at 30° tilt. Therefore, the actual height should be double the measured height.

Suitable nanovolcano geometries and structural parameters are critical for effective transfection and high cell viability. High densities (small pitch distances) of nanostructures have a "bed-of-nails" effect, where force is uniformly distributed among nanostructures,[51] resulting in small penetration forces. Lower densities (large pitch distances) are favorable for penetration with increased force, but reducing the number of nanovolcanos underlying each cell results in lower numbers of payload particles delivered. In addition, nanovolcanos with intermediate heights are preferred since those that are too short (<0.5 µm) or too tall (>6.3 µm) result in lower transfection efficiency.[8] Taking these observations into consideration, we chose 2 µm as the pitch, which is defined by the original sphere size, and ~3.0 µm as the height of nanovolcanos. These parameters also fall in the effective penetration regime based on the adhesion and traction model proposed by Melosh and coworkers.[68]

Cell viability depends strongly on the sizes of the nanostructures. Recent studies show that cell membranes can self-repair and "heal" lost plasma membrane when the damage is

limited.[74] As a result, no detrimental effects on cell viability should be seem when the size of nanostructures is below certain threshold. For example, both in nanostraw[2] (~100 nm) and porous nanoneedle[9] (<50 nm) systems, no apparent cell damage was found after intracellular delivery. The top and side views of a nanovolcano are shown in **Figure 6.1c** and **6.1d**, respectively. The typical edge size (indicated by red arrows) is 19 ± 5 nm. Since the edge thickness of nanovolcano rims is much smaller (<20 nm) than other reported nanosystems, a minimal damage and high cell viability is expected; we test this strategy below.

Table 6.1. Summary of Fabrication Conditions and Measured Dimensions of Nanovolcanos

	C_4F_8/SF_6 Ratio	Etching Time	Pitch (μm)	Height (μm)	Hole Diameter (nm)
#1	23/27	5 min	2.0	3.0 ± 0.1	610 ± 20
#2	25/27	5 min	2.0	2.5 ± 0.1	740 ± 30
#3	23/27	2 min	2.0	1.6 ± 0.1	1000 ± 30
#4	23/27	3.5 min	1.0	1.8 ± 0.1	550 ± 20
#5	23/27	10 min	5.0	4.7 ± 0.1	1650 ± 50

The nanovolcanos are further combined with supramolecular nanoparticles (SMNPs) with encapsulated biomolecular cargos to enhance delivery efficiency. In other configurations, we recently reported that supramolecular nanoparticles can be used to encapsulate a variety of biomolecular cargos with large payloads.[75-83] A typical process used here is schematically illustrated in **Figure 6.2a**. Three molecular building blocks, cyclodextrin-grafted polyethyleneimine (CD-PEI), adamantane-grafted polyamidoamine dendrimer (Ad-PAMAM), and adamantane-grafted poly(ethylene glycol) (Ad-PEG), are prepared and purified based on previous methods.[75] The CD-PEI and Ad-PAMAM precursors are first self-assembles into

cationic hydrogel networks through recognition between cyclodextrin (CD) and adamantane (Ad) motifs, thus forming the cores of nanoparticles with encapsulated biomolecular cargos. The Ad-PEG acts as a capping ligand to constrain the growth of cationic hydrogel network and increases solubility in water. Because the assembly of SMNPs is a reversible process (**Figure 6.2b**), the dissociation of SMNPs after uptake releases biomolecular cargos into the cells. The average diameter of SMNPs is 130 ± 30 nm, as measured by dynamic light scattering (**Figure S6.1**).

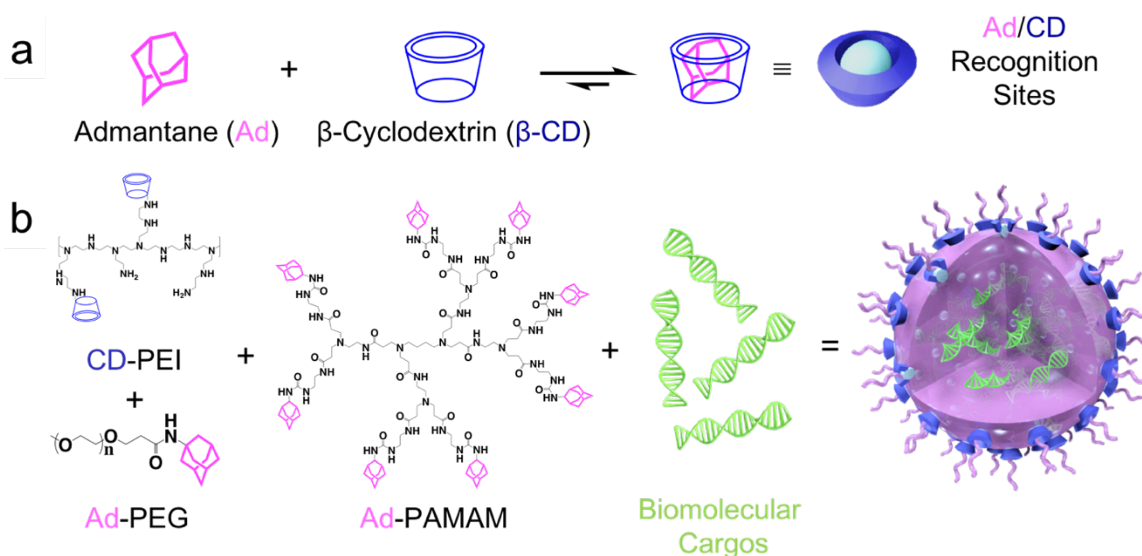

Figure 6.2. (a) The reversible assembly of supramolecular nanoparticles (SMNPs) relies on the molecular recognition between adamantane (Ad) and β-cyclodextrin (β-CD) motifs. (b) Three molecular building blocks of supramolecular nanoparticles: cyclodextrin-grafted polyethyleneimine (CD-PEI) and adamantane-grafted polyamidoamine dendrimer (Ad-PAMAM) first assemble into hydrogel networks that encapsulate desired biomolecular cargos (*e.g.*, nucleic acids) within the cationic core. The addition of adamantane-grafted poly(ethylene glycol) (Ad-PEG) both constrains the growth of SMNPs and increases water solubility.

The transfection process using nanovolcanos loaded with SMNPs is illustrated in **Figure 6.3a**. First, a two-step surface modification procedure was employed to functionalize silicon nanovolcanos with Ad-motifs and then freshly prepared SMNPs were assembled onto the nanovolcanos. The multivalent supramolecular interactions between Ad motifs on nanovolcanos and CD motifs on SMNPs led to local enrichment of SMNPs from solution onto the Ad-grafted nanovolcanos.[6] After addition of SMNPs, the substrates were examined by SEM to test if the SMNPs were loaded successfully (**Figure 6.3b**). The SMNPs are false-colored in red for better visualization (the original SEM image is shown in **Figure S6.5**). The delivery and the payloads can be controlled by depositing varying amount of SMNPs solution and changing the amount of target materials encapsulated in each SMNP.

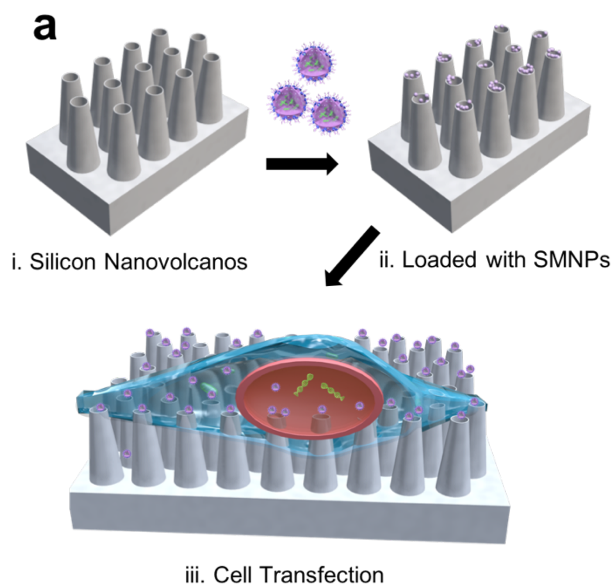

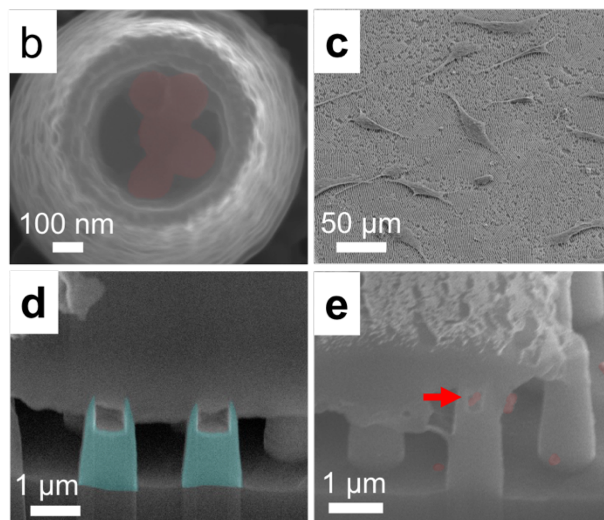

Figure 6.3. (a) Schematic overview of the nanovolcano-mediated cell transfection process: (i) first, silicon nanovolcanos are functionalized with Ad-motifs *via* a two-step surface modification procedure. (ii) freshly prepared supramolecular nanoparticles (SMNPs) are loaded into the nanovolcanos. (iii) U87 glioblastoma cells cultured on top of substrates. Scanning electron microscopy (SEM) reveals several key stages during the transfection process. (b) Upon addition of the SMNP suspension, the nanovolcanos were fully loaded with nanoparticles (false-colored in red). (c) Overview of U87 cells cultured on top of

nanovolcanos. (d) Cross-sectional SEM image of nanovolcanos interacting with a U87 cell. The nanovolcanos are false-colored in blue to visualize their relative positions compared to the cell membrane. The tops of nanovolcanos penetrated the cell membranes. (e) Cross-sectional SEM image demonstrating the active intracellular uptake of two nanoparticles (false-colored in red). Note: (d) and (e) were milled by focused ion beam (FIB) and imaged by tilting the stage 52°. The original SEM images can be found in Supporting Information, Figure S6.5.

U87 glioblastoma cells were introduced into 24 well plates with loaded nanovolcano substrates placed at the bottom. **Figure 6.3c** shows the morphologies of U87 cells after incubation for 24 h (37 °C, 5% CO_2). The cells were observed to extend and to wrap around nanovolcanos. This wrapping behavior increases adhesive interactions between cells and substrates, which facilitates the penetration process.[51,68] Direct penetration of the cell membrane is likely a critical step in the intracellular delivery of bimolecular cargos. However, the dynamics and mechanism of penetration remain unclear and whether delivery is by cell membrane penetration or endocytosis is under debate. Interpretations of some reported experiments conclude that there is direct penetration of the cell membrane,[2,9,20] while others suggest deformation but not penetration.[84] Recent experimental observations indicate that penetration could be a stochastic event that does not happen at high frequency.[8,52] In order to test whether physical penetration prompts cell transfection in nanovolcano systems, we examined two key stages during cell transfection by fabricating cross-sectional samples using focused ion beam (FIB) and imaging them with SEM. In **Figure 6.3d**, the nanovolcanos are false colored in blue to visualize their positions relative to the cell membrane (original SEM image can be found in **Figure S6.5**). We conclude that the tops of the nanovolcanos physically penetrate the cell

membrane (we note that one could also argue that the observation could be an artifact of the preparation of the sample for SEM imaging). This observation agrees with the prediction that nanostructures with diameters <50 nm have high probabilities of penetration.[68] We also observed active uptake of two SMNPs (false-colored in red, the original SEM image is shown in **Figure S6.5**) in cross-sectional images (**Figure 6.3e**), which illustrated delivery in nanovolcano-mediated transfection process. The original images can be found in **Figure S6.5**.

We will first evaluate the performance of nanovolcano substrates by delivery of membrane-impermeable enhanced green fluorescence protein (eGFP) plasmid to U87 cells, which is summarized in **Figure 6.4a**. eGFP-encapsulated SMNPs are synthesized with different amounts of eGFP plasmid (from 50 to 1000 ng) encapsulated as the cores. The nanovolcano substrates are preloaded with eGFP-encapsulated SMNPs and then 2×10^5 U87 glioblastoma cells are introduced to each well. Once cells are settled on top of nanovolcanos, the sharp edges could penetrate the cell membranes and eGFP plasmids encapsulated in SMNPs can be delivered intracellularly and efficiently. Two control experiments will be conducted in parallel to evaluate the transfection performance of nanovolcanos. The first control experiment replaces nanovolcano substrates with flat silicon that is pre-functionalized with Ad motifs. Commercially available lipofectamine agent is used in the second control experiment. The transfection efficiency using the nanovolcano platform will be compared with commercially available lipofectamine 2000. After intracellular delivery, cell viability was inspected with an acridine orange/ethidium bromide assay. To test the ability of the nanovolcano platform to deliver genetic materials further, SMNPs loaded with siRNA for silencing GFP expression will be delivered to GFP-expressing U87 cells (**Figure 6.4b**). The transfection efficiency and cell viability are also compared with commercially available lipofectamine agents.

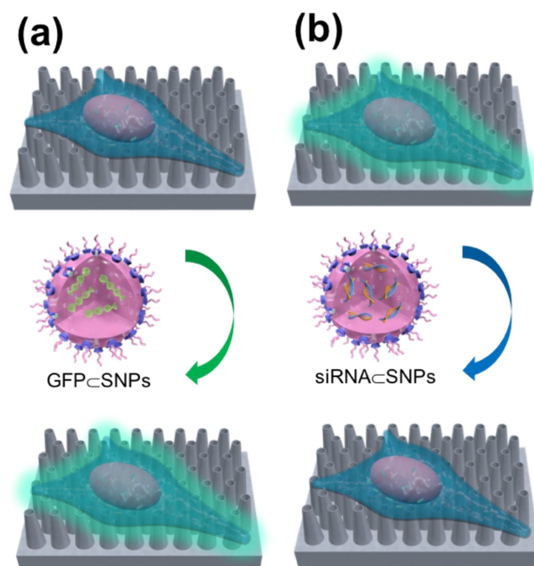

Figure 6.4. (a) Supramolecular nanoparticles (SMNPs) encapsulated with eGFP plasmid are used to transfect U87 cells. (b) Supramolecular nanoparticles (SMNPs) loaded with anti-GFP short interfering RNA (siRNA) are delivered to GFP-expressing U87 cells.

6.5 Conclusions and Prospects

We have fabricated nanovolcano substrates through a modified MP-NSL technique, which is fully tunable and scalable to large areas. The mechanical stability, sub-20-nm sharp rim features, and tunable loading capacity of nanovolcanos make it a superior system in intracellular delivery in terms of efficiency and cell viability compared to currently used methods. In addition, these physical methods[64] lack the additional safety concerns of viral transfection. We expect that this platform can deliver therapeutic payloads of interest and can offer solutions to clinically relevant applications.

Additional opportunities exist for driving the payloads into cells using, light, ultrasound, or heat, as for the nanocannons developed by Professor Joseph Wang and coworkers.[57,59,60,63] Additional complementary surface chemistries could be used to adhere multiple different payloads to the nanovolcano surfaces.[85] Thinning or replication techniques can be applied to develop flexible nanovolcano devices for medical applications, such as the microneedle patches for drug delivery as developed by Professor Zhen Gu and co-workers.[86,87]

6.6 Supplementary Materials

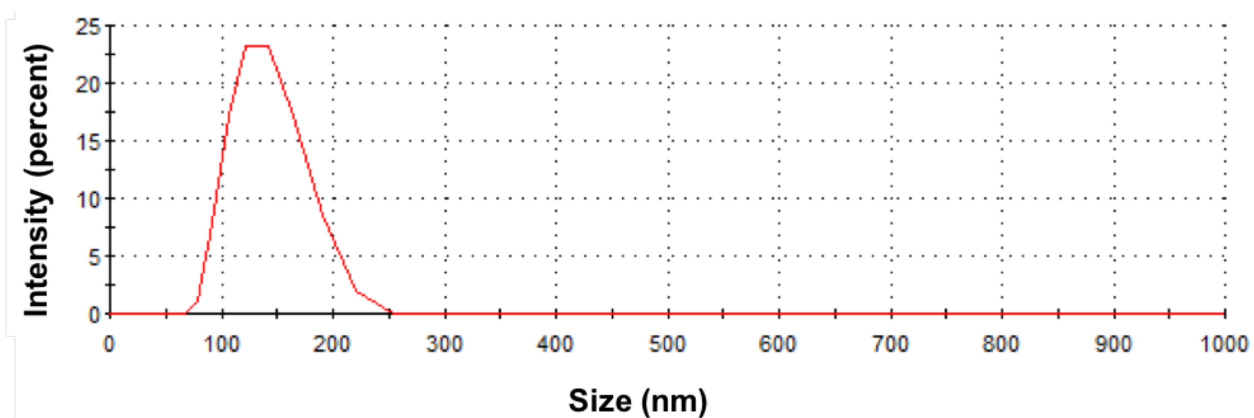

Figure S6.1. The size distribution of supramolecular nanoparticles (SMNPs) measured by dynamic light scattering (DLS). The average diameter of SMNPs is 130 ± 30 nm.

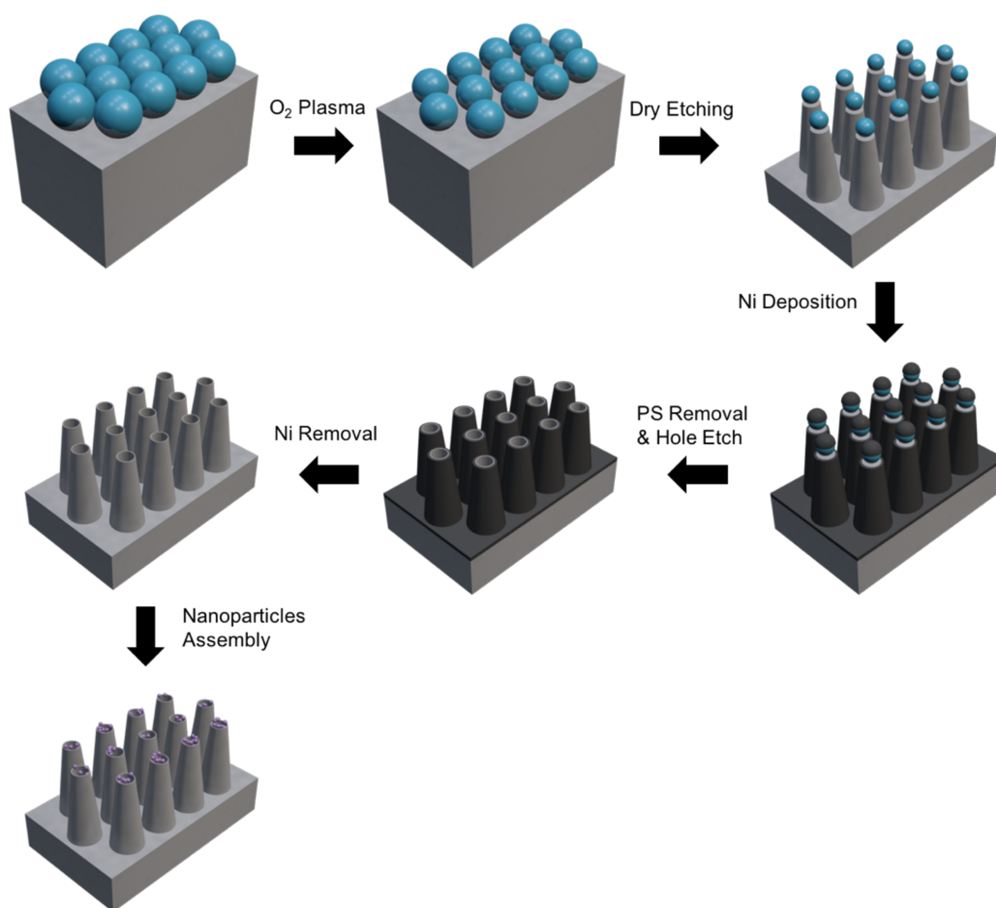

Figure S6.2. Full fabrication process of silicon nanovolcanos. (1) polystyrene microspheres are assembled into close-packed monolayers at water/air interface and then transferred to silicon substrate. (2) Oxygen plasma is used to reduce sphere size. (3) Single-step deep reactive ion etching (DRIE) is used to etch silicon with desired cone angle. (4) A thin film of nickel (~15 nm) is deposited as the protection layer. (5) Polystyrene spheres are removed by adhesive tape and a second single-step DRIE is used for hole etching. (6) Nickel film is removed by immersing substrates into hydrochloric acid. (7) Assemble supramolecular nanoparticles into the holes.

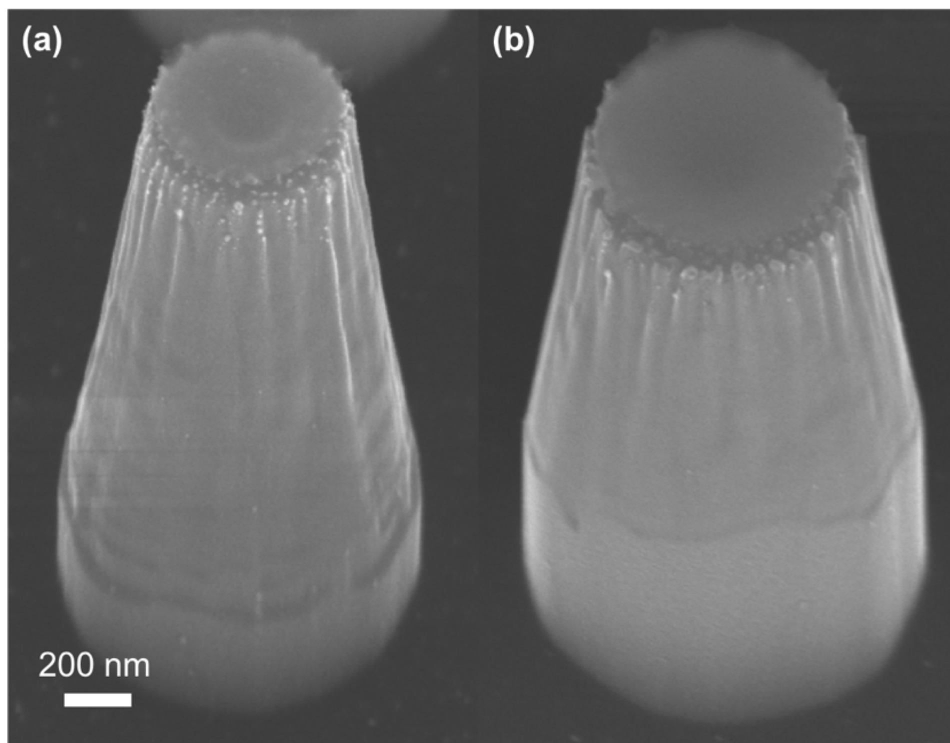

Figure S6.3. Dry etching of silicon nanocones with different C_4F_8/SF_6 ratio. The apex diameters as well as hole diameters become larger with increased C_4F_8. For example, in (a) C_4F_8/SF_6 = 23 sccm/27 sccm, and in (b) C_4F_8/SF_6 = 25 sccm/27 sccm.

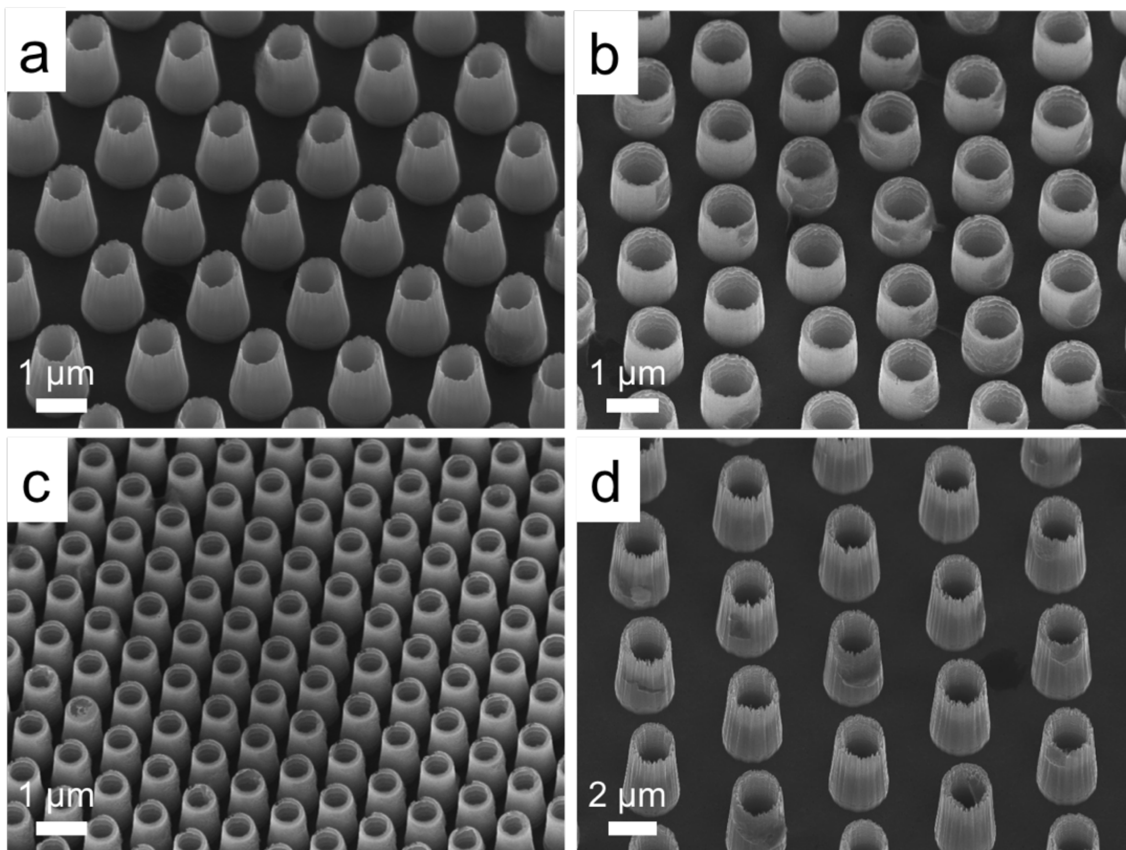

Figure S6.4. Representative scanning electron microscope (SEM) images of silicon nanovolcanos with different parameters. (a) Column #2 in Table 6.1: pitch = 2.0 μm; height = 2.5 ± 0.1 μm; hole diameter = 740 ± 30 nm. (b) Column #3 in Table 6.1: pitch = 2.0 μm; height = 1.6 ± 0.1 μm; hole diameter = 1000 ± 30 nm. (c) Column #4 in Table 6.1: pitch = 1.0 μm; height = 1.8 ± 0.1 μm; hole diameter = 550 ± 20 nm. (b) Column #5 in Table 6.1: pitch = 5.0 μm; height = 4.7 ± 0.1 μm; hole diameter = 1650 ± 50 nm.

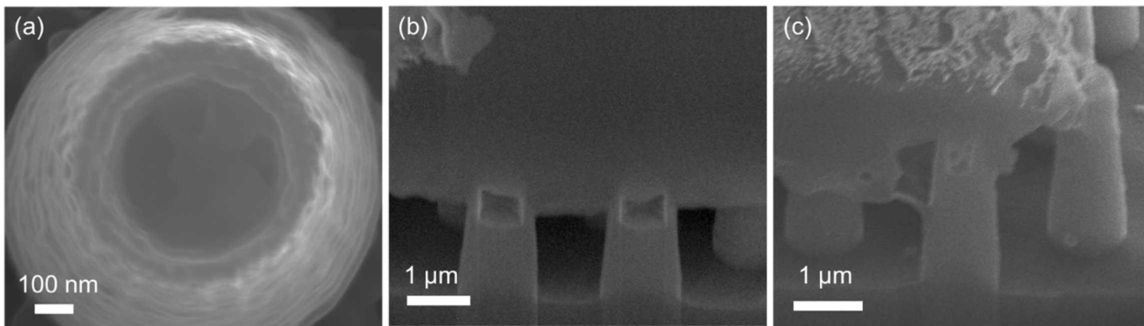

Figure S6.5. Original scanning electron microscope (SEM) images for Figure 6.3b, 6.3d, and 6.3e.

6.7 References

(1) Kim, W.; Ng, J. K.; Kunitake, M. E.; Conklin, B. R.; Yang, P. Interfacing Silicon Nanowires with Mammalian Cells. *J. Am. Chem. Soc.* **2007**, *129*, 7228–7229.

(2) VanDersarl, J. J.; Xu, A. M.; Melosh, N. A. Nanostraws for Direct Fluidic Intracellular Access. *Nano Lett.* **2012**, *12*, 3881–3886.

(3) Peer, E.; Artzy-Schnirman, A.; Gepstein, L.; Sivan, U. Hollow Nanoneedle Array and Its Utilization for Repeated Administration of Biomolecules to the Same Cells. *ACS Nano* **2012**, *6*, 4940–4946.

(4) Xie, X.; Xu, A. M.; Leal-Ortiz, S.; Cao, Y.; Garner, C. C.; Melosh, N. A. Nanostraw–Electroporation System for Highly Efficient Intracellular Delivery and Transfection. *ACS Nano* **2013**, *7*, 4351–4358.

(5) Yoo, S. M.; Kang, M.; Kang, T.; Kim, D. M.; Lee, S. Y.; Kim, B. Electrotriggered, Spatioselective, Quantitative Gene Delivery into a Single Cell Nucleus by Au Nanowire Nanoinjector. *Nano Lett.* **2013**, *13*, 2431–2435.

(6) Peng, J.; Garcia, M. A.; Choi, J.-S.; Zhao, L.; Chen, K.-J.; Bernstein, J. R.; Peyda, P.; Hsiao, Y.-S.; Liu, K. W.; Lin, W.-Y.; Pyle, A. D.; Wang, H.; Hou, S.; Tseng, H.-R. Molecular Recognition Enables Nanosubstrate-Mediated Delivery of Gene-Encapsulated Nanoparticles with High Efficiency. *ACS Nano* **2014**, *8*, 4621–4629.

(7) Wang, Y.; Yang, Y.; Yan, L.; Kwok, S. Y.; Li, W.; Wang, Z.; Zhu, X.; Zhu, G.; Zhang, W.; Chen, X.; Shi, P. Poking Cells for Efficient Vector-Free Intracellular Delivery. *Nat. Commun.* **2014**, *5*, 4466.

(8) Elnathan, R.; Delalat, B.; Brodoceanu, D.; Alhmoud, H.; Harding, F. J.; Buehler, K.; Nelson, A.; Isa, L.; Kraus, T.; Voelcker, N. H. Maximizing Transfection Efficiency of Vertically Aligned Silicon Nanowire Arrays. *Adv. Fun. Mater.* **2015**, *25*, 7215–7225.

(9) Chiappini, C.; De Rosa, E.; Martinez, J. O.; Liu, X.; Steele, J.; Stevens, M. M.; Tasciotti, E. Biodegradable Silicon Nanoneedles Delivering Nucleic Acids Intracellularly Induce Localized *in Vivo* Neovascularization. *Nat. Mater.* **2015**, *14*, 532–539.

(10) Qin, X.-F.; An, D. S.; Chen, I. S. Y.; Baltimore, D. Inhibiting HIV-1 Infection in Human T Cells by Lentiviral-Mediated Delivery of Small Interfering RNA against CCR5. *Proc. Natl. Acad. Sci. U. S. A.* **2003**, *100*, 183–188.

(11) Shalek, A. K.; Gaublomme, J. T.; Wang, L.; Yosef, N.; Chevrier, N.; Andersen, M. S.; Robinson, J. T.; Pochet, N.; Neuberg, D.; Gertner, R. S.; Amit, I.; Brown, J. R.; Hacohen, N.; Regev, A.; Wu, C. J.; Park, H. Nanowire-Mediated Delivery Enables Functional Interrogation of Primary Immune Cells: Application to the Analysis of Chronic Lymphocytic Leukemia. *Nano Lett.* **2012**, *12*, 6498–6504.

(12) Nair, B. G.; Hagiwara, K.; Ueda, M.; Yu, H.-H.; Tseng, H.-R.; Ito, Y. High Density of Aligned Nanowire Treated with Polydopamine for Efficient Gene Silencing by siRNA According to Cell Membrane Perturbation. *ACS Appl. Mater. Interfaces* **2016**, *8*, 18693–18700.

(13) Yang, C.; Panwar, N.; Wang, Y.; Zhang, B.; Liu, M.; Toh, H.; Yoon, H. S.; Tjin, S. C.; Chong, P. H. J.; Law, W.-C.; Chen, C.-K.; Yong, K.-T. Biodegradable Charged Polyester-Based Vectors (BCPVs) as an Efficient Non-Viral Transfection Nanoagent for Gene Knockdown of the BCR-ABL Hybrid Oncogene in a Human Chronic Myeloid Leukemia Cell Line. *Nanoscale* **2016**, *8*, 9405–9416.

(14) Lin, G.; Chen, C.-K.; Yin, F.; Yang, C.; Tian, J.; Chen, T.; Xu, G.; He, C.; Lin, M. C.-M.; Wang, J.; Lu, F.; Wang, X.; Yong, K.-T. Biodegradable Nanoparticles as siRNA Carriers for *in Vivo* Gene Silencing and Pancreatic Cancer Therapy. *J. Mater. Chem. B* **2017**, *5*, 3327–3337.

(15) Liu, Y.; Wang, H.; Kamei, K.-i.; Yan, M.; Chen, K.-J.; Yuan, Q.; Shi, L.; Lu, Y.; Tseng, H.-R. Delivery of Intact Transcription Factor by Using Self-Assembled Supramolecular Nanoparticles. *Angew. Chem. Int. Ed.* **2011**, *123*, 3114–3118.

(16) Sharei, A.; Zoldan, J.; Adamo, A.; Sim, W. Y.; Cho, N.; Jackson, E.; Mao, S.; Schneider, S.; Han, M.-J.; Lytton-Jean, A.; Basto, P. A.; Jhunjhunwala, S.; Lee, J.; Heller, D. A.; Kang, J. W.; Hartoularos, G. C.; Kim, K.-S.; Anderson, D. G.; Langer, R.; Jensen, K. F. A Vector-Free Microfluidic Platform for Intracellular Delivery. *Proc. Natl. Acad. Sci. U. S. A.* **2013**, *110*, 2082–2087.

(17) Wu, Y.-C.; Wu, T.-H.; Clemens, D. L.; Lee, B.-Y.; Wen, X.; Horwitz, M. A.; Teitell, M. A.; Chiou, P.-Y. Massively Parallel Delivery of Large Cargo into Mammalian Cells with Light Pulses. *Nat. Meth.* **2015**, *12*, 439–444.

(18) Schumann, K.; Lin, S.; Boyer, E.; Simeonov, D. R.; Subramaniam, M.; Gate, R. E.; Haliburton, G. E.; Ye, C. J.; Bluestone, J. A.; Doudna, J. A.; Marson, A. Generation of Knock-in Primary Human T Cells Using Cas9 Ribonucleoproteins. *Proc. Natl. Acad. Sci.* **2015**, *112*, 10437–10442.

(19) Mout, R.; Ray, M.; Yesilbag Tonga, G.; Lee, Y.-W.; Tay, T.; Sasaki, K.; Rotello, V. M. Direct Cytosolic Delivery of CRISPR/Cas9-Ribonucleoprotein for Efficient Gene Editing. *ACS Nano* **2017**, *11*, 2452–2458.

(20) Shalek, A. K.; Robinson, J. T.; Karp, E. S.; Lee, J. S.; Ahn, D.-R.; Yoon, M.-H.; Sutton, A.; Jorgolli, M.; Gertner, R. S.; Gujral, T. S.; MacBeath, G.; Yang, E. G.; Park, H. Vertical Silicon Nanowires as a Universal Platform for Delivering Biomolecules into Living Cells. *Proc. Natl. Acad. Sci.* **2010**, *107*, 1870–1875.

(21) Erogbogbo, F.; Yong, K.-T.; Roy, I.; Xu, G.; Prasad, P. N.; Swihart, M. T. Biocompatible Luminescent Silicon Quantum Dots for Imaging of Cancer Cells. *ACS Nano* **2008**, *2*, 873–878.

(22) Yong, K.-T.; Ding, H.; Roy, I.; Law, W.-C.; Bergey, E. J.; Maitra, A.; Prasad, P. N. Imaging Pancreatic Cancer Using Bioconjugated Inp Quantum Dots. *ACS Nano* **2009**, *3*, 502–510.

(23) Park, S.; Kim, Y.-S.; Kim, W. B.; Jon, S. Carbon Nanosyringe Array as a Platform for Intracellular Delivery. *Nano Lett.* **2009**, *9*, 1325–1329.

(24) Chiappini, C.; Martinez, J. O.; De Rosa, E.; Almeida, C. S.; Tasciotti, E.; Stevens, M. M. Biodegradable Nanoneedles for Localized Delivery of Nanoparticles *in Vivo*: Exploring the Biointerface. *ACS Nano* **2015**, *9*, 5500–5509.

(25) Zhao, C.; Bai, Z.; Liu, X.; Zhang, Y.; Zou, B.; Zhong, H. Small Gsh-Capped Cuins2 Quantum Dots: Mpa-Assisted Aqueous Phase Transfer and Bioimaging Applications. *ACS Appl. Mater. Interfaces* **2015**, *7*, 17623–17629.

(26) Durney, A. R.; Frenette, L. C.; Hodvedt, E. C.; Krauss, T. D.; Mukaibo, H. Fabrication of Tapered Microtube Arrays and Their Application as a Microalgal Injection Platform. *ACS Appl. Mater. Interfaces* **2016**, *8*, 34198–34208.

(27) Michalet, X.; Pinaud, F. F.; Bentolila, L. A.; Tsay, J. M.; Doose, S.; Li, J. J.; Sundaresan, G.; Wu, A. M.; Gambhir, S. S.; Weiss, S. Quantum Dots for Live Cells, *in Vivo* Imaging, and Diagnostics. *Science* **2005**, *307*, 538–544.

(28) Xu, X.; Li, H.; Hasan, D.; Ruoff, R. S.; Wang, A. X.; Fan, D. L. Near-Field Enhanced Plasmonic-Magnetic Bifunctional Nanotubes for Single Cell Bioanalysis. *Adv. Fun. Mater.* **2013**, *23*, 4332–4338.

(29) Na, Y.-R.; Kim, S. Y.; Gaublomme, J. T.; Shalek, A. K.; Jorgolli, M.; Park, H.; Yang, E. G. Probing Enzymatic Activity inside Living Cells Using a Nanowire–Cell "Sandwich" Assay. *Nano Lett.* **2013**, *13*, 153–158.

(30) Hanson, L.; Zhao, W.; Lou, H.-Y.; Lin, Z. C.; Lee, S. W.; Chowdary, P.; Cui, Y.; Cui, B. Vertical Nanopillars for in Situ Probing of Nuclear Mechanics in Adherent Cells. *Nat. Nanotechnol.* **2015**, *10*, 554–562.

(31) Xu, X.; Kim, K.; Fan, D. Tunable Release of Multiplex Biochemicals by Plasmonically Active Rotary Nanomotors. *Angew. Chem. Int. Ed.* **2015**, *54*, 2525–2529.

(32) Chiappini, C. Nanoneedle-Based Sensing in Biological Systems. *ACS Sensors* **2017**, *2*, 1086–1102.

(33) Cao, Y.; Hjort, M.; Chen, H.; Birey, F.; Leal-Ortiz, S. A.; Han, C. M.; Santiago, J. G.; Paşca, S. P.; Wu, J. C.; Melosh, N. A. Nondestructive Nanostraw Intracellular Sampling for Longitudinal Cell Monitoring. *Proc. Natl. Acad. Sci.* **2017**, *114*, E1866–E1874.

(34) Kay, M. A. State-of-the-Art Gene-Based Therapies: The Road Ahead. *Nat. Rev. Genet.* **2011**, *12*, 316–328.

(35) Naldini, L. *Ex Vivo* Gene Transfer and Correction for Cell-Based Therapies. *Nat. Rev. Genet.* **2011**, *12*, 301–315.

(36) Yin, H.; Kanasty, R. L.; Eltoukhy, A. A.; Vegas, A. J.; Dorkin, J. R.; Anderson, D. G. Non-Viral Vectors for Gene-Based Therapy. *Nat. Rev. Genet.* **2014**, *15*, 541–555.

(37) Tebas, P.; Stein, D.; Tang, W. W.; Frank, I.; Wang, S. Q.; Lee, G.; Spratt, S. K.; Surosky, R. T.; Giedlin, M. A.; Nichol, G.; Holmes, M. C.; Gregory, P. D.; Ando, D. G.; Kalos, M.; Collman, R. G.; Binder-Scholl, G.; Plesa, G.; Hwang, W.-T.; Levine, B. L.; June, C. H. Gene Editing of CCR5 in Autologous CD4 T Cells of Persons Infected with HIV. *N. Engl. J. Med.* **2014**, *370*, 901–910.

(38) Naldini, L. Gene Therapy Returns to Centre Stage. *Nature* **2015**, *526*, 351–360.

(39) Fox, C. B.; Cao, Y.; Nemeth, C. L.; Chirra, H. D.; Chevalier, R. W.; Xu, A. M.; Melosh, N. A.; Desai, T. A. Fabrication of Sealed Nanostraw Microdevices for Oral Drug Delivery. *ACS Nano* **2016**, *10*, 5873–5881.

(40) Hasani-Sadrabadi, M. M.; Taranejoo, S.; Dashtimoghadam, E.; Bahlakeh, G.; Majedi, F. S.; VanDersarl, J. J.; Janmaleki, M.; Sharifi, F.; Bertsch, A.; Hourigan, K.; Tayebi, L.; Renaud, P.; Jacob, K. I. Microfluidic Manipulation of Core/Shell Nanoparticles for Oral Delivery of Chemotherapeutics: A New Treatment Approach for Colorectal Cancer. *Adv. Mater.* **2016**, *28*, 4134–4141.

(41) Rosenberg, S. A.; Restifo, N. P. Adoptive Cell Transfer as Personalized Immunotherapy for Human Cancer. *Science* **2015**, *348*, 62–68.

(42) Cavazzana-Calvo, M.; Payen, E.; Negre, O.; Wang, G.; Hehir, K.; Fusil, F.; Down, J.; Denaro, M.; Brady, T.; Westerman, K.; Cavallesco, R.; Gillet-Legrand, B.; Caccavelli, L.; Sgarra, R.; Maouche-Chrétien, L.; Bernaudin, F.; Girot, R.; Dorazio, R.; Mulder, G.-J.; Polack, A.; Bank, A.; Soulier, J.; Larghero, J.; Kabbara, N.; Dalle, B.; Gourmel, B.; Socie, G.; Chrétien, S.; Cartier, N.; Aubourg, P.; Fischer, A.; Cornetta, K.; Galacteros, F.; Beuzard, Y.; Gluckman, E.; Bushman, F.; Hacein-Bey-Abina, S.; Leboulch, P. Transfusion Independence and HMGA2 Activation after Gene Therapy of Human β-Thalassaemia. *Nature* **2010**, *467*, 318–322.

(43) Hou, S.; Choi, J.-S.; Chen, K.-J.; Zhang, Y.; Peng, J.; Garcia, M. A.; Yu, J.-H.; Thakore-Shah, K.; Ro, T.; Chen, J.-F.; Peyda, P.; Fan, G.; Pyle, A. D.; Wang, H.; Tseng, H.-R. Supramolecular Nanosubstrate-Mediated Delivery for Reprogramming and Transdifferentiation of Mammalian Cells. *Small* **2015**, *11*, 2499–2504.

(44) Thomas, C. E.; Ehrhardt, A.; Kay, M. A. Progress and Problems with the Use of Viral Vectors for Gene Therapy. *Nat. Rev. Genet.* **2003**, *4*, 346–358.

(45) Fu, J.; Wang, Y.-K.; Yang, M. T.; Desai, R. A.; Yu, X.; Liu, Z.; Chen, C. S. Mechanical Regulation of Cell Function with Geometrically Modulated Elastomeric Substrates. *Nat. Methods* **2010**, *7*, 733–736.

(46) Chopra, A.; Krishnan, S.; Simmel, F. C. Electrotransfection of Polyamine Folded DNA Origami Structures. *Nano Lett.* **2016**, *16*, 6683–6690.

(47) Wu, T.-H.; Teslaa, T.; Kalim, S.; French, C. T.; Moghadam, S.; Wall, R.; Miller, J. F.; Witte, O. N.; Teitell, M. A.; Chiou, P.-Y. Photothermal Nanoblade for Large Cargo Delivery into Mammalian Cells. *Anal. Chem.* **2011**, *83*, 1321–1327.

(48) Wu, T.-H.; Sagullo, E.; Case, D.; Zheng, X.; Li, Y.; Hong, Jason S.; TeSlaa, T.; Patananan, Alexander N.; McCaffery, J. M.; Niazi, K.; Braas, D.; Koehler, Carla M.; Graeber, Thomas G.; Chiou, P.-Y.; Teitell, Michael A. Mitochondrial Transfer by Photothermal Nanoblade Restores Metabolite Profile in Mammalian Cells. *Cell Metab.* **2016**, *23*, 921–929.

(49) Stewart, M. P.; Sharei, A.; Ding, X.; Sahay, G.; Langer, R.; Jensen, K. F. *In Vitro* and *ex Vivo* Strategies for Intracellular Delivery. *Nature* **2016**, *538*, 183–192.

(50) Xu, X.; Liu, C.; Kim, K.; Fan, D. L. Electric-Driven Rotation of Silicon Nanowires and Silicon Nanowire Motors. *Adv. Fun. Mater.* **2014**, *24*, 4843–4850.

(51) Xie, X.; Xu, A. M.; Angle, M. R.; Tayebi, N.; Verma, P.; Melosh, N. A. Mechanical Model of Vertical Nanowire Cell Penetration. *Nano Lett.* **2013**, *13*, 6002–6008.

(52) Xu, A. M.; Aalipour, A.; Leal-Ortiz, S.; Mekhdjian, A. H.; Xie, X.; Dunn, A. R.; Garner, C. C.; Melosh, N. A. Quantification of Nanowire Penetration into Living Cells. *Nat. Commun.* **2014**, *5*, 3613.

(53) Saklayen, N.; Huber, M.; Madrid, M.; Nuzzo, V.; Vulis, D. I.; Shen, W.; Nelson, J.; McClelland, A. A.; Heisterkamp, A.; Mazur, E. Intracellular Delivery Using Nanosecond-Laser Excitation of Large-Area Plasmonic Substrates. *ACS Nano* **2017**, *11*, 3671–3680.

(54) Xu, X.; Yang, Q.; Cheung, K. M.; Zhao, C.; Wattanatorn, N.; Belling, J. N.; Abendroth, J. M.; Slaughter, L. S.; Mirkin, C. A.; Andrews, A. M.; Weiss, P. S. Polymer-Pen Chemical Lift-Off Lithography. *Nano Lett.* **2017**, *17*, 3302–3311.

(55) Fan, D.; Yin, Z.; Cheong, R.; Zhu, F. Q.; Cammarata, R. C.; Chien, C. L.; Levchenko, A. Subcellular-Resolution Delivery of a Cytokine through Precisely Manipulated Nanowires. *Nat. Nanotechnol.* **2010**, *5*, 545−551.

(56) Xu, X.; Kim, K.; Li, H.; Fan, D. L. Ordered Arrays of Raman Nanosensors for Ultrasensitive and Location Predictable Biochemical Detection. *Adv. Mater.* **2012**, *24*, 5457–5463.

(57) Garcia-Gradilla, V.; Orozco, J.; Sattayasamitsathit, S.; Soto, F.; Kuralay, F.; Pourazary, A.; Katzenberg, A.; Gao, W.; Shen, Y.; Wang, J. Functionalized Ultrasound-Propelled Magnetically Guided Nanomotors: Toward Practical Biomedical Applications. *ACS Nano* **2013**, *7*, 9232–9240.

(58) Kim, K.; Xu, X.; Guo, J.; Fan, D. L. Ultrahigh-Speed Rotating Nanoelectromechanical System Devices Assembled from Nanoscale Building Blocks. *Nat. Commun.* **2014**, *5*, 3632.

(59) Soto, F.; Martin, A.; Ibsen, S.; Vaidyanathan, M.; Garcia-Gradilla, V.; Levin, Y.; Escarpa, A.; Esener, S. C.; Wang, J. Acoustic Microcannons: Toward Advanced Microballistics. *ACS Nano* **2016**, *10*, 1522–1528.

(60) Li, J.; Rozen, I.; Wang, J. Rocket Science at the Nanoscale. *ACS Nano* **2016**, *10*, 5619–5634.

(61) Magdanz, V.; Medina-Sánchez, M.; Schwarz, L.; Xu, H.; Elgeti, J.; Schmidt, O. G. Spermatozoa as Functional Components of Robotic Microswimmers. *Adv. Mater.* **2017**, *29*, 1606301.

(62) Ren, L.; Zhou, D.; Mao, Z.; Xu, P.; Huang, T. J.; Mallouk, T. E. Rheotaxis of Bimetallic Micromotors Driven by Chemical–Acoustic Hybrid Power. *ACS Nano* **2017**, *11*, 10591−10598.

(63) Hansen-Bruhn, M.; de Ávila, B. E.-F.; Beltrán-Gastélum, M.; Zhao, J.; Ramírez-Herrera, D. E.; Angsantikul, P.; Gothelf, K. V.; Zhang, L.; Wang, J. Active Intracellular Delivery of a Cas9/sgRNA Complex Using Ultrasound-Propelled Nanomotors. *Angew. Chem. Int. Ed.* **2018**, *57*, 2657–2661.

(64) Xu, X.; Hou, S.; Wattanatorn, N.; Wang, F.; Yang, Q.; Zhao, C.; Yu, X.; Tseng, H.-R.; Jonas, S. J.; Weiss, P. S. Precision-Guided Nanospears for Targeted and High-Throughput Intracellular Gene Delivery. *ACS Nano* **2018**, *12*, 4503–4511.

(65) Xu, X.; Yang, Q.; Wattanatorn, N.; Zhao, C.; Chiang, N.; Jonas, S. J.; Weiss, P. S. Multiple-Patterning Nanosphere Lithography for Fabricating Periodic Three-Dimensional Hierarchical Nanostructures. *ACS Nano* **2017**, *11*, 10384–10391.

(66) Davis, M. E.; Zuckerman, J. E.; Choi, C. H. J.; Seligson, D.; Tolcher, A.; Alabi, C. A.; Yen, Y.; Heidel, J. D.; Ribas, A. Evidence of RNAi in Humans from Systemically Administered siRNA *via* Targeted Nanoparticles. *Nature* **2010**, *464*, 1067–1070.

(67) Davis, M. E.; Brewster, M. E. Cyclodextrin-Based Pharmaceutics: Past, Present and Future. *Nat. Rev. Drug Discov.* **2004**, *3*, 1023–1035.

(68) Xie, X.; Aalipour, A.; Gupta, S. V.; Melosh, N. A. Determining the Time Window for Dynamic Nanowire Cell Penetration Processes. *ACS Nano* **2015**, *9*, 11667–11677.

(69) Hulteen, J. C.; Duyne, R. P. V. Nanosphere Lithography: A Materials General Fabrication Process for Periodic Particle Array Surfaces. *J. Vac. Sci. Technol. A* **1995**, *13*, 1553–1558.

(70) Zheng, Y. B.; Payton, J. L.; Chung, C.-H.; Liu, R.; Cheunkar, S.; Pathem, B. K.; Yang, Y.; Jensen, L.; Weiss, P. S. Surface-Enhanced Raman Spectroscopy to Probe Reversibly Photoswitchable Azobenzene in Controlled Nanoscale Environments. *Nano Lett.* **2011**, *11*, 3447–3452.

(71) Haynes, C. L.; Van Duyne, R. P. Nanosphere Lithography: A Versatile Nanofabrication Tool for Studies of Size-Dependent Nanoparticle Optics. *J. Phys. Chem. B* **2001**, *105*, 5599–5611.

(72) Chen, K.; Rajeeva, B. B.; Wu, Z.; Rukavina, M.; Dao, T. D.; Ishii, S.; Aono, M.; Nagao, T.; Zheng, Y. Moiré Nanosphere Lithography. *ACS Nano* **2015**, *9*, 6031–6040.

(73) Gao, P.; He, J.; Zhou, S.; Yang, X.; Li, S.; Sheng, J.; Wang, D.; Yu, T.; Ye, J.; Cui, Y. Large-Area Nanosphere Self-Assembly by a Micro-Propulsive Injection Method for High Throughput Periodic Surface Nanotexturing. *Nano Lett.* **2015**, *15*, 4591–4598.

(74) Tang, S. K. Y.; Marshall, W. F. Self-Repairing Cells: How Single Cells Heal Membrane Ruptures and Restore Lost Structures. *Science* **2017**, *356*, 1022–1025.

(75) Wang, H.; Wang, S.; Su, H.; Chen, K.-J.; Armijo, A. L.; Lin, W.-Y.; Wang, Y.; Sun, J.; Kamei, K.-I.; Czernin, J.; Radu, C. G.; Tseng, H.-R. A Supramolecular Approach for Preparation of Size-Controlled Nanoparticles. *Angew. Chem. Int. Ed.* **2009**, *48*, 4344–4348.

(76) Wang, H.; Liu, K.; Chen, K.-J.; Lu, Y.; Wang, S.; Lin, W.-Y.; Guo, F.; Kamei, K.-i.; Chen, Y.-C.; Ohashi, M.; Wang, M.; Garcia, M. A.; Zhao, X.-Z.; Shen, C. K. F.; Tseng, H.-R. A Rapid Pathway toward a Superb Gene Delivery System: Programming Structural and Functional Diversity into a Supramolecular Nanoparticle Library. *ACS Nano* **2010**, *4*, 6235–6243.

(77) Wang, H.; Chen, K.-J.; Wang, S.; Ohashi, M.; Kamei, K.-i.; Sun, J.; Ha, J. H.; Liu, K.; Tseng, H.-R. A Small Library of DNA-Encapsulated Supramolecular Nanoparticles for Targeted Gene Delivery. *Chem. Comm.* **2010**, *46*, 1851–1853.

(78) Hou, S.; Choi, J.-S.; Garcia, M. A.; Xing, Y.; Chen, K.-J.; Chen, Y.-M.; Jiang, Z. K.; Ro, T.; Wu, L.; Stout, D. B.; Tomlinson, J. S.; Wang, H.; Chen, K.; Tseng, H.-R.; Lin, W.-Y. Pretargeted Positron Emission Tomography Imaging That Employs Supramolecular Nanoparticles with *in Vivo* Bioorthogonal Chemistry. *ACS Nano* **2016**, *10*, 1417–1424.

(79) Choi, J.-S.; Zhu, Y.; Li, H.; Peyda, P.; Nguyen, T. T.; Shen, M. Y.; Yang, Y. M.; Zhu, J.; Liu, M.; Lee, M. M.; Sun, S.-S.; Yang, Y.; Yu, H.-h.; Chen, K.; Chuang, G. S.; Tseng, H.-R. Cross-Linked Fluorescent Supramolecular Nanoparticles as Finite Tattoo Pigments with Controllable Intradermal Retention Times. *ACS Nano* **2017**, *11*, 153–162.

(80) Wang, S.; Chen, K.-J.; Wu, T.-H.; Wang, H.; Lin, W.-Y.; Ohashi, M.; Chiou, P.-Y.; Tseng, H.-R. Photothermal Effects of Supramolecularly Assembled Gold Nanoparticles for the Targeted Treatment of Cancer Cells. *Angew. Chem. Int. Ed.* **2010**, *49*, 3777–3781.

(81) Liu, K.; Wang, H.; Chen, K.-J.; Guo, F.; Lin, W.-Y.; Chen, Y.-C.; Phung, D. L.; Tseng, H.-R.; Clifton, Shen, C. K.-F. A Digital Microfluidic Droplet Generator Produces Self-Assembled Supramolecular Nanoparticles for Targeted Cell Imaging. *Nanotechnology* **2010**, *21*, 445603.

(82) Chen, K.-J.; Tang, L.; Garcia, M. A.; Wang, H.; Lu, H.; Lin, W.-Y.; Hou, S.; Yin, Q.; Shen, C. K.-F.; Cheng, J.; Tseng, H.-R. The Therapeutic Efficacy of Camptothecin-Encapsulated Supramolecular Nanoparticles. *Biomaterials* **2012**, *33*, 1162–1169.

(83) Chen, K.-J.; Wolahan, S. M.; Wang, H.; Hsu, C.-H.; Chang, H.-W.; Durazo, A.; Hwang, L.-P.; Garcia, M. A.; Jiang, Z. K.; Wu, L.; Lin, Y.-Y.; Tseng, H.-R. A Small Mri Contrast Agent Library of Gadolinium(Iii)-Encapsulated Supramolecular Nanoparticles for Improved Relaxivity and Sensitivity. *Biomaterials* **2011**, *32*, 2160–2165.

(84) Hanson, L.; Lin, Z. C.; Xie, C.; Cui, Y.; Cui, B. Characterization of the Cell–Nanopillar Interface by Transmission Electron Microscopy. *Nano Lett.* **2012**, *12*, 5815–5820.

(85) Smith, R. K.; Lewis, P. A.; Weiss, P. S. Patterning Self-Assembled Monolayers. *Prog. Surf. Sci.* **2004**, *75*, 1–68.

(86) Wang, J.; Ye, Y.; Yu, J.; Kahkoska, A. R.; Zhang, X.; Wang, C.; Sun, W.; Corder, R. D.; Chen, Z.; Khan, S. A.; Buse, J. B.; Gu, Z. Core–Shell Microneedle Gel for Self-Regulated Insulin Delivery. *ACS Nano* **2018**, *12*, 2466–2473.

(87) Zhang, Y.; Liu, Q.; Yu, J.; Yu, S.; Wang, J.; Qiang, L.; Gu, Z., Locally Induced Adipose Tissue Browning by Microneedle Patch for Obesity Treatment. *ACS Nano* **2017**, *11*, 9223–9230.